Investigation Of Geodesics And Shadows Of Black Hole Spacetimes

Thesis Submitted for the Degree of
Doctor of Philosophy (Science)
in
Physics (Theoretical)

by
Anish Das

Department of Physics
University of Calcutta
2023

Dedicated to my mother

Acknowledgements

This thesis is an outcome of the efforts incorporated for the last five years at Satyendra Nath Bose National Centre for Basic Sciences (SNBNCBS), Salt Lake, Kolkata. The thesis would not have been possible without the help and support of a lot of people.

First and foremost, I thank my supervisor, Dr. Sunandan Gangopadhyay for giving me the opportunity to work under him in this project. His continuous interest and regular involvement in the work and his brilliant insights in physics has always been a blessing for me. His enthusiasm and dedication towards research and his work ethics has always inspired me to learn more and work even harder. The discussions that I had with him always increased my interest towards the subject even further.

I would also like to thank my collaborator and a great brother Dr. Ashis Saha to be always there in need. His enthusiasm and knowledge on various aspects helped me greatly in our collaborative projects. Besides, his regular push and involvement helped me in my work immensely.

Apart from that I would like thank my group mates especially Mr. Ankur Srivastava, Mrs. Rituparna Mandal and Mr. Anirban Roy Chowdhury for fruitful academic discussions and necessary assistance. Also, I would like to thank Mr. Sidhhartha Biswas for filling the vacancy of an elder brother during my Ph.D journey. I also thank Mr. Ritwick Sarkar for being the younger brother with whom I can share my thoughts and discuss throroughly about anything and everything. Also, I would thank Mr. Shivam Mishra for making the journey enjoyable and memorable. I would also like to thank my baymates for many memories and their help and cooperation in times of need.

I would also like to mention the support of Ria Di (Ms. Debangana Naha) who has always guided me in my tough times and always invoked positivity in me. Thank you for listening to all the rubbish and gibberish I share whenever I feel depressed. Also, I would thank Mr. Debdip Roy who inspired me to pursue a career in Physics. I would like to thank our beloved BCR Sir (Dr. Bidhan Chandra Roy) for incorporating enormous taste of physics within me by making Physics as simple as possible. I would also like to thank my friend Mr. Md. Baset Ali to push me to never give up in life. Besides, I would like to thank Mr. Tanmoyendu Chakraborty for being a support in need and a guide and a motivator. Also I thank Mr. Debarshi Dey for being an inspiration in many aspects of life and teaching me the practicality of life.

Also, I would like to thank SNBNCBS for financial assistance that they provided in terms of monthly fellowship during this entire period. This helped me carry out my research fruitfully and independently.

Finally I would like to thank the support of my parents for being there for me and helping me achieve what I intended to. They always supported me and have always been my backbone throughout my journey. Also I want to thank the support of my relatives during the period of my upbringing and even to this day.

সার- সংক্ষেপ

এই থিসিসে আমরা কৃষ্ণ গহ্বর (black hole) এর কাছাকাছি থাকা ভরহীন (massless) এবং ভরপ্রাপ্ত (massive) উভয় কনার গতিপথ অধ্যায়ন করেছি নানান পরিস্থিতিতে। আমাদের প্রাথমিক কৌতূহল কৃষ্ণ গহ্বর এর ছায়া (black hole shadow) অধ্যায়ন। অস্থির (unstable) ভরহীন কনার গতিপথ (null geodesics) প্রবল মাধ্যাকর্ষণের মাধ্যমে কৃষ্ণ গহ্বরের ছায়া তৈরি করে।ওপর দিকে ভর প্রাপ্ত কনার কক্ষপথ (timelike geodesics) কৃষ্ণ গহ্বর এর চারিদিকে ভর যুক্ত কনার নানান বৈশিষ্ট্য বিষয়ে আমাদের অবগত করে। উপরন্তু এই থিসিস এর আরো একটি গুরুতবপূর্ণ বিষয় হলো কৃষ্ণ গহ্বরের ছায়ায় প্লাজমার (plasma) প্রভাব অধ্যায়ন। কৃষ্ণ গহ্বর এর ছায়া অধ্যয়নের গুরুত্ব এই যে, এটা প্রথম সরাসরি দ্রষ্টব্য প্রমাণ কৃষ্ণ গহ্বরের অস্তিত্বের।

আমাদের প্রথম কাজ যেটা আমরা অধ্যায় (chapter) ২ এ বিশ্লেষণ করেছি, সেখানে আমরা কৃষ্ণ গহ্বরের ছায়া গণনা এবং বিশ্লেষণ করেছি একটা ঊর্ধ্বতন বক্রতা সম্পন্ন মাধ্যাকর্ষীয় তত্ব তে, যার নাম গাউস – বন্নেট (Gauss Bonnet) মাধ্যাকর্ষীয় তত্ব। আমরা একটা আধান (charge) সম্পন্ন কৃষ্ণ গহ্বর ধারণা করি যেটা খোচিত আছে একটি আসিম্পটিকালি (asymptotically) AdS সেইসাথে মিনকাউজকি (Minkowski) পটভূমি তে।আমরা কৃষ্ণ গহ্বরের ছায়া অধ্যায়ন করেছি d=5 মাত্রায় (dimension), কারণ স্পেস টাইম এর গতিবিধি তে গাউস – বন্নেট মাধ্যাকর্ষীয় তত্ব প্রভাব ফেলে d>=5 মাত্রায়। গাউস বন্নেট এর স্থিথিমাপ γ এর প্রভাবের প্রকৃতি নির্ভর করে স্পেস টাইম এর পটভূমির ওপর (AdS কিংবা Minkowski)। এছাড়াও কৃষ্ণ গহ্বর এর ছায়া কৃষ্ণ গহ্বর এর আধান Q দ্বারা প্রভাবিত হয়। আমরা এও আবিষ্কার করি যে প্লাসমার উপস্থিতিতে, কৃষ্ণ গহ্বর এর ছায়া উল্লেখযোগ্যভাবে পরিবর্তিত হয়। অবশেষে আমরা লক্ষ করি যে বক্রতার স্থিথিমাপ γ কৃষ্ণ গহ্বরের শক্তি নিঃসরণ এর হার কে প্রভাবিত করে যা গহ্বরের ছায়ার ব্যাসার্ধের ওপর নির্ভর করে।

অধ্যায় (chapters) ৩ এবং ৪ এ আমরা চর্চা করেছি একটা ডার্ক ম্যাটার প্রার্থীর (dark matter candidate) (যার নাম পারফেক্ট ফ্লুইড ডার্ক ম্যাটার (PFDM))প্রভাব কনার গতিপথ আর তার সম্পর্কিত স্থিথিমাপ এ।অধ্যায় ৩ এ আমরা ভারপ্রাপ্ত এবং ভরহীন উভয় কনার গতিপথ চর্চায় নিবদ্ধ হয়েছি এবং বিশ্লেষণ করেছি কীভাবে পিএফডিএম এর স্থিথিমাপ (parameter) সংযুক্ত স্থিথিমাপ গুলো কে প্রভাবিত করে। ভরহীন কনার ক্ষেত্রে আমরা ফোটন এর ব্যাসার্ধ গণনা করেছি অন্যদিকে ভারপ্রাপ্ত কনার ক্ষেত্রে আমরা গণনা করেছি প্রতি ইউনিট ভর শক্তি E এবং প্রতি ইউনিট ভর কৌণিক বেগ L । এছাড়াও আমরা পেনরশ প্রক্রিয়ার (Penrose process) সহজতম সংস্করণ এর চর্চা এবং এর দক্ষতার উপর পিডিএফএম চর্চা করেছি।

অধ্যায় (chapter) ৪ এ আমরা ফোটন (photon) এর কক্ষপথের ব্যাসার্ধ চর্চা করেছি একই স্পেস টাইম (spacetime) পটভূমি তে রেডিয়াল প্লাজমা বিতরণ (radial plasma distribution) কে অন্তর্ভুক্ত করে।এছাড়া আমরা কৃষ্ণ গহ্বরের ছায়া বিস্তারিত ভাবে বিশ্লেষণ এবং চর্চা করেছি। আমরা গ্রাফিক্যালি (graphically) কৃষ্ণ গহ্বরের ছায়ার গঠনের ওপর পিএফডিএম আর প্লাজমার প্রভাব চর্চা করেছি। এছাড়াও আমরা বিভিন্ন ধরনের প্লাজমা বিতরণ (distribution) বিবেচনা করেছি আমাদের বিশ্লেষণে। অবশেষে আমরা পিএফডিএম এবং প্লাজমা র স্থিথিমাপ (parameter) k কে সীমাবদ্ধ করেছি M87* অতিরিক্ত ভর প্রাপ্ত কৃষ্ণ গহ্বরের (supermassive black hole) বিশ্লেষণাত্মক ভাবে গণনা করা ফলাফলের সাথে এর পর্যবেক্ষণ মূলক গণনার তুলনা করে।

অধ্যায় （chapter） ৫ এ আমরা শোয়ার্জসচাইল্ড （Schwarzschild） এবং শোয়ার্জসচাইল্ড ডি – সিটার （Schwarzschild de −Sitter） কৃষ্ণ গহ্বরের ছায়ার চর্চা করেছি। ছায়াটিকে বিশ্লিষ্ট করা হয়েছে একটা স্থির পর্যবেক্ষকের দৃষ্টিকোণ থেকে। বিশ্ব প্রসারণের বাস্তবসম্মত দৃশ্যকল্প কে বিবেচনা করে, আমরা একজন চলনশীল পর্যবেক্ষকের দৃষ্টিকোণ থেকে কৃষ্ণ গহ্বরের ছায়া বিশ্লেষণ সম্পন্ন করি। এই কাজ করবার জন্য, আমরা ধরে নিচ্ছি যে বিশ্বের সম্প্রসারণ মহাবিশ্ব তত্ব সংক্রান্ত ধ্রুবক （cosmological constant） Λ দ্বারা চালিত এবং আমরা একটি সম্পর্ক সন্ধান করি স্থির এবং চলনশীল পর্যবেক্ষক দারা দেখা ছায়ার মধ্যে। আমরা তারপর সংখ্যাগত ভাবে ছায়ার মান গণনা করি এবং তুলনা করি M87* এবং Sgr A* কৃষ্ণ গহ্বরের পর্যবেক্ষক মূলক মানের সাথে। আমরা প্লাজমার পটভূমি কে নিগম্ভুক্ত করি এবং প্লাজমার স্থিথিমাপ （parameter） k কে পর্যবেক্ষণ মূলক ছায়ার আকার দ্বারা সীমাবদ্ধ করি।

Abstract

In this thesis, we study the geodesics (both null and timelike) around black holes in different scenarios. Our main interest lies in the analytical study of black hole shadow. The unstable photon orbits (null geodesics) form the shadows of black hole via the phenomena of strong gravitational lensing. On the other hand, the study of timelike geodesics depicts many features of the behaviour of massive particles around black holes. Additionally another important aspect of this thesis is the consideration of a material media (of plasmic nature) on the observed structure of the black hole shadow. The importance of the study of the black hole shadow lies in the fact that it serves as the first direct observable evidence of a black hole.

In our first work entailed in chapter 2, we calculated and analysed the black hole shadow and other related parameters in higher curvature gravity, namely the Gauss-Bonnet gravity. We considered a charged black hole embedded in asymptotically AdS as well as asymptotically Minkowski spacetime background. We study the black hole shadow in $d = 5$ spacetime dimensions since the spacetime dynamics gets effected by Gauss Bonnet gravity only in $d \geq 5$ dimensions. The nature of the impact of the Gauss Bonnet parameter γ on the shadow size varies depending on the background spacetime (AdS or Minkowski). Also, the shadow size gets effected by the black hole charge Q. We also find that in presence of a plasma background the black hole shadow gets modified significantly. Finally, we observe that the curvature parameter γ effects the black hole's rate of energy emission which has dependence on the shadow radius R_s.

In chapters 3 and 4 we have studied the impact of a dark matter candidate namely the perfect fluid dark matter (PFDM) on the geodesics and its related parameters. In chapter 3, we focus on the study of geodesics of both massive and massless particles and analyse how the PFDM parameter effects the associated parameters. In case of massless particles we calculated the radius of photon orbits r_p whereas for massive particles we calculated the energy per unit mass E and angular momentum per unit mass L. Also, we studied the simplest version of the Penrose process and the effect of PFDM parameter on its efficiency.

In chapter 4 we studied the radius of photon orbits in the same spacetime background incorporating a radial plasma distribution. We also analyse and study the shadow of the black hole in detail. We graphically studied the effect of PFDM as well as plasma on the structure of the black hole shadow. Also, we considered different types of plasma distribution for our analysis. Finally we put constraints on the PFDM parameter and plasma parameter by comparing our analytically calculated results with the observational one for M87* supermassive black hole.

In chapter 5, we studied the black hole shadow of Schwarzschild and Schwarzschild de-Sitter or Kottler black hole. The shadow is being analysed from the viewpoint of a static observer. Considering the realistic scenario of the expansion of the universe, we carry out the analysis of measuring the shadow from the viewpoint of a comoving observer. In order to do so, we assume the expansion to be driven by a postive cosmological constant Λ and find a relation between the shadow size measured by a static and a comoving observer. Then we numerically compute the values of the shadow sizes and compare them with the observed values of M87* and Sgr A* black holes. We incorporate the plasma background and put bounds on the plasma parameter k using the values of the observed shadow size.

List of Publications

1. **Anish Das**, Ashis Saha, Sunandan Gangopadhyay, *Shadow of charged black holes in Gauss-Bonnet gravity*, *Eur.Phys.J.C* **80** (2020) 3, 180.
2. **Anish Das**, Ashis Saha, Sunandan Gangopadhyay, *Investigation of circular geodesics in a rotating charged black hole in the presence of perfect fluid dark matter*, *Class. Quantum Grav.* **38** (2021) 065015.
3. **Anish Das**, Ashis Saha, Sunandan Gangopadhyay, *Study of circular geodesics and shadow of rotating charged black hole surrounded by perfect fluid dark matter immersed in plasma*, *Class. Quantum Grav.* **39** (2022) 075005.
4. **Anish Das**, Ashis Saha, Sunandan Gangopadhyay, *Shadow of Kottler black hole in the presence of plasma for a co-moving observer*, *Class. Quantum Grav.* **40** (2023) 015008.
5. **Anish Das**, Anirban Roy Chowdhury, Sunandan Gangopadhyay, *Stability, quasinormal modes in a charged black hole in perfect fluid dark matter*, arxiv: 2306.00646.

The first four papers are included in the thesis.

Contents

Chapter 1

Introduction and Overview

Among the extreme compact objects in the universe, black holes are the simplest and can be described using few parameters. The only elements required for their construction is the concept of space and time [1]-[3]. The theory of stellar evolution [4]-[6] shows that black holes are inevitable consequences of the stellar evolution. Thus we expect to find black holes amongst the stars residing in the galaxies. There were a lot of indirect evidences of the existence of black holes from time to time [7]. But in the present century with advancement of technology it has been possible to detect the mearging of black holes via gravitational wave signals for the first time in 2015 [8] and observe them directly in terms of the shadow image in 2019 [9].

The idea of the existence of highly compact objects which does not emit light dates back to 'dark stars' coined by Laplace and Michell [10] towards the close of 18th century. Einstein suggested general relativity near the end of 1915 [11], and Karl Schwarzschild promptly developed the simplest black hole solution in 1916 [12]. However, it was not until much later that the exact properties of black holes were discovered. In the year 1958, David Finkelstein [13] was the first person who realized the actual meaning of the black hole's event horizon (*the surface of no return*). Even the astrophysical implications of such solutions are not seriously considered. Prominent researchers such as Arthur Eddington were inclined to believe that unknown mechanisms could prevent massive objects from collapsing, thereby stopping the formation of black holes. In 1963, Roy Kerr found a solution to a spinning black hole, now named after him as the Kerr solution [14]. This is an important step, since almost all astronomical objects naturally acquire non-zero angular momentum. In 1965, Ezra Newman and his colleagues obtained the solution of a rotating, charged black hole, now known as the Kerr-Newman solution [15]. It was understood from the works of Werner Israel and colaborators [16]-[18], that black holes are simple macroscopic objects and can be fully characterized only by their mass M, spin a, and charge Q. This result goes by the name of no-hair theorem [19]. However, violations of the no-hair theorem are possible if we consider theories beyond Einstein's theory of general relativity [20]. In the late 1960s, Penrose and Hawking proved that, under general assumptions, gravitational collapse would inevitably lead to the formation of singularities [21]-[22]. This provoked Penrose to make the proposition of the cosmic censorship conjecture (CCC), which states that singularities created by gravitational collapse should remain hidden behind a surface named the event horizon and end product of any gravitational collapse should produce a black hole [23]. In the year 1964, both Yakov Zel'dovich [24] and Edwin Salpeter [25] independently proposed that the source of power of the quasars is a supermassive black hole residing at the centre. In the beginning of 1970s, Thomas

Bolton and his collaborators identified the X-ray source, namely Cygnus X-1 as the first stellar-mass black hole candidate [26], [27]. From then onwards, numerous astronomical observations have pointed to the existence of stellar-mass black holes residing in binaries and galactic centers. Due to technological progress along with advancement in observational facilities, it has been possible to study the physical properties of black holes and their vicinity. The discovery of gravitational waves from the union of two black holes by the LIGO experiment in September 2015 [8] opened a new window for studying these gravitational objects.

1.1 Importance of studying black holes

The importance of studying black holes is far and wide. They are the extreme ultra compact object to exist with a very strong gravity in their immediate vicinity. They provide the perfect ground to study the connection between quantum mechanics and gravity. Also, black holes behave as thermodynamic objects [28] and have been found to radiate (Hawking radiation) [29] and obey thermodynamic laws [30], [31]. Black hole radiation hints that they may act as grounds to study aspects of quantum gravity [32]-[35]. Thus black holes serve as important objects to study fundamental physics and help us gain insight into the missing links of fundamental physics.

1.2 Different types of black holes and their evidences

At present we have very strong evidence mainly of two classes of astrophysical black holes [36]. Black holes of falling in the stellar-mass category have masses in the range of 3 - 100 $M_{\odot}$. Most of them can be found to be existing in X-ray binaries whose evidence can be found from study of their orbital motion of the companion stellar object [37]. Stellar-mass black holes can also be found in binary systems such as black hole-black hole or black hole-neutron star. In this case, they can be detected by the gravitational waves emitted during the end stage of coalescence [8]. Attempts are also made in order to find isolated stellar-mass black holes using microlensing techniques [38], [39].
The mass of the supermassive black holes lie in the range 10^5 - 10^{10} $M_{\odot}$ and they are expected to reside at the centre of active galactic nuclei [40]. There may also exist a third class of black holes, namely the intermediate mass black holes, whose mass fills the gap between stellar-mass and supermassive black holes but their nature is more uncertain, because there are not dynamical measurements of their masses [41]. Recently the gravitational waves GW190521 was detected resulting from the mearger of two stellar mass black holes producing an intermediate mass black hole of mass 142 $M_{\odot}$ [42]. This provides the first speculative evidence of the existence and thereby the detection of intermediate mass black holes. Also there are mini or micro or quantum mechanical black holes [43] having mass less than 1 $M_{\odot}$ [44]. Thes kind of black holes are first proposed by Hawking in 1971 [45]. There are currently two popular techniques to probe the spacetime geometry around astrophysical black holes with electromagnetic radiation. They are the continuum-fitting method [46] and the analysis of the X-ray reflection spectrum (often called the iron line method) [47]. In the recent times the quasi-periodic oscillations (QPOs) observed in the X-ray power spectrum [48] black holes also serve as a promising tool. Their frequency can be measured with high precision and this could permit one to constraint the properties of the compact object. However, till today we do not know the exact mechanism that cause these phenomena, and the measurements vary with varying models, implying

that the technique cannot be used for fundamental physics tests. Today it is has been possible to image the accretion flow around a black hole with great precision and hence we have been able to visualise the black hole "shadow" [49]. Very-long baseline interferometric (VLBI) observations working at sub-millimeter wavelengths have imaged the shadow of M87* [9], [50]-[57] and SgrA* [58]-[63]. Also the gravitational wave detection have opended a new window for the study of astrophysical black holes by the detection of gravitational waves from the coalescence of two black holes in 2015 and many more onwards. The observed data from the black hole shadow as well as gravitational waves help us constraint various models and get insight in the region close to black holes.

1.3 Importance of studying geodesics around black holes

Geodesics are trajectories of particles that are in free fall in any arbitrary spacetime background [64]. Simply, we can say that geodesics are the generalized versions of the straight line that move in a curved background [65].

We know that the motion of any particle in Newtonian gravity is dictated by the equation of force

$$m_I \frac{d^2 r}{dt^2} = F = -\frac{GMm_G}{r^2} \tag{1.1}$$

where m_I and m_G are respectively the inertial and gravitational mass of the particle that is moving in the gravitational field of a particle of mass M. F is the force that acts on the particle of mass m, G is Newton's gravitational constant, and $m_I, m_G << M$ such that it doesn't affect the gravitational field created by M.

The gravitational field in the case of Einsteinian gravity is given by the curvature of spacetime. Also Einstein's theory of gravity is based on the fact that $M_I = m_G$ (weak equivalence principle) [66]. The curvature is represented in terms of the metric tensor $g_{\mu\nu}$ and its derivatives. The equation of motion of any particle in the gravitational field thereby the curved spacetime background is given by the geodesic equation. The equation of the geodesics of particles takes the form [67]

$$\frac{d^2 x^\mu}{d\lambda^2} + \Gamma^\mu_{\nu\rho} \frac{dx^\nu}{d\lambda} \frac{dx^\rho}{d\lambda} = 0 \tag{1.2}$$

where x^μ is the position of the particle, λ is the parameter dictating the particle trajectory and $\Gamma^\mu_{\nu\rho}$ is the Christoffel symbol which is related to the metric tensor $g_{\mu\nu}$ as [67]

$$\Gamma^\mu_{\nu\rho} = \frac{1}{2} g^{\mu\sigma} \Bigg(g_{\nu\sigma,\rho} + g_{\sigma\rho,\nu} - g_{\nu\rho,\sigma} \Bigg) . \tag{1.3}$$

Since the metric tensor $g_{\mu\nu}$ has $4 \times 4 = 16$ components and thereby the Christoffel symbol $\Gamma^\mu_{\nu\rho}$ has $4 \times 4 \times 4 = 64$ components. Thus the calculation is hectic and the four equations can be found to be inter-related with all coordinates and hence the solution cannot be obtained trivially. In order to obtain the solution trivially we look into the symmetry of the metric $g_{\mu\nu}$ and use the Euler-Lagrange equation by defining a Lagrangian $\mathcal{L}$ as $\mathcal{L} = \frac{1}{2} g_{\mu\nu} \dot{x}^\mu \dot{x}^\nu$ [1], [67].

Geodesics are used in almost all important calculations in any spacetime geometry. The basic tests which confirm the validity of Einstein's theory need the study of geodesics around any static or rotating spacetime background.

1.3.1 Perihelion precession

The planets move around the sun in closed elliptical orbits as predicted by Newton's theory of gravity. There is a little deviation of the ellipse due to the gravitational interaction of the other planets. But the incorporation of the planet-planet gravitational interaction cannot explain the precession. In the case of general relativity, the first approximation gives the results obtained using Newtonian gravity and the second approximation results in the exact precessional values. In order to obtain the results we need the knowledge of the geodesics of r and ϕ and thereby calculate the change $\Delta\phi$ to obtain the desired result [66], [67]

$$\Delta\phi = \frac{6\pi GM}{c^2 R(1-e)} \tag{1.4}$$

where, M, R, and e give the mass of the central object (sun), the semi-major axis, and the eccentricity of the orbit respectively.

1.3.2 Gravitational deflection

Deflection implies the deviation of particles from their original trajectory. In the presence of any massive object, the trajectory of any particle gets deflected either towards or away from the massive object [67]. This deviation can be calculated by studying the particle trajectories and thereby their geodesics.

1.3.3 Determination and study of potential

From the study of geodesics, we obtain the equation of motion along r and θ which provides us with the potential along those directions $V_{eff}(r)$ and $V_{eff}(\theta)$ [1]. The study of these potentials will help us obtain the possible regions for the existence of bound and unbound orbits [68], [69]. Besides on close and thorough analysis of the potentials, we can get an insight into the possible stable and unstable orbits which would help us in understanding different astrophysical structures and their formation mechanism.

1.3.4 Black hole perturbation and stability

The presence of any type of matter field around any massive object is a realistic scenario. This field can act as perturbation over the existing gravitational field of the massive object. Due to such perturbation, the total system either can be stable or become unstable [1], [2]. The problem can be analyzed by studying the geodesics of particles in such cases.

1.3.5 Detection and observation of compact objects

The study of geodesics plays an important role in the detection and observation of compact objects such as black holes, neutron stars, etc. In order to study them, the study of null geodesics in particular plays a vital role. The merging of compact objects takes place in several steps. The final merged object before reaching a stable configuration can be dealt with as a perturbed object. These

perturbed objects give out signals whose frequencies dissipate and have the form $\omega = \omega_R + \omega_I$ where the first part is real and the second part is imaginary [70], [71]. The high-frequency signals can be related to the unstable geodesics of photons [72]-[74].
Again the observational structure of compact objects namely black holes is formed by photons moving around black holes in unstable orbits. The shadow is formed due to the strong gravitational deflection of light rays which traverse very close to the black hole and move in orbits where a mere perturbation can kick them either in the black hole abyss or towards infinity. Light rays which propagate towards infinity are responsible for shadow formation and hence give the appearance of the black hole image.

1.3.6 Various astrophysical processes in the vicinity of black holes

It is very difficult to study the very close regimes of a black hole. The information from the closest encounter with the black hole can be achieved from the unstable photons that somehow reach the observer. Beyond that, everything is sucked up and nothing comes out at all. But there are many theories and proposed processes which occur further close to a black hole and also there are processes that describe ways to extract energy out of a black hole. Penrose process is the simplest of all processes that describe a mechanism to extract energy from a black hole [75],[76]. The process depends on the size of the ergosphere and is most prominent in the equatorial plane. To study such a process, we need to understand and analyze geodesics in the equatorial plane. Apart from that, there are other processes like the Blanford-Znajek process [77],[78] useful for extracting electromagnetic energy from a black hole.
Apart from the above-mentioned phenomena and processes, there are many astrophysical scenarios [78] where the study of geodesics around massive, ultra-compact objects is inevitable. In this thesis, we are mainly interested in studying null geodesics in order to understand and analyze black hole shadows in varying scenarios. Also, we are interested in studying timelike geodesics in certain cases along the study of the Penrose process in detail.

1.4 Black hole shadow

Black holes capture everything that falls into it and emits nothing. Thus even from a very naive consideration, one can simply imply that an observer will see a dark spot in the location where the black hole is supposed to be. But due to strong gravitational bending of light rays by black hole's gravity, the size and the shape of the dark spot are quite different from what we naively expect based on Euclidean geometry. For a spherically symmetric black hole, the difference between the black hole shadow and the Euclidean image of the black hole is only in angular size [79]. The shadow is about two and a half times larger than the corresponding Euclidean image. But in case of a rotating black hole, the shape of the black hole shadow becomes different along with it's size. The shadow gets deformed and flattened on one side giving an appearance of D shape for extremal black hole [1]. The size and the shape of the shadow depends not only on the black hole parameters but also on the observer's position who measures it [79].
Historically there have been many names used to refer to the visual appearance of a black hole as

- escape cone [80];
- the apparent shape of black hole [1], [81];

- cross section [82];
- image, optical appearance, photograph [83], [84];
- cross section of photon gravitational capture [85];
- black hole shadow [49];
- silhouette [86], [87];
- photon ring [88], [89];
- critical curve [90].

Despite different names and various physical formulation all the concepts are strongly intertwined. By now the word 'shadow' has become the most used one. The term 'shadow' has several meanings in various languages. The most usual meaning is the dark area created on a surface (screen) by any obstacle located between a light source and the surface. For example, it may be the shadow of the human body or of a building or a tree or any other object on the ground at a sunny day. *Another meaning of the word 'shadow' is a dark silhouette of a body which occurs when we look at it against a bright background. In this case, we see not the details of this body, but only the shape* [79]. We use the word "shadow" in its second meaning when referring to the black hole shadow. As a result, the black hole's shadow can be thought of as a silhouette of darkness on any brilliant background that has been affected by gravitational light bending [91], [92].

we consider an observer who is some distance from the black hole to comprehend the theoretical framework of the black hole shadow. Then, we may categorize all light beams that go from this observer point into the past into two groups- those that travel to the horizon and those that are diverted by the black hole and travel to infinity. We also investigate the possibility that there are abundant light sources throughout the universe, but none of them are located between the black hole and the observer. The dark part of the observer's sky is what we call the shadow [49]. The boundary corresponds to a ray of light trapped in spacetime, reaching neither infinity nor the horizon. In the Schwarzschild spacetime and other similar spacetimes that are spherically symmetric, these light rays asymptote to an unstable photon sphere (a sphere filled with circular null geodesics) [93] that are unstable to radial perturbations [2].

Black holes cast shadow in a region known as the '*observer's sky*' [94], [95]. The observer's sky is defined as the plane passing through the black hole's centre. The plane runs perpendicular to the straight line joining the observer to the black hole. The plane is conventionally designated as '*celestial plane*' and defined by celestial coordinates (α, β) [94], [96]. We define a coordinate system with the origin being at the black hole. The coordinate system reduces to the flat Euclidean at spatial infinity. The coordinates of the observer is $(r_0, \theta_0, 0)$.

The shadow gets formed by rays of light coming from any background source. We assume that the source is placed at a large distance away from the black hole and the observer is also placed at quite a large distance away from the black hole. There is no source between the black hole and the observer. Light rays coming from the the background source move close to the black hole and get deviated and thereby reach the observer. For the observer, the light ray seems to be coming along a tangent which at the observer's position is given as [97]

$$\vec{T} = \left(\left.\frac{dx}{dr}\right|_{r=r_0}, \left.\frac{dy}{dr}\right|_{r=r_0}, \left.\frac{dz}{dr}\right|_{r=r_0} \right) .$$

The cartesian coordinates (x, y, z) and spherical polar coordinates (r, θ, ϕ) are related in the following way

$$\begin{aligned} x &= r \sin\theta \cos\phi \\ y &= r \sin\theta \sin\phi \\ z &= r \cos\theta \ . \end{aligned} \tag{1.5}$$

The components of the tangent vector using eq.(1.5) take the form

$$\begin{aligned} \left.\frac{dx}{dr}\right|_{r=r_0} &= \sin\theta_0 + r_0 \cos\theta_0 \left.\frac{d\theta}{dr}\right|_{r=r_0} \\ \left.\frac{dy}{dr}\right|_{r=r_0} &= r_0 \sin\theta_0 \left.\frac{d\phi}{dr}\right|_{r=r_0} \\ \left.\frac{dz}{dr}\right|_{r=r_0} &= \cos\theta_0 - r_0 \sin\theta_0 \left.\frac{d\theta}{dr}\right|_{r=r_0} \end{aligned} \tag{1.6}$$

where we have used $r = r_0, \theta = \theta_0$ and $\phi = 0$. The light which reaches the observer comes from the unstable circular photon orbits. The orbits intersect the celestial plane at some point. The intersecting point in the coordinate system centred at the black hole is given in terms of the celestial coordinates as $P \equiv (x_1, y_1, z_1) = (-\beta \cos\theta_0, \alpha, \beta \sin\theta_0)$ and the observer is located at the point $O \equiv (x, y, z) = (r_0 \sin\theta_0, 0, r_0 \cos\theta_0)$. The light ray passes through the points P and O. The equation of a tangent passing through two points in 3-D is given as [94]

$$\frac{x - x_1}{\left.\frac{dx}{dr}\right|_{r_0}} = \frac{y - y_1}{\left.\frac{dy}{dr}\right|_{r_0}} = \frac{z - z_1}{\left.\frac{dz}{dr}\right|_{r_0}} \ .$$

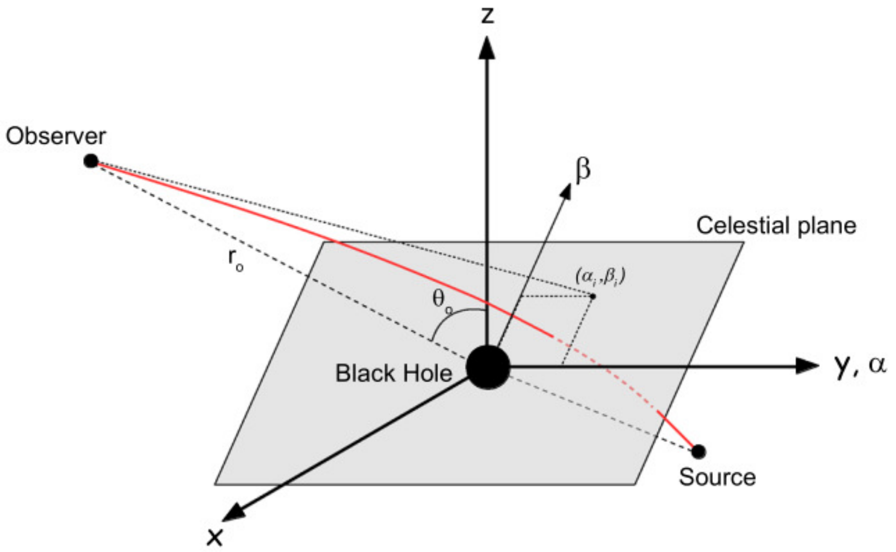

Figure 1.1: Basic diagram to interpret celestial coordinates [96]

Equating the first and third terms we get the expression for β as

$$\beta = r^2 \frac{d\theta}{dr}\bigg|_{r_0,\theta_0} . \tag{1.7}$$

By equating the second and third expressions and replacing β we get α as

$$\alpha = -r^2 \sin\theta \frac{d\phi}{dr}\bigg|_{r_0,\theta_0} . \tag{1.8}$$

The observer is placed far away from the black hole such that theoretically we can consider $r_0 = \infty$ [1], [81]. Thus the celestial coordinates (α, β) gets mathematically represented as [94]

$$\begin{aligned} \alpha &= \lim_{r_0\to\infty} -r^2 \sin\theta \frac{d\phi}{dr}\bigg|_{r_0,\theta_0} \\ \beta &= \lim_{r_0\to\infty} r^2 \frac{d\theta}{dr}\bigg|_{r_0,\theta_0} . \end{aligned} \tag{1.9}$$

1.5 Angular size of any object as observed by moving observers

Here we derive the expression for the size of an object measured from the viewpoint of a moving observer in terms of the one observed by a static observer [98]. To do so we consider two observers with 3-velocity of the moving observer designated as $\vec{v}$. Also, we consider two light rays Γ_1 and Γ_2 [99], the tangent to those rays are K and W subject to the condition (by definition)

$$g_{\mu\nu} K^\mu K^\nu = 0 = g_{\mu\nu} W^\mu W^\nu . \tag{1.10}$$

The 4-velocities of the static and moving observer are U^μ and V^μ which are subject to the condition

$$g_{\mu\nu} U^\mu U^\nu = -1 = g_{\mu\nu} V^\mu V^\nu . \tag{1.11}$$

Also, the relative velocity between the static and comoving observer are subject to the condition [98], [99]

$$g_{\mu\nu} U^\mu V^\nu = -\gamma = -\frac{1}{\sqrt{1-v^2}} . \tag{1.12}$$

We wish to calculate the angle between the two light rays as measured in 3-space by the two observers. The angles are designated as ψ_1 and ψ_2 and we want to find a relation between these angles in terms of v.

$\overline{K}$ and $\overline{W}$ are the projections of K and W respectively on the local space of the static observer such that the projections are spacelike and normal to the 4-velocity of the observer. Mathematically it takes the form

$$g_{ij} \overline{K}^i \overline{K}^j < 0 \ \ ; \ \ g_{ij} \overline{W}^i \overline{W}^j < 0 \tag{1.13}$$

$$g_{\mu\nu} \overline{K}^\mu U^\nu = g_{\mu\nu} \overline{W}^\mu U^\nu = 0 . \tag{1.14}$$

Now, $\overline{K}^{\mu}$ and $\overline{W}^{\mu}$ can be written as a projection along K^{μ} and W^{μ} respectively and also along U^{μ}. Mathematically it can be represented as

$$\overline{K}^{\mu} = K^{\mu} + (K^{\alpha}U_{\alpha})U^{\mu} \ \ ; \ \ \overline{W}^{\mu} = W^{\mu} + (W^{\alpha}U_{\alpha})U^{\mu} \ . \tag{1.15}$$

The angle between the two rays as measured by the observer with 4-velocity U^{μ} is ψ_1 and can be written as

$$\cos\psi_1 = \frac{g_{\mu\nu}\overline{K}^{\mu}\overline{W}^{\nu}}{\sqrt{g_{\mu\nu}\overline{K}^{\mu}\overline{K}^{\nu}}\sqrt{g_{\mu\nu}\overline{W}^{\mu}\overline{W}^{\nu}}} \ . \tag{1.16}$$

Now to calculate $\cos\psi_1$ we use the conditions in eq.(1.14) and normalisation condition along with the relation in eq.(1.15). Thus we finally obtain [99]

$$\cos\psi_1 = 1 + \frac{g_{\mu\nu}K^{\mu}W^{\nu}}{(g_{\alpha\beta}K^{\alpha}U^{\beta})(g_{\gamma\delta}W^{\delta}U^{\delta})} \ . \tag{1.17}$$

Similarly we obtain $\cos\psi_2$ as

$$\cos\psi_2 = 1 + \frac{g_{\mu\nu}K^{\mu}W^{\nu}}{(g_{\alpha\beta}K^{\alpha}V^{\beta})(g_{\gamma\delta}W^{\gamma}V^{\delta})} \tag{1.18}$$

and the relation between the two angles $\cos\psi_1$ and $\cos\psi_2$ takes the form [98]

$$\frac{\cos\psi_1 - 1}{\cos\psi_2 - 1} = \frac{(g_{\alpha\beta}K^{\alpha}V^{\beta})(g_{\gamma\delta}W^{\gamma}V^{\delta})}{(g_{\alpha\beta}K^{\alpha}U^{\beta})(g_{\gamma\delta}W^{\gamma}U^{\delta})} \ . \tag{1.19}$$

We wish to express ψ_2 in terms of ψ_1 and the 3-velocity v between the observers. For this, we use the relation given in eq.(1.12). Also, we need to assume that the direction of light ray and the 4-velocity of one observer coincide in the frame of another observer. Mathematically, it can be written as [99]

$$K^{\mu} = AU^{\mu} + BV^{\mu} \tag{1.20}$$

with A and B being the unknown coefficients to be determined. To obtain the coefficients, we use $g_{\mu\nu}K^{\mu}K^{\nu} = 0$, $g_{\mu\nu}U^{\mu}U^{\nu} = g_{\mu\nu}V^{\mu}V^{\nu} = -1$ and $g_{\mu\nu}U^{\mu}V^{\nu} = -\gamma$. The expression for the ratio of A and B take the form

$$\frac{A}{B} = (\gamma v - \gamma) \ . \tag{1.21}$$

Replacing the expression of K^{μ} from eq.(1.20) and using $\frac{A}{B}$ and after some rearrangement, we get [93], [99]

$$\cos\psi_2 = \frac{\cos\psi_1 - v}{1 - v\cos\psi_1} \ . \tag{1.22}$$

1.6 Black holes surrounded by plasma

The universe is made of almost 99% plasma [100]. Whatever we see in the cosmos is made of plasma which is also considered to be the fourth state of matter [101]. The life forms existing in earth fall into those tiny 1% of matter devoid of plasma. Since everything is made of plasma and it is hard to think of anything (including black holes) to exist in isolation, thus the presence of plasma around black holes is kind of inevitable. The presence of plasma around black holes is mostly in the form of accretion disks [78] having different structures and modelled differently. Here we are not interested in accretion disks rather how plasma in the accretion disks affect spacetime dynamics.

The material from any star or compact object (other than black hole) can rupture due to strong gravity of the black hole and move around black holes. The immensely strong gravity of black holes makes those matter move very rapidly. The kinetic energy of the motion and due to internal friction [78] increases the temperature of the material and ionizes the matter into electrons and ions. The ions are heavy and remain static in their particular places. On the other hand, the electrons are lighter and can readily move around. If the electrons present in plasma are displaced from their equilibrium position then electric field gets created. In order to restore the neutrality, the electrons will be dragged back to their original position and they start to oscillate about the position of equilibrium [102]. The electrons oscillate about their equilibrium position occurs with a characteristic frequency known as the *plasma frequency.* The oscillation of the electrons is way too fast for the heavy ions to respond, so they may be considered as fixed. We derive the expression for the plasma frequency ω_p in the following section.

1.6.1 Derivation of plasma frequency (ω_p)

In order to derive the expression for ω_p, we make some assumptions [101]. These are —(**i**) The ions are fixed in space with a uniform distribution; (**ii**) There is no thermal motion implying $KT = 0$; (**iii**) There is no applied magnetic field; (**iv**) The plasma is infinitely extended; and (**v**) The electron motion is constrained in the x-direction only[1]. The final assumption results in

$$\nabla = \hat{x}\frac{\partial}{\partial x}\ ;\ \mathbf{E} = E\hat{x}\ ;\ \nabla\times\mathbf{E} = 0\ ;\ \mathbf{E} = -\nabla\phi\ . \tag{1.23}$$

Here $\mathbf{E}$ and E are the 3-vector and component of the electric field along the x-direction. Due to the absence of magnetic field $\mathbf{B}$ we have $\nabla\times\mathbf{E} = 0$ leading to $\mathbf{E}$ being represented in terms of the gradient of potential ϕ. Due to the absence of a magnetic field, the oscillation is totally electrostatic. The equation of motion for electrons and the continuity equation takes the form

$$m_e n_e\left[\frac{\partial\mathbf{v}_e}{\partial t} + (\mathbf{v}_e.\nabla)\mathbf{v}_e\right] = -en_e\mathbf{E} \tag{1.24}$$

$$\frac{\partial n_e}{\partial t} + \nabla.(n_e\mathbf{v}_e) = 0\ . \tag{1.25}$$

Here, m_e, n_e, and v_e are the mass, number density, and 3-velocity of the electrons respectively. e is the charge of the electron. In order to solve the above equations, we need to use the property of inertia of electrons and thereby the deviation from neutrality [101]. Thus we get

$$\nabla.\mathbf{E} = \frac{\partial\mathbf{E}}{\partial x} = 4\pi e(n_i - n_e) \tag{1.26}$$

---

[1] Later we can generalise the final expression valid for any direction.

with n_i the number density of ions. Also additionally we need to assume the property of linearisation, that is the amplitude of oscillation is small and we need to neglect higher powers of amplitude factors. We separate the dependent variables into an *equilibrium* part (designated by subscript 0) and a perturbation (designated by subscript 1) as [101]

$$n_e = n_0 + n_1 \;\; ; \;\; \mathbf{v}_e = \mathbf{v}_0 + \mathbf{v}_1 \;\; ; \;\; \mathbf{E} = \mathbf{E}_0 + \mathbf{E}_1 \; . \tag{1.27}$$

The equilibrium quantities (designated by subscript 0) are constant as

$$\nabla n_0 = \mathbf{v}_0 = \mathbf{E}_0 = 0 \tag{1.28}$$

$$\frac{\partial n_0}{\partial t} = \frac{\partial \mathbf{v}_0}{\partial t} = \frac{\partial \mathbf{E}_0}{\partial t} = 0 \; . \tag{1.29}$$

Again neglecting quadratic terms in equations of motion and the above conditions we get eq.(s) (1.24) and (1.25) as

$$m_e \frac{\partial \mathbf{v}_1}{\partial t} = -e\mathbf{E}_1 \tag{1.30}$$

$$\frac{\partial n_1}{\partial t} + n_0 \nabla . \mathbf{v}_1 = 0 \; . \tag{1.31}$$

Also, eq. (1.26) gets modified to

$$\nabla . \mathbf{E} = -4\pi e n_1 \; . \tag{1.32}$$

We assume the oscillating quantities to behave sinusoidally as [100], [101]

$$\begin{aligned} \mathbf{v}_1 &= v_1 e^{i(kx-\omega t)} \hat{\mathbf{x}} \\ n_1 &= n_1 e^{i(kx-\omega t)} \\ \mathbf{E} &= E e^{i(kx-\omega t)} \hat{\mathbf{x}} \; . \end{aligned} \tag{1.33}$$

The gradient ∇ and time derivative $\frac{\partial}{\partial t}$ can be replaced by $-i\omega$ and $ik\hat{\mathbf{x}}$. Using them we get

$$\begin{aligned} -im_e \omega v_1 &= -eE_1 \\ -i\omega n_1 &= -in_0 k v_1 \\ ikE_1 &= -4\pi e n_1 \; . \end{aligned} \tag{1.34}$$

Replacing E_1 in first equation from the third and then replacing n_1 from the second we get

$$-im_e \omega v_1 = -e\frac{-4\pi e n_1}{ik} = e\frac{4\pi e}{ik}\frac{n_0 k v_1}{\omega} = -i\frac{4\pi e^2 n_0}{\omega} v_1 \; . \tag{1.35}$$

If v_1 does not vanish ($v \neq 0$), then we get

$$\omega^2 = \omega_p^2 = \frac{4\pi n_0 e^2}{m_e} \; . \tag{1.36}$$

1.6.2 Derivation of Hamiltonian ($\mathcal{H}$) for photons moving in the plasma background

The derivation of the refractive index and thereby the Hamiltonian is based on [103]. First we consider infinity of 3-spaces in spacetime. The 3-space can be timelike, null or spacelike depending on their corresponding normals which can be spacelike, null or timelike respectively. These 3-spaces are designated as 3-waves or waves. There is an associated phase angle ϕ with every wave. The phase angle increases monotonically and we define the waves or 3-waves as phase waves. The waves having $\phi = 2n\pi$ are designated as crests. Since the phase angle ϕ is a function of spacetime position, so a function can be defined as (in 1-D) [103]

$$f(x) = -\frac{h}{2\pi}\phi \ . \tag{1.37}$$

The waves are defined as $f(x) =$ constant with h being any small universal constant which we take to be the Planck's constant. As we pass from crest to crest, we have

$$df = -h \ . \tag{1.38}$$

We define the worldline of the observer to be timelike with 4-velocity V^μ such that $g_{\mu\rho}V^\mu V^\rho = -1$. Now we define a quantity p_μ as [103]

$$p_\mu = \frac{df}{dx^\mu} \ . \tag{1.39}$$

In passing from crest to crest, if we suppose that the position changes by dx^μ and proper time elapsed be ds, then the 4-velocity of the observer being $v^\mu = \frac{dx^\mu}{ds}$. Using this we get

$$p_\mu dx^\mu = p_\mu v^\mu ds = df = -h \ . \tag{1.40}$$

Thus, the time period $\tau (= ds)$ and the frequency $\nu (= \frac{1}{\tau})$ of the wave are given as

$$\tau = ds = -\frac{h}{p_\mu v^\mu} \ \ ; \ \ \nu = \frac{1}{\tau} = -\frac{p_\mu v^\mu}{h} \tag{1.41}$$

giving, $h\nu = -p_\mu v^\mu$. Again h is very small so the frequency is high which is true in the case of validity of *geometrical optics*. The waves we talked about above are basically optical waves and we are interested in determining the velocity of those waves.

Let us suppose the observer is moving along worldline O and the waves moving along worldline W. The two worldlines intersect at A. We want to determine the velocity of the waves as measured by the observer.

We assume a fictitious particle moving with the wave, having the equation $f(x) =$ constant. The infinitesimal displacement along the wave is dx^μ and dy^μ is the displacement of the wave with respect to the observer and orthogonal to the worldline of the observer. The displacement dy^μ takes place in time ds, so the velocity of the fictitious particle moving along the wave with respect to the observer

$$u' = \frac{dy^\mu}{ds} \ \ ; \ \ u'^2 = \frac{dy_\mu dy^\mu}{ds^2} \ . \tag{1.42}$$

Now the velocity v^μ of the observer is perpendicular to dy^μ which gives $g_{\mu\rho}v^\mu dy^\rho = v_\rho dy^\rho = 0$. Also,

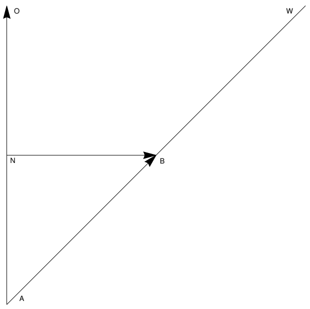

Figure 1.2: Geometric representation of observer and photon wave.

in the geometrical optics limit, we have the Planck's constant $h \to 0$ which implies $p_\mu dx^\mu = 0$. Also, we have [103]

$$dy^\mu = dx^\mu - v^\mu ds \ . \tag{1.43}$$

Since, the observer moves along the worldline which is timelike, so we have $g_{\mu\rho} v^\mu v^\rho = -1$. Using this condition in above eq. (1.43) and multiplying the above equation by v_μ from the left, we get

$$v_\mu dy^\mu = v_\mu dx^\mu - v_\mu v^\mu ds \quad \implies 0 = v_\mu dx^\mu + ds \quad \implies ds = -v_\mu dx^\mu \ . \tag{1.44}$$

Replacing ds in eq.(1.43) we have

$$dy^\mu = dx^\mu + v^\mu v_\rho dx^\rho \ . \tag{1.45}$$

Multiplying the above equation by $g_{\mu\rho}$ from left and dy^ρ from right we get

$$dy_\mu dy^\mu = dx_\mu dx^\mu + (v_\mu dx^\mu)^2 \ . \tag{1.46}$$

Using the definition of u'^2 we obtain

$$\begin{aligned} u'^2 &= \frac{dy_\mu dy^\mu}{ds^2} \\ &= 1 + \frac{dx_\mu dx^\mu}{(v_\rho dx^\rho)^2} \ . \end{aligned} \tag{1.47}$$

Now, we wish to find the velocity u of the wave which is defined as the minimum value of u'. So, we need to minimize u' as obtained in eq.(1.47) with an additional condition given by [103]

$$p_\mu dx^\mu = 0 \ . \tag{1.48}$$

To approach the problem we define

$$dx^\mu = \tilde{\alpha} v^\mu + p^\mu \tag{1.49}$$

with $\tilde{\alpha}$ being the Lagrange's multiplier. Multiplying p_μ from the left in above equation, we get

$$\tilde{\alpha} = -\frac{p_\mu p^\mu}{p_\rho v^\rho} \ . \tag{1.50}$$

In order to obtain the velocity of the wave, we need to determine $dx_\mu dx^\mu$ for which we multiply eq.(1.49) from the left by dx_μ which gives

$$dx_\mu dx^\mu = \tilde{\alpha}(p_\mu v^\mu - \tilde{\alpha}) \ . \tag{1.51}$$

Also, to obtain $v_\mu dx^\mu$ we multiply eq.(1.49) from left by v_μ which gives

$$v_\mu dx^\mu = p_\mu v^\mu - \tilde{\alpha} \ . \tag{1.52}$$

Using the above obtained results of eq.(1.51) and (1.52) we get

$$u^2 = \frac{p_\rho v^\rho}{p_\mu v^\mu - \tilde{\alpha}} \ . \tag{1.53}$$

The slowness of the waves which is more fundamental is defined as u^{-1} giving [103]

$$\frac{1}{u^2} = 1 + \frac{p_\mu p^\mu}{(p_\rho v^\rho)^2} \ . \tag{1.54}$$

In case of waves moving through any medium which is a very general case, we need to define the index of refraction n of the medium. The index of refraction depends on the wave frequency and other local properties. The refractive index is defined as the inverse of the phase velocity and hence we obtain the medium equation as [103], [104]

$$n^2 = 1 + \frac{p_\mu p^\mu}{(p_\rho v^\rho)^2} \ . \tag{1.55}$$

In case of a medium we study the motion of the optical waves with respect to the medium, so the velocity v^μ is the velocity of the medium and in general we assume the medium to be static. Using this we define the Hamiltonian for the motion of photons in any medium as [96],[104]

$$\mathcal{H} = \frac{1}{2}\Big[g^{\mu\rho}p_\mu p_\rho - (n^2 - 1)(p_\rho v^\rho)^2\Big] \tag{1.56}$$

with the constraint that $\mathcal{H} = 0$. The Hamiltonian can also be written in another form as [104]-[106]

$$\mathcal{H} = \frac{1}{2}\Big[g^{\mu\rho}p_\mu p_\rho + \omega_p^2\Big] \tag{1.57}$$

with the refractive index n defined as [104], [105]

$$n^2 = 1 - \left(\frac{\omega_p}{\omega}\right)^2 \ . \tag{1.58}$$

Here ω_p and ω respectively represent the plasma frequency and frequency of photons as measured by any arbitrary observer. The above eq.(1.57) can be derived considering magnetised plasma as in [107]. The consideration of of a magnetised plasma is realistic [78], since the accreation disc does have a magnetic field. But for simplicity and for making analytical calculations possible, we have worked with nonmagnetised plasma in this thesis.

In the above few sections we have developed the necessary prerequisites for the study of geodesics around black holes and the formation of black hole shadow. Analytical research on the formation of black hole images (*black hole shadow*) began with the work of Synge [80], who obtained the shadow of a spherically symmetric black hole to be circular in shape. Next, Luminet [83] studied the shadow of a black hole surrounded by accretion disks. Research on shadows of Kerr and Kerr-Newman black holes has been done in [81], [108] and [109]. With advancement in technology and thereby having improved observational data, shadows of black holes were studied in general relativity with various added characteristics [110]-[127]. Also shadows of black holes were studied in theories of modified gravity in [95]-[96], [106], [128]-[131] along with higher dimensional theories of gravity in [132]-[134]. Shadow of black holes including plasma have been done extensively in the literature. We mention a few of them [105],[135]-[143].

In our first project we studied the black hole shadow in one of the simplest curvature corrected theory of gravity namely Gauss-Bonnet gravity [144]-[146]. It has been known for quite a while, that the different theories of particle physics, the string theory [147], [148] in particular, require higher dimensions in order to preserve the symmetries of the system. Also, there are many articles that explain the need for higher dimensions purely on classical grounds [149]. In order to consider the high energy effects of a theory, the general way is to consider a higher power of the basic variable [150]. While dealing with gravity, the fundamental entity is the curvature tensor given by the Riemann curvature [151], and thus in order to take into account the effects of higher energy, we must consider terms with higher powers of Riemann tensor in the action [150], [151]. Additionally, we demand that the systems dynamics be described by second-order equations. The way out to this is to consider the Lovelock action [151], which is pertinent in dimensions $d > 4$ implying that high energy effects are possible to observe only in higher dimensions. Thus it makes a good case for studying gravity in higher dimensions. The analysis has been shown in chapter 2.

We calculated the black hole shadow in the case of higher dimensions in a flat Minkowski background [152], [106]. The shadow is influenced by the Gauss-Bonnet parameter γ. We found that the effect of γ noticed in our work is the same observed in the case of $D = 4$ dimensions [153]. Thus the effect of γ on some spacetime properties remains the same even with the variation of spacetime dimensions. In the case of black holes in an AdS background, the black hole shadows can be related with some parameters of the boundary CFT theory [154]. We know that CFT theories have relations with the black hole quasinormal modes [155]. And also there is a relation between the black hole shadow radius R_s and the QNMs ω [73]. Thus we can get insight of the CFT parameters by studying black hole shadows in AdS background.

In the next two chapters 3 and 4 we incorporated the presence of dark matter in a black hole background [156], [157]. The reason being dark matter dominates the matter content and is supposed to be present in extended regions in space. Also dark matter influences structure formation and must also influence the dynamics of particles near and around black holes. So we considered a model of perfect fluid dark matter (PFDM) put forward in [158], [159] influenced by the works in [160]-[162]. In chapter 3, we studied the geodesics of photons and calculated the radius of those orbits. For massive particles, we studied the geodesics of charged and uncharged ones with an analysis of their energy E and angular momentum L. Also we discussed the Penrose process in detail. In chapter 4, we incorporated the effect of plasma in the background and studied the effect of plasma on photon orbits and thereby the effect of PFDM and plasma on the shadow of black hole. We also constraint the PFDM parameter and plasma parameter using the observational results of M87* [9] black hole.

In chapter 5, we consider the impact of universal expansion on the observed size of a black hole shadow [163]. The effect is supposed to be caused by the presence of a positive cosmological constant $\Lambda(>0)$ [93]. We carried out our analysis in case of a static black hole for simplicity. Besides, we also immerse the black hole in a plasma background and constrain the plasma parameter using the observational results of M87* [9] and Sgr A* [58].

We finally conclude in chapter 6. In this thesis we mainly focussed on the study of black hole shadow structure depending on various speculative as well as realistic scenarios and have tried to constrain the parameters accordingly based on the observational results. These helped us gain insight on the validation of various models as well as possibility of existence of various matter in the black hole vicinity.

Chapter 2

Charged black holes in higher curvature Gauss-Bonnet gravity

The study of black holes in general relativity started in a full fledged manner from late sixties and the interest towards learning more about it went on increasing with time. There are many facets of black holes and since the gravitational field near a black hole is way too strong, so they became grounds of speculation, prediction and verification of theories which can be validated only at high enough energies. The aspect of quantum gravity, that is quantising gravity (the spacetime background itself) [32] and unifying all theories together is the biggest aim of fundamental scientific research. String theory and its various versions [147], [148] try to put all theories in the same footing and low energy versions of string theory can yield some similarities with the real world scenarios, as what has been speculated. Besides, there are other theories which only try to quantise gravity like the loop quantum gravity (*LQG*) [164].

The low energy effective action of string theory gives rise to higher curvature gravity theories as found by Boulware and Deser [165]. The same can also be obtained by Lovelock's theory of gravity [151] whose first order modification gives the higher curvature gravity namely the Gauss Bonnet gravity. The speciality of Lovelock theory is that the dynamical equations are represented as second order differential equations in metric tensor $g_{\mu\nu}$. The Gauss Bonnet theory is the simplest development towards higher energy, thereby higher curvature gravity theory [150]. The theory could be useful to test strong gravity regimes where Einstein's theory fails. Also, this might give us hint towards the validation of theories like string theory. Again we know our spacetime dimension is (3+1) dimensional whereas Gauss Bonnet gravity plays no role in spacetime dynamics in (3+1) dimensions and is only effective on spacetime dynamics in $d \geq (4+1)$ [144]. So the validation of Gauss Bonnet gravity (if any) will also provide the hint towards extra dimensions.

The study of black holes in any theory is simple and fascinating compared to other objects. So we take interest in studying black holes in a particular case namely Gauss Bonnet gravity and study its characteristics spacetime using the geodesics of particles moving in the background. We study the null geodesics around black holes residing in asymptotically Minkowski and *AdS* background. The study in Minkowski background help us gain insight of the presence of higher dimensions, validation of string theory, etc. On the other hand, the study of black holes in asymptotically *AdS* background may help us gain some knowledge in the boundary *CFT* theory by the *AdS*/*CFT* correspondance. It can be pointed out that some of the observables of the black hole has a mapping with some

quantities in the CFT side. Hence, our study will shred light on those corresponding quantities in higher curvature gravity and might constrain them. We use the null geodesics to calculate observables, primarily the black hole shadow. Again we consider the presence of a material media around black holes and analyse it's impact on the black hole observables.
In the references [152] and [166], the shadow of black holes considering Gauss-Bonnet gravity theory has been examined with spin and in higher dimensions. In this chapter, we studied a charged black hole shadow in asymptotically AdS and Minkowski spacetime in $d = 5$ dimensions. Also, we studied the black holes energy emission rate and how the curvature effects it. The study detailed in this chapter is based on our first work [106].

2.1 Charged black holes in Gauss-Bonnet gravity

The Eintein-Hilbert action considering a negative cosmological constant ($\Lambda < 0$) together with the electromagnetic field and an additional higher curvature Gauss-Bonnet term in general d spacetime dimensions take the form [144]

$$S = \frac{1}{16\pi G}\int d^dx\sqrt{-g}\left[\frac{(d-1)(d-2)}{l^2} + R + \gamma\Big(R^2 - 4R_{ab}R^{ab} + R_{abcd}R^{abcd}\Big) - 4\pi G F_{ab}F^{ab}\right] \tag{2.1}$$

with $F_{ab}(= \partial_a A_b - \partial_b A_a)$ giving the Maxwell field strength tensor (A_a being the 4-potential of the electromagnetic field). Here γ (≥ 0), gives the Gauss-Bonnet parameter having the dimension of $(length)^2$ and $\Lambda = -\frac{(d-1)(d-2)}{2l^2}$ gives the negative cosmological constant with l designating the AdS radius. Extremizing the action we obtain the field equation as [144]

$$\begin{aligned} R_{ab} - \frac{1}{2}g_{ab}R &= \frac{(d-1)(d-2)}{2l^2}g_{ab} + 8\pi G\Big(F_{ag}F^g_b - \frac{1}{4}g_{ab}F_{gh}F^{gh}\Big) + \gamma\Big[\frac{1}{2}g_{ab}\Big(R^2 - 4R_{cd}R^{cd} + R_{cdef}R^{cdef}\Big) \\ &- 2RR_{ab} + 4R_{ac}R^c_b + 4R_{cd}R^{c\ \,d}_{\ a\ \,b} - 2R_{acde}R^{cde}_b\Big]. \end{aligned} \tag{2.2}$$

To solve the equation, we assume a metric ansatz of the form [146]

$$ds^2 = -f(r)dt^2 + \frac{dr^2}{f(r)} + r^2 h_{ij}dx^i dx^j \tag{2.3}$$

where $h_{ij}dx^i dx^j$ denotes the line element of the $(d-2)$-dimensional hypersurface. Inserting eq.(2.3) in eq.(2.2) $f(r)$ is obtained as [146]

$$f(r) = 1 + \frac{r^2}{2\tilde{\gamma}}\left(1 - \sqrt{1 - \frac{4\tilde{\gamma}}{l^2}}\sqrt{1 + \frac{m}{r^{d-1}} - \frac{q^2}{r^{2d-4}}}\right) \tag{2.4}$$

with $\tilde{\gamma}$ and γ related as $\tilde{\gamma} = (d-3)(d-4)\gamma$. The integration constants m and q are related to the black hole mass M and charge Q respectively as

$$M = \frac{(d-2)\Sigma_k\Big(1 - \frac{4\tilde{\gamma}}{l^2}\Big)}{64\pi G\tilde{\gamma}}m\ ,\ \Sigma_k = \frac{2\pi^{(\frac{d-1}{2})}}{\Gamma(\frac{d-1}{2})} \tag{2.5}$$

$$Q = \sqrt{\frac{\pi(d-2)(d-3)\left(1-\frac{4\tilde{\gamma}}{l^2}\right)}{2\tilde{\gamma}G}}\; q \; . \tag{2.6}$$

Taking the limit of $\tilde{\gamma} \to 0$, eq.(5.2) boils down to

$$f(r) = 1 + \frac{r^2}{l^2} - \frac{16\pi GM}{(d-2)\Sigma_k}\frac{1}{r^{d-3}} + \frac{GQ^2}{2\pi(d-2)(d-3)}\frac{1}{r^{2d-6}} \; . \tag{2.7}$$

The bove solution in eq.(4.3) corresponds to a d-dimensional Reissner-Nordström black hole solution in an AdS background. The validity of the lapse function $f(r)$ in eq.(5.2)contrains γ imposing the condition $(1 - \frac{4\tilde{\gamma}}{l^2}) \geq 0$, which gives $\gamma \leq \frac{l^2}{4(d-3)(d-4)}$. As we are interested in stable black holes, the stability condition puts additional constraint on the Gauss-Bonnet parameter, namely, $\frac{\tilde{\gamma}}{l^2} \geq \frac{1}{36}$ [144]. Thus for charged black holes in AdS_5 background γ is constrained as

$$0.01388 \leq \gamma \leq 0.125. \tag{2.8}$$

2.2 Black hole geodesics

We want to figure out the size and shape of the black hole shadow, as was already indicated. We must first identify the geodesics that the photons around the black hole have traced in order to derive the silhouette of the black hole shadow. We consider a particle having mass m_0 orbiting the hole in order to construct the formalism. By establishing the constants of motion along the corresponding symmetry direction, the metric's symmetry reduces the challenge of locating geodesics. We move forward as follows. The tangent vector along the curve $x^\mu = x^\mu(\lambda)$, where λ stands for the affine parameter, is $u^\mu = \frac{dx^\mu}{d\lambda}$. We assume k^μ to be a vector in the symmetry direction. Afterward, by applying the Killing equation [167], we can show

$$k^\mu u_\mu = constant \tag{2.9}$$

where x^μ denotes the trajectory of a geodesic [167].
The line element of the above mentioned charged black hole in $d = 5$ spacetime dimension takes the form [168]

$$ds^2 = -f(r)dt^2 + \frac{dr^2}{f(r)} + r^2 d\theta^2 + r^2\sin^2\theta d\phi^2 + r^2\cos^2\theta d\psi^2 \tag{2.10}$$

with the lapse function in $d = 5$ dimension given as [146]

$$f(r) = 1 + \frac{r^2\left(1 - \sqrt{1 - \frac{8\gamma}{l^2} + \frac{64\gamma M}{3\pi r^4} - \frac{2\gamma Q^2}{3\pi r^6}}\right)}{4\gamma} \; . \tag{2.11}$$

2.2.1 Symmetry of the metric

Now we use the symmetry of the metric to evaluate the geodesics. From the metric, we observe that the coffiecients are independent of time coordinate t. This implies the existence of a timelike Killing vector k^{μ}=(1,0,0,0,0). From eq.(5.9) we get for t ($\mu = 0$)

$$k^0 u_0 = u_0 = -E \ . \tag{2.12}$$

The choice of sign is made for calculational convenience. Here E is a constant giving the energy per unit mass of the concerned particle moving in the geodesic and is measured by any observer stationed at infinity. Similar analysis gives the other constants of motion. If we check the metric, we find that the coefficients lack any term in ϕ and ψ. Thus they correspond to symmetry directions and correspond to constnats of motion. Hence using k^{μ}=(0,0,0,1,0) and k^{μ}=(0,0,0,0,1) respectively for ϕ and ψ, we get

$$k^3 u_3 = u_3 = L_{\phi} \tag{2.13}$$

$$k^4 u_4 = u_4 = L_{\psi} \ . \tag{2.14}$$

Here L_{ϕ} and L_{ψ} are the constants which give angular momentum per unit mass respectively along ϕ and ψ for the massive particle moving along geodesic as measured by an observer stationed at infinity.

The equation of the geodesics along the symmetry directions in terms of constants E, L_{ϕ} and L_{ψ} take the form

$$u^0 = g^{0\nu} u_{\nu} = g^{00} u_0 = \frac{E}{f(r)} \tag{2.15}$$

$$u^3 = g^{3\nu} u_{\nu} = g^{33} u_3 = \frac{L_{\phi}}{r^2 \sin^2\theta} \tag{2.16}$$

$$u^4 = g^{4\nu} u_{\nu} = g^{44} u_4 = \frac{L_{\psi}}{r^2 \cos^2\theta} \tag{2.17}$$

which can be rewritten as

$$\begin{aligned} \frac{dt}{d\lambda} &= \frac{E}{f(r)} & (2.18)\\ \frac{d\phi}{d\lambda} &= \frac{L_{\phi}}{r^2 \sin^2\theta} & (2.19)\\ \frac{d\psi}{d\lambda} &= \frac{L_{\psi}}{r^2 \cos^2\theta} \ . & (2.20) \end{aligned}$$

2.2.2 Hamilton-Jacobi formulation

The equations for t, ϕ and ψ are evaluated using the symmetry of the metric Now, the other two equations for r and θ can be evaluated using the Hamilton-Jacobi equation [1]

$$\frac{\partial S}{\partial \lambda} + \frac{1}{2} g^{\mu\sigma} \frac{\partial S}{\partial x^{\mu}} \frac{\partial S}{\partial x^{\sigma}} = 0 \ . \tag{2.21}$$

To obtain a solution of eq.(4.10), an ansatz S is assumed [1]

$$S = \frac{1}{2}m_0^2\lambda - Et + L_\phi \phi + L_\psi \psi + S_r(r) + S_\theta(\theta) \tag{2.22}$$

with m_0 giving the rest mass of particle concerned as mentioned previously. Here λ serves as the affine parameter with the functions $S_\theta(\theta)$, $S_r(r)$ being respectively explicit functions of θ, r. Using eq.(4.11) in eq.(4.10), we get

$$\Big(\frac{\partial S_\theta}{\partial \theta}\Big)^2 + L_\phi^2 \cot^2\theta + L_\psi^2 \tan^2\theta + \frac{1}{2}m_0^2 - \frac{r^2E^2}{f(r)} + r^2 f(r)\Big(\frac{\partial S_r}{\partial r}\Big)^2 + L_\phi^2 + L_\psi^2 = 0\ . \tag{2.23}$$

After some rearrangement with θ dependent terms on left of equality and r dependent terms on the right of equality we obtain

$$\Big(\frac{\partial S_\theta}{\partial \theta}\Big)^2 + L_\phi^2 \cot^2\theta + L_\psi^2 \tan^2\theta + \frac{1}{2}m_0^2 = \frac{r^2E^2}{f(r)} - r^2 f(r)\Big(\frac{\partial S_r}{\partial r}\Big)^2 - L_\phi^2 - L_\psi^2 = \kappa\ . \tag{2.24}$$

Here due to the equality both sides are equal to a constant denoted by κ and termed as the separation constant.

Using the relation,

$$p_\mu = \frac{\partial S}{\partial x^\mu} = \frac{\partial \mathcal{L}}{\partial \dot{x}^\mu} \tag{2.25}$$

with a Lagrangian

$$\mathcal{L} = \frac{1}{2}g_{\mu\nu}\dot{x}^\mu \dot{x}^\nu\ ,\ \dot{x}^\mu \equiv \frac{dx^\mu}{d\lambda} \tag{2.26}$$

we obtain the equations for S_θ and S_r as

$$\frac{\partial S_\theta}{\partial \theta} = r^2 \frac{\partial \theta}{\partial \lambda} \tag{2.27}$$

$$\frac{\partial S_r}{\partial r} = r^2 \frac{\partial r}{\partial \lambda}\ . \tag{2.28}$$

Using the relations (2.27, 2.28) in eq.(2.24) and setting $m_0 = 0$ we obtain the null geodesics as

$$r^2\Big(\frac{d\theta}{d\lambda}\Big) = \sqrt{\Theta(\theta)} \tag{2.29}$$

$$r^2\Big(\frac{dr}{d\lambda}\Big) = \sqrt{R(r)} \tag{2.30}$$

where

$$\Theta(\theta) = \kappa - L_\phi^2 \cot^2\theta - L_\psi^2 \tan^2\theta \tag{2.31}$$

$$R(r) = r^4E^2 - \Big(L^2 + \kappa\Big)r^2 f(r)\ . \tag{2.32}$$

The separation constant κ is also known as the Carter constant. We must note that the eq.(s)(4.12, 2.30) respectively correspond to the geodesic equations for θ, r.

Eq.(2.30) can be rewritten as [106]

$$\left(\frac{dr}{d\lambda}\right)^2 + V_{eff}(r) = 0 \tag{2.33}$$

where V_{eff} is the effective radial potential given by

$$V_{eff}(r) = \frac{f(r)}{r^2}\Big(\kappa + L^2\Big) - E^2 \tag{2.34}$$

$$L^2 \equiv L_\phi^2 + L_\psi^2.$$

2.2.3 Unstable circular geodesics

The black hole shadow is formed by photons (null geodesics). All photons don't form the shadow boundary. Those photons that travel in unstable circular orbits and makes their way out to the observer forms the shadow. So, we need to determine the radius r_p of those specific photon orbits. The conditions are [1], [64]

$$V_{eff}(r)\Bigg|_{r=r_p} = \frac{\partial V_{eff}(r)}{\partial r}\Bigg|_{r=r_p} = 0 \tag{2.35}$$

along with

$$\frac{\partial^2 V_{eff}(r)}{\partial r^2}\Bigg|_{r=r_p} < 0\ . \tag{2.36}$$

Now the first condition in eq.(5.42) that is $V_{eff}(r = r_p) = 0$ results into

$$\begin{aligned} \frac{{r_p}^2}{f(r_p)} &= \eta + (\xi_1^2 + \xi_2^2) \\ &\equiv \eta + \xi^2\ ,\ \xi^2 \equiv \xi_1^2 + \xi_2^2 \end{aligned} \tag{2.37}$$

with the Chandrasekhar constants η, ξ_1 and ξ_2 [1] defined as

$$\eta = \frac{\kappa}{E^2},\ \ \xi_1 = \frac{L_\phi}{E},\ \xi_2 = \frac{L_\psi}{E}\ . \tag{2.38}$$

The second condition in that is eq.(5.42) $\frac{\partial V_{eff}(r)}{\partial r}\Big|_{r=r_p} = 0$ results into

$$\Big(rf'(r) - 2f(r)\Big)\Bigg|_{r=r_p} = 0. \tag{2.39}$$

Replacing the lapse function $f(r)$ and it's derivative $f'(r)$ in eq.(2.39) we get [106]

$$144\pi^2\Big(1 - \frac{8\gamma}{l^2}\Big)r_p^8 + \left(3072\pi\gamma M - 4096M^2\right) r_p^4 - \left(96\pi\gamma Q^2 - 384MQ^2\right) r_p^2 - 9Q^2 = 0 \tag{2.40}$$

with $f'(r)$ given as

$$f'(r)=\frac{1}{\sqrt{1-\frac{8\gamma}{l^2}+\frac{64\gamma M}{3\pi r^4}-\frac{2\gamma Q^2}{3\pi r^6}}}\left[\frac{r}{2\gamma}\left(\sqrt{1-\frac{8\gamma}{l^2}+\frac{64\gamma M}{3\pi r^4}-\frac{2\gamma Q^2}{3\pi r^6}}\right)-\frac{r^2}{2\gamma}+\frac{4r}{l^2}-\frac{Q^2}{6\pi r^5}\right]~. \tag{2.41}$$

Using $r_p^2=x$, eq,(5.3) reduces to a fourth order equation in x taking the form

$$144\pi^2\Big(1-\frac{8\gamma}{l^2}\Big)x^4+\big(3072\pi\gamma M-4096M^2\big)\,x^2-\big(96\pi\gamma Q^2-384MQ^2\big)\,x-9Q^2=0~. \tag{2.42}$$

In principle, the exact analytical solution of the above eq.(5.3) can be obtained. Taking the limit $Q\to 0$ we obtain the solution of x as

$$x=\frac{8\sqrt{4l^2M^2-3\pi\gamma l^2M}}{3\pi\sqrt{l^2-8\gamma}} \tag{2.43}$$

which in turn terms of r_p becomes [106]

$$r_p=\sqrt{\frac{8\sqrt{4l^2M^2-3\pi\gamma l^2M}}{3\pi\sqrt{l^2-8\gamma}}}~. \tag{2.44}$$

However in case of non-zero Q, we fix the values of the black hole mass M, AdS radius l and GB parameter γ to obtain the solution of eq.(5.3) numerically. The solution gives the values of photon sphere radius r_p fordifferent values of black hole charge Q.

To obtain the radius r_p in asymptotically flat spacetime, we take the limit $l\to\infty$ which reduces eq.(5.3) to the form

$$144\pi^2x^4+\big(3072\pi\gamma M-4096M^2\big)\,x^2-\big(96\pi\gamma Q^2-384MQ^2\big)\,x-9Q^2=0~. \tag{2.45}$$

Here also the solution of r_p is readily obtained in $Q\to 0$ limit as [106]

$$r_p=\sqrt{\frac{8\sqrt{4M^2-3\pi\gamma M}}{3\pi}}~. \tag{2.46}$$

The above solution in eq.(5.4) can be obtained from eq.(5.20) by setting $l\to\infty$. Also, for $Q\neq 0$, we numerically obtain the solution for r_p fixing the values of M and γ and varying the charge Q. The numerical values are displayed in Table 1 below.

2.3 Constructing the black hole shadow

Since the shadow is formed in the celestial plane, we need to obtain the coordinates (α,β) defining that plane. The celestial coordinates in $d=5$ spacetime dimensions takes the form [168]

$$\begin{aligned}\alpha &= \lim_{r\to\infty}-\Big(r^2\sin\theta\frac{d\phi}{dr}+r^2\cos\theta\frac{d\psi}{dr}\Big)\\ \beta &= \lim_{r\to\infty}r^2\sin\theta\frac{d\theta}{dr}~.\end{aligned} \tag{2.47}$$

We have already discussed the celestial coordinates in detail in the first chapter.
Using the geodesic equations given in eq.(s)(3.69), (4.12), (2.30), we obtain the values of $\frac{d\phi}{dr}$, $\frac{d\psi}{dr}$ and $\frac{d\theta}{dr}$ as

$$\frac{d\phi}{dr} = \frac{L_\phi \csc^2\theta}{r^2\sqrt{E^2 - \frac{f(r)}{r^2}(\kappa + L_\phi^2 + L_\psi^2)}} \tag{2.48}$$

$$\frac{d\psi}{dr} = \frac{L_\phi \sec^2\theta}{r^2\sqrt{E^2 - \frac{f(r)}{r^2}(\kappa + L_\phi^2 + L_\psi^2)}} \tag{2.49}$$

$$\frac{d\theta}{dr} = \frac{1}{r^2}\sqrt{\frac{\kappa - L_\phi^2 cot^2\theta - L_\psi^2\tan^2\theta}{E^2 - \frac{f(r)}{r^2}(\kappa + L_\phi^2 + L_\psi^2)}}\,. \tag{2.50}$$

Using $\frac{d\phi}{dr}$, $\frac{d\psi}{dr}$ and $\frac{d\theta}{dr}$ the celestial coordiantes (α, β) take the form

$$\alpha = -\frac{(\xi_1\csc\theta + \xi_2\sec\theta)}{\sqrt{1 - \frac{(\eta+\xi_1^2+\xi_2^2)\left(1-\sqrt{1-\frac{8\gamma}{l^2}}\right)}{4\gamma}}}\ ;\ \ \beta = \pm\sqrt{\frac{(\eta - \xi_1^2\cot^2\theta - \xi_2^2\tan^2\theta)}{1 - \frac{((\eta+\xi_1^2+\xi_2^2))\left(1-\sqrt{1-\frac{8\gamma}{l^2}}\right)}{4\gamma}}}\,. \tag{2.51}$$

We consider specifically two observer positions, one at the pole where $\theta = 0$, and the other at $\theta = \frac{\pi}{2}$ [106], [168]. When $\theta = \frac{\pi}{2}$ we have $L_\psi = 0$ ($\implies \xi_2 = 0$) and thereby we obtain $\xi_1 = \xi$. Again for $\theta = 0$ we have $L_\phi = 0$ ($\implies \xi_1 = 0$) giving $\xi_2 = \xi$. The celestial coordinates in both the above cases have the same form as

$$\alpha = -\frac{\xi}{\sqrt{1 - \frac{(\eta+\xi^2)\left(1-\sqrt{1-\frac{8\gamma}{l^2}}\right)}{4\gamma}}}\ ;\ \ \beta = \pm\sqrt{\frac{\eta}{1 - \frac{((\eta+\xi^2)\left(1-\sqrt{1-\frac{8\gamma}{l^2}}\right)}{4\gamma}}}\,. \tag{2.52}$$

Squaring and adding α and β casewise gives the same expression

$$\alpha^2 + \beta^2 = \frac{\left(\eta + \xi^2\right)}{\left(1 - \frac{(\eta+\xi^2)\left(1-\sqrt{1-\frac{8\gamma}{l^2}}\right)}{4\gamma}\right)} \equiv R_s^2 \tag{2.53}$$

which represents a circle in the celestial plane $\alpha - \beta$ with radius R_s. Here R_s in eq.(3.2) gives the black hole shadow radius which in terms of r_p, γ and l takes the form [106]

$$R_s = \sqrt{\frac{\left(\eta + \xi^2\right)}{1 - \frac{(\eta+\xi^2)\left(1-\sqrt{1-\frac{8\gamma}{l^2}}\right)}{4\gamma}}} = \sqrt{\frac{\left(\frac{r_p^2}{f(r_p)}\right)}{1 - \frac{(\frac{r_p^2}{f(r_p)})\left(1-\sqrt{1-\frac{8\gamma}{l^2}}\right)}{4\gamma}}}\,. \tag{2.54}$$

In Table 1 we show the computed values of the black hole shadow radius R_s and photon radius r_p for different values of charge Q of the black hole and GB parameter γ.

Black hole in AdS background

γ	Q	r_p	R_s
0.04	0	1.39975	2.00449
	1	1.38123	1.98767
0.06	0	1.47698	2.12972
	1	1.4588	2.11347
0.08	0	1.59651	2.31911
	1	1.57907	2.30379
0.1	0	1.82177	2.66738
	1	1.80591	2.65369

Black hole in Minkowski background

γ	Q	r_p	R_s
0.0	0	1.3029	1.8426
	1	1.28429	1.82518
0.1	0	1.21829	1.78379
	1	1.19385	1.76286
0.2	0	1.11106	1.71234
	1	1.07415	1.68495

Table 2.1: Photon radius r_p and shadow radius R_s with different values of Gauss-Bonnet parameter γ and charge $Q = 0, 1$ with $M = 1$.

2.3.1 Graphical representation and observation

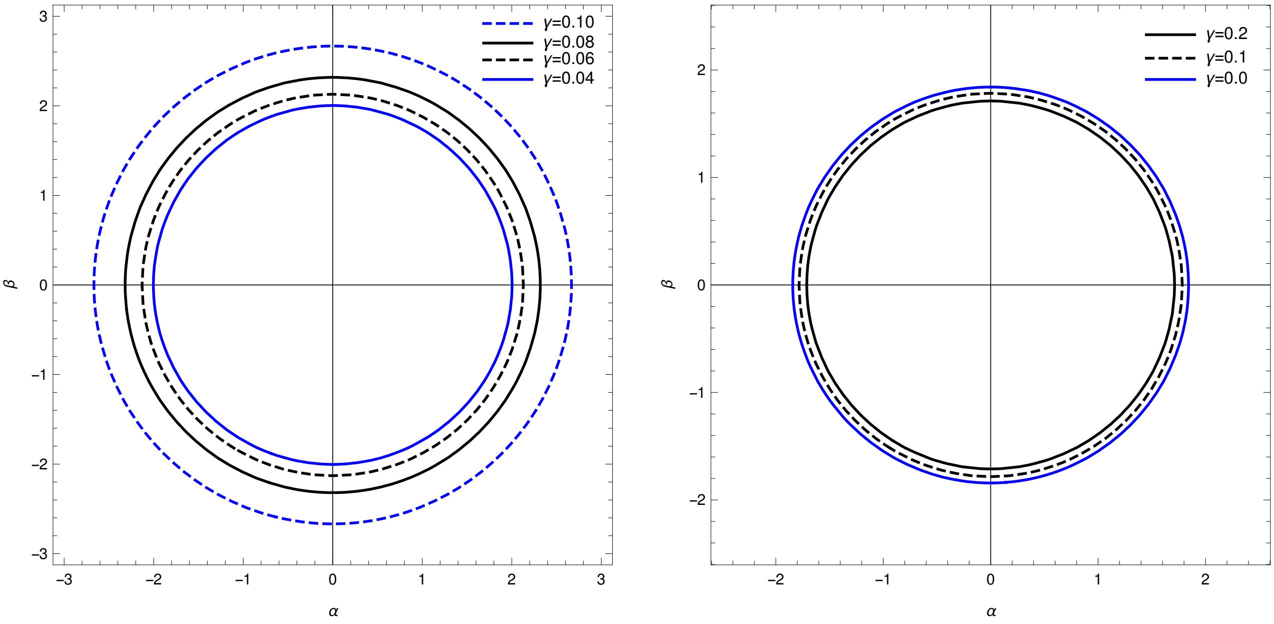

(a) AdS black hole spacetime

(b) Asymptotically flat black hole spacetime

Figure 2.1: Silhouette of black hole shadow in the $(\alpha - \beta)$ plane with variation in Gauss-Bonnet parameter γ setting $Q = 0$.

In the Figures 2.1 and 2.2, we thoroughly observed the variation in size of the black hole shadow with change in values of the GB parameter γ. We found that for the black holes embedded in an AdS background (having AdS radius $l = 1$), an increase in the value of the GB parameter γ enlarges the size of the black hole shadow. On the contrary in case of black holes embedded in a Minkowski background (having $l = \infty$), the size of the black hole shadow reduces with an increase in the GB parameter γ. This observation tells us that the effect of higher curvature gravity corrections effects the black hole shadow differently based on the asymptotic background. Also we have shown the Fig. 2.1 by considering the black hole charge $Q = 0$ and Fig. 2.2 by considering $Q = 1$. By observing the shadows, we find that the shadow size decreases with increase in black hole charge Q. This can be explained by the fact that the shadow of a black hole is an image of the black hole event horizon. The event horizon decreases with increase in charge Q which gets reflected on the size of the black hole shadow.

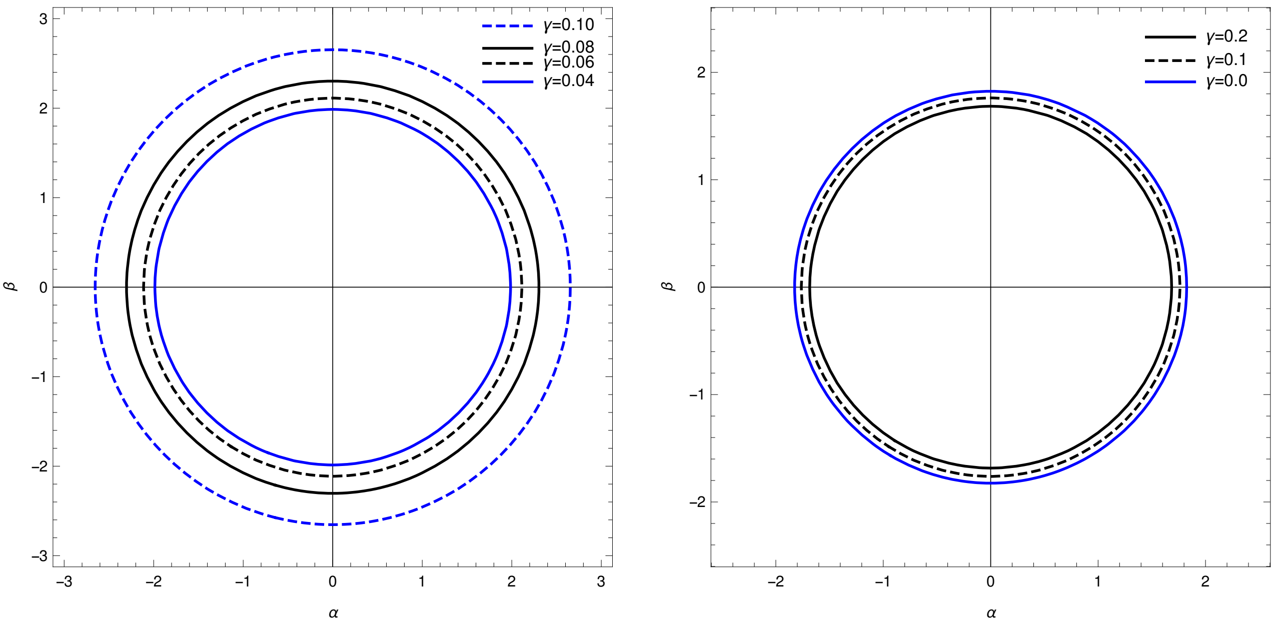

(a) AdS black hole (b) Asymptotically flat black hole

Figure 2.2: Silhouette of black hole shadow in the $(\alpha - \beta)$ plane with variation in Gauss-Bonnet parameter γ setting $Q = 1$.

2.4 Black hole in presence of plasma

Here we incorporate an additional plasma in the background of the black hole. The presence of plasma impacts the spacetime metric and thereby the Hamiltonian $\mathcal{H}$ of the photons as dicussed earlier. We are primarily interested in studying the impact of plasma on the black hole shadow. To do so we need to determine the geodesics as we have done previously. Since the plasma is a dispersive medium, it has a refractive index n which is a function of position and photon frequency ω and can be written as $n = n(x^i, \omega)$. The insertion of plasma modifies the Hamiltonian and thus the particle trajectories (in this case photons) gets modified. The modified energy of a particle having 4-velocity u^α in plasma medium resukts into $E = \hbar\omega = -p_\alpha u^\alpha$. The refractive index n of the plasma medium can be written photon 4-momentum and the plasma frequency as [103]

$$n^2 = 1 + \frac{p_\alpha p^\alpha}{(p_\mu u^\mu)^2} \ . \tag{2.55}$$

The modified Hamiltonian for photons in presence of a plasma background takes the form [103]

$$\mathcal{H} = \frac{1}{2}\left[g^{\mu\nu}p_\mu p_\nu + (n^2 - 1)g^{00}p_0^2\right] \ . \tag{2.56}$$

Using the dispersion relation in presence of plasma [103], [104] and the expression for particle energy E in plasma (setting $\hbar = 1$) we obtain the refractive index n in terms of plasma frequency ω_p and photon frequency ω as [104]

$$n^2 = 1 - \left(\frac{\omega_p}{\omega}\right)^2 \tag{2.57}$$

For analytical calculations, we consider a specific form of plasma frequency ω_p taking the form [100]

$$\omega_p = \frac{4\pi e^2 N(r)}{m_e} \ . \tag{2.58}$$

In the above equation e, $N(r)$ and m_e represents the charge, number density and mass of electrons in the plasma medium respectively. For simplicity, we consider $N = N(r)$. As given in [103, 104], the physically relevant form of $N(r)$ is assumed to be $N_0(\frac{r_0}{r})^h$ where N_0, r_0 are constants. Substituting the given form of $N(r)$ in the plasma frequency ω_p and using eq.(3.65) we obtain the relation

$$\left(\frac{\omega_p}{\omega}\right)^2 = \frac{k}{r^h} \ , \ k \geqslant 0. \tag{2.59}$$

The refractive index n in eq.(3.65) takes the form

$$n = \sqrt{1 - \frac{k}{r^h}} \ . \tag{2.60}$$

The power h characterizes different properties of the plasma medium. h can take different values as in [104] but we shall work with $h = 1$ which takes into account the minimum dependence on r [104, 96]. Thus the expression of the refractive index in this work reads

$$n = \sqrt{1 - \frac{k}{r}} \ . \tag{2.61}$$

The modified form of the Hamilton-Jacobi equation in presence of the plasma medium reads [103]

$$\left(\frac{\partial S}{\partial \lambda}\right) + \frac{1}{2}\left[g^{\mu\sigma}\frac{\partial S}{\partial x^\mu}\frac{\partial S}{\partial x^\sigma} - (n^2 - 1)\left(\frac{\partial S}{\partial t}\sqrt{-g^{tt}}\right)^2\right] = 0. \tag{2.62}$$

2.5 Null geodesics and shadow in presence of plasma

2.5.1 Determination of null geodesics

Using the Hamiltonian as given in eq.(2.56) and the Hamilton's equations of motion

$$\dot{x}^\mu = \frac{\partial \mathcal{H}}{\partial p_\mu} \ \ ; \ \ \dot{p}_\mu = -\frac{\partial \mathcal{H}}{\partial x^\mu} \tag{2.63}$$

we can obtain the equations for t, ϕ, ψ. On the other hand the r, θ equations can be obtained using the modified Hamilton-Jacobi equation as given in eq.(2.62). The null geodesics for t, ϕ, ψ, r, θ in plasma becomes

$$\frac{dt}{d\lambda} = \frac{n^2 E}{f(r)} \tag{2.64}$$

$$\frac{d\phi}{d\lambda} = \frac{L_\phi}{r^2 \sin^2\theta} \tag{2.65}$$

$$\frac{d\psi}{d\lambda} = \frac{L_\psi}{r^2 \cos^2\theta} \tag{2.66}$$

$$r^2\Big(\frac{dr}{d\lambda}\Big) = \pm\sqrt{R_{pl}(r)} \tag{2.67}$$

$$r^2\Big(\frac{d\theta}{d\lambda}\Big) = \pm\sqrt{\Theta_{pl}(\theta)} \tag{2.68}$$

where

$$R_{pl}(r) = n^2 r^4 E^2 - (L^2+\kappa) r^2 f(r) \tag{2.69}$$

$$\Theta_{pl}(\theta) = \kappa - L_\phi^2 \cot^2\theta - L_\psi^2 \tan^2\theta\ . \tag{2.70}$$

The effective potential along the radial direction in presence of plasma is of the form [106]

$$V^{pl}_{eff}(r) = \frac{f(r)}{r^2}\Big(\kappa + L^2\Big) - n^2E^2\ . \tag{2.71}$$

The condition for the circular orbits are given by [1], [64]

$$V^{pl}_{eff}(r)\Bigg|_{r=r_p^{(pl)}} = 0\ ,\ \ \frac{\partial V^{pl}_{eff}(r)}{\partial r}\Bigg|_{r=r_p^{(pl)}} = 0 \tag{2.72}$$

with the condition for unstability of orbits and thereby maxima of the potential $V^{pl}_{eff}(r)$ is given by

$$\frac{\partial^2 V^{pl}_{eff}(r)}{\partial r^2}\Bigg|_{r=r_p^{(pl)}} < 0. \tag{2.73}$$

The conditions in eq.(2.72) gives [106]

$$\eta + \xi^2 = \frac{n^2(r) r^2}{f(r)}\Bigg|_{r=r_p^{(pl)}} \tag{2.74}$$

and

$$\Bigg(n(r) r f'(r) - 2n(r) f(r) - 2n'(r) r f(r)\Bigg)\Bigg|_{r=r_p^{(pl)}} = 0 \tag{2.75}$$

respectively. Using the expressions for $f(r)$ and $f'(r)$ from eq.(s)(2.11, 2.41) and $n'(r) = \frac{k}{2r^2\sqrt{1-\frac{k}{r}}}$ (which is obtained from eq.(2.61)) in eq.(2.75), we get an equation for the radius of the photon sphere which looks too complicated and therefore we do not present it here. Further, in this case it is not possible to obtain an exact solution of eq.(2.75) even in the limit $Q \to 0$. So we proceed to solve it numerically. The presence of the plasma medium introduces an extra parameter k in eq.(2.75). We then obtain the values for the photon sphere radius r_p by numerically solving eq.(2.75).

2.5.2 Determination of black hole shadow

Proceeding as before, we obtain expressions for $\frac{d\phi}{dr}$, $\frac{d\psi}{dr}$ and $\frac{d\theta}{dr}$ which are then used to determine the celestial coordinates (α, β) in presence of the plasma medium. The expressions are

$$\frac{d\phi}{dr} = \frac{L_\phi \csc^2\theta}{r^2\sqrt{n^2E^2 - \frac{f(r)}{r^2}(\kappa + L_\phi^2 + L_\psi^2)}} \tag{2.76}$$

$$\frac{d\psi}{dr} = \frac{L_\phi \sec^2\theta}{r^2\sqrt{n^2E^2 - \frac{f(r)}{r^2}(\kappa + L_\phi^2 + L_\psi^2)}} \tag{2.77}$$

$$\frac{d\theta}{dr} = \frac{1}{r^2}\sqrt{\frac{\kappa - L_\phi^2 cot^2\theta - L_\psi^2\tan^2\theta}{n^2E^2 - \frac{f(r)}{r^2}(\kappa + L_\phi^2 + L_\psi^2)}}\,. \tag{2.78}$$

Using the expressions of $\frac{d\phi}{dr}$, $\frac{d\psi}{dr}$ and $\frac{d\theta}{dr}$, we obtain α and β as

$$\alpha = -\frac{\xi_1\csc\theta + \xi_2\sec\theta}{\sqrt{1 - \frac{(\eta+\xi_1^2+\xi_2^2)\left(1-\sqrt{1-\frac{8\gamma}{l^2}}\right)}{4\gamma}}}\ ;\ \beta = \pm\sqrt{\frac{(\eta - \xi_1^2\cot^2\theta - \xi_2^2\tan^2\theta)}{1 - \frac{((\eta+\xi_1^2+\xi_2^2))\left(1-\sqrt{1-\frac{8\gamma}{l^2}}\right)}{4\gamma}}}\,. \tag{2.79}$$

Similar to non-plasma case, considering observers at $\theta = 0$ and $\theta = \frac{\pi}{2}$, the celestial coordinate read

$$\alpha = -\frac{\xi}{\sqrt{1 - \frac{(\eta+\xi^2)\left(1-\sqrt{1-\frac{8\gamma}{l^2}}\right)}{4\gamma}}}\ ;\ \beta = \pm\sqrt{\frac{\eta}{1 - \frac{((\eta+\xi^2)\left(1-\sqrt{1-\frac{8\gamma}{l^2}}\right)}{4\gamma}}}\,. \tag{2.80}$$

By combining the celestial coordinates given in eq.(4.20) and using eq.(2.74), we get [106]

$$\alpha^2 + \beta^2 = \left.\left(\frac{\left(\frac{n^2r^2}{f(r)}\right)}{1 - \frac{\left(\frac{n^2r^2}{f(r)}\right)\left(1-\sqrt{1-\frac{8\gamma}{l^2}}\right)}{4\gamma}}\right)\right|_{r=r_p^{(pl)}} \equiv R_s^2 \tag{2.81}$$

where R_s is the radius of the black hole shadow in presence of the plasma medium.

k=0.2

γ	Q	r_p	R_s
0.04	0	1.26288	1.43158
	1	1.24274	1.41829
0.06	0	1.31468	1.48548
	1	1.2944	1.47241
0.08	0	1.39359	1.56276
	1	1.37341	1.55104
0.1	0	1.53788	1.69368
	1	1.51837	1.68354

k=0.4

γ	Q	r_p	R_s
0.04	0	1.12849	1.06052
	1	1.10497	1.04703
0.06	0	1.15842	1.0894
	1	1.13371	1.07626
0.08	0	1.20383	1.13058
	1	1.17771	1.11801
0.1	0	1.28534	1.19967
	1	1.25751	1.18815

Table 2.2: Photon radius r_p and shadow radius R_s with different values of Gauss-Bonnet parameter γ and charge $Q = 0, 1$ with $M = 1$. The black hole lies in AdS background.

k=0.2

γ	Q	r_p	R_s
0.0	0	1.27491	1.69362
	1	1.25564	1.67527
0.1	0	1.18351	1.62844
	1	1.15749	1.60587
0.2	0	1.06441	1.56832
	1	1.02237	1.51562

k=0.4

γ	Q	r_p	R_s
0.0	0	1.23863	1.52487
	1	1.21834	1.50498
0.1	0	1.13633	1.44876
	1	1.1075	1.42313
0.2	0	0.995559	1.34738
	1	0.941962	1.30724

Table 2.3: Photon radius r_p and shadow radius R_s with different values of Gauss-Bonnet parameter γ and charge $Q = 0, 1$ with $M = 1$. The black hole lies in Minkowski background.

2.5.3 Graphical representation and observation

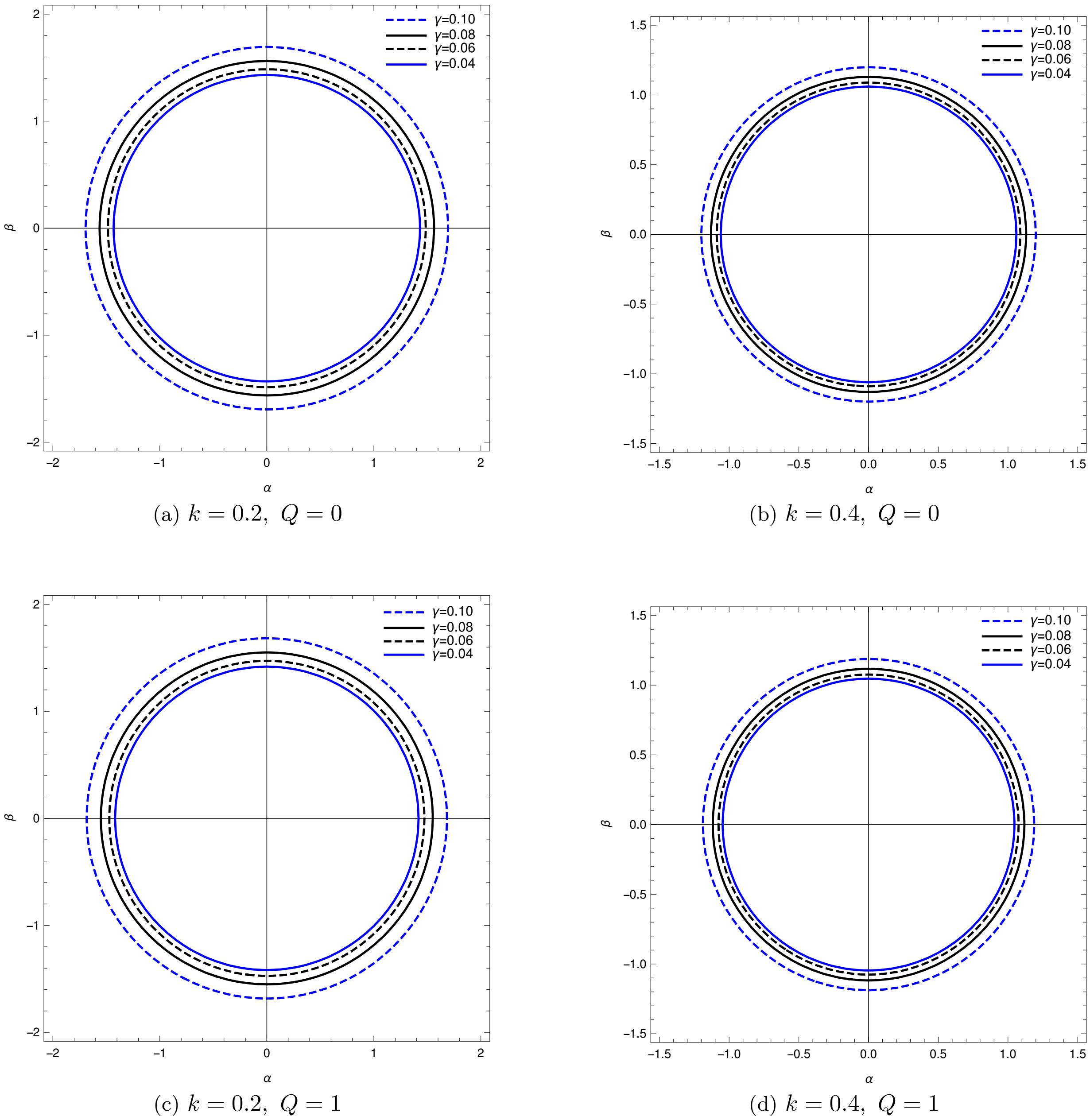

(a) $k = 0.2,\ Q = 0$

(b) $k = 0.4,\ Q = 0$

(c) $k = 0.2,\ Q = 1$

(d) $k = 0.4,\ Q = 1$

Figure 2.3: Silhouette of black hole shadow in the $(\alpha - \beta)$ plane with variation in Gauss-Bonnet parameter γ in AdS background.

In Figure (2.3), we have shown the silhouette of the black hole shadow of a charged black hole immersed in plasma in aymptotically AdS background. We plot the shadow varying the GB parameter γ and considering black hole charge $Q = 0, 1$ and plasma parameter k to be 0.2 and 0.4. Analaysing the plots, we find that as early observations, the shadow size increases with γ and decreases with charge Q even in presence of plasma. Thus the presence of plasma does not effect their nature of impact on the black hole shadow. Also we find that with increment in k, the shadow radius shrinks.

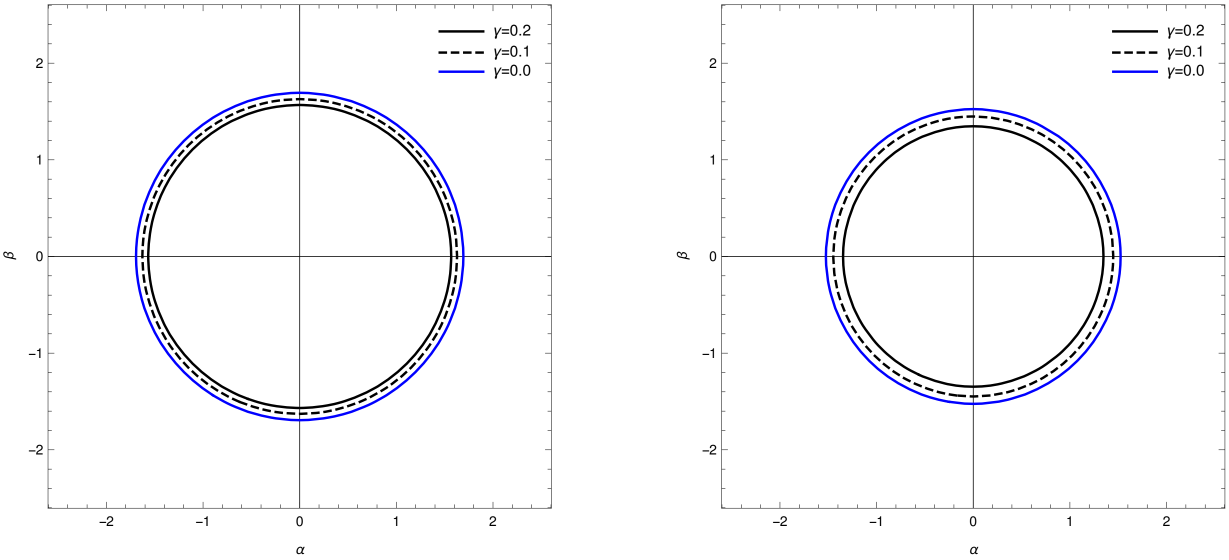

(a) $k = 0.2,\ Q = 0$

(b) $k = 0.4,\ Q = 0$

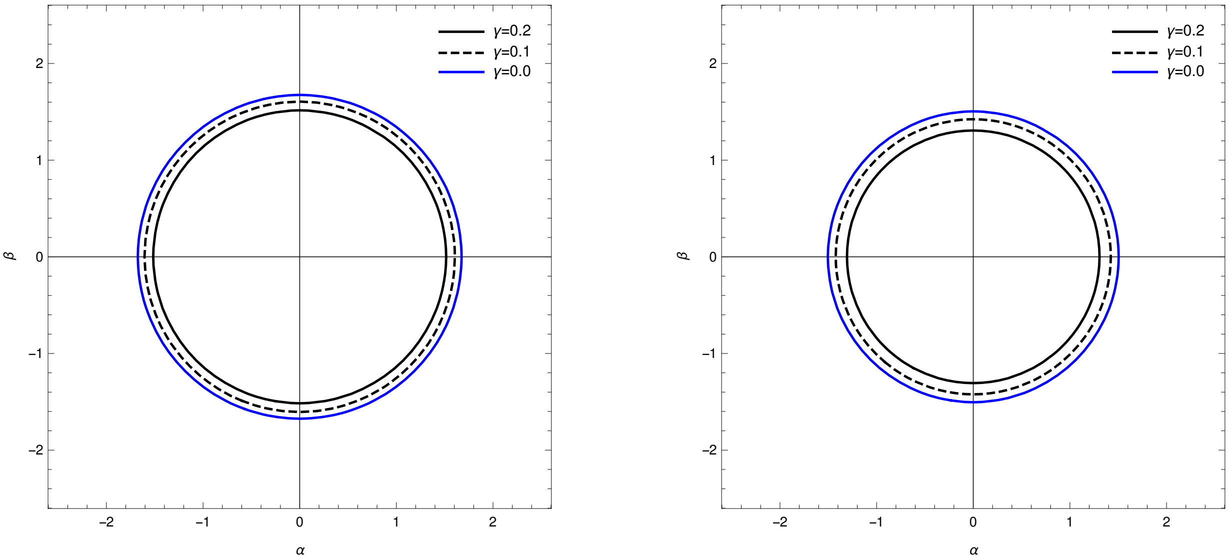

(c) $k = 0.2,\ Q = 1$

(d) $k = 0.4,\ Q = 1$

Figure 2.4: Silhouette of black hole shadow in the $(\alpha - \beta)$ plane with variation in Gauss-Bonnet parameter γ setting $Q = 0$ in Minkowski background.

In Figure (2.4), we have shown the silhouette of the black hole shadow of a charged black hole immersed in plasma in aymptotically Minkowski background. We plot the shadow varying the GB parameter γ and considering black hole charge $Q = 0, 1$ and plasma parameter k to be 0.2 and 0.4. Analaysing the plots, we find that as early observations, the shadow size decreases both with γ and charge Q even in presence of plasma. Thus the presence of plasma does not effect their nature of impact on the black hole shadow. Also we find that with increment in k, the shadow radius shrinks.

2.6 Energy emission rate

Here we study the energy emission rate of charged Gauss-Bonnet black holes in asymptotically AdS_{4+1} and asymptotically flat spacetime. Mathematically the energy emission rate takes the form [169]

$$\frac{d^2Z(\omega)}{d\omega dt} = \frac{2\pi^2\sigma_{lim}}{exp\left(\frac{\omega}{T_H}\right) - 1}\omega^3 \tag{2.82}$$

with $Z(\omega)$, ω , T_H respectively giving the energy of emission, frequency of radiated emission and Hawking temperature corresponding to the black hole. The Hawking temperature in $d = 5$ dimensions can be obtained from eq.(5.2) to be

$$T_H = \frac{f'(r)}{4\pi}\bigg|_{r=r_+} = \frac{(4Q^2r_+ - 128Mr_+^3) + (256Mr_+^2 - 12Q^2)}{96\pi^2 r_+^7} \tag{2.83}$$

where r_+ is the radius of the event horizon of the black hole.

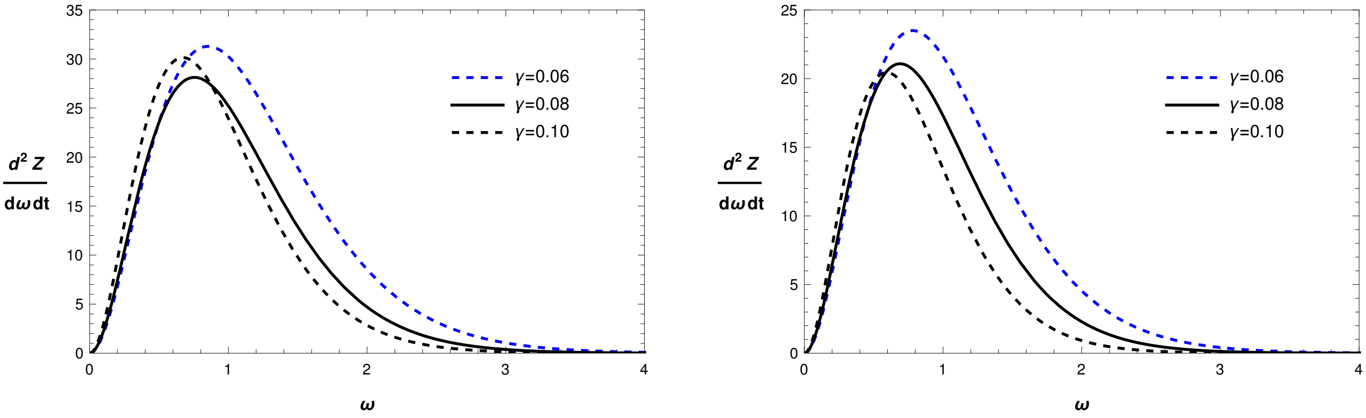

(a) k=0, Q=0

(b) k=0, Q=1

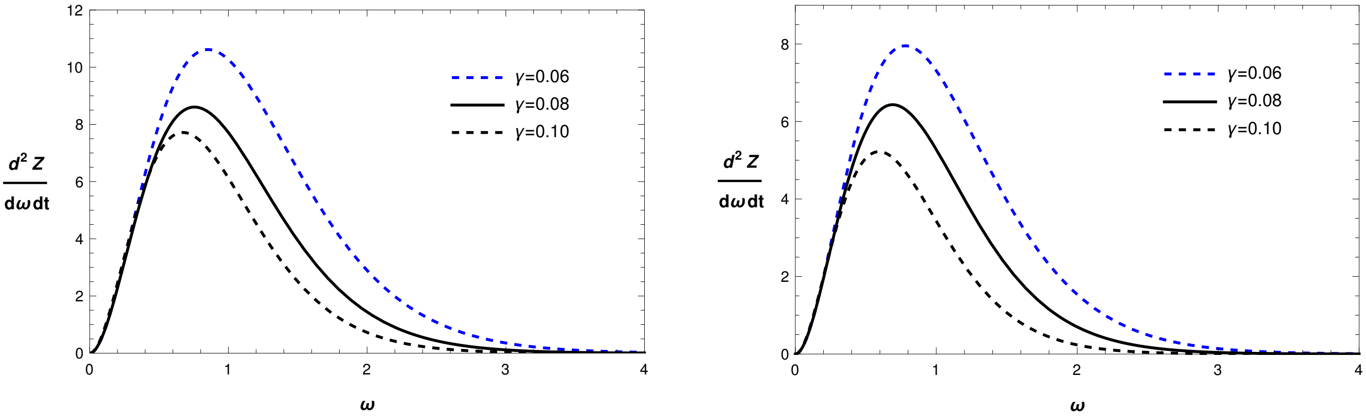

(c) k=0.2, Q=0

(d) k=0.2, Q=1

Figure 2.5: Plots of energy emission rate of charged black hole with variation in emitted frequency (ω) for varying values of Gauss-Bonnet parameter γ in asymptotically AdS background.

The expression for σ_{lim}, which is the limiting constant value is expressed in d spacetime dimensions as [170, 171]

$$\sigma_{lim} = \frac{\pi^{\frac{d-2}{2}} R_s^{d-2}}{\Gamma\left(\frac{d}{2}\right)} \tag{2.84}$$

where R_s is the radius of the shadow. In $d = 5$ dimensions, σ_{lim} reads [106]

$$\sigma_{lim} \approx \frac{4\pi R_s^3}{3} \ . \tag{2.85}$$

The form of the energy emission rate in $d = 5$ dimensions therefore becomes [106]

$$\frac{d^2 Z(\omega)}{d\omega dt} = \frac{8\pi^3 R_s^3}{3\left(exp\left(\frac{\omega}{T_H}\right) - 1\right)}\omega^3 \ . \tag{2.86}$$

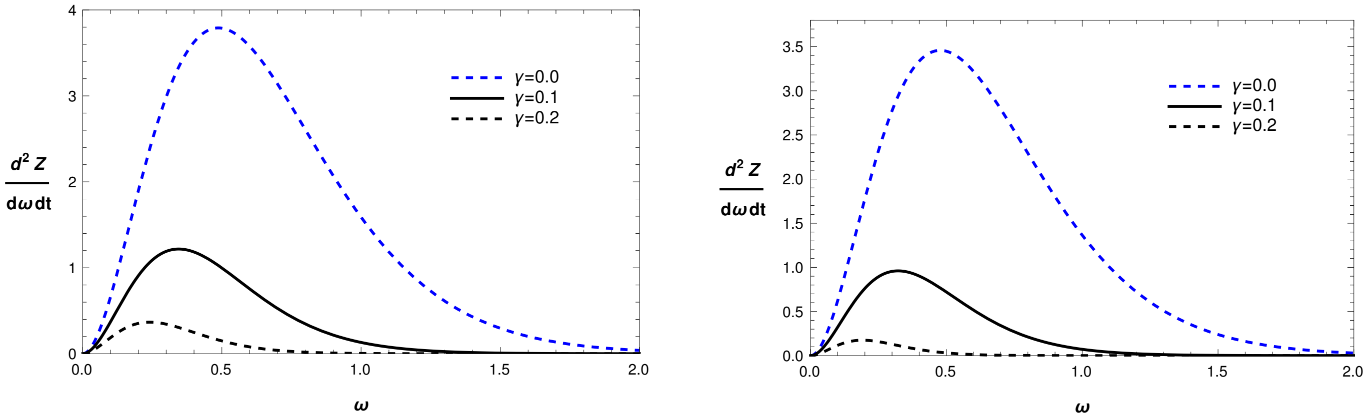

(a) k=0, Q=0

(b) k=0, Q=1

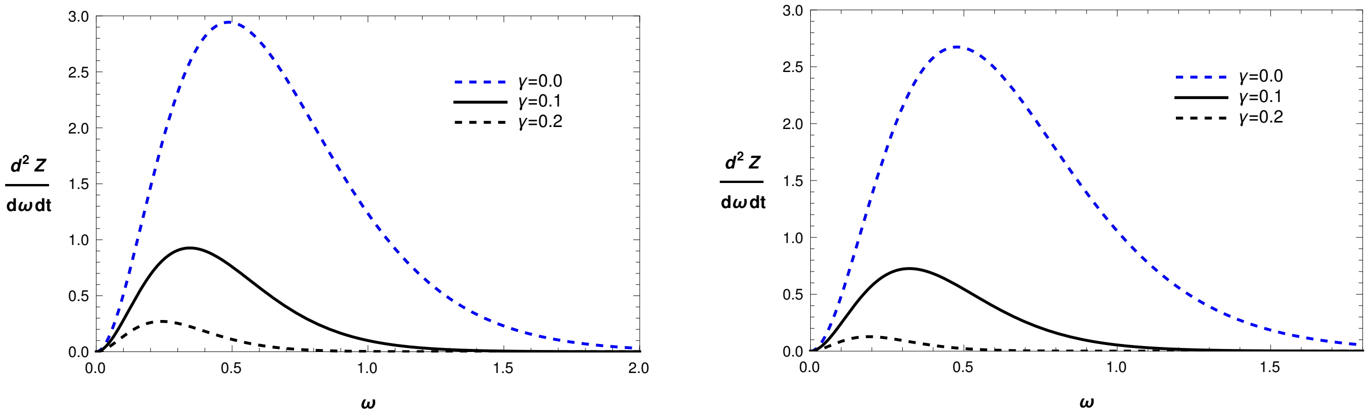

(c) k=0.2, Q=0

(d) k=0.2, Q=1

Figure 2.6: Plots of energy emission rate of charged black hole with variation in emitted frequency (ω) for varying values of Gauss-Bonnet parameter γ in asymptotically Minkowski background.

In Figures 2.5, 2.6 we plot the variation of energy emission rate $\frac{d^2 Z(\omega)}{d\omega dt}$ with the frequency of the emitted radiation ω for different values of Gauss-Bonnet parameter γ. The plots are shown for charge $Q = 0, 1$ and plasma parameter $k = 0, 0.2$. The plots in Fig.2.5 are shown for asymptotically AdS ($l = 1$) black hole and in Fig.2.1 for asymptotically Minkowski ($l = \infty$) black hole spacetime. We find that the emission rate decreases with increment in γ both for AdS and Minkowski spacetime.

We also find that plasma influences the energy emission rate drastically. The effect is more prominent in AdS black hole compared to aymptotically flat black hole.

2.7 Summary

In this chapter we discussed the shadow of a charged black hole in higher curvature Gauss-Bonnet gravity as seen by a distant observer in $d = 5$ spacetime dimensions. The reason for considering dimensions greater than $d = 4$ is that the Gauss Bonnet term effects spacetime dynamics in dimensions $d \geq 5$. Though the universe in which we live is found to be $(3 + 1)$ dimensional, yet the study of astrophysical objects like black holes and their shadow in higher dimension is worthwhile. We investigated shadow in AdS as well as Minkowski background. The study of black holes in AdS background can help us gain insight of the boundary CFT theory via AdS/CFT correspondence [154]. Also many works have been done which helps us relate some aspects in the AdS/CFT side with the photon orbits [172]-[174]. Also, studying black hole shadows in Minkowski background in higher dimensions in Gauss-Bonnet gravity can help us gain knowledge of higher curvature and speculative evidence of higher dimensions (if there are any). Again the nature of impact of Gauss-Bonnet parameter on black hole shadow can be interpolated to observable dimensions [153]. In this chapter we computed the null geodesics in $d = 5$ dimensions for charged black holes both in aymptotically AdS and Minkowski spacetimes. Then we used the null geodesics to obtain the celestial coordinates which thereby gives the radius of the black hole shadow R_s. We computed the values of photon radius r_p and shadow radius R_s taking into consideration the effect of various parameters and represent them graphically. We observe the effect of the Gauss Bonnet parameter γ on R_s which yields contrasting results for AdS black hole and asymptotically flat black hole spacetime [106]. We infer from Fig(s).(2.1), (2.2) that for AdS $(l = 1)$ spacetime, the increase in γ increases R_s whereas the opposite is observed in case of the black holes in Minkowski spacetime $(l \rightarrow \infty)$. The charge Q also has an effect on R_s. We observe that the shadow radius R_s decreases with increase in charge Q in both AdS and asymptotically flat (Minkowski) spacetime. This can be explained by the fact that the event horizon decreases with increase in charge Q, so is the black hole shadow which indirectly gives the event horizon's size [79]. We then introduce a plasma background in order to observe the effect of refractive index (n) of the medium on the unstable circular photon orbits. It is observed that an increase in the plasma parameter results in decrease in the radius of the shadow R_s. The effect of n is similar in both spacetimes (asymptotically AdS and Minkowski). Due to higher higher vaue of n, the light gets more deviated and seems to come from much closer region to the black hole thereby effectiving the size of photon radius r_p and hence of R_s. Finally we compute the energy emission rate of the charged Gauss-Bonnet black hole and represent them graphically. We observe that the energy emission rate decreases with increase in the value of γ in both AdS and asymptotically flat spacetime which can be observed in fig(s).(2.5), (2.6). We would like to mention that one of the main motivations of this work is to probe the signature of higher curvature correction in the shadow of black holes which in turn also brings out possibilities of the existence of extra dimensions.

Chapter 3

Rotating charged black hole in presence of perfect fluid dark matter

Dark matter and dark energy are intriguing topics of study and demand our attention in their own right. Besides 68% dark energy and 5% conventional matter, the cosmos includes roughly 27% dark matter [175], [176]. Dark matter is thought to be everywhere in and beyond the observable universe through evidence obtained from indirect measurements, and the amount grows as we move out from the galactic center [177]. Different dark matter theories can be highly helpful in explaining both the large and small-scale structure of the universe [178]−[180]. In addition, it has been computed that dark matter is present surrounding black holes as "*halos*". Many observations such as rotation curves of galaxies [177] and dynamical motion of galaxy clusters [181] predicted the existence of dark matter in the universe. The widely accepted model for dark matter is the cold dark matter model (CDM) whose primary candidate are WIMPs. But the CDM model breaks down at smaller scales [179]. To deal with the drawbacks of the CDM model, warm and fuzzy dark matter models have been proposed. All these models fall in the category of perfect fluid dark matter (PFDM). The perfect fluid model was first introduced in [158] where Kerr de-Sitter/anti-de-Sitter black hole in such a background was discussed thoroughly. The idea for such a model developed with works of Kiselev in [160], [161] and carried further by Li and Yang in [162]. This model has recently gained wide attention in the scientific community and huge number of works have been done in the recent years. Shadows of black holes immersed in perfect fluid dark matter have been studied for rotating black holes with and without a cosmological constant [182, 159], as well as for non-rotating charged black holes [183]. Dark matter consists of non-baryonic matter, and its presence around black holes can greatly modify the spacetime dynamics and hence effect various astrophysical aspects. The geodesics around a black hole immersed in PFDM (perfect fluid dark matter) should in principle be significantly affected by the presence of excess matter and can thus lead to interesting observations. In addition, black holes are sources of extreme energy, which can be obtained via the Penrose process [75]. The efficiency of the process is maximum at the event horizon of the black hole and requires particles with negative energy and angular momentum to be absorbed into the black hole. The process takes place in a region known as the *ergosphere* which exists only in case of rotating black holes. There have been various studies on the Penrose process and thus the energy extraction from the black hole, for example [76],[184]-[186] where the energy extraction of rotating particles was studied and it is also found that the efficiency of Penrose process increases in case of higher dimensions. In this work, we study the Penrose process for rotating charged black holes in the presence of PFDM.

In this chapter, we have obtained and discussed the solution of a stationary charged black hole surrounded by perfect fluid dark matter (PFDM) and study its different energy conditions [156]. Then we obtain the rotating version of the black hole solution by utilising the Newman-Janis algorithm [187]-[189]. An unique and interesting variation of the black hole event horizon with respect to the PFDM parameter α was observed [182]. We studied in detail the impact of PFDM on the geodesics corresponding to both massless and massive particles in the vicinity of a rotating charged black hole. After that, we calculated and analysed the circular geodesics of photons and used them to determine the radius of unstable photon orbits. In addition, we investigated how the dark matter parameter α, the spin (a) and charge (Q) of the black hole affect the photon radius. For massive particles, in addition to the effective potential (V_{eff}), the energy (E) and angular momentum (L) of the particle are also calculated. The effect of the PFDM parameter α, black hole spin (a), and charge (Q) on these calculated quantities has been analysed and discussed thoroughly. We then examined the Penrose process. Then we investigated how the PFDM parameter α affects the size of the ergosphere, the negative energy of the particle and thus the efficiency of the Penrose process. This chapter is based on our work in [156].

In the next chapter we studied the black hole shadow in the same background incorporating plasma medium.

3.1 Charged static black hole in perfect fluid dark matter

We consider a $(3+1)$-D gravity theory minimally coupled to a U(1) gauge field, in the presence of dark matter having perfect fluid nature. The action can be written as [156, 158, 159, 162, 183, 184]

$$S = \int d^4x\sqrt{-g}\Big(\frac{R}{16\pi G} - \frac{1}{4}F^{\mu\nu}F_{\mu\nu} + \mathcal{L}_{DM}\Big)\ . \tag{3.1}$$

Here, R is the Ricci scalar and G is the Newton's gravitational constant. $F_{\mu\nu}$ is the Maxwell field strength tensor which is related with the electromagnetic potential A_μ as $F_{\mu\nu} = \partial_\mu A_\nu - \partial_\nu A_\mu$, and $\mathcal{L}_{\mathcal{DM}}$ gives the Lagrangian density for the perfect fluid dark matter (PFDM). Extremizing the action we get the Einstein field equations as [156]

$$R_{\mu\nu} - \frac{1}{2}g_{\mu\nu}R = 8\pi G(T^M_{\mu\nu} - T^{DM}_{\mu\nu})\ . \tag{3.2}$$

Here, $T^M_{\mu\nu}$ corresponds to the energy-momentum tensor corresponding to the ordinary matter (Maxwell field) whose diagonal representation is [190]

$$(T^\mu_{\ \nu})^M = diag\left(-\frac{Q^2}{8\pi Gr^4}, -\frac{Q^2}{8\pi Gr^4}, \frac{Q^2}{8\pi Gr^4}, \frac{Q^2}{8\pi Gr^4}\right) \tag{3.3}$$

where Q being the electric charge. Again, $T^{DM}_{\mu\nu}$ represents the energy-momentum tensor of the perfect fluid dark matter (PFDM) [158]. It is specified as

$$(T^\mu_{\ \nu})^{DM} = diag(-\rho, P_r, P_\theta, P_\phi)\ ;\ P_r = -\rho\ ;\ P_\theta = P_\phi = P \tag{3.4}$$

where ρ and P give the density and pressure of the perfect fluid dark matter respectively. Following [158, 162], we further consider

$$(T^{\theta}_{\ \theta})^{DM} = (T^{t}_{\ t})^{DM}(1-\epsilon) \ \ ; \ \ (T^{\phi}_{\ \phi})^{DM} = (T^{r}_{\ r})^{DM}(1-\epsilon) \tag{3.5}$$

where ϵ is a constant. Using eq.(3.4) in eq.(3.5), the equation of state for the PFDM takes the form [158]

$$\frac{P}{\rho} = (\epsilon - 1) \ . \tag{3.6}$$

3.1.1 Black hole solution

We wish to obtain a static and spherically symmetric solution. So, we assume a metric ansatz of the form

$$ds^2 = -e^{\nu}dt^2 + e^{\lambda}dr^2 + r^2(d\theta^2 + \sin^2\theta d\phi^2) \tag{3.7}$$

with ν, λ being functions of r only. The field equations read

$$e^{-\lambda}\Big(\frac{1}{r^2} - \frac{\lambda^{'}}{r}\Big) - \frac{1}{r^2} = 8\pi G\Big(\rho - \frac{Q^2}{8\pi G r^4}\Big) \tag{3.8}$$

$$e^{-\lambda}\Big(\frac{1}{r^2} + \frac{\nu^{'}}{r}\Big) - \frac{1}{r^2} = 8\pi G\Big(-P_r - \frac{Q^2}{8\pi G r^4}\Big) \tag{3.9}$$

$$\frac{e^{-\lambda}}{2}\Big(\nu'' + \frac{\nu'^2}{2} + \frac{\nu' - \lambda^{'}}{r} - \frac{\nu^{'}\lambda^{'}}{2}\Big) = 8\pi G\Big(-P + \frac{Q^2}{8\pi G r^4}\Big) \tag{3.10}$$

$$\frac{e^{-\lambda}}{2}\Big(\nu'' + \frac{\nu'^2}{2} + \frac{\nu' - \lambda^{'}}{r} - \frac{\nu^{'}\lambda^{'}}{2}\Big) = 8\pi G\Big(-P + \frac{Q^2}{8\pi G r^4}\Big) \tag{3.11}$$

where prime signifies the first order differentiation with respect to the radial coordinate r. Equations (3.8) and (3.10) can be rearranged to the form

$$\begin{aligned} e^{-\lambda}\Big(\frac{1}{r^2} - \frac{\lambda^{'}}{r}\Big) - \frac{1}{r^2} + \frac{Q^2}{r^4} &= 8\pi G\rho \\ \frac{e^{-\lambda}}{2}\Big(\nu'' + \frac{\nu'^2}{2} + \frac{\nu' - \lambda^{'}}{r} - \frac{\nu'\lambda^{'}}{2}\Big) - \frac{Q^2}{r^4} &= -8\pi G P \ . \end{aligned} \tag{3.12}$$

Taking the ratio of the equations in (3.12) and using the equation of state (eq.3.6), we obtain

$$\frac{e^{-\lambda}}{2}\Big(\nu'' + \frac{\nu'^2}{2} + \frac{\nu' - \lambda^{'}}{r} - \frac{\nu'\lambda^{'}}{2}\Big) - \frac{Q^2}{r^4} = (1-\epsilon)\Bigg[e^{-\lambda}\Big(\frac{1}{r^2} - \frac{\lambda^{'}}{r}\Big) - \frac{1}{r^2} + \frac{Q^2}{r^4}\Bigg] \ . \tag{3.13}$$

Now subtracting eq.(3.9) from eq.(3.8) and using eq.(3.4), we get

$$\begin{aligned} \nu' + \lambda' &= 0 \\ \nu + \lambda &= \mathcal{C} \end{aligned} \tag{3.14}$$

where, $\mathcal{C}$ is the constant of integration. Now, rescaling the time coordinate, the integration constant

$\mathcal{C}$ can be set to zero. This implies

$$\nu = -\lambda \ . \tag{3.15}$$

Setting $\nu = \ln(1-U)$ where $U \equiv U(r)$ simplifies eq.(3.13) to the following form

$$\frac{U''}{2} + \epsilon \frac{U}{r} + (\epsilon - 1)\frac{U}{r^2} + (2-\epsilon)\frac{Q^2}{r^4} = 0 \ . \tag{3.16}$$

Eq.(3.16) can be solved for different values of ϵ [162]. However we are particularly interested in the solution for $\epsilon = \frac{3}{2}$ [160, 162]. For $\epsilon = \frac{3}{2}$, eq.(3.16) reduces to the following form

$$r^2 U'' + 3rU' + U + \frac{Q^2}{r^2} = 0 \ . \tag{3.17}$$

The solution of the above equation is obtained to be

$$U(r) = \frac{r_s}{r} - \frac{Q^2}{r^2} - \frac{\alpha}{r} \ln\left(\frac{r}{|\alpha|}\right) \tag{3.18}$$

where r_s and α are integration constants. In order to evaluate r_s, we set $Q = 0$ and $\alpha = 0$. In this limit, by utilizing the weak field approximation, r_s is obtained to be $2GM$[1]. The lapse function therefore becomes

$$f(r) = e^{\nu} = e^{-\lambda} = e^{\ln(1-U)} = 1 - U = 1 - \frac{2GM}{r} + \frac{Q^2}{r^2} + \frac{\alpha}{r}\ln\left(\frac{r}{|\alpha|}\right) \tag{3.19}$$

corresponding to the following metric of a static, spherically symmetric, charged black hole in PFDM of the form

$$ds^2 = -f(r)dt^2 + \frac{1}{f(r)}dr^2 + r^2 d\theta^2 + r^2 \sin^2\theta d\phi^2 \ . \tag{3.20}$$

It is reassuring to observe that the above geometry reduces to the well-known black hole solutions in the literature. In the limit $\alpha \to 0$, eq.(3.19) coincides with the Reissner-Nordström black hole solution and in the limit $\alpha \to 0, Q \to 0$ it reduces to the Schwarzschild solution. Further, in the limit $Q \to 0$ the above geometry matches with the solution given in [162, 182].

3.1.2 Validity of the energy conditions

We now check the validity of the energy conditions of the above solution. For that we first derive the density (ρ) of PFDM. Substituting $e^{-\lambda}$ given in eq.(3.19) in eq.(3.8) we get [156]

$$\rho = \frac{\alpha}{8\pi G r^3} \ . \tag{3.21}$$

Similarly, from rest of the equations, we obtain the pressure components of the energy-momentum tensor $(T^{\mu}_{\ \nu})^{DM}$ of the dark matter. This reads [156]

$$P_r = -\rho = -\frac{\alpha}{8\pi G r^3}, \ P_\theta = P_\phi = \frac{1}{2}\rho \ . \tag{3.22}$$

---

[1] The calculation is shown in Appendix A.

WEC or weak energy condition can written as [64, 191]

$$T_{\mu\nu}\xi^{\mu}\xi^{\nu} \geq 0 \tag{3.23}$$

where ξ^{μ} and ξ^{ν} are time-like vectors. WEC signifies that the total energy density of all matter fields as measured by an observer moving along a time-like curve is always positive. Eq.(3.23) implies $\rho_s \geq 0$ and $\rho_s + P_i^{total} \geq 0$ $(i = r, \theta, \phi)$ (where P_i^{total} is the pressure in any spatial direction) [156]. Here, ρ_s is given as $\left(\rho - \frac{Q^2}{8\pi G r^4}\right)$ [156]. Hence, in order to satisfy the WEC, the following condition must hold

$$\rho_s = \frac{\alpha}{8\pi G r^3} - \frac{Q^2}{8\pi G r^4} \geq 0. \tag{3.24}$$

The above condition reduces to $\frac{\alpha}{8\pi G r^3} \geq 0$ when the (ordinary) matter field is absent (that is $Q = 0$).

3.2 Rotating black hole using Newman-Janis algorithm

In general all black holes in the universe are rotating. So the inclusion of spin a to black hole metric makes the scenario realistic. In order to incorporate spin (a), we wish to utilise the Newman-Janis algorithm [187], [192] which is one of the most effective technique to incorporate spin to any system in absence of cosmological constant. Let us discuss the algorithm by considering a general metric of the form

$$ds^2 = -f(r)dt^2 + \frac{1}{g(r)}dr^2 + h(r)\Big(d\theta^2 + \sin^2\theta d\phi^2\Big) \tag{3.25}$$

and follow the approach accordingly as described in [189]. We first express the metric in Eddington-Finkelstein coordinates (u) having the transformation

$$dt = du + \frac{dr}{\sqrt{f(r)g(r)}} \ . \tag{3.26}$$

The metric in Eddington-Finkelstein coordinates take the form

$$ds^2 = -f(r)du^2 - 2\sqrt{\frac{f(r)}{g(r)}}dudr + h(r)\Big(d\theta^2 + \sin^2\theta d\phi^2\Big) \ . \tag{3.27}$$

Then we introduce null tetrads $Z^{\mu} = \Big(l^{\mu}, n^{\mu}, m^{\mu}, \overline{m}^{\mu}\Big)$. The metric tensor can be written in terms of null tetrads as

$$g^{\mu\nu} = -l^{\mu}n^{\nu} - l^{\nu}n^{\mu} + m^{\mu}\overline{m}^{\nu} + m^{\nu}\overline{m}^{\mu} \ . \tag{3.28}$$

The null tetrads follow the relations $l^{\mu}n_{\mu} = -m^{\mu}\overline{m}_{\mu} = 1$ with the other possible combinations giving zeroes. To obtain the inverse metric, we need to represent the tetrad components in terms of (u, r, θ, ϕ). This reads

$$l^{\mu} = \delta^{\mu}_{r}$$

$$n^{\mu} = \sqrt{\frac{g(r)}{f(r)}}\delta^{\mu}_{u} - \frac{g(r)}{2}\delta^{\mu}_{r}$$

$$m^\mu = \frac{1}{\sqrt{2h(r)}}\Big(\delta^\mu_\theta + \frac{i}{\sin\theta}\delta^\mu_\phi\Big) \ . \tag{3.29}$$

In order to add spin to the metric solution, we use the transformations $u \to u^{'} = u - ia\cos\theta$ and $r \to r^{'} = r + ia\cos\theta$. The null tetrads get modified following the relation

$$Z'^{\mu}_{\ \beta} = \frac{\partial x'^{\mu}}{\partial x^\nu} Z^{\nu}_{\ \beta} \ . \tag{3.30}$$

Here μ denotes the components of the tetrads along u, r, θ, ϕ directions whereas β denotes the null tetrads $(l, n, m, \bar{m})$. Thus the above transformation gives a new set of tetrads

$$l'^{\mu} = \delta^\mu_r; \ \ n'^{\mu} = \sqrt{\frac{g(r)}{f(r)}}\delta^\mu_u - \frac{f(r)}{2}\delta^\mu_r; \ \ m'^{\mu} = \frac{1}{\sqrt{2h(r)}}\Big(ia\sin\theta\Big(\delta^\mu_u - \delta^\mu_r\Big) + \delta^\mu_\theta + \frac{i}{\sin\theta}\delta^\mu_\phi\Big) \ .$$

As r and u got transformed, hence the components of the metric tensor will also modify. Hence, we get $f(r) \to F(r,\theta)$, $g(r) \to G(r,\theta)$ and $h(r) \to H(r,\theta)$. The non-zero components of the inverse metric tensor are

$$g^{uu} = \frac{a^2\sin^2\theta}{H} \ ; \ g^{rr} = G + \frac{a^2\sin^2\theta}{H} \ ; \ g^{ur} = g^{ru} = -\sqrt{\frac{G}{F}} - \frac{a^2\sin^2\theta}{H}$$

$$g^{\theta\theta} = \frac{1}{H} \ ; \ g^{\phi\phi} = \frac{1}{H\sin^2\theta} \ ; \ g^{u\phi} = g^{\phi u} = \frac{a}{H} \ ; \ g^{r\phi} = g^{\phi r} = -\frac{a}{H} \ .$$

Using the above metric components, we obtain the non-zero components of the covariant metric tensor as

$$g_{uu} = -F \ ; \ g_{ur} = g_{ru} = -\sqrt{\frac{F}{G}} \ ; \ g_{u\phi} = g_{\phi u} = \Big(-a\sqrt{\frac{F}{G}} + aF\Big)\sin^2\theta$$

$$g_{\theta\theta} = H \ ; \ g_{\phi\phi} = \sin^2\theta\Big(H + 2a^2\sin^2\theta\sqrt{\frac{F}{G}} - a^2F\sin^2\theta\Big) \ ; \ g_{r\phi} = g_{\phi r} = a\sin^2\theta\sqrt{\frac{F}{G}} \ .$$

Thus the metric in Eddington Finkelstein coordinates read

$$\begin{aligned} ds^2 = -Fdu^2 - 2\sqrt{\frac{F}{G}}dudr + 2a\sin^2\theta\Big(F - \sqrt{\frac{F}{G}}\Big)dud\phi + 2a\sin^2\theta\sqrt{\frac{F}{G}}drd\phi \\ +Hd\theta^2 + \sin^2\theta\Big[H + a^2\sin^2\theta\Big(2\sqrt{\frac{F}{G}} - F\Big)\Big]d\phi^2 \ . \end{aligned} \tag{3.31}$$

Now we want to remove u and express the metric in Boyer-Lindquist coordinates. This can be achieved by using the transformation $du = dt + \xi_1(r)dr$ and $d\phi = d\phi + \xi_2(r)dr$. Only the diagonal elements and $dtd\phi$ component of the metric survives, rest are zero. This condition gives the values of ξ_1 and ξ_2 as

$$\xi_1(r) = \frac{-\Big(\sqrt{\frac{G}{F}}H + a^2\sin^2\theta\Big)}{\Big(GH + a^2\sin^2\theta\Big)} \quad ; \quad \xi_2(r) = \frac{-a}{\Big(GH + a^2\sin^2\theta\Big)}$$

and the metric becomes

$$ds^2 = -Fdt^2 + \Big(\frac{H}{GH + a^2\sin^2\theta}\Big)dr^2 + Hd\theta^2 + 2a\sin^2\theta\Big(F - \sqrt{\frac{F}{G}}\Big)dtd\phi + \sin^2\theta\Big[H + a^2\sin^2\theta\Big(2\sqrt{\frac{F}{G}} - F\Big)\Big]d\phi^2 \ . \tag{3.32}$$

Now to incorporate spin a into F, G, H and also to keep the terms real, we use the transformation $r^p \to \frac{r^{p+2}}{r^2+a^2\cos^2\theta} = \frac{r^{p+2}}{\rho^2}$; $p \geq 0$ following [188]. This approach of incorporating spin (a) into the terms, leads to the modifies F, G, H as

$$f(r) \to F(r) = 1 - \frac{2Mr}{\rho^2} + \frac{Q^2}{\rho^2} + \frac{\alpha r}{\rho^2}ln\Big(\frac{r}{|\alpha|}\Big)$$

$$g(r) \to G(r) = 1 - \frac{2Mr}{\rho^2} + \frac{Q^2}{\rho^2} + \frac{\alpha r}{\rho^2}ln\Big(\frac{r}{|\alpha|}\Big)$$

$$h(r) \to H(r) = \rho^2 \ .$$

Using the above relations, we obtain the final expression for the rotating charged black hole metric in PFDM as

$$ds^2 = -\frac{1}{\rho^2}\Big(\Delta - a^2\sin^2\theta\Big)dt^2 + \frac{\rho^2}{\Delta}dr^2 + \rho^2 d\theta^2 - \frac{2a\sin^2\theta}{\rho^2}\Big[2Mr - Q^2 - \alpha r\ln\Big(\frac{r}{|\alpha|}\Big)\Big]dtd\phi + \sin^2\theta\Big[r^2 + a^2 + \frac{a^2\sin^2\theta}{\rho^2}\Big(2Mr - Q^2 - \alpha r\ln\Big(\frac{r}{|\alpha|}\Big)\Big)\Big]d\phi^2 \tag{3.33}$$

with $\quad \Delta = r^2 + a^2 - 2Mr + Q^2 + \alpha r\ln\Big(\frac{r}{|\alpha|}\Big)$ and $\quad \rho^2 = r^2 + a^2\cos^2\theta$.

3.3 Analysis of the solution

The solution in eq. (3.33) gives the solution of a rotating charged black hole immersed in perfect fluid dark matter. The horizon of the black hole is dictated by the solution $\Delta = 0$. The horizon gets influenced by PFDM parameter α, the black hole spin a and charge Q. The contribution of PFDM in the system comes via the logarithmic term. The term can be either positive or negative depending on the sign of α. The authors in [158] have discussed about the importance and significance of both positive and negative values of α. In this work we are primarily interested in the positive values of α. The allowed maximum value for α is $\alpha_{max} = 2M$ [158, 159]. For the sake of simplicity, we will consider $M = 1$ in our subsequent analysis. The PFDM term influences the structure of the spacetime and hence the trajectories of the geodesics.

Table 3.1 shows the values of the inner horizon (r_{h-}) and outer horizon (r_{h+}) of the black hole for various values of α at constant spin parameter $a = 0.5$ and charge $Q = 0.3$ of the black hole. We find that the outer horizon (r_{h+}) decreases with the increase in α upto a critical value α_c (which in this case $\alpha_c \approx 0.47$).

α	0.1	0.2	0.3	0.4	0.47	0.5	0.6	0.7	0.8	0.9	1.0
r_{h+}	1.5	1.37	1.30	1.27	1.265	1.267	1.28	1.30	1.34	1.37	1.415
r_{h-}	0.2	0.185	0.17	0.1525	0.14	0.135	0.12	0.105	0.095	0.085	0.075

Table 3.1: Inner (r_{h-}) and outer (r_{h+}) horizon radius of the black hole for different values of α with fixed $a = 0.5,\ Q = 0.3$.

However, beyond this critical value (α_c), the outer horizon (r_{h+}) starts to increase steadily. Also we find that with increment in the value of α, the inner horizon radius (r_{h-}) monotonically decreases. This critical value α_c can be interpreted as the point of reflection. The point of reflection can be observed by plotting $\Delta(r)$ with r at fixed values of spin (a) and charge (Q) of the black hole. The critical point corresponds to the turning point of $\Delta(r)$ subject to the condition $\left.\frac{d\Delta(r)}{dr}\right|_{r=r_{h+}} = 0$.

a	Q	α_c
0.1	0.0	0.602
0.1	0.8	0.454
0.2	0.0	0.596
0.2	0.8	0.432
0.3	0.0	0.574
0.3	0.8	0.402
0.4	0.0	0.552
0.4	0.7	0.454

a	Q	α_c
0.5	0.0	0.536
0.5	0.7	0.418
0.6	0.0	0.510
0.6	0.6	0.418
0.7	0.0	0.484
0.7	0.5	0.418
0.8	0.0	0.465
0.8	0.3	0.400

Table 3.2: Critical values of PFDM parameter (α_c) for valid combinations of spin (a) and charge (Q) of the black hole.

This effect on the event horizon of the black hole gets reflected on the black hole shadow [182] as discussed in the next chapter. Due to such effect observed on event horizon of black hole, we are interested in analysing different properties of the black hole spacetime in two different ranges of α, namely, the lower range $\alpha < \alpha_c$ and the higher range $\alpha > \alpha_c$. This observation of the apparent increase in the size of the black hole after a critical value α_c can be explained by PFDM's contribution to the mass of the black hole system. So as discussed in [182], we consider that the total system consists of two parts, one is the original BH with mass M and the other part coming from the perfect fluid dark matter with mass $M^{'}$. So, when the PFDM parameter α is less than the critical value α_c, then the dark matter opposes the effect of the original black hole system, hence the effective horizon is less than $2M$. But as α gradually increases and becomes $\alpha > \alpha_c$, the total system's mass is dictated by the dark matter component. Thus, the event horizon monotonically increases after α_c. In Table 3.2, we have shown the values of α_c for different possible combinations of spin a and charge Q which has been used in the subsequent analysis. We observe that the obtained values of α_c lies within the range $\alpha_c \in [0.4 - 0.602]$ depending upon the values of spin (a) and charge (Q). On the basis of these values, we define the lower range of values of α which are less than these values and higher range of values of α which are greater than these values.

3.4 Circular geodesics

As mentioned above, we are interested in studying geodesics. For simplicity we constrain ourselves to the study of geodesics in the equatorial plane ($\theta = \frac{\pi}{2}$). The consideration of equatorial plane simplifies some functions as

$$\Delta = r^2 + a^2 - 2Mr + Q^2 + \alpha r \ln\left(\frac{r}{|\alpha|}\right) \;\; ; \;\; \rho^2 = r^2 \ .$$

In order to continue the analysis, we consider a particle whose Lagrangian $\mathcal{L} = \frac{1}{2} g_{\mu\nu}\dot{x}^\mu \dot{x}^\nu$ [1]. $\dot{x}^\mu = u^\mu = \frac{dx^\mu}{d\lambda}$ denotes the four-velocity of the particle. The affine parameter corresponds to the proper time (τ) in case of the massive particles moving along timelike geodesics. The Lagrangian is expressed in terms of metric and we observe that the metric coefficients are independent of t and ϕ. Hence the metric is invariant along those directions (directions of symmetry) as discussed in the previous chapter. The metric invariance along those directions gives two conserved quantities E and L. The quantities E and L physically represent the specific energy (energy per unit mass) and angular momentum (angular momentum per unit mass) of the particle respectively measured by stationary observer at infinity. In terms of these quantities, the geodesic equations of t and ϕ take the form

$$\dot{t} = \frac{1}{r^2}\Big[\frac{r^2 + a^2}{\Delta}\Big(E(r^2 + a^2) - aL\Big) + a(L - aE)\Big] \tag{3.34}$$

$$\dot{\phi} = \frac{1}{r^2}\Big[\frac{a}{\Delta}\Big(E(r^2 + a^2) - aL\Big) + (L - aE)\Big] \ . \tag{3.35}$$

The Hamiltonian $\mathcal{H} = p_\mu \dot{x}^\mu - \mathcal{L}$ reads

$$2\mathcal{H} = p_0\dot{x}^0 + p_1\dot{x}^1 + p_3\dot{x}^3 = -Et + L\dot{\phi} + \frac{r^2}{\Delta}\dot{r}^2 = constant = \delta \ . \tag{3.36}$$

with $\delta = -1, 0, 1$ for timelike, null and spacelike geodesics respectively. We are primarily interested in null and timelike geodesics which are physically relevant. Substituting the values of $\dot{t}$ and $\dot{\phi}$ from eq(s).(3.34) and (3.35) in eq.(3.36), we obtain the geodesic equation for r as

$$\dot{r}^2 = \frac{1}{r^4}\Big[\Big(E(r^2 + a^2) - aL\Big)^2 - \Delta(L - aE)^2\Big] + \frac{\Delta}{r^2}\,\delta \ . \tag{3.37}$$

The radial geodesic equation is useful for the analysis of the circular geodesics and also for determining the effective potential.

3.4.1 Null geodesics and photon orbit radius

First we study the null geodesics subject to the condition $\delta = 0$. Hence the radial equation becomes

$$\dot{r}^2 = \frac{1}{r^4}\Big[\Big(E(r^2 + a^2) - aL\Big)^2 - \Delta(L - aE)^2\Big] \equiv F(r) \ . \tag{3.38}$$

We define $\frac{L}{E} = D$ as the impact parameter reducing two constants L and E into a single one D. In terms of D, the above eq.(3.38) becomes

$$\dot{r}^2 = \frac{E^2}{r^2}\Big[r^2 + \frac{2M}{r}(a-D)^2 - \frac{Q^2}{r^2}(a-D)^2 - \frac{\alpha}{r}ln(\frac{r}{\alpha}) + (a^2-D^2)\Big] \ . \tag{3.39}$$

In general $D \neq a$, but for the trivial case considering $D = a$, we get the geodesics for t, ϕ and r reduce to

$$\frac{dt}{d\lambda} = \frac{r^2+a^2}{\Delta}E \ \ ; \ \ \frac{d\phi}{d\lambda} = \frac{a}{\Delta}E \ \ ; \ \ \frac{dr}{d\lambda} = \pm E \ . \tag{3.40}$$

a=0.5,Q=0.3

α	r_{p1}
0.1	1.85
0.2	1.69
0.3	1.62
0.4	1.60
0.9	1.81
1.0	1.87
1.1	1.94
1.2	2.05

Q=0.3, α=0.2, 1.0

α	a	r_{p1}
0.2	0.1	2.18
0.2	0.4	1.83
0.2	0.7	1.345
1.0	0.1	2.15
1.0	0.4	1.95
1.0	0.7	1.7

a=0.5, α=0.2, 1.0

α	Q	r_{p1}
0.2	0.0	1.78
0.2	0.3	1.7
0.2	0.6	1.4
1.0	0.0	1.9
1.0	0.3	1.87
1.0	0.6	1.7

Table 3.3: Radius (r_{p1}) of the co-rotating (prograde) photon orbits.

a=0.5, Q=0.3

α	r_{p2}
0.1	2.95
0.2	2.755
0.3	2.605
0.4	2.515
0.9	2.47
1.0	2.505
1.1	2.545
1.2	2.59

Q=0.3, α=0.2, 1.0

α	a	r_{p2}
0.2	0.1	2.39
0.2	0.4	2.67
0.2	0.7	2.92
0.2	1.0	3.15
1.0	0.1	2.28
1.0	0.4	2.45
1.0	0.7	2.61
1.0	1.0	2.745

a=0.5, α=0.2, 1.0

α	Q	r_{p2}
0.2	0.0	2.82
0.2	0.3	2.75
0.2	0.6	2.54
0.2	0.9	2.40
1.0	0.0	2.55
1.0	0.3	2.5
1.0	0.6	2.34
1.0	0.9	2.1

Table 3.4: Radius (r_{p2}) of the counter rotating (retrograde) photon orbits.

For the general case ($D \neq a$), we wish to find the circular photon orbits. The conditions that constrain them are $F(r)\Big|_{r=r_p} = F'(r)\Big|_{r=r_p} = 0$ [193]. These two conditions yield

$$r_p^2 + \frac{2M}{r_p}(a-D)^2 - \frac{Q^2}{r_p^2}(a-D)^2 - \frac{\alpha}{r_p}ln(\frac{r_p}{|\alpha|})(a-D)^2 + (a^2-D^2) = 0 \tag{3.41}$$

$$2r_p - \frac{2M}{r_p^2}(a-D)^2 + \frac{2Q^2}{r_p^3}(a-D)^2 + \frac{\alpha}{r_p^2}ln(\frac{r_p}{|\alpha|})(a-D)^2 - \frac{\alpha}{r_p^2}(a-D)^2 = 0 \ . \tag{3.42}$$

Solving for D from eq.(3.42), we get

$$D = a \mp \sqrt{\frac{2r_p^5}{2Mr_p^2 - 2Q^2r_p - \alpha r_p^2 ln(\frac{r_p}{|\alpha|}) + \alpha r_p^2}} \ . \tag{3.43}$$

Here the signs ∓ corresponds to counter rotating (-) and co-rotating (+) orbits around the black hole. Substituting the expression for D in eq.(3.41), we obtain the equation useful for determining the radius of the photon orbits

$$6Mr_p^3-4Q^2r_p^2-3\alpha r_p^3\ln\left(\frac{r_p}{|\alpha|}\right)+\alpha r_p^3-2r_p^4\pm 2a\sqrt{2r_p^4\Big(2Mr_p-2Q^2-\alpha r_p\ln\left(\frac{r_p}{|\alpha|}\right)+\alpha r_p\Big)}=0\ . \quad (3.44)$$

The ± signs denote the counter rotating and the co-rotating photon orbits. Tables (3.3) and (3.4) show the photon sphere radius (r_p) with the variation in spin (a), charge (Q) and the PFDM parameter (α). Here r_{p1} and r_{p2} correspond to the co-rotating and counter rotating photon sphere radius.

Since the black hole horizon shows different behaviour in different regime of PFDM parameter α, so we have analysed the different geodesics and the corresponding characteristics of the particles in two separate regime. One is the lower regime of α ($\alpha < \alpha_c$) whereas, the other is the higher regime of α ($\alpha > \alpha_c$).

From the above Table(s) (3.3),(3.4), it is clear that for the lower regime, that is for $\alpha < \alpha_c$, the photon radius corresponding to both the co-rotating (r_{p1}) and the counter-rotating (r_{p2}) orbits decreases with increment in the PFDM parameter. On the other hand, in the higher regime where $\alpha > \alpha_c$, increment in α increases the photon radius as is evident from the variation in the outer event horizon radius (r_{h+}).

Also, with increase in the black hole spin a, the radius of the counter rotating orbits (r_{p2}) increases while that of the co-rotating orbits (r_{p1}) decreases for both regime of α ($\alpha > \alpha_c$ and $\alpha < \alpha_c$). The presence of the charge (Q) also affects the radius of the photon sphere as can be observed from the Tables (3.3), (3.4). With increase in the black hole charge (Q), the photon sphere radius decreases both for co-rotating (r_{p2}) and counter rotating (r_{p1}) orbits considering α=0.2 ($\alpha < \alpha_c$) and α=1.0 ($\alpha > \alpha_c$). Besides we also find that the radius of counter rotating orbits (r_{p2}) are larger than the co-rotating orbits (r_{p1}) of the photons moving around the black hole. Thus the corotating photons lie closer to the black hole.

3.4.2 Time-like geodesics and the calculation of energy (E) and angular momentum (L) for massive particles

In this section, we consider massive particles which are subject to the condition $\delta = -1$. This modifies the radial equation (3.37) into the form

$$\dot{r}^2=\Big[E^2+\frac{2M}{r^3}(aE-L)^2-\frac{Q^2}{r^4}(aE-L)^2-\frac{\alpha}{r^3}ln\Big(\frac{r}{|\alpha|}\Big)+\frac{1}{r^2}(a^2E^2-L^2)\Big]-\frac{\Delta}{r^2}\equiv\tilde{F}(r)\ . \quad (3.45)$$

For the trivial case, $L = aE$, the radial equation simplifies to the form

$$\frac{dr}{d\tau}=\Big(E^2-\frac{\Delta}{r^2}\Big)^{\frac{1}{2}}\ . \quad (3.46)$$

So the proper time τ can be evaluated as

$$\tau=\int\Big(E^2-\frac{\Delta}{r^2}\Big)^{-\frac{1}{2}}dr\ . \quad (3.47)$$

For elaborate discussion and analysis, we consider the general case ($L \neq aE$). We wish to calculate the energy (E) and the angular momentum (L) of the particle and show it's variation with PFDM parameter α. In this case, we proceed by assuming $x = L - aE$ and rewrite the above equation in terms of x and E. The conditions for circular orbits are $\tilde{F}(r) = \tilde{F}'(r) = 0$ [193]. Using them we get

$$\tilde{F}(r) = x^2\Big(a^2 - \Delta\Big) + r^4E^2 - 2aEr^2x - \Delta r^2 = 0 \tag{3.48}$$

$$\tilde{F}'(r) = 4r^3E^2 - 4aErx - 2\Delta r - \Delta^{'}(r^2 + x^2) = 0 \ . \tag{3.49}$$

The expression for E is obtained by eliminating E^2 from eq.(s)(3.48), (3.49) as

$$E = \frac{1}{r^2ax}\Big[\Big(a^2 - \Delta + \frac{r\Delta^{'}}{4}\Big)x^2 + \Big(\frac{\Delta^{'}}{4}r^3 - \frac{\Delta}{2}r^2\Big)\Big] \ . \tag{3.50}$$

On replacing E from eq.(3.50) in eq.(3.48), we get an equation in x as[2]

$$\begin{aligned}\Big[4\Big(\Delta - a^2 - \frac{r\Delta^{'}}{4}\Big)^2 - 4a^2\Big(a^2 - \Delta + \frac{r\Delta^{'}}{2}\Big)\Big]x^4 + \Big[\Big(4a^2 - 4\Delta + r\Delta^{'}\Big) \\ \times\Big(\frac{r^3\Delta^{'}}{2} - r^2\Delta\Big) - 2r^3a^2\Delta^{'}\Big]x^2 + \Big[r^2\Delta - \frac{r^3\Delta^{'}}{2}\Big]^2 = 0 \ .\end{aligned} \tag{3.51}$$

The equation is quadratic in x^2 with the discriminant

$$\Delta_D = 16a^2\Delta^2r^4\Big[a^2 - \Delta + \frac{r\Delta^{'}}{2}\Big] \ . \tag{3.52}$$

Now we can factorize the coefficient of x^4 as

$$4\Big(\Delta - a^2 - \frac{r\Delta^{'}}{4}\Big)^2 - 4a^2\Big(a^2 - \Delta + \frac{r\Delta^{'}}{2}\Big) = \mathcal{F}_+\mathcal{F}_- \tag{3.53}$$

where

$$\mathcal{F}_\pm = 2\Big(\Delta - a^2 - \frac{r\Delta^{'}}{4}\Big) \pm 2a\sqrt{\Big(a^2 - \Delta + \frac{r\Delta^{'}}{2}\Big)} \ . \tag{3.54}$$

Rewriting $\mathcal{F}_- \equiv \mathcal{F}_\mp$ and $\mathcal{F}_+ \equiv \mathcal{F}_\pm$ the expression for x^2 takes the form

$$x^2 = \frac{-\Big[\Big(4a^2 - 4\Delta + r\Delta^{'}\Big) \times \Big(\frac{r^3\Delta^{'}}{2} - r^2\Delta\Big) - 2r^3a^2\Delta^{'}\Big] \pm 4a\Delta r^2\sqrt{\Big[a^2 - \Delta + \frac{r\Delta^{'}}{2}\Big]}}{\mathcal{F}_\mp\mathcal{F}_\pm} \ . \tag{3.55}$$

The presence of ± sign makes it hard to simplify the expression for x^2. The simplified solution for x^2 becomes [156]

$$x^2 = r^2\frac{\Big(K \pm \mathcal{F}_\mp\Big)}{\mathcal{F}_\pm\mathcal{F}_\mp}\mathcal{F}_\pm = r^2\frac{\Big(\Delta - \mathcal{F}_\mp\Big)}{\mathcal{F}_\mp} \ ; \ K = \Delta \ . \tag{3.56}$$

---

[2] The calculation is shown in Appendix B

The solution for x becomes

$$x = \pm \frac{r}{\sqrt{\mathcal{F}_{\mp}}} \left[a \pm \sqrt{a^2 - \Delta + \frac{r\Delta'}{2}} \right] . \tag{3.57}$$

Replacing the values of x, the expression for energy becomes

$$E = \frac{1}{\sqrt{\mathcal{F}_{\mp}} r} \left[\Delta - a \left(a \pm \sqrt{a^2 - \Delta + \frac{r\Delta'}{2}} \right) \right] \tag{3.58}$$

and that of angular momentum becomes

$$L = \frac{1}{\sqrt{\mathcal{F}_{\mp}} r} \left[a \left(\Delta - a^2 - r^2 \right) \mp \left(r^2 + a^2 \right) \sqrt{a^2 - \Delta + \frac{r\Delta'}{2}} \right] . \tag{3.59}$$

3.4.3 Graphical representation and observation

The plots of the above expressions for energy (E) and angular momentum (L) with respect to the radial distance (r) gives an idea about the possibility of existence of orbits of massive particles around the black hole. The study also gives an idea about the spacetime structure around the black hole. Also, in our case it helps us to get an insight about the impact of the surrounding dark matter on the geodesics.

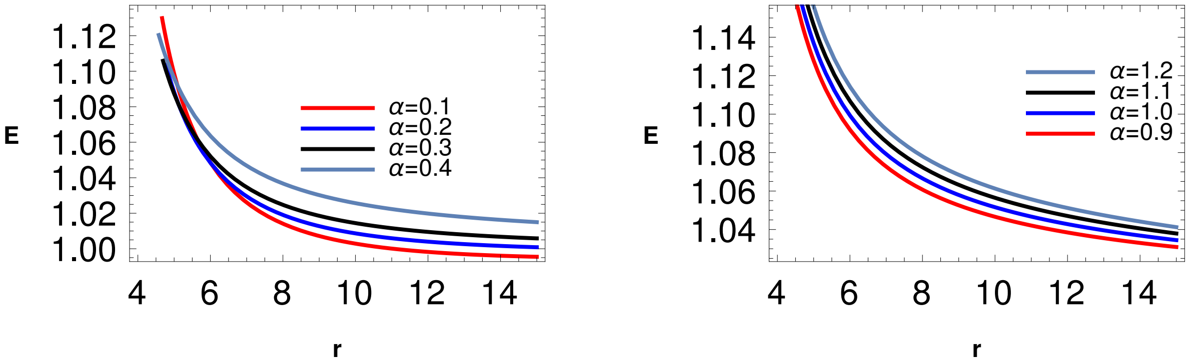

(a) a=0.5, Q = 0.3

(b) a=0.5, Q = 0.3

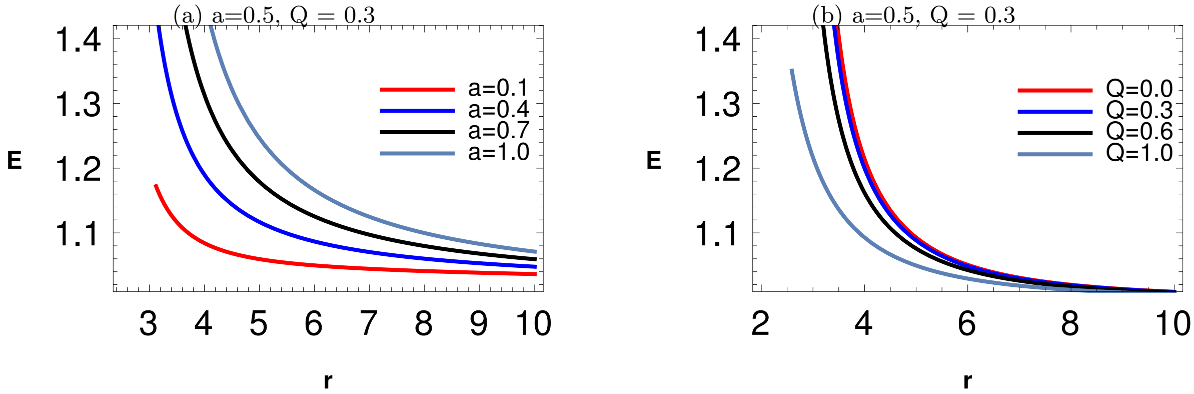

(c) $\alpha = 0.2$, Q=0.3

(d) a=0.5, $\alpha = 0.2$

Figure 3.1: Graphical representation of energy E of particles moving along co-rotating orbits.

In Fig.(3.1) we have graphically presented the energy of a co-rotating particle. We find that the energy (E) of the co-rotating particle falls with distance (r) from the black hole. Also the energy approaches unity which is the energy of a particle of unit mass as observed by a stationary observer at infinity.

The effect of the dark matter (α) is found to be similar for both lower values ($\alpha < \alpha_c$) and higher values ($\alpha > \alpha_c$) of α as evident from Fig.(3.1). In both cases, we observe that the energy of the particle increases with increase in the value of the PFDM parameter α.

From Fig.(3.1) it is clear that since the co-rotating particle is near the black hole, the spin (a) of the black hole assists it's motion via dragging. Hence the energy of the particle increases but with increasing distance the dragging effect reduces thereby decreasing the energy of the particle.

Again, for a fixed value of spin a and PFDM parameter α, increment in charge (Q) results in decrease in the energy of the particle. The possible explanation for such an observation can be that the mass of the black hole reduces with increase in black hole charge Q. Thus the energy of the black hole decreases which results in a decrease in the rotational energy of the particles.

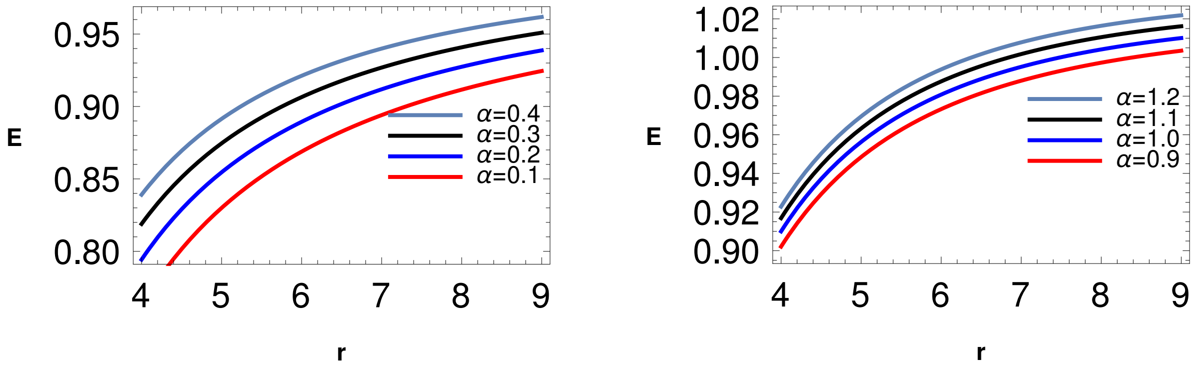

(a) a=0.5, Q=0.3

(b) a=0.5, Q=0.3

Figure 3.2: Graphical representation of energy E of particles moving along counter rotating orbits with varying PFDM parameter α.

In Fig.(3.2), we represent the variation of energy (E) of the counter-rotating particle with distance (r) from the black hole. Similar to the co-rotating case, here too the energy E of the particle approaches unity. As the particle moves opposite to the black hole spin, so the motion of the black hole hinders the particle motion. Hence the particle has lesser energy when it is closer to the black hole.

In this case, the effect of dark matter (α) is similar for both lower ($\alpha < \alpha_c$) and higher values ($\alpha > \alpha_c$). In both cases increment in α increases the energy of the particle which is similar to that observed in the co-rotating case. This has been shown in Fig.(3.2).

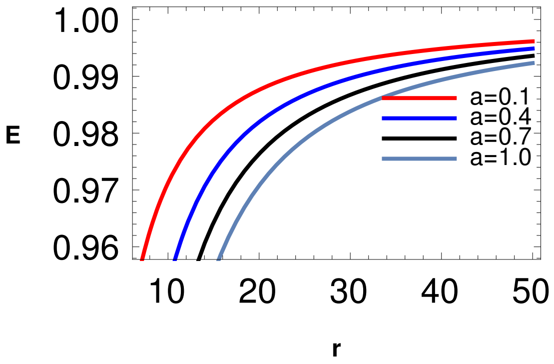

Figure 3.3: Graphical representation of energy E of particles moving along counter rotating orbits with varying spin a.

The increment in black hole spin (a) for a fixed value of α decreases the energy of the particle as is evident from Fig.(3.3). This observation can be explained by the fact that with increase in spin a of the black hole, the rotational kinectic energy of the black hole increases resulting in the decrease in the energy of the particles in order to keep the total energy fixed.

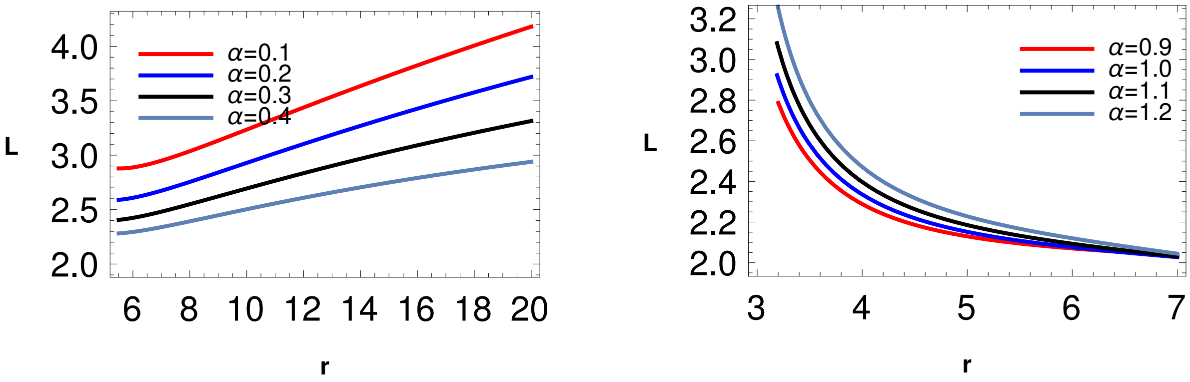

(a) $a = 0.5$, $Q = 0.3$ (b) $a = 0.5$, $Q = 0.3$

Figure 3.4: Graphical representation of angular momentum L of particles moving along co-rotating orbits.

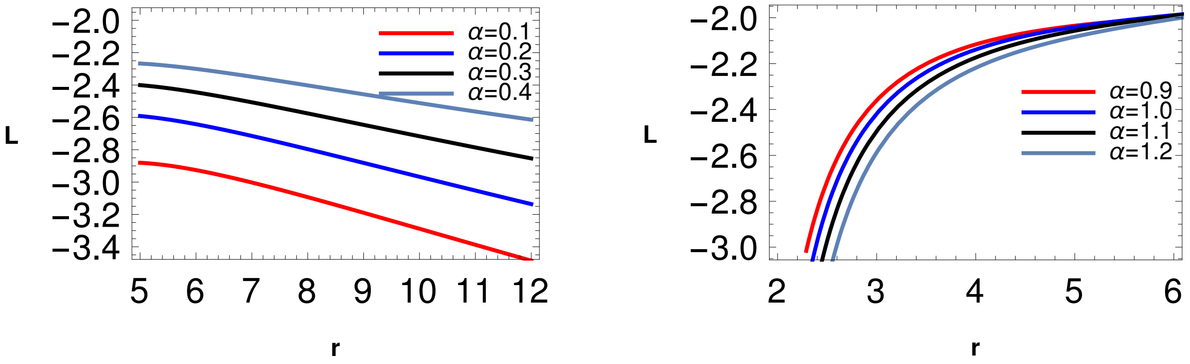

(a) $a = 0.5$, $Q = 0.3$ (b) $a = 0.5$, $Q = 0.3$

Figure 3.5: Graphical representation of angular momentum L of particles moving along counter rotating orbits.

The plots of the angular momentum present a completely different picture with respect to the different range of the PFDM parameter α.

Fig.(3.4) graphically represents the angular momentum L of the particles moving in prograde (co-rotating) orbits. The plots show that for smaller values of α ($\alpha < \alpha_c$), increase in α decreases the angular momentum whereas the reverse is observed in case of the higher values of α ($\alpha > \alpha_c$).

The angular momentum of the particles in the retrograde (counter-rotating) orbits are negative since they move opposite to the direction of rotation of the black hole as shown in Fig.(3.5). It can be observed that for $\alpha < \alpha_c$, the increment in the value of α reduces the angular momentum of the massive test particle. However, for $\alpha > \alpha_c$, it increases the angular momentum.

3.4.4 Geodesics of charged particle

After studying the geodesics of massless and uncharged massive particles, we move our attention to the study of geodesics of charged massive particles. Incorporating the interactions of the gauge fields, the Hamiltonian of the charged particle takes the form[194]

$$2\mathcal{H} = g^{\mu\nu}\Big(p_\mu + qA_\mu\Big)\Big(p_\nu + qA_\nu\Big) = \epsilon = -1 \tag{3.60}$$

with the electromagnetic potential for rotating charged black hole coupled to PFDM given by [195]

$$A = A_\mu dx^\mu = \frac{Qr}{\rho^2}\Big(dt - a\sin^2\theta d\phi\Big)\ . \tag{3.61}$$

Using the transformation relation $\mathcal{H} = p_\mu \dot{x}^\mu - \mathcal{L}$, we obtain the Lagrangian of the massive charged particle as

$$\mathcal{L} = \frac{1}{2}g_{\mu\nu}\dot{x}^\mu\dot{x}^\nu - qA_\mu\dot{x}^\mu \tag{3.62}$$

where q denotes the charge of the particle. We consider the charged particle of unit mass $m = 1$. For the sake of simplicity, using the symmetry of the metric we compute the conserved quantities E and L which have same physical meaning as mentioned previously. Also since we are interested in the equatorial geodesics, we impose $\theta = \frac{\pi}{2}$ implying $\dot{\theta} = 0$ which leads to following the geodesic equations

$$\dot{t} = \frac{1}{r^2}\left[\frac{r^2+a^2}{\Delta}\left(\Big(E - \frac{qQ}{r}\Big)\Big(r^2+a^2\Big) - a\Big(L - \frac{qaQ}{r}\Big)\right) + a\left(\Big(L - \frac{qaQ}{r}\Big) - a\Big(E - \frac{qQ}{r}\Big)\right)\right] \tag{3.63}$$

$$\dot{\phi} = \frac{1}{r^2}\left[\frac{a}{\Delta}\left(\Big(E - \frac{qQ}{r}\Big)(r^2+a^2) - a\Big(L - \frac{qaQ}{r}\Big)\right) + \left(\Big(L - \frac{qaQ}{r}\Big) - a\Big(E - \frac{qQ}{r}\Big)\right)\right] \tag{3.64}$$

$$\begin{aligned}\dot{r}^2 = -\frac{\Delta}{r^2} + \frac{\Big(E - \frac{qQ}{r}\Big)^2}{r^4}\left[\Big(r^2+a^2\Big)^2 - a^2\Delta\right] - \frac{2a}{r^4}\Big(r^2+a^2-\Delta\Big)\Big(E - \frac{qQ}{r}\Big)\Big(L - \frac{qaQ}{r}\Big) \\ -\frac{1}{r^4}\Big(\Delta - a^2\Big)\Big(L - \frac{qaQ}{r}\Big)^2\ .\end{aligned} \tag{3.65}$$

In order to determine the circular orbits, we use the conditions $\bar{F}(r) = \bar{F}'(r) = 0$ with $\bar{F}(r)$ given as

$$\begin{aligned}\bar{F}(r) = -\frac{\Delta}{r^2} + \frac{\Big(E - \frac{qQ}{r}\Big)^2}{r^4}\left[\Big(r^2+a^2\Big)^2 - a^2\Delta\right] - \frac{2a}{r^4}\Big(r^2+a^2-\Delta\Big)\Big(E - \frac{qQ}{r}\Big)\Big(L - \frac{qaQ}{r}\Big) \\ -\frac{1}{r^4}\Big(\Delta - a^2\Big)\Big(L - \frac{qaQ}{r}\Big)^2\ .\end{aligned} \tag{3.66}$$

It is difficult to obtain an exact solution for E and L from the above conditions. We can approach the problem by assuming $\frac{q}{m} \ll 1$ (particle with small specific charge) and incorporating Taylor expansion about $\frac{q}{m} = 0$ [196] we find E and L to be

$$E(q) = E(0) + qE'(0) + O(q^2) + ... \tag{3.67}$$

$$L(q) = L(0) + qL'(0) + O(q^2) + ...\ . \tag{3.68}$$

The approximate solutions of E and L satisfy the condition of circular orbits given as $\bar{F}(r) = \bar{F}'(r) = 0$. We display the plots in Fig.(s) 3.6 - 3.9.

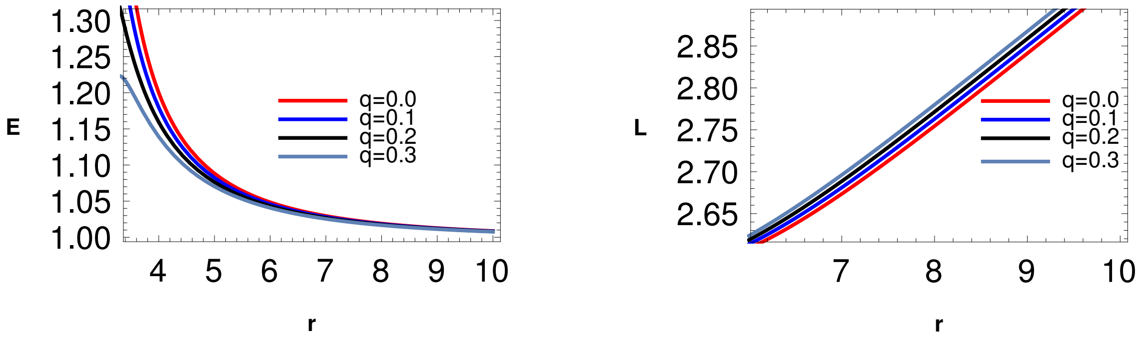

Figure 3.6: Graphical representation of energy and angular momentum of co-rotating charged particles with α=0.2, Q=0.3 and a=0.5.

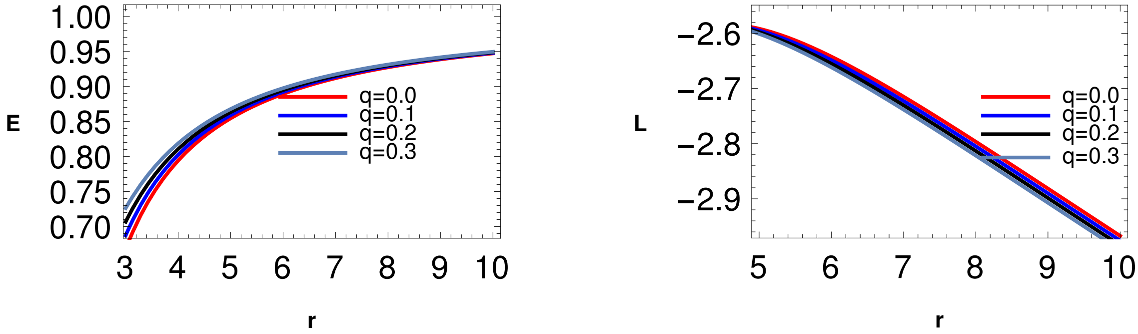

Figure 3.7: Graphical representation of energy and angular momentum of counter rotating charged particles with α=0.2, Q=0.3 and a=0.5.

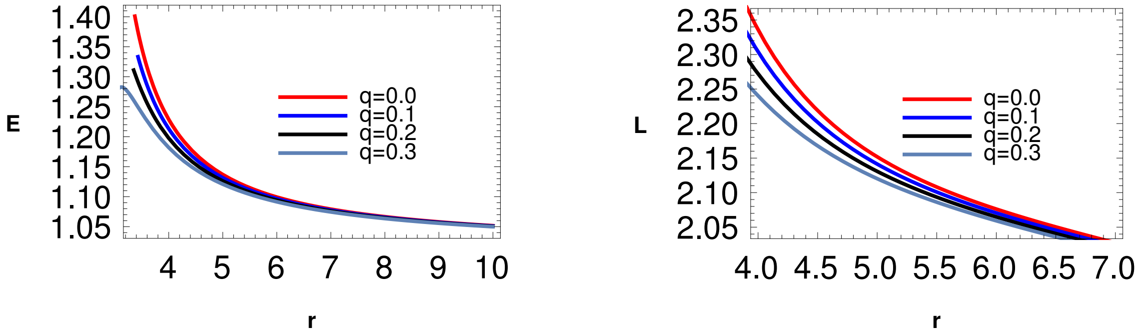

Figure 3.8: Graphical representation of energy and angular momentum of co-rotating charged particles with α=1.0, Q=0.3 and a=0.5.

From Fig(s).(3.6), (3.7), (3.8) and (3.9) we observe that both for $\alpha < \alpha_c$ and $\alpha > \alpha_c$, the increment in charge q of the particle from 0.0 to 0.3, decreases the energy (E) of co-rotating particles whereas there is an increase in the energy (E) for counter rotating particles. Also, we find that in both cases the energy of the charged particle tend towards unity.

Again, we observe that for $\alpha = 0.2$ the angular momentum (L) both for co-rotating and counter rotating particles increase with increase in charge q of the particle. However, for $\alpha = 1.0$ we find that with increase in the value of charge q, angular momentum (L) for co-rotating and counter rotating particles decreases.

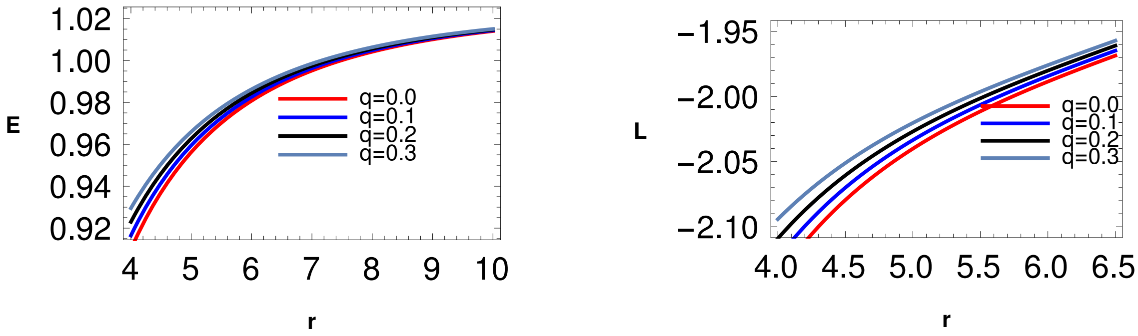

Figure 3.9: Graphical representation of energy and angular momentum of counter rotating charged particles with α=1.0, Q=0.3 and a=0.5.

The above observation depict that the particle's charge q responses quite differently depending on the value of PFDM parameter α. Also it implies that the particle with more charge (q) is hindered more if the dark matter intensity increases.

3.5 Nature of the effective potential

Here, we study the effective potential which results in both stable and unstable orbits depending upon the condition $\frac{\partial^2 V_{eff}}{\partial r^2} > 0$ or $\frac{\partial^2 V_{eff}}{\partial r^2} < 0$ respectively. The stable and unstable orbits correspond to the local minima and maxima of the effective potential which we obtain from the radial geodesic equation. The potential depends on the following parameters, the charge of the black hole (Q), spin parameter (a), the perfect fluid dark matter parameter α and on the charge of the particle (q).
The effective potential in case of the massive particles obtained from the corresponding radial geodesic equation eq.(3.45) reads

$$\dot{r}^2 + V_{eff} = E^2 \tag{3.69}$$

where the effective potential V_{eff} is given by

$$V_{eff} = -\frac{2M}{r^3}(aE-L)^2 + \frac{Q^2}{r^4}(aE-L)^2 + \frac{\alpha}{r^3}\ln\left(\frac{r}{|\alpha|}\right) - \frac{1}{r^2}(a^2E^2 - L^2) + \frac{\Delta}{r^2}\ . \tag{3.70}$$

For circular geodesics, we impose the condition for a circular trajectory of constant radius r that is $\dot{r} = 0$. In case of photons, the effective potential eq.(3.38) takes the form

$$V_{eff} = -\frac{2M}{r^3}(aE-L)^2 + \frac{Q^2}{r^4}(aE-L)^2 + \frac{\alpha}{r^3}\ln\left(\frac{r}{|\alpha|}\right) - \frac{1}{r^2}(a^2E^2 - L^2)\ . \tag{3.71}$$

Also for massive particles with charge q, the effective potential takes the following form

$$\begin{aligned} V_{eff} = E^2 + \frac{(\Delta - a^2)\left(L - \frac{aqQ}{r}\right)^2}{r^4} + \frac{2a\,(a^2 - \Delta + r^2)\left(E - \frac{qQ}{r}\right)\left(L - \frac{aqQ}{r}\right)}{r^4} \\ - \frac{\left((a^2+r^2)^2 - a^2\Delta\right)\left(E - \frac{qQ}{r}\right)}{r^4} + \frac{\Delta}{r^2}\ . \end{aligned} \tag{3.72}$$

In the trivial case when $L = aE$, the radial equations and effective potentials become

$$\dot{r}_{massive} = \pm\sqrt{E^2 - \frac{\Delta}{r^2}} \;\; ; \;\; \dot{r}_{null} = \pm E \tag{3.73}$$

$$V_{massive} = \frac{\Delta}{r^2} \;\; ; \;\; V_{null} = 0 \; . \tag{3.74}$$

In Fig.(3.10), we graphically show the plots of the effective potential for null geodesics and the corresponding ones for timelike geodesics in Fig.(3.11).

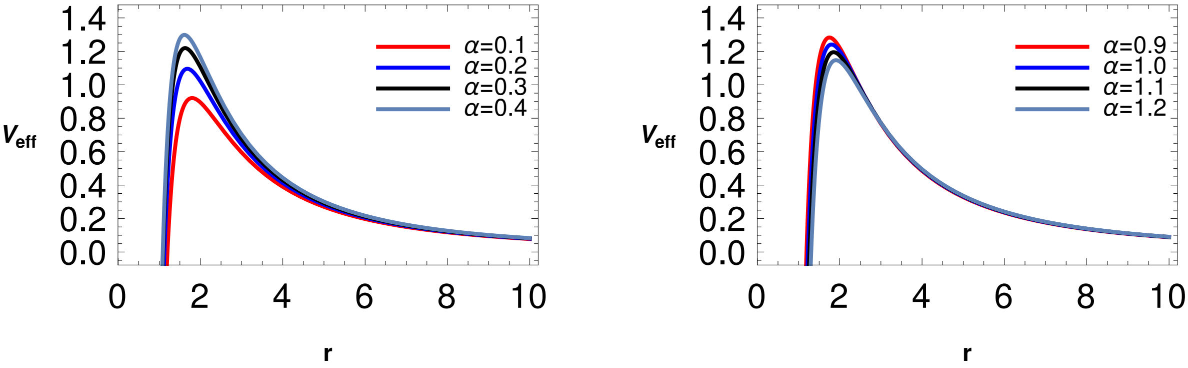

(a) $a = 0.5$, $Q = 0.3$, $L = 3.0$ (b) $a = 0.5$, $Q = 0.3$, $L = 3.0$

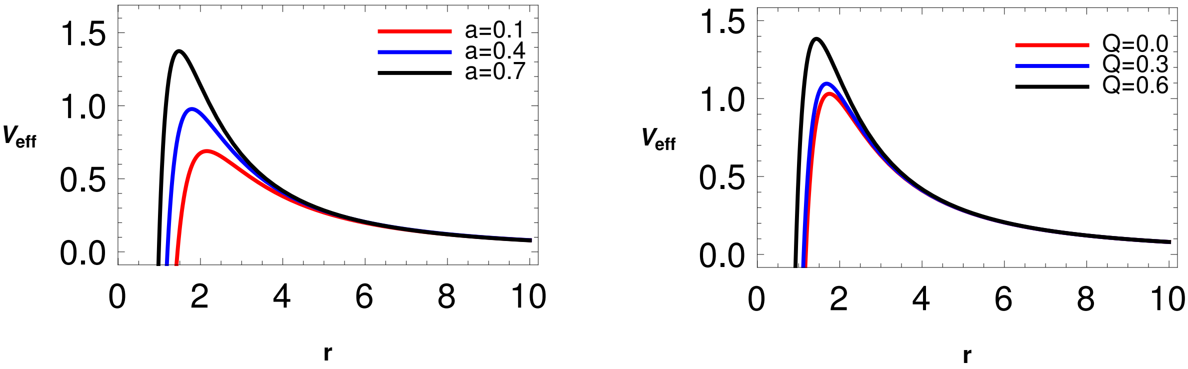

(c) α=0.2, $Q = 0.3$, $L = 3.0$ (d) a=0.5, α=0.2, $L = 3.0$

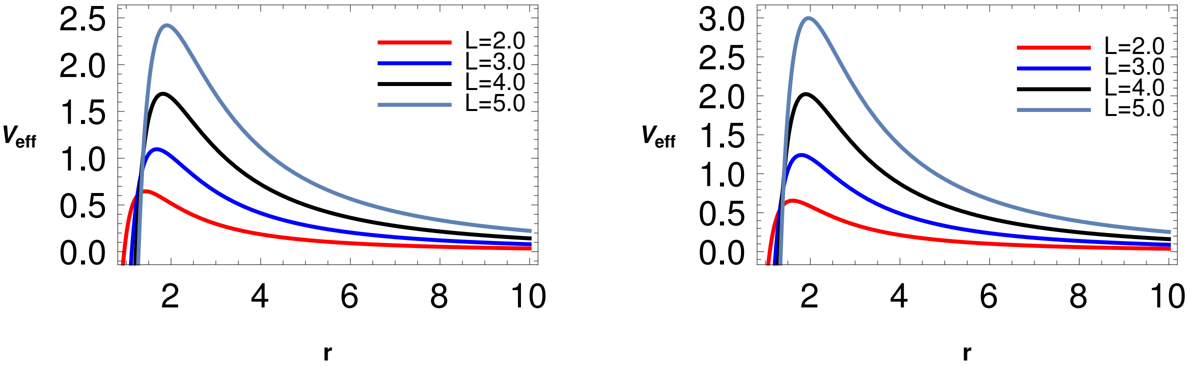

(e) $a = 0.5$, α=0.2, $Q = 0.3$ (f) $a = 0.5$, α=1.0, $Q = 0.3$

Figure 3.10: Plots of effective potential for null geodesics with variation in a, Q, L and α.

In Fig.(s)(3.10) and (3.11), we find that the effective potential for both null and timelike geodesics, increases with an increase in the value of PFDM parameter α for the lower regime $\alpha < \alpha_c$. However for the higher regime, that is $\alpha > \alpha_c$ the effective potential decreases with increase in the PFDM parameter α.

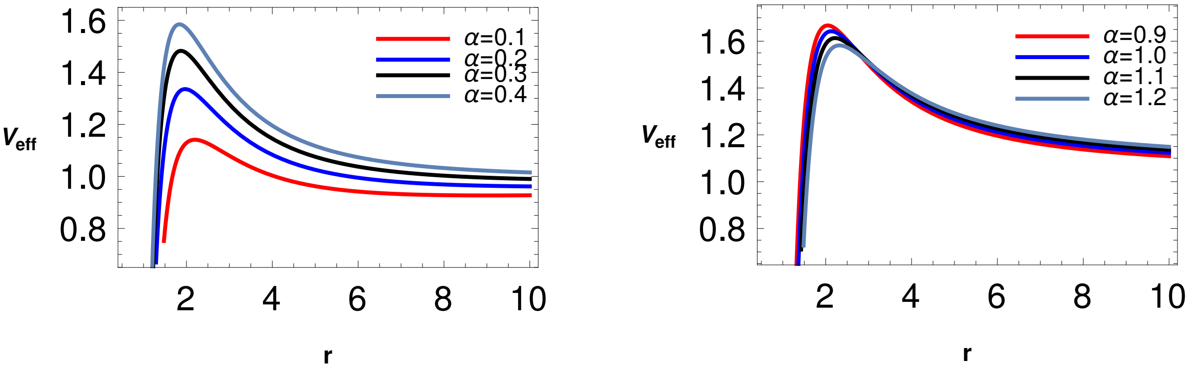

(a) $a = 0.5$, $Q = 0.3$, $L = 3.0$ (b) $a = 0.5$, $Q = 0.3$, $L = 3.0$

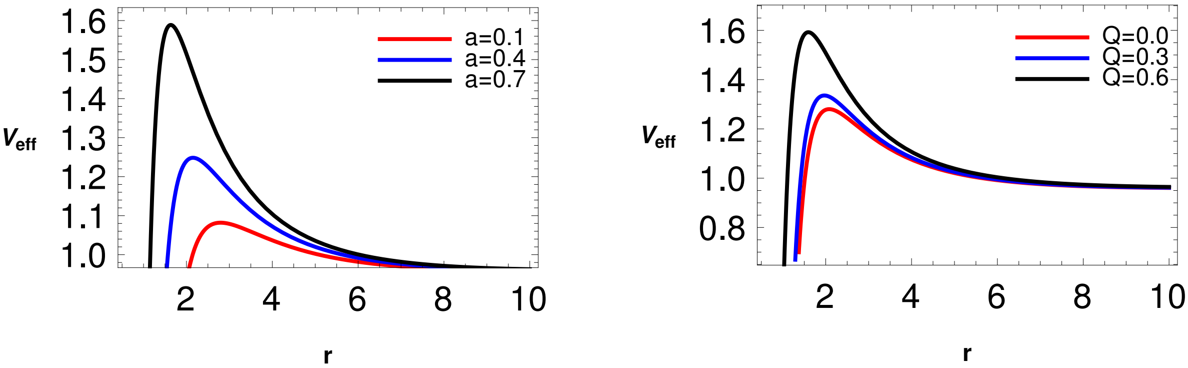

(c) α=0.2, $Q = 0.3$, $L = 3.0$ (d) a=0.5, α=0.2, $L = 3.0$

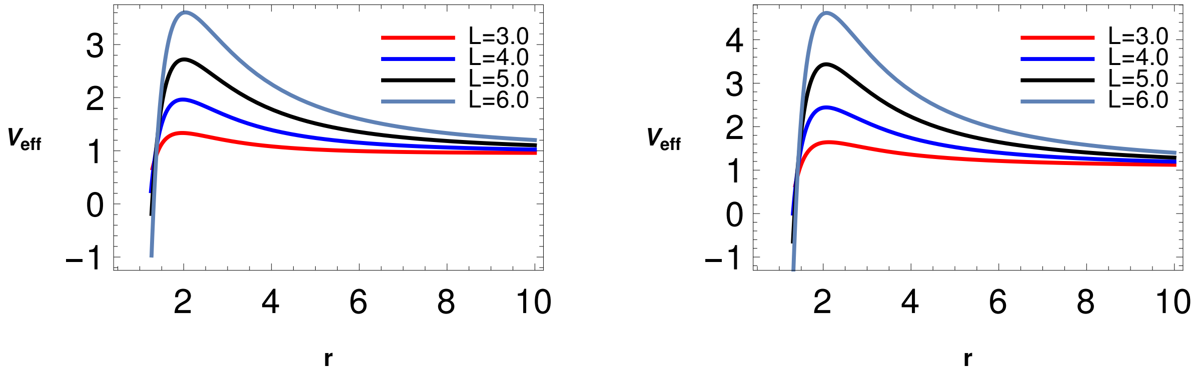

(e) $a = 0.5$, α=0.2, $Q = 0.3$ (f) $a = 0.5$, α=1.0, $Q = 0.3$

Figure 3.11: Plots of effective potential for timelike geodesics with variation in a, Q, L and α.

Also, we observe that the potential increases with increase in the black hole spin (a) and charge (Q) both for $\alpha < \alpha_c$ and $\alpha > \alpha_c$. This has been observed for effective potential (V_{eff}) corresponding to both null and timelike geodesics.

Besides we also observe that in both cases, with increase in angular momentum (L) of the particle, the effective potential rises in both cases ($\alpha < \alpha_c$ and $\alpha > \alpha_c$) and the maxima shifts towards larger radial distance r.

3.6 Penrose process

Black hole is a vessel of extreme amount of energy. There are many theorised processes that are responsible to gain energy (extract energy) from the black hole. One of them is the Penrose process named after Roger Penrose who proposed the mechanism in [75]. In case of a rotating black hole a region gets created between the outer event horizon ($g^{rr} = 0$) and the stationary limit surface ($g_{tt} = 0$). These two surfaces meet at the poles and have largest separation in the equatorial plane. This varying annular region is known as the *ergosphere*. In case of static black hole this region vanishes. The speciality of this region is that the Killing vector $\frac{\partial}{\partial t}$ which has a unit norm as observed by a stationary observer at infinity becomes spacelike within the region. The symmetry of the metric along with the change in the said Killing vector results in energy conservation and hence the energy in this region can be negative. This fact can be utilised to extract energy from the black hole.

3.6.1 Extraction of black hole energy and efficiency of Penrose process

Let an uncharged massive particle (uncharged) with positive energy fall into this ergoregion and split into two particle, one with positive energy and the other with negative energy. The negative energy particle is absorbed by the black hole and that with positive energy comes out of the black hole having relatively greater energy than the particle that entered the black hole, thus resulting in energy gain (effective energy extraction).

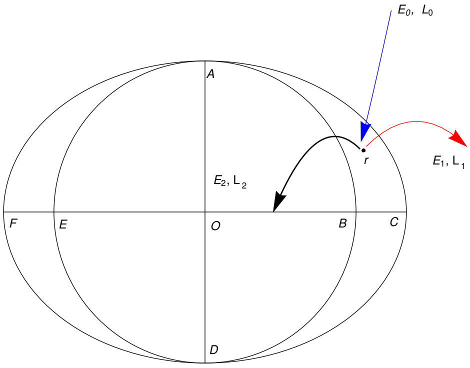

Figure 3.12: Diagrammatic representation of the Penrose process.

The condition of negative energy of the particle can be found using the condition for circular orbits [193]. The radial equation with $\dot{r} = 0$ results in

$$E^2\Big[\Big(r^2+a^2\Big)^2 - a^2\Delta\Big] - E\Big[2aL\Big(r^2+a^2-\Delta\Big) + L^2\Big(a^2-\Delta\Big) + \Delta r^2\delta\Big] = 0 \tag{3.75}$$

which can be solved for both E and L as given by

$$E = \frac{aL\Big(r^2+a^2-\Delta\Big) \pm r\sqrt{\Delta\Big[r^2L^2 - \delta\Big(\Big(r^2+a^2\Big)^2 - a^2\Delta\Big)\Big]}}{\Big(r^2+a^2\Big)^2 - a^2\Delta} \tag{3.76}$$

$$L = \frac{aE\Big(r^2+a^2-\Delta\Big) \pm r\sqrt{\Delta\Big[r^2E^2 + \delta\Big(\Delta - a^2\Big)\Big]}}{\Big(a^2-\Delta\Big)}\ . \tag{3.77}$$

If we assume positive sign in eq.(3.76) along with the condition

$$a^2L^2\Big(r^2+a^2-\Delta\Big)^2 > \Delta r^2\Big[r^2L^2-\delta\Big(\Big(r^2+a^2\Big)^2-a^2\Delta\Big)\Big] \tag{3.78}$$

and $L<0$, then $E<0$, i.e., particle with negative energy is possible. This tells us that $E<0$ is possible only if $L<0$ which is the case for counter rotating orbits. The negative energy particle following counter rotating orbits must lie within the ergoregion. The expression for the negative energy particles take the form

$$E=\frac{aL\Big(r^2+a^2-\Delta\Big)-r\sqrt{\Delta\Big[r^2L^2-\delta\Big(\Big(r^2+a^2\Big)^2-a^2\Delta\Big)\Big]}}{\Big(r^2+a^2\Big)^2-a^2\Delta}\ . \tag{3.79}$$

The plots for negative energy with the variation in different parameters are shown in Fig.3.13.
In order to discuss the Penrose process in detail, we must start by considering a massive uncharged particle of energy E_0 entering the ergosphere and let, it breaks down into two photons with energies E_1 and E_2. Let the angular momentum of the particles be L_0 (entering), L_1 (leaving) and L_2 (captured). Also let the energy of the particle entering the ergosphere be $E_0=1$. Hence the angular momentum of the particles are

$$L_0=\frac{a\Big(r^2+a^2-\Delta\Big)+r\sqrt{\Delta\Big[r^2-\Big(\Delta-a^2\Big)\Big]}}{\Big(a^2-\Delta\Big)}\quad ;\quad \delta=-1 \tag{3.80}$$

$$L_1=\frac{aE_1\Big(r^2+a^2-\Delta\Big)+r\sqrt{\Delta\Big(r^2E_1^2\Big)}}{\Big(a^2-\Delta\Big)}=b_1E_1 \tag{3.81}$$

$$L_2=\frac{aE_2\Big(r^2+a^2-\Delta\Big)-r\sqrt{\Delta\Big(r^2E_2^2\Big)}}{\Big(a^2-\Delta\Big)}=b_2E_2 \tag{3.82}$$

where

$$b_1=\frac{a\Big(r^2+a^2-\Delta\Big)+r^2\sqrt{\Delta}}{\Big(a^2-\Delta\Big)}\quad ;\quad b_2=\frac{a\Big(r^2+a^2-\Delta\Big)-r^2\sqrt{\Delta}}{\Big(a^2-\Delta\Big)}\ . \tag{3.83}$$

By the conservation of energy and angular momentum we get

$$E_0=E_1+E_2=1\quad ;\quad L_0=b_1E_1+b_2E_2\ . \tag{3.84}$$

Solving for E_1 and E_2 we obtain

$$E_1=\frac{1}{2}\left[1+\sqrt{\frac{r^2+a^2-\Delta}{r^2}}\right] \tag{3.85}$$

$$E_2 = \frac{1}{2}\left[1 - \sqrt{\frac{r^2 + a^2 - \Delta}{r^2}}\right] \tag{3.86}$$

where E_1 and E_2 corresponds to the positive and negative energies of the two particles. Thus the particle with energy E_2 is captured by the black hole while that with energy E_1 comes out of the black hole resulting in an energy gain of

$$\begin{aligned} \Delta E = E_1 - 1 &= -E_2 \\ &= \frac{1}{2}\left[\sqrt{\frac{r^2 + a^2 - \Delta}{r^2}} - 1\right] \\ &= \frac{1}{2}\left[\sqrt{\frac{2Mr - Q^2 - \alpha r \ln\left(\frac{r}{|\alpha|}\right)}{r^2}} - 1\right]. \end{aligned} \tag{3.87}$$

In the limit $a \to 0$, the ergosphere vanishes and the region of ergosphere corresponds to event horizon with radius r_{h+} and hence $\Delta = 0$ and we get energy gain $\Delta E = 0$, $E_1 = 1$ and $E_2 = 0$ and thus no particle with negative energy exists. Fig.(3.14) shows the plots of energy gain ΔE from the black hole.

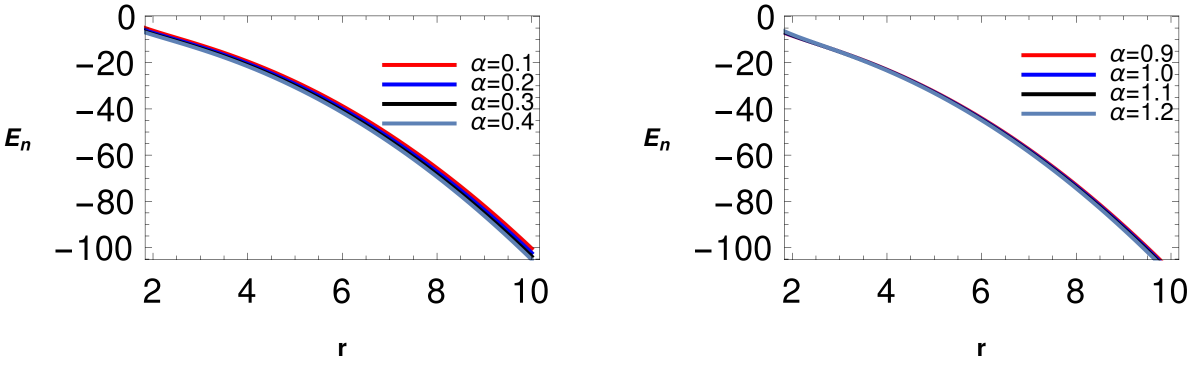

(a) $a = 0.5$, $Q = 0.3$, $L = -3.0$

(b) $a = 0.5$, $Q = 0.3$, $L = -3.0$

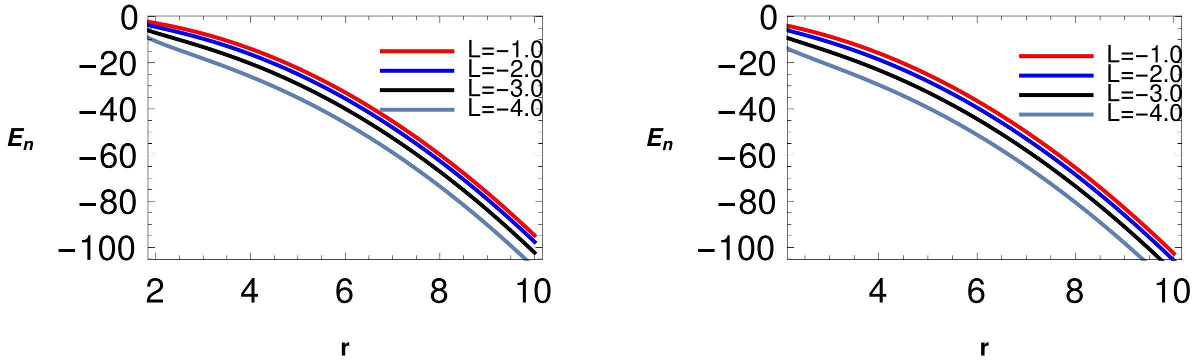

(c) $a = 0.5$, α=0.2, $Q = 0.3$

(d) $a = 0.5$, α=1.0, $Q = 0.3$

Figure 3.13: Plots for negative energy ($E_n < 0$) of a particle with variation in L and α.

Fig.(3.13) shows that the negative energy increases with increment in α both for $\alpha < \alpha_c$ and $\alpha > \alpha_c$. However the change is less prominent for higher α values.

The increase in charge Q and the negative angular momentum ($L < 0$) increases the negative energy of the particle quite significantly. This results in higher negative energy of the particle absorbed by the black hole and effectively leads to higher energy gain from the black hole.

The energy gain from the black hole via., the Penrose process is astrophysically very important and significant. Also more the negative energy absorbed by the black hole more is the gain in positive energy via Penrose process due to energy conservation. The plots of energy gain in Fig.(3.14) shows us the impact of different black hole parameters energy gain from the black hole.

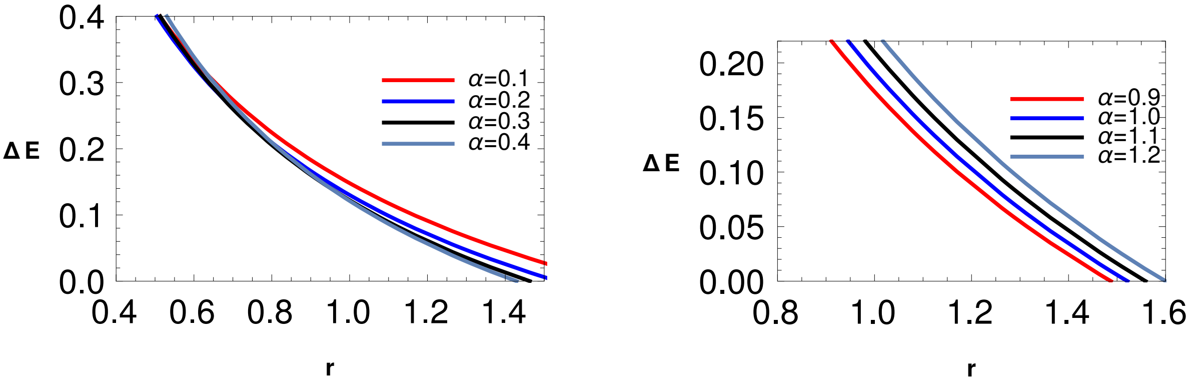

(a) $a = 0.5$, $Q = 0.3$ (b) $a = 0.5$, $Q = 0.3$

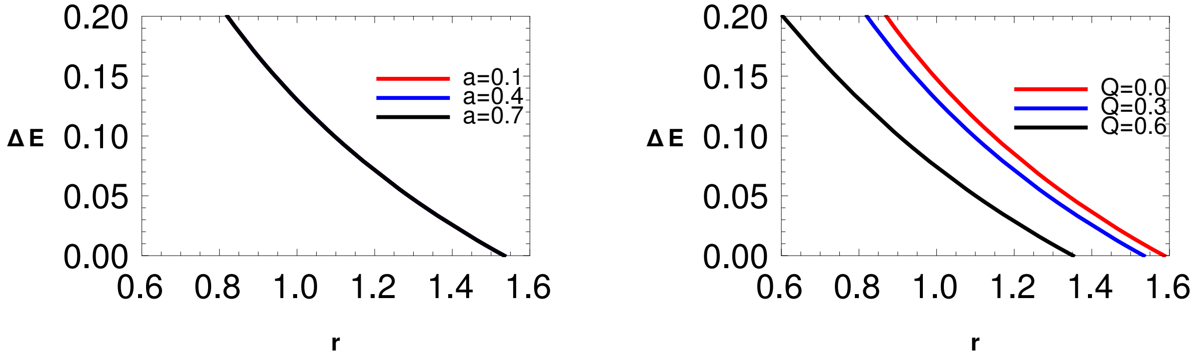

(c) α=0.2, $Q = 0.3$ (d) $a = 0.5$, α=0.2

Figure 3.14: Plots showing energy gain from the black hole with variation in a, Q and α.

We find that energy gain increases with increase in the PFDM parameter α both for $\alpha < \alpha_c$ and $\alpha > \alpha_c$. The increment is more significant for lower range values of PFDM parameter α.

With increase in charge (Q) of the black hole, energy gain (ΔE) decreases for $\alpha < \alpha_c$. The reason being the size of the ergosphere decreases with increase in charge Q as well as $\alpha < \alpha_c$.

3.7 Summary

In this work, we obtain a static, charged black hole solution surrounded by perfect fluid dark matter (PFDM). Then, we incorporated the Newman-Janis algorithm and derived the metric corresponding to a rotating, charged black hole surrounded by perfect fluid dark matter. Then we thoroughly studied the black hole spacetime in detail. We found that the event horizon radius of the black hole is greatly affected by the PFDM parameter α. We observe that there exists a certain value α_c (for fixed spin a and charge Q) upto which the outer event horizon radius (r_{h+}) decreases with the increase in the value of α. However, after α_c, we notice that r_{h+} starts to increase monotonically. On

the basis of this critical value, we define two range of values for α. Such a unique observation can be a result of the fact that the dark matter contributes to the effective mass of the black hole system.
We then studied the null geodesics where we computed the radius of photon sphere both for prograde and retrograde orbits. We found that with increment in PFDM parameter α, the photon radius decreases for $\alpha < \alpha_c$ and increases for $\alpha < \alpha_c$. Besides we also found that increment in the value of spin parameter (a) increases the radius of photon orbits.
Then we observed the energy (E) and angular momentum (L) for massive particles traversing along prograde and retrograde orbits. The energy (E) of the particle in prograde orbits decreases whereas that of retrograde orbits increases with increase in the radial distance (r) from the black hole and gets close to unity as the particle approaches infinity. The increment in the values of α and spin (a) increases the energy of the particle considerably for the prograde orbits. On the other hand in case of retrograde orbits, the energy (E) increases with the increase in α but falls with the increasing value of the spin (a). This is because when the particle spins along the black hole, the black hole helps its motion whereas in the reverse case it opposes.
The most important observation is in the case of angular momentum of the particle which decreases with increase in value of α for $\alpha < \alpha_c$ and increases for $\alpha > \alpha_c$ for both types of orbits. Also we observe that with increase in the spin (a) of the black hole, the angular momentum (L) of the particle increases for co-rotating particles both for $\alpha < \alpha_c$ and $\alpha > \alpha_c$. But for counter-rotating particles, the angular momentum (L) rises for $\alpha < \alpha_c$ while it reduces for $\alpha > \alpha_c$. We found that with the increase in the charge (Q) of the black hole, the angular momentum (L) of the particle decreases.
Then we studied the energy E and angular momentum L of the charged particles with the variation in the charge (q) of the particle. We found that with increment in particle's charge (q), the energy falls in case of prograde orbits and increases in case of retrograde orbits. Besides we observe that angular momentum (L) increases with increase in q for $\alpha < \alpha_c$ and falls for $\alpha > \alpha_c$.
After that we studied the effective potential (V_{eff}) of the black hole as encountered by photons and massive particles. We found that V_{eff} increases with increase in spin (a) and charge (Q) of the black hole as also with angular momentum (L) of the particle. The change is quite sharp with the change in the angular momentum (L). Also with increment in α (where $\alpha < \alpha_c$), the potential increases whereas for $\alpha > \alpha_c$, it decreases slightly. The potential of the black hole for the charged particle is analysed with variation in q and we found that potential increases with increase in the charge from -0.3 to 0.3.
Finally, we studied the Penrose process. The negative energy particles are very important and are indirectly resposnible for the energy gain from black hole. We observed that negative energy considerably increases with increase in negative angular momentum (counter-rotating particle) and also with increase in the charge (Q) of the black hole. The effect of dark matter on the negative energy is less pronounced even though negative energy slightly increases. More the negative energy absorbed by the black hole, more is the gain, and we found that the energy gain via Penrose process increases due to the presence of dark matter in the system. We also observed that more the black hole charge (Q), less is the energy gain (extraction of energy) and hence less efficient is the Penrose process.

Chapter 4

Rotating charged black hole in presence of perfect fluid dark matter immersed in plasma

In this chapter we plan to study geodesics around black holes surrounded by PFDM in presence of a plasma background. The black hole studied in the previous chapter has been considered here with an additional material media. The consideration is quite natural since the universe is filled with 99% of plasma [100]. Besides we also explained in the introduction of this thesis that rupture of massive companion stars around black holes can produce accretion disks having huge energy and temperature [102]. The material in such disks is of plasmic nature. We will basically focus on the study of null geodesics. Again the radius of photon orbits (r_{p1} and r_{p2}) have been calculated and its dependence on plasma has been found [157]. Besides we also study the shadow of black hole using the null geodesics and the methodologies developed and discussed earlier. Study of black hole shadows considering plasma has been conducted in [105],[135]-[143]. We aim to study black hole shadow considering radial power law distribution of plasma as well as having radial and angular dependence. Also we wish to consider cases of both homogeneous [197] and inhomogeneous plasma [106]. We also constrain the PFDM and plasma parameter using the observational results of M87* supermassive black hole [9]. We work in geometric units, where we consider $c = G = 1$. Apart from the discussion and analysis, all our mathematical calculations and results are obtained using $M = 1$. This chapter is based on our work in [157].

4.1 Black hole spacetime in perfect fluid dark matter

The rotating version of the solution has the form [156]

$$ds^2 = -\frac{1}{\zeta^2}\Big(\Delta - a^2\sin^2\theta\Big)dt^2 + \frac{\zeta^2}{\Delta}dr^2 + \zeta^2 d\theta^2 - \frac{2a\sin^2\theta}{\zeta^2}\Big[r^2 + a^2 - \Delta\Big]dtd\phi$$
$$+\sin^2\theta\Big[r^2 + a^2 + \frac{a^2\sin^2\theta}{\zeta^2}\Big(r^2 + a^2 - \Delta\Big)\Big]d\phi^2 \qquad (4.1)$$

with

$$\Delta = r^2 + a^2 - 2Mr + Q^2 + \chi r \ln\left(\frac{r}{|\chi|}\right), \; \zeta^2 = r^2 + a^2 \cos^2\theta \; . \tag{4.2}$$

In this work we have used χ in place of α since we have designated the celestial coordinates by (α, β). The black hole event horizon is obtained using the condition $\Delta = 0$. After studying the spacetime, we find that the black hole has two horizons. One of the horizons is close to $r = 0$ but not at $r = 0$ which can be observed from the plots. The other horizon is close to $r = 1.5$, where we have set $M = 1$. The presence of PFDM does not increase the number of horizons of the black hole. Yet it does modify the location of the horizon surface. The detailed analysis of the spacetime geometry has been discussed in the previous chapter.

4.2 Black hole immersed in plasma

Here we consider a rotating charged black hole surrounded by PFDM immersed in a plasma background. We neglect any interaction between PFDM and plasma. The consideration of plasma is realistic, since most black holes are surrounded by material media as mentioned earlier. Plasma is a dispersive medium where light rays deviate depending on their frequency. The Hamiltonian of the light rays in such a background can be written as [105], [135]

$$H(x^\mu, p_\mu) = \frac{1}{2}\left[g^{\mu\nu} p_\mu p_\nu + \omega_p^2\right] \tag{4.3}$$

where ω_p denotes the plasma frequency which can be a function of both r and θ in general. For most part of our analysis in this chapter, we consider only r dependence for simplicity. The refractive index (n) of the material medium depends on the plasma frequency (ω_p) and the frequency of photons (ω) measured by a static observer. The expression of $n(r, \omega)$ takes the form [104]

$$n^2(r, \omega) = 1 - \left(\frac{\omega_p(r)}{\omega}\right)^2 . \tag{4.4}$$

As the observation is performed by a static observer, hence the energy of the photons become $\hbar\omega = -p_0 u^0 = -p_0\sqrt{-g^{00}}$ [104]. Replacing the expression of n and photon energy from above in eq.(4.3), the Hamiltonian becomes

$$H(x^\mu, p_\mu) = \frac{1}{2}\left[g^{\mu\nu} p_\mu p_\nu - (n^2 - 1)\left(p_0\sqrt{-g^{00}}\right)^2\right] . \tag{4.5}$$

To evaluate the geodesics, we need an explicit form for the plasma frequency ω_p. For simplified analytical calculations, we consider ω_p to be a function r only as mentioned earlier. Here we assume an extensively studied distribution in the literature, the radial power law distribution, with ω_p given as [104]

$$\omega_p^2 = \frac{4\pi e^2 N(r)}{m_e} \tag{4.6}$$

where e gives the electronic charge, m_e gives the mass of the electron and $N(r)$ being the plasma number density. The plasma density following [103], [104] has the form

$$N(r) = N_0\left(\frac{r_0}{r}\right)^h \tag{4.7}$$

where N_0 and r_0 are constants and h can take integer values with $h \geq 0$. The final form of the refractive index $n(r)$ along with $\frac{\omega_p}{\omega}$ becomes

$$\left(\frac{\omega_p}{\omega}\right)^2 = \frac{k}{r^h} \quad ; \quad n(r) = \sqrt{1 - \frac{k}{r^h}} \ . \tag{4.8}$$

Here k is a constant which gives the weightage of plasma around the black hole, also $h = 1,2,3$ [104]. In this work, we shall consider $h = 0$ corresponding to $n(r)$ =constant and designated as the homogeneous plasma media and $h = 1$ corresponding to inhomogeneous plasma distribution.

Also we consider a case where the plasma frequency $\omega_p(r, \theta)$ is dependent on both r and θ such that [105]

$$\omega_p(r, \theta)^2 = \frac{f_r(r) + f_\theta(\theta)}{r^2 + a^2 \cos^2\theta} \ . \tag{4.9}$$

We have carried out the shadow analysis considering this general case in the subsequent discussion.

4.3 Circular null geodesics in plasma

The photons propagating along null geodesics can either move in the direction of black hole's rotation (co-rotating photons) or in the opposite direction (counter rotating photons). In this section we want to determine the radius of the photon orbits. In order to so, we need to determine the radial geodesic equation and impose the condition for circular geodesics. To fulfill our target, we first need a Hamiltonian ($\mathcal{H}$) which will be needful to determine the trajectories of photons moving in the equatorial plane. The Hamiltonian given in eq.(4.5) takes the form

$$\mathcal{H} = \frac{1}{2}\Big[g^{\mu\nu}p_\mu p_\nu + (n^2 - 1)g^{00}p_0^2\Big] \tag{4.10}$$

with $\mathcal{H} = 0$ for photons. As we are interested in the geodesics constrained to the equatorial plane so we set $\theta = \frac{\pi}{2}$ which gives the geodesic along θ as $\dot{\theta} = 0$.

The rest of the geodesics can be calculated using Hamilton's equation of motion

$$\dot{x}^\mu = \frac{\partial \mathcal{H}}{\partial p_\mu} \quad ; \quad \dot{p}_\mu = -\frac{\partial \mathcal{H}}{\partial x^\mu} \ . \tag{4.11}$$

The Hamiltonian depends on the metric ($g_{\mu\nu}$) as well as on the refractive index of plasma ($n(r)$). The metric does not explicitly depend on $x_0(= t)$ and $x_3(= \phi)$. Thus utilising Hamilton's second equation of motion we obtain the constants $p_0 = -E$ and $p_3 = L_\phi$. E and L_ϕ respectively give the energy and angular momentum of the photon as measured by a stationary observer at infinity. The geodesics corresponding to t and ϕ take the form [157]

$$r^2\dot{t} = \frac{r^2 + a^2}{\Delta}\Big[n^2(r^2 + a^2)E - aL_\phi\Big] + a\Big[L_\phi - an^2E\Big] \tag{4.12}$$

$$r^2\dot{\phi} = \frac{a}{\Delta}\Big[(r^2 + a^2)E - aL_\phi\Big] + \Big[L_\phi - aE\Big] \ . \tag{4.13}$$

To determine the geodesic along r, we use a Lagrangian of the form $\mathcal{L} = \frac{1}{2}g_{\mu\nu}\dot{x}^\mu\dot{x}^\nu$. The Lagrangian can be used to obtain the momentum along r as $p_r = \frac{\partial \mathcal{L}}{\partial \dot{r}} = \frac{\partial S}{\partial r} = g_{rr}\dot{r}^2$. Since there is no proper time in case of light rays, so we parametrize them using an affine parameter λ. With the above equations in hand, we get the radial geodesic as

$$\dot{r}^2 = \frac{1}{r^4}\left[\Big(E(r^2+a^2) - aL_\phi\Big)^2 - \Delta(aE - L_\phi)^2 + (n^2-1)\Big(E^2(r^2+a^2)^2 - \Delta E^2 a^2\Big)\right] . \tag{4.14}$$

In order to obtain the circular co-rotating and counter rotating null orbits discussed above, we define the impact parameter as $\frac{L_\phi}{E} = D$. The radial eq.(4.14) in terms of D gets modified to[157]

$$\dot{r}^2 = \frac{E^2}{r^4}\left[\Big((r^2+a^2) - aD\Big)^2 - \Delta(a - D)^2 + (n^2-1)\Big((r^2+a^2)^2 - \Delta a^2\Big)\right] . \tag{4.15}$$

Rearranging eq.(4.15), we have

$$\frac{r^2\dot{r}^2}{E^2} = \frac{1}{r^2}\left[\Big((r^2+a^2) - aD\Big)^2 - \Delta(a - D)^2 + (n^2-1)\Big((r^2+a^2)^2 - \Delta a^2\Big)\right] = F(r) . \tag{4.16}$$

The condition for circular geodesics is $F(r) = 0 = F'(r)$. Using them, we obtain the constraint equations

$$r^2 + (a^2 - D^2) + \frac{2M}{r}(a-D)^2 - \frac{Q^2}{r^2}(a-D)^2 - \frac{\chi}{r}(a-D)^2 \ln\Big(\frac{r}{|\chi|}\Big) + (n^2-1)\Big(r^2 + a^2 + a^2\Big(\frac{2M}{r} - \frac{Q^2}{r^2} - \frac{\chi}{r}\ln\Big(\frac{r}{|\chi|}\Big)\Big)\Big) = 0 . \tag{4.17}$$

$$\begin{aligned} 2r - \frac{2M}{r^2}(a-D)^2 + \frac{2Q^2}{r^3}(a-D)^2 + \frac{\chi}{r^2}(a-D)^2\ln(\frac{r}{|\chi|}) - \frac{\chi}{r^2}(a-D)^2 + \\ (n^2-1)\Big(2r - a^2\Big(\frac{2M}{r^2} - \frac{2Q^2}{r^3} - \frac{\chi}{r^2}\ln(\frac{r}{|\chi|}) + \frac{\chi}{r^2}\Big)\Big) + 2nn'\Big(r^2 + a^2 + a^2\Big(\frac{2M}{r} - \frac{Q^2}{r^2} - \frac{\chi}{r}\ln\Big(\frac{r}{|\chi|}\Big)\Big)\Big) = 0 \end{aligned} \tag{4.18}$$

where, $n^{'} \equiv \frac{dn}{dr}$. Solving eq.(4.18) for $(a - D)$, we have

$$(a-D) = \pm\sqrt{\frac{2r^5 + (n^2-1)\Big[2r^5 - a^2\Big(2Mr^2 - 2Q^2r - \chi r^2\ln(\frac{r}{|\chi|}) + \chi r^2\Big)\Big] + 2nn'\Big[r^4(r^2+a^2) + a^2\Big(2Mr^3 - Q^2r^2 - \chi r^3\ln(\frac{r}{|\chi|})\Big)\Big]}{2Mr^2 - 2Q^2r - \chi r^2\ln(\frac{r}{|\chi|}) + \chi r^2}} \tag{4.19}$$

Thus the impact parameter becomes [157]

$$D = a \mp \sqrt{\frac{2r^5 + (n^2-1)\Big[2r^5 - a^2\Big(2Mr^2 - 2Q^2r - \chi r^2\ln(\frac{r}{|\chi|}) + \chi r^2\Big)\Big] + 2nn'\Big[r^4(r^2+a^2) + a^2\Big(2Mr^3 - Q^2r^2 - \chi r^3\ln(\frac{r}{|\chi|})\Big)\Big]}{2Mr^2 - 2Q^2r - \chi r^2\ln(\frac{r}{|\chi|}) + \chi r^2}} \tag{4.20}$$

The $\mp$ sign corresponds to counter and co-rotating geodesics of photons moving in the black hole spacetime. In case of non-plasmic background, that is, $n = 1, n' = 0$ we get [156]

$$D = a \mp \sqrt{\frac{2r^5}{2Mr^2 - 2Q^2r - \chi r^2\ln(\frac{r}{|\chi|}) + \chi r^2}} \tag{4.21}$$

which corresponds to the expression obtained in the previous chapter.

Replacing D from eq.(4.20) in eq.(4.17) we get an equation in r which depends only on the spacetime parameters (M, Q, χ, n). The equation is independent of E and L_ϕ The solution of the equation (which is complicated and not shown) gives the photon orbit radius (r_p) both for co-rotating (r_{p1}) and counter rotating (r_{p2}) orbits. Table(s) 4.1 and 4.2 tabulate the values of the photon orbit radius both for co-rotating and counter rotating orbits with different values of plasma parameter (k). We obtain the Table(s) below by setting M to unity.

χ **=0.2**

k	r_{p1}
0.0	1.645
0.2	1.480
0.27	1.381

χ **=1.0**

k	r_{p1}
0.0	1.742
0.2	1.632
0.38	1.418

χ **=0.2**

k	r_{p1}
0.0	1.645
0.2	1.507
0.31	1.385

χ **=1.0**

k	r_{p1}
0.0	1.742
0.2	1.632
0.4	1.492

Table 4.1: Tabular representation of co-rotating photon orbit radius r_{p1} around black hole with spin a=0.5 and charge Q=0.3. The first two are for homogeneous plasma and the next two for inhomogeneous plasma.

Table 4.1 represents the values of the circular photon orbit radius for a ste of values of plasma parameter k. The table shows that an increase in the plasma parameter k decreases the radius of co-rotating photon orbits r_{p1} both for homogeneous and inhomogeneous radial plasma ditribution. Besides the radius of co-rotating orbits have smaller values implying their existence closer to the black hole. The effect of plasma parameter k on the radius of the orbits remains identical for both lower ($\chi < \chi_c$) and higher ($\chi > \chi_c$) regimes of PFDM parameter χ. The critical value of the PFDM parameter for spin $a = 0.5$ and charge $Q = 0.3$ is $\chi_c = 0.467$. Again our investigation revealed that the photon orbits do not exist for all possible values of the plasma parameter k. After a certain critical value of plasma parameter $k \geq k_c$, the radius of the photon orbit goes well below the event horizon radius (r_{h+}) and thereby has no physical meaning and hence do not exist. Thus there is a bound to the value of k depending on certain combinations of the black hole parameters (M, Q, χ).

χ **=0.2**

k	r_{p2}
0.0	2.782
0.2	2.825
0.4	2.886

χ **=1.0**

k	r_{p2}
0.0	2.608
0.2	2.640
0.4	2.685

χ **=0.2**

k	r_{p2}
0.0	2.782
0.2	2.761
0.4	2.737

χ **=1.0**

k	r_{p2}
0.0	2.608
0.2	2.587
0.4	2.564

Table 4.2: Tabular representation of counter rotating photon orbit radius r_{p2} around black hole with spin a=0.5 and charge Q=0.3. The first two are for homogeneous plasma and the next two for inhomogeneous plasma.

On the other hand, Table 4.2 shows that an increase in plasma parameter k increases the radius of counter rotating photon orbits r_{p2} in case of homogenous radial plasma distribution whereas it decreases in case of inhomogenous distribution. The effect of plasma parameter k on the photon orbit radius remains same both for $\chi < \chi_c$ and $\chi > \chi_c$. In this case also, we find that the photon orbits exist only upto a certain critical value of the plasma parameter k.

4.4 Black hole shadow

In this section, we wish to calculate the black hole shadow for various plasma distribution. Shadows of black holes are formed due to bending of light rays which traverse through regions of strong gravity. More specifically, when light from a distant source comes near a black hole, the rays get deflected. The deflected rays after encircling the black hole either plunges into the black hole or escapes to infinity. The light rays from unstable circular orbits which reaches the observer at infinity forms the *circular* or *deformed circular* boundary curve. The dark disk inside the curve is called the black hole shadow. The shadow is formed in the celestial plane characterised by the celestial coordinates α and β. They are defined for an observer stationed at infinity as

$$\alpha = \lim_{r_0 \to \infty} -r_0^2 \sin\theta_0 \Big(\frac{d\phi}{dr}\Big)\Bigg|_{r_0,\theta_0} \tag{4.22}$$

$$\beta = \lim_{r_0 \to \infty} r_0^2 \Big(\frac{d\theta}{dr}\Big)\Bigg|_{r_0,\theta_0} \tag{4.23}$$

where the position of the observer is represented by the coordinates r_0 and θ_0. Here, r_0 gives the radial distance of the observer from the black hole and θ_0 corresponds to the inclination angle of the observer's line of sight with the axis of rotation of the black hole.

4.4.1 Shadow with a general plasma distribution

In this section, we consider a general distribution of plasma where the plasma frequency ω_p is a function of both r and θ [79],[105],[143]. We start from the Hamiltonian

$$\mathcal{H}(x^\mu, p_\mu) = \frac{1}{2}\Big[g^{\mu\nu}p_\mu p_\nu + \omega_p(r,\theta)^2\Big] \ . \tag{4.24}$$

The refractive index n becomes

$$n(r,\theta)^2 = 1 - \Big(\frac{\omega_p(r,\theta)}{\omega}\Big)^2 \ . \tag{4.25}$$

Here, ω corresponds to the photon frequency as measured by any arbitrary observer in the domain of outer communication, that is between outer event horizon (r_{h+}) to infinity. The photon frequency as measured by a stationary observer at infinity is ω_0 which is related to ω by the relation [157]

$$\omega = \frac{\omega_0}{\sqrt{-g_{00}}} = \frac{\omega_0 \zeta}{\sqrt{\Delta - a^2 \sin^2\theta}} \ . \tag{4.26}$$

Now, our task is to calculate the geodesics necessary for obtaining the black hole shadow. For this we use the Hamilton's equation of motion. Just as we have done in our previous analysis, here too we find that the Hamiltonian ($\mathcal{H}$) is independent of t and ϕ. Hence the corresponding constants of motion are $p_0 = -E$ and $p_3 = L_\phi$ where, E and L_ϕ correspond to the energy and angular momentum of photons as measured by a stationary observer at infinity. Again the energy E and frequency ω_0 are related as $E = \hbar\omega_0$, which gives $E = \omega_0$ for $\hbar = 1$.

Using Hamilton's equation of motion $\dot{x}^\mu = \frac{\partial H}{\partial p_\mu}$, we get the equations for t and ϕ as [157]

$$\zeta^2 \dot{t} = \frac{r^2 + a^2}{\Delta}\Big[(r^2+a^2)E - aL_\phi\Big] + a\Big[L_\phi - aE\sin^2\theta\Big] \tag{4.27}$$

$$\zeta^2 \dot{\phi} = \frac{a}{\Delta}\Big[(r^2+a^2)E - aL_\phi\Big] + \Big[L_\phi \csc^2\theta - aE\Big] \ . \tag{4.28}$$

To obtain the geodesics for r and θ, we use the Hamilton-Jacobi equation which for photons immersed in plasma turns out to be

$$\mathcal{H}\Big(x^{\mu}, \frac{\partial S}{\partial x^{\mu}}\Big) = \frac{1}{2}\Big[g^{\mu\nu}\frac{\partial S}{\partial x^{\mu}}\frac{\partial S}{\partial x^{\nu}} + \omega_p(r,\theta)^2\Big] = 0 \ . \tag{4.29}$$

In order to solve the above eq.(4.29), we consider an ansatz S [68]

$$S = -Et + L_{\phi}\phi + S_r(r) + S_{\theta}(\theta) \tag{4.30}$$

and substitute it in eq.(4.29) to get

$$-\frac{1}{\Delta}\Big[(r^2+a^2)E - aL_{\phi}\Big]^2 + (L_{\phi}\csc\theta - aE\sin\theta)^2 + \Delta\Big(\frac{\partial S_r}{\partial r}\Big)^2 + \Big(\frac{\partial S_{\theta}}{\partial \theta}\Big)^2 + \omega_p^2\zeta^2 = 0 \ . \tag{4.31}$$

The above equation can be separated into two equations of r and θ, if we assume $\omega_p^2(r,\theta)$ to be [105]

$$\omega_p^2(r,\theta) = \frac{f_r(r) + f_{\theta}(\theta)}{r^2 + a^2\cos^2\theta} \tag{4.32}$$

where $f_r(r)$ and $f_{\theta}(\theta)$ are respectively the functions of r and θ only. This form of $\omega_p^2(r,\theta)$ modifies the refractive index $n(r,\theta)$ to

$$n(r,\theta)^2 = 1 - \Big(\frac{f_r(r) + f_{\theta}(\theta)}{(r^2 + a^2\cos^2\theta)\omega^2}\Big) \ . \tag{4.33}$$

Using eq.(4.32) in eq.(4.31), we get

$$\Big(\frac{\partial S_{\theta}}{\partial \theta}\Big)^2 + (L_{\phi}\csc\theta - aE\sin\theta)^2 + f_{\theta}(\theta) = \frac{1}{\Delta}\Big[(r^2+a^2)E - aL_{\phi}\Big]^2 - \Delta\Big(\frac{\partial S_r}{\partial r}\Big)^2 - f_r(r) = constant = \kappa \tag{4.34}$$

with κ being the generalised Carter constant. The equations for θ and r take the form

$$\zeta^2\dot{\theta} = \pm\sqrt{\Theta(\theta)} \tag{4.35}$$

$$\zeta^2\dot{r} = \pm\sqrt{R(r)} \tag{4.36}$$

with the expressions for $\Theta(\theta)$ and $R(r)$ as

$$\Theta(\theta) = \kappa - (L_{\phi}\csc\theta - aE\sin\theta)^2 - f_{\theta}(\theta) \tag{4.37}$$

$$R(r) = \Big[(r^2+a^2)E - aL_{\phi}\Big]^2 - \Delta\Big(\kappa + f_r(r)\Big) \ . \tag{4.38}$$

As discussed earlier, the black hole shadow is formed by the photons moving in the unstable circular geodesics. The geodesics are subject to the condition $R(r) = 0$ and $\frac{\partial R(r)}{\partial r} = 0$. Using the conditions, we obtain

$$\Big[(r^2+a^2) - a\xi\Big]^2 = \Delta\Big[\eta + \tilde{f}_r(r)\Big] \tag{4.39}$$

$$4r\Big[(r^2+a^2)-a\xi\Big]-\Delta\tilde{f}_r(r)=\Delta^{'}\Big[\eta+\tilde{f}_r(r)\Big] \tag{4.40}$$

where $\xi=\frac{L_\phi}{E}$, $\eta=\frac{\kappa}{E^2}$ and $\tilde{f}_r(r)=\frac{f_r(r)}{E^2}$. Also we define another variable $\tilde{f}_\theta(\theta)=\frac{f_\theta(\theta)}{E^2}$ which will be useful later [157] for various computations. Also, ξ and η are called the Chandrasekhar constants discussed in first chapter. Eliminating η from eq.(s) (4.39) and (4.40), we get an equation in ξ as

$$A\xi^2+2B\xi+C=0 \tag{4.41}$$

where

$$\begin{aligned}A=a^2\Delta^{'}\ \ ;\ \ B=2ar\Delta-a\Delta^{'}(r^2+a^2)\ ;\\ C=\Big[\Delta^{'}(r^2+a^2)^2-4r\Delta(r^2+a^2)+\Delta^2\tilde{f}_r^{\prime}(r)\Big]\end{aligned} \tag{4.42}$$

with $\tilde{f}_r^{\prime}(r)$ giving the derivative of $\tilde{f}_r(r)$ with respect to r. Solving for ξ, we get

$$\xi=-\frac{B}{A}\pm\sqrt{\left(\frac{B}{A}\right)^2-\frac{C}{A}}\ . \tag{4.43}$$

In order to graphically obtain the silhouette of the black hole shadow, we need to consider negative sign in the expression for ξ. The expression for η obtained from eq.(4.39) is of the form

$$\eta=\frac{1}{\Delta}\Bigg[(r^2+a^2)-a\xi\Bigg]^2-\tilde{f}_r^{\prime}(r)\ . \tag{4.44}$$

The expression of the celestial coordinates α and β shows that for determining the black hole shadow which is formed in the $(\alpha-\beta)$ plane, we need the geodesics for ϕ, θ and r as given in eq.(s) (4.28), (4.35) and (4.36) respectively. The expressions for $\frac{d\phi}{dr}$ and $\frac{d\theta}{dr}$ take the form

$$\left(\frac{d\phi}{dr}\right)=\frac{\frac{a}{\Delta}\Big[(r^2+a^2)E-aL_\phi\Big]+\Big[L_\phi\csc^2\theta-aE\Big]}{\sqrt{\Big[(r^2+a^2)E-aL_\phi\Big]^2-\Delta\Big(\kappa+f_r(r)\Big)}} \tag{4.45}$$

$$\left(\frac{d\theta}{dr}\right)=\sqrt{\frac{\kappa-(L_\phi\csc\theta-aE\sin\theta)^2-f_\theta(\theta)}{\Big[(r^2+a^2)E-aL_\phi\Big]^2-\Delta\Big(\kappa+f_r(r)\Big)}}\ . \tag{4.46}$$

Using the above eq.(s) (4.45), (4.46) in the expressions for α and β, we have

$$\alpha=-\xi\csc\theta_0\ \ ;\ \ \beta=\pm\sqrt{\eta-(\xi\csc\theta-a\sin\theta)^2-\tilde{f}_\theta(\theta)}\ . \tag{4.47}$$

The shadow can be drawn by parametrically plotting α and β along X and Y axis respectively. We have shown the plots below for two different plasma distribution. First by setting $f_r(r)=\omega_c^2\sqrt{M^3r}$ and $f_\theta(\theta)=0$ [105] and the second by setting $f_r(r)=0$ and $f_\theta(\theta)=\omega_c^2M^2(1+2\sin^2\theta)$ [105]. Putting $f_r(r)=\omega_c^2\sqrt{M^3r}$ and $f_\theta(\theta)=0$ (with $M=1$) we get the expressions in eq.(s) (4.45), (4.46) and (4.47) to be

$$\left(\frac{d\phi}{dr}\right) = \frac{\frac{a}{\Delta}\Big[(r^2+a^2)E - aL_\phi\Big] + \Big[L_\phi \csc^2\theta - aE\Big]}{\sqrt{\Big[(r^2+a^2)E - aL_\phi\Big]^2 - \Delta\Big(\kappa + \omega_c^2\sqrt{r}\Big)}} \tag{4.48}$$

$$\left(\frac{d\theta}{dr}\right) = \sqrt{\frac{\kappa - (L_\phi \csc\theta - aE\sin\theta)^2}{\Big[(r^2+a^2)E - aL_\phi\Big]^2 - \Delta\Big(\kappa + \omega_c^2\sqrt{r}\Big)}} \tag{4.49}$$

$$\alpha = -\xi \csc\theta_0 \;\; ; \;\; \beta = \pm\sqrt{\eta - (\xi\csc\theta - a\sin\theta)^2} \; . \tag{4.50}$$

Again, by putting $f_r(r) = 0$ and $f_\theta(\theta) = \omega_c^2 M^2(1 + 2\sin^2\theta)$ (with $M = 1$), the expressions in eq.(s) (4.45), (4.46) and (4.47) become

$$\left(\frac{d\phi}{dr}\right) = \frac{\frac{a}{\Delta}\Big[(r^2+a^2)E - aL_\phi\Big] + \Big[L_\phi \csc^2\theta - aE\Big]}{\sqrt{\Big[(r^2+a^2)E - aL_\phi\Big]^2 - \Delta\kappa}} \tag{4.51}$$

$$\left(\frac{d\theta}{dr}\right) = \sqrt{\frac{\kappa - (L_\phi \csc\theta - aE\sin\theta)^2 - \omega_c^2(1 + 2\sin^2\theta)}{\Big[(r^2+a^2)E - aL_\phi\Big]^2 - \Delta\kappa}} \tag{4.52}$$

$$\alpha = -\xi \csc\theta_0 \;\; ; \;\; \beta = \pm\sqrt{\eta - (\xi\csc\theta - a\sin\theta)^2 - \left(\frac{\omega_c}{\omega_0}\right)^2(1 + 2\sin^2\theta)} \; . \tag{4.53}$$

4.4.2 Shadow with radial plasma distribution

In this section, we want to study the black hole shadow in a scenario where the refractive index $n(r)$ depends only on r. For this we evaluate the geodesics of light rays using the Hamiltonian ($\mathcal{H}$) given as

$$\mathcal{H} = \frac{1}{2}\Big[g^{\mu\nu}p_\mu p_\nu + (n^2 - 1)g^{00}p_0^2\Big] \; . \tag{4.54}$$

Using Hamilton's equation of motion, the expressions for t and ϕ geodesics in an arbitrary plane reads

$$\zeta^2\dot{t} = \frac{r^2+a^2}{\Delta}\Big[n^2(r^2+a^2)E - aL_\phi\Big] + a\Big[L_\phi - an^2E\sin^2\theta\Big] \tag{4.55}$$

$$\zeta^2\dot{\phi} = \frac{a}{\Delta}\Big[(r^2+a^2)E - aL_\phi\Big] + \Big[L_\phi\csc^2\theta - aE\Big] \; . \tag{4.56}$$

To obtain the geodesics along r and θ, we use the Hamilton-Jacobi equation, which takes the form

$$\frac{\partial S}{\partial\lambda} = -\mathcal{H} = -\frac{1}{2}\left[g^{\mu\nu}\Big(\frac{\partial S}{\partial x^\mu}\Big)\Big(\frac{\partial S}{\partial x^\nu}\Big) + (n^2-1)g^{00}\Big(\frac{\partial S}{\partial x^0}\Big)^2\right] \; . \tag{4.57}$$

In order to solve the above equation, we need to choose an ansatz for S [1] as done earlier

$$S = -Et + L_\phi\phi + S_r(r) + S_\theta(\theta) \; . \tag{4.58}$$

Replacing S in eq.(4.57), we have

$$
\begin{aligned}
-\frac{(n^2-1)}{\Delta}E^2(r^2+a^2)^2-\frac{1}{\Delta}\Big[(r^2+a^2)E-aL_\phi\Big]^2+(n^2-1)a^2E^2\sin^2\theta-a^2E^2\cos^2\theta \\
+L_\phi^2\cot^2\theta+(aE-L_\phi)^2+\Delta\Big(\frac{\partial S_r}{\partial r}\Big)^2+\Big(\frac{\partial S_\theta}{\partial\theta}\Big)^2=0\ .
\end{aligned}
\tag{4.59}
$$

Now we wish to separate the above equation in r and θ variables just like our previous analysis. But here we find some mathematical problems that hinder the method of separation. By inspecting the term $n(r)^2a^2E^2\sin^2\theta$, we observe that it is in general, not possible to separate $n(r)$ from $\sin\theta$. So we have to consider special cases where the separation is possible. Here in this work we study two such possiblities.

Inhomogeneous plasma

In the first case, we consider $n=n(r)=\sqrt{1-\frac{k}{r}}$. This hinders the separation of eq.(4.59) into functions of r and θ. However, we can separate it if we consider near equatorial plane [96]. The near equatorial plane approximation is taken as $\theta\approx\frac{\Pi}{2}+\epsilon$, with ϵ being a very small angle. It must be noted that the unstable photon orbits are not restricted to the near equatorial planes, they can travel through any arbitrary plane. Yet for an observer at infinity, this approximation is valid and gives accurate and desirable results for the black hole shadow. Again, since we are considering geodesics in the near equatorial plane, we simultaneously place the observer in the equatorial plane, that is, $\theta_0=\frac{\pi}{2}$. This assumption modifies the geodesics as well as the celestial coordinates (α,β).
Setting $\theta=\frac{\Pi}{2}+\epsilon$, eq.(4.59) becomes

$$
\begin{aligned}
-\frac{(n^2-1)}{\Delta}E^2(r^2+a^2)^2-\frac{1}{\Delta}\Big[(r^2+a^2)E-aL_\phi\Big]^2+(n^2-1)a^2E^2 \\
+(aE-L_\phi)^2+\Delta\Big(\frac{\partial S_r}{\partial r}\Big)^2+\Big(\frac{\partial S_\epsilon}{\partial\epsilon}\Big)^2=0\ .
\end{aligned}
\tag{4.60}
$$

Introducing Carter constant κ [1] as in the previous case, we can split the equation into two parts as

$$
\begin{aligned}
\frac{(n^2-1)}{\Delta}E^2(r^2+a^2)^2+\frac{1}{\Delta}\Big[(r^2+a^2)E-aL_\phi\Big]^2-(n^2-1)a^2E^2 \\
-(aE-L_\phi)^2-\Delta\Big(\frac{\partial S_r}{\partial r}\Big)^2=\Big(\frac{\partial S_\epsilon}{\partial\epsilon}\Big)^2=\kappa\ .
\end{aligned}
\tag{4.61}
$$

Using $\frac{\partial\mathcal{L}}{\partial\dot{x}^\mu}=\frac{\partial S}{\partial x^\mu}$, we get equation(s) for r and ϵ as

$$
r^2\dot{r}=\sqrt{R(r)}
\tag{4.62}
$$

$$
r^2\dot{\epsilon}=\sqrt{\Theta(\epsilon)}
\tag{4.63}
$$

where the expressions for $R(r)$ and $\Theta(\epsilon)$ takes the form

$$
R(r)=(n^2-1)E^2(r^2+a^2)^2+\Big[(r^2+a^2)E-aL_\phi\Big]^2-\Delta\Big[(n^2-1)a^2E^2+(aE-L_\phi)^2+\kappa\Big]
\tag{4.64}
$$

$$\Theta(\epsilon) = \kappa \ . \tag{4.65}$$

Since, shadows are formed by light rays moving in unstable circular orbits, so we use the conditions $R(r) = \frac{\partial R(r)}{\partial r} = 0$ as before. The conditions read

$$(n^2-1)(r^2+a^2)^2 + \Big[(r^2+a^2) - a\xi\Big]^2 = \Delta\Big[(n^2-1)a^2 + (a-\xi)^2 + \eta\Big] \tag{4.66}$$

$$4r(n^2-1)(r^2+a^2) + 4r\Big[(r^2+a^2) - a\xi\Big] - 2nn^{'}\Delta a^2 + 2(r^2+a^2)nn^{'} = \Delta^{'}\Big[(n^2-1)a^2 + (a-\xi)^2 + \eta\Big] \ . \tag{4.67}$$

Eliminating η from the above equations, we get a quadratic equation ξ as

$$A\xi^2 + 2B\xi + C = 0 \tag{4.68}$$

with the expressions for A, B and C taking the form

$$\begin{aligned} A = a^2\Delta^{'} \ \ ; \ \ B = 2ar\Delta - a\Delta^{'}(r^2+a^2) \ ; \\ C = \Big[n^2\Delta^{'}(r^2+a^2)^2 - 4r\Delta n^2(r^2+a^2) + 2nn^{'}\Delta^2 a^2 - 2(r^2+a^2)^2 nn^{'}\Delta\Big] \ . \end{aligned} \tag{4.69}$$

Solving for ξ, we have

$$\xi = -\frac{B}{A} \pm \sqrt{\left(\frac{B}{A}\right)^2 - \frac{C}{A}} \ . \tag{4.70}$$

The expression for η takes the form

$$\eta = \frac{1}{\Delta}\left[(n^2-1)(r^2+a^2)^2 + \Big[(r^2+a^2) - a\xi\Big]^2\right] - (n^2-1)a^2 - (a-\xi)^2 \ . \tag{4.71}$$

The constants ξ and η are the quantities in terms of which shadow radius R_s is evaluated.
In order to determine α and β, we need to calculate $\left(\frac{d\phi}{dr}\right)$ and $\left(\frac{d\epsilon}{dr}\right)$. The geodesics for ϕ, ϵ and r have the form (considering near equatorial plane)

$$\left(\frac{d\phi}{d\lambda}\right) = \frac{a}{\Delta r^2}\Big[(r^2+a^2)E - aL_\phi\Big] + \frac{1}{r^2}\Big[L_\phi - aE\Big] \tag{4.72}$$

$$\left(\frac{d\epsilon}{d\lambda}\right) = \frac{\sqrt{\kappa}}{r^2} \tag{4.73}$$

$$\left(\frac{dr}{d\lambda}\right) = \frac{1}{r^2}\sqrt{(n^2-1)E^2(r^2+a^2)^2 + \Big[(r^2+a^2)E - aL_\phi\Big]^2 - \Delta\Big[(n^2-1)a^2E^2 + (aE-L_\phi)^2 + \kappa\Big]} \ . \tag{4.74}$$

Using the above geodesics, we get the relevant equations as

$$\Big(\frac{d\phi}{dr}\Big) = \frac{\frac{a}{\Delta}\Big[(r^2+a^2)E - aL_\phi\Big] + \Big[L_\phi \csc^2\theta - aE\Big]}{\sqrt{(n^2-1)E^2(r^2+a^2)^2 + \Big[(r^2+a^2)E - aL_\phi\Big]^2 - \Delta\Big[(n^2-1)a^2E^2 + (aE-L_\phi)^2 + \kappa\Big]}} \tag{4.75}$$

$$\Big(\frac{d\epsilon}{dr}\Big) = \sqrt{\frac{\kappa}{(n^2-1)E^2(r^2+a^2)^2 + \Big[(r^2+a^2)E - aL_\phi\Big]^2 - \Delta\Big[(n^2-1)a^2E^2 + (aE-L_\phi)^2 + \kappa\Big]}} \ . \tag{4.76}$$

Now replacing the above relations in the expressions for α and β, we get the celestial coordinates as

$$\alpha = -\frac{\xi}{n} \ \ ; \ \ \beta = \pm\frac{\sqrt{\eta}}{n} \ . \tag{4.77}$$

Plotting α along X-axis vs β along Y-axis, we get the silhouette of the black hole shadow.

Homogeneous plasma

In the second case, we consider $n(r)$ =constant=$\sqrt{1-k}$. The t and ϕ geodesics are the same as obtained in the previous case. In this case we find that eq.(4.59) is separable. Using the Cartar constant κ [1], we get

$$\Big(\frac{\partial S_\theta}{\partial\theta}\Big)^2 + (n^2-1)a^2E^2\sin^2\theta - a^2E^2\cos^2\theta + L_\phi^2\cot^2\theta = -\Delta\Big(\frac{\partial S_r}{\partial r}\Big)^2 + \frac{(n^2-1)}{\Delta}E^2(r^2+a^2)^2 \tag{4.78}$$

$$+\frac{1}{\Delta}\Big[(r^2+a^2)E + aL_\phi\Big]^2 - (aE-L_\phi)^2 = \kappa \ .$$

This results into r and θ equation(s) as

$$\zeta^2\dot{r} = \sqrt{R(r)} \tag{4.79}$$

$$\zeta^2\dot{\theta} = \sqrt{\Theta(\theta)} \ . \tag{4.80}$$

The expressions for $R(r)$ and $\Theta(\theta)$ take the form

$$R(r) = (n^2-1)E^2(r^2+a^2)^2 + \Big[(r^2+a^2)E - aL_\phi\Big]^2 - \Delta\Big[(aE-L_\phi)^2 + \kappa\Big] \tag{4.81}$$

$$\Theta(\theta) = \kappa - (n^2-1)a^2E^2\sin^2\theta + a^2E^2\cos^2\theta - L_\phi^2\cot^2\theta \ . \tag{4.82}$$

As discussed earlier, the condition for unstable circular orbits which form the black hole shadow boundary are $R(r) = \frac{\partial R}{\partial r} = 0$. Using the conditions we get the constraint equations

$$(n^2-1)(r^2+a^2)^2 + \Big[(r^2+a^2) - a\xi\Big]^2 = \Delta\Big[\eta + (a-\xi)^2\Big] \tag{4.83}$$

$$4rn^2(r^2+a^2) - 4ra\xi = \Delta^{'}\Big[\eta + (a-\xi)^2\Big] \ . \tag{4.84}$$

Eliminating η from the above equation(s), we get an equation in ξ of the form

$$A\xi^2 + 2B\xi + C = 0 \tag{4.85}$$

where, A, B, C has the form

$$\begin{aligned} A = a^2\Delta^{'} \ \ ; \ \ B &= 2ar\Delta - a\Delta^{'}(r^2+a^2) \ ; \\ C &= \Big[n^2\Delta^{'}(r^2+a^2)^2 - 4r\Delta n^2(r^2+a^2)\Big] \ . \end{aligned} \tag{4.86}$$

Solving the above equation, ξ becomes

$$\xi = -\frac{B}{A} \pm \sqrt{\Big(\frac{B}{A}\Big)^2 - \frac{C}{A}} \ . \tag{4.87}$$

The expression for η becomes

$$\eta = \frac{1}{\Delta}\Bigg[(n^2-1)(r^2+a^2)^2 + \Big[(r^2+a^2) - a\xi\Big]^2\Bigg] - (a-\xi)^2 \ . \tag{4.88}$$

In order to calculate the celestial coordinates (α, β) we need to make use of the geodesics equations(s) for r, θ and ϕ as given in eq.(s) (4.79), (4.80) and (4.56) respectively. Using them, we get the expressions for $\frac{d\phi}{dr}$ and $\frac{d\theta}{dr}$ as

$$\Big(\frac{d\phi}{dr}\Big) = \frac{\frac{a}{\Delta}\Big[(r^2+a^2)E - aL_\phi\Big] + \Big[L_\phi \csc^2\theta - aE\Big]}{\sqrt{(n^2-1)E^2(r^2+a^2)^2 + \Big[(r^2+a^2)E - aL_\phi\Big]^2 - \Delta\Big[(aE-L_\phi)^2 + \kappa\Big]}} \tag{4.89}$$

$$\Big(\frac{d\theta}{dr}\Big) = \sqrt{\frac{\kappa - (n^2-1)a^2E^2\sin^2\theta + a^2E^2\cos^2\theta - L_\phi^2\cot^2\theta}{(n^2-1)E^2(r^2+a^2)^2 + \Big[(r^2+a^2)E - aL_\phi\Big]^2 - \Delta\Big[(aE-L_\phi)^2 + \kappa\Big]}} \ . \tag{4.90}$$

Replacing the above eq.(s) in the expressions for α and β, we have

$$\alpha = -\frac{\xi}{n}\csc\theta \ \ ; \ \ \beta = \pm\frac{\sqrt{\eta - (n^2-1)a^2\sin^2\theta + a^2\cos^2\theta - \xi^2\cot^2\theta}}{n} \ . \tag{4.91}$$

The shadow can be obtained by plotting α along X axis and β along Y axis. In this case, the observer is fixed at radial infinity ($r_0 = \infty$) and the inclination of the observer with respect to the direction of black hole spin (a) can be varied. So we consider three angular positions as $\theta_0 = \frac{\pi}{4}$, $\theta_0 = \frac{\pi}{3}$ and $\theta_0 = \frac{\pi}{2}$.

Before ending this section, we want to mention that the general case (Case 4.4.1) in which n is a function of both r and θ boils down to the case $n = \sqrt{1-k}$. This can be seen as follows. Setting $f_r(r) = \omega_c^2 r^2$ and $f_\theta(\theta) = \omega_c^2 a^2\cos^2\theta$, we get $\omega_p(r,\theta) = \omega_c =$ constant. Now we write the Hamiltonian

($\mathcal{H}$) in the form [107]

$$\mathcal{H}(x^\mu, p_\mu) = \frac{1}{2}\Big[g^{\mu\nu}p_\mu p_\nu + \widetilde{\omega}_p(r,\theta)^2\Big] \tag{4.92}$$

where $\widetilde{\omega}_p$ is given by

$$\widetilde{\omega}_p = \frac{\omega_p}{\sqrt{-g_{00}}} = \frac{\omega_c}{\sqrt{-g_{00}}}\ . \tag{4.93}$$

The refractive index is defined as [104]

$$n^2(r,\theta) = 1 - \frac{\widetilde{\omega}_p^2}{\omega^2} = 1 - \left(\frac{\omega_c}{\omega_0}\right)^2 = 1 - k = constant \tag{4.94}$$

where we have defined $\left(\frac{\omega_c}{\omega_0}\right)^2 = k$ and used $\omega = \frac{\omega_0}{\sqrt{-g_{00}}}$. Substituting ω_c in terms of n, we get

$$\begin{aligned}\mathcal{H}(x^\mu, p_\mu) &= \frac{1}{2}\Big[g^{\mu\nu}p_\mu p_\nu - g^{00}\omega_c^2\Big] \\ &= \frac{1}{2}\Big[g^{\mu\nu}p_\mu p_\nu + (n^2-1)g^{00}\omega_0^2\Big]\ ,\ n = \sqrt{1-k}\ .\end{aligned} \tag{4.95}$$

This is the same Hamiltonian as in Case 4.4.2 with $p_0 = -E = -\omega_0$.

4.5 Impact of the spacetime parameters on the black hole shadow

The motion of any particle in the black hole spacetime is influenced by the parameters describing the spacetime. The same is true for unstable photons that either plunge into the black hole singularity or fly off to infinity. Those that fly off to infinity reach the observer and form the boundary of the black hole shadow. Thus the shadow formed by photons gets impacted by the spacetime parameters. The parameters describing the spacetime are spin (a) and charge (Q) of the black hole, $PFDM$ parameter (χ) and the plasma parameter (k). Now we show the plots and discuss how the parameters effect the black hole shadow.

4.5.1 Influence of spin a, charge Q and PFDM parameter χ on the shadow

In Fig.5.2, we plot the silhouette of the black hole shadow for different values of spin (a). To highlight the influence of spin parameter a we fixed the rest of the black hole parameters (Q = 0.2, χ = 0.2, 1.0, k = 0.2) and varied a. The plots are shown for inhomogeneous radial plasma distribution with refractive index $n(r) = \sqrt{1 - \frac{k}{r}}$. Earlier we have discussed about the two ranges of PFDM parameter χ separated by the critical value χ_c. The left plot is shown considering $\chi < \chi_c$ whereas the right one is shown for $\chi > \chi_c$. The value of χ_c varies with variation in the values of black hole spin a with fixed charge Q as discussed in the previous chapter. The shadow is larger in case of $\chi < \chi_c$, whereas, they are comparatively smaller in case of $\chi > \chi_c$. Besides, we find that with increase in spin (a) of the black hole, the shadow gets rotated and slightly deformed. This is due to the rotational drag force on the unstable photons moving in close vicinity of the black hole.

Fig.4.2 depict the effect of charge (Q) on the silhouette of the black hole shadow. Just like the previous case we have shown two ranges of χ. We fix the black hole parameters to constant values (a = 0.4, χ = 0.2, 1.0, k = 0.2). The plots are shown for inhomogeneous plasma with $n(r) = \sqrt{1 - \frac{k}{r}}$.

Here too, we find that the shadow size in the lower regime of χ that is $\chi < \chi_c$ is greater than that in the higher regime where $\chi > \chi_c$. Also the plots narrate that with the increase in black hole charge (Q), the shadow size reduces in both cases ($\chi < \chi_c$ and $\chi > \chi_c$). The reason for the observation can be assigned to the fact that the event horizon radius $r_{h+} = M + \sqrt{M^2 - Q^2}$ without dark matter (χ=0) and plasma (k=0). The expression entails that the black hole size decreases with increase in charge Q which gets reflected in the shadow size as well. The influence of charge on shadow reamins same even in presence of χ and k. The black hole shadow which is a manifestation of the event horizon (though comparatively larger), thereby decreases.

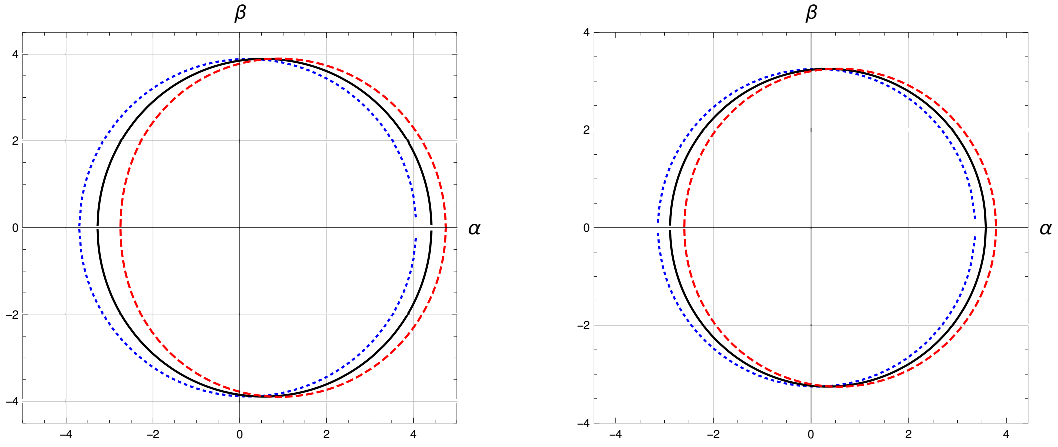

(a) Q = 0.2, k = 0.2, χ = 0.2 (b) Q = 0.2, k = 0.2, χ = 1.0

Figure 4.1: Graphical representation of the black hole shadow for different values of spin (a). The colored plots are for different spin values-blue dotted ($a = 0.1$), black ($a = 0.3$), red dashed ($a = 0.5$).

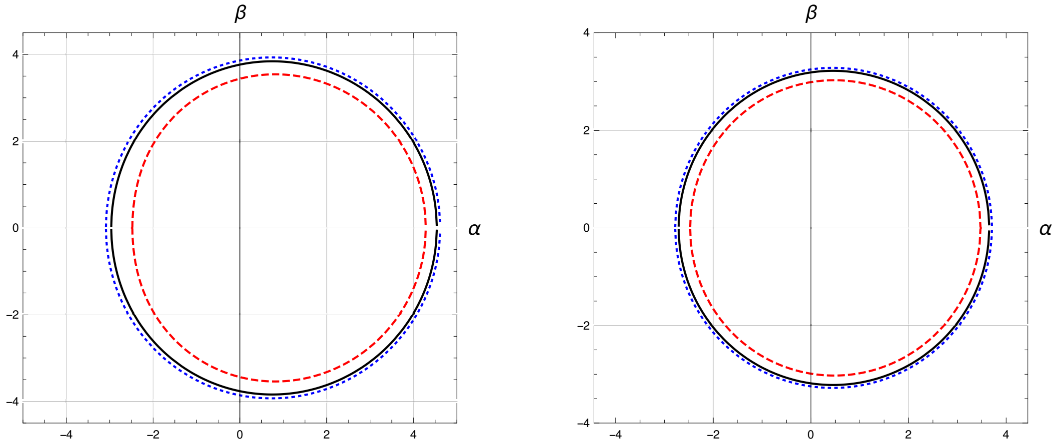

(a) a = 0.4, k = 0.2, χ = 0.2 (b) a = 0.4, k = 0.2, χ = 1.0

Figure 4.2: Graphical representation of the black hole shadow for different values of charge (Q). The colored plots are for different charge values-blue dotted ($Q = 0.0$), black ($Q = 0.3$), red dashed ($Q = 0.6$).

Fig.4.3 shows the variation of the shadow size for different values of PFDM parameter χ. The plots are shown for inhomogeneous plasma with the refractive index $n(r) = \sqrt{1 - \frac{k}{r}}$. From previous analysis, we find that the outer event horizon radius (r_{h+}) decreases with increase in χ for $\chi < \chi_c$ and increases for $\chi > \chi_c$. The analogical results are observed in case of black hole shadow. We found that for $\chi < \chi_c$, the shadow decreases non-uniformly and gets distorted with increase in χ. On the other hand, for $\chi > \chi_c$, the shadow increases uniformly with increase in χ, though the effect is less pronounced than for $\chi < \chi_c$. Such kind of observation results from the fact that PFDM effectively gives the mass of the total system as discussed previously.

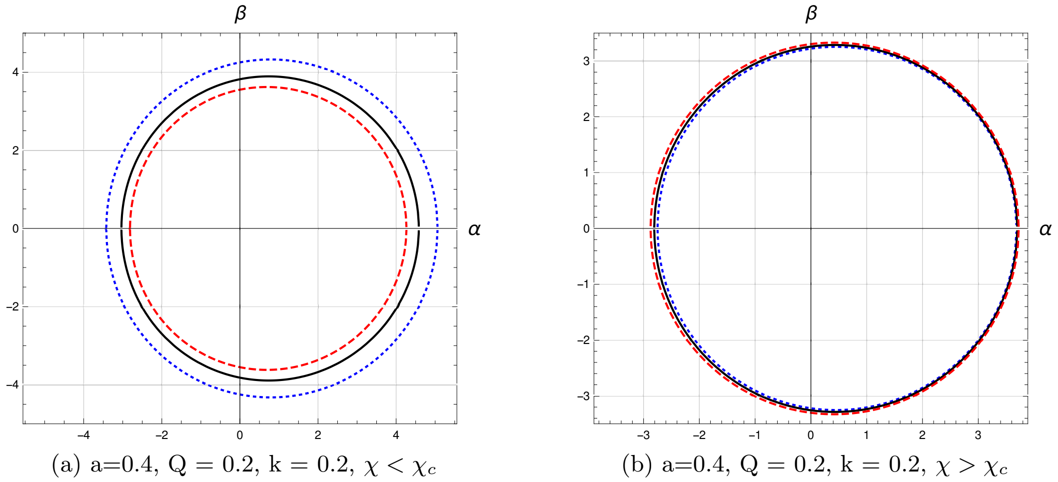

(a) a=0.4, Q = 0.2, k = 0.2, $\chi < \chi_c$

(b) a=0.4, Q = 0.2, k = 0.2, $\chi > \chi_c$

Figure 4.3: Graphical representation of the black hole shadow for different values of PFDM parameter (χ). The colored plots are for different values of χ-blue dotted ($\chi = 0.1$), black ($\chi = 0.2$), red dashed ($\chi = 0.3$) for the left plot and blue dotted ($\chi = 1.0$), black ($\chi = 1.1$), red dashed ($\chi = 1.2$) for the right plot.

4.5.2 Influence of plasma on the shadow

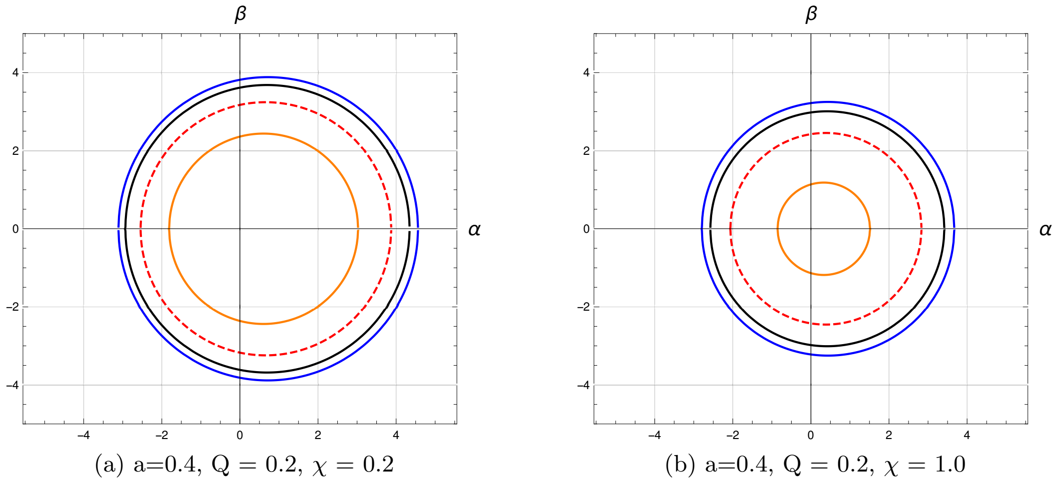

(a) a=0.4, Q = 0.2, $\chi = 0.2$

(b) a=0.4, Q = 0.2, $\chi = 1.0$

Figure 4.4: Graphical representation of the silhouette of the black hole shadow with $f_r(r) = \omega_c^2\sqrt{M^3 r}$ and $f_\theta(\theta) = 0$ and different values of $\left(\frac{\omega_c}{\omega_0}\right)^2$ with $\left(\frac{\omega_c}{\omega_0}\right)^2 = 0.0$ (blue), $\left(\frac{\omega_c}{\omega_0}\right)^2 = 1.0$ (black), $\left(\frac{\omega_c}{\omega_0}\right)^2 = 3.0$ (red dotted) and $\left(\frac{\omega_c}{\omega_0}\right)^2 = 6.0$ (orange).

In Figure 4.4, we have shown the variation of black hole shadow by setting the function $f_r(r) = \omega_c^2\sqrt{r}$, $f_\theta(\theta) = 0$, and $M = 1$. The plots are shown for fixed values of black hole spin $a = 0.4$ and charge $Q = 0.2$. Also the plots are shown with the observer placed in the equatorial plane, $\theta_0 = \frac{\pi}{2}$. The left plot is for PFDM parameter $\chi = 0.2$ and the right one for PFDM parameter $\chi = 1.0$. We have taken these two values since $\chi = 0.2$ is less than χ_c whereas, $\chi = 1.0$ is greater than χ_c for the considered combination of spin a and charge Q. The plots show that shadow size decreases with increase in plasma parameter ω_c. Besides, we also observe that the shadow size is significantly smaller in case of $\chi = 1.0$ as compared to that in $\chi = 0.2$.

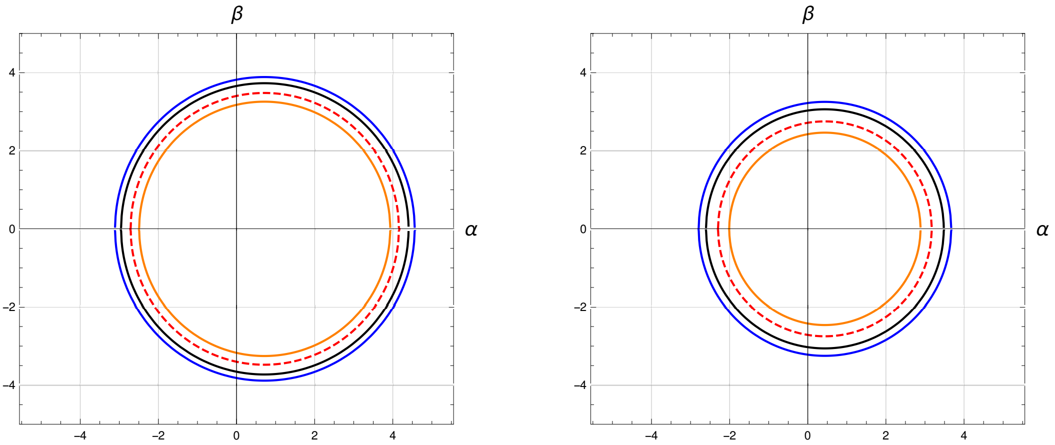

(a) a=0.4, Q = 0.2, $\chi = 0.2$ (b) a=0.4, Q = 0.2, $\chi = 1.0$

Figure 4.5: Graphical representation of the silhouette of the black hole shadow with $f_r(r) = 0$ and $f_\theta(\theta) = \omega_c^2 M^2\Big(1+2\sin^2\theta\Big)$ and different values of $\left(\frac{\omega_c}{\omega_0}\right)^2$ with $\left(\frac{\omega_c}{\omega_0}\right)^2 = 0.0$ (blue), $\left(\frac{\omega_c}{\omega_0}\right)^2 = 0.4$ (black),$\left(\frac{\omega_c}{\omega_0}\right)^2 = 1.0$ (red dotted) and $\left(\frac{\omega_c}{\omega_0}\right)^2 = 1.5$ (orange).

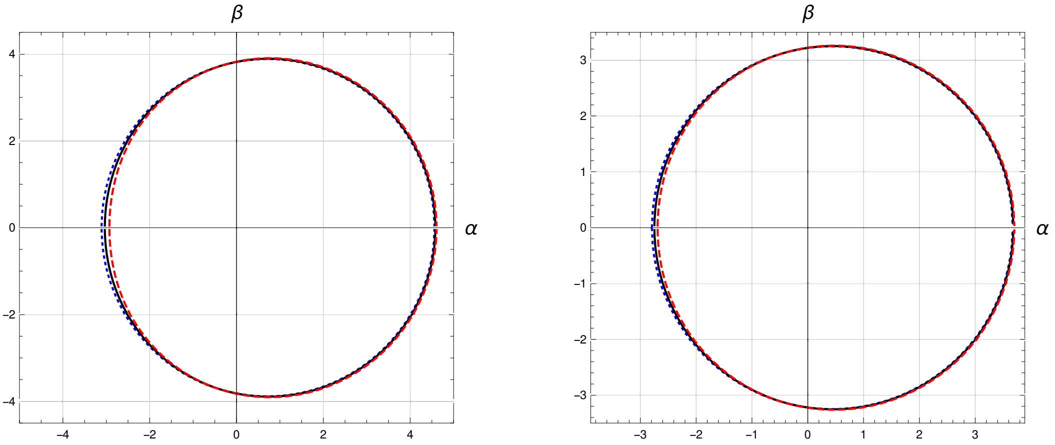

(a) a=0.4, Q = 0.2, $\chi = 0.2$ (b) a=0.4, Q = 0.2, $\chi = 1.0$

Figure 4.6: Graphical representation of the silhouette of the black hole shadow with inhomogeneous radial plasma distribution. The colored plots are for different values of plasma parameter-blue dotted ($k = 0.0$), black ($k = 0.2$), red dashed ($k = 0.4$).

Figure 4.5 shows the variation of black hole shadow by setting the functions $f_r(r) = 0$ and $f_\theta(\theta) = \omega_c^2\Big(1 + 2\sin^2\theta\Big)$, and $M = 1$. The plots are shown with the black hole spin and charge fixed at $a = 0.4$ and $Q = 0.2$ respectively. Also, the plots are shown with the observer situated in the equatorial plane, $\theta_0 = \frac{\pi}{2}$ as done previously. The left plot is for dark matter parameter $\chi = 0.2$ and the right one is for $\chi = 1.0$. The plots show that shadow size once again decreases with increase in plasma parameter ω_c as in the earlier case.

We plot the effect of inhomogeneous plasma ($n = n(r)$) on the black hole shadow in Fig.4.6. We have shown the plots both for $\chi < \chi_c$ and $\chi > \chi_c$. We observe that the co-rotating photon radius (r_{p1}) which correspond to the extreme left of α axis decreases with increase in plasma parameter k. The same happens in case of counter rotating radius (r_{p2}) which corresponds to the extreme right of the α axis. The effect is identical to that obtained previously following a numerical approach. The cumulative effect of the two extreme orbit produces the unstable photon orbit which forms the black hole shadow. The effect remains the same both for $\chi < \chi_c$ and $\chi > \chi_c$. The shadow size is comparatively larger in case of $\chi < \chi_c$ than that in $\chi > \chi_c$.

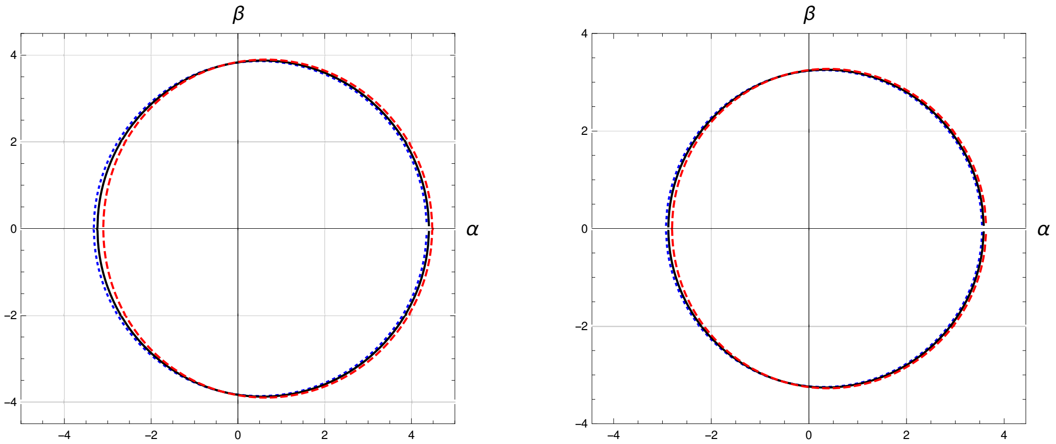

(a) a=0.4, Q $= 0.2$, $\chi = 0.2$ (b) a=0.4, Q $= 0.2$, χ =1.0

Figure 4.7: Graphical representation of the silhouette of the black hole shadow with homogeneous plasma distribution. The colored plots are for different values of plasma parameter-blue dotted ($k = 0.0$), black ($k = 0.2$), red dashed ($k = 0.4$). The plots are for $\theta_0 = \frac{\pi}{4}$.

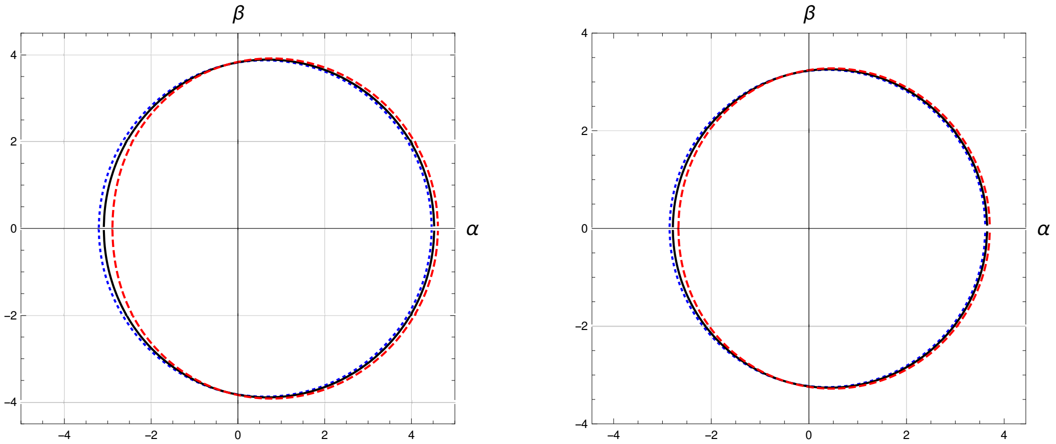

(a) a=0.4, Q $= 0.2$, $\chi = 0.2$ (b) a=0.4, Q $= 0.2$, χ =1.0

Figure 4.8: Graphical representation of the silhouette of the black hole shadow with homogeneous plasma distribution. The colored plots are for different values of plasma parameter-blue dotted ($k = 0.0$), black ($k = 0.2$), red dashed ($k = 0.4$). The plots are for $\theta_0 = \frac{\pi}{3}$.

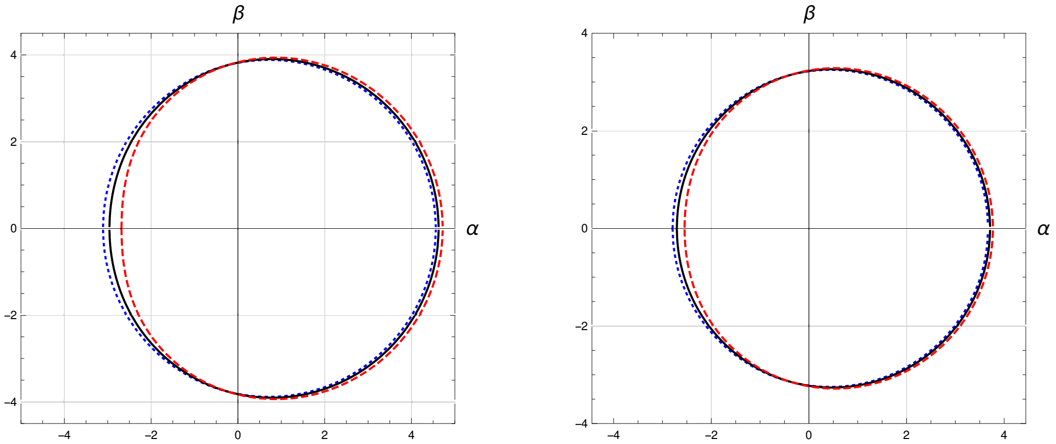

(a) a=0.4, Q $= 0.2$, $\chi = 0.2$ (b) a=0.4, Q $= 0.2$, χ =1.0

Figure 4.9: Graphical representation of the silhouette of the black hole shadow with homogeneous plasma distribution. The colored plots are for different values of plasma parameter-blue dotted ($k = 0.0$), black ($k = 0.2$), red dashed ($k = 0.4$). The plots are for $\theta_0 = \frac{\pi}{2}$.

In Fig.(s)(4.7, 4.8, 4.9), we have shown the effect of homogeneous plasma (n=constant) on the black hole shadow. The observation is carried out for different observer positions at $\theta_0 = \frac{\pi}{4}$, $\theta_0 = \frac{\pi}{3}$ and $\theta_0 = \frac{\pi}{2}$ respectively. The extreme right point on the α axis corresponds to the radius of counter rotating photon orbits [198]. On the other hand, the extreme left point on the α axis corresponds to the radius of co-rotating orbit. The radius (r_{p1}) of co-rotating photons is found to decrease with increase in plasma parameter k, whereas that of counter rotating photons (r_{p2}) is observed to increase with increase in k. The same is observed both for $PFDM$ parameter $\chi = 0.2$ and 1.0. Also the shadow size is comparatively larger in case of $\chi = 0.2$ with respect to that in $\chi = 1.0$.

4.6 Effective potential (V_{eff})

In this section, we study and analyse the effective potential (V_{eff}) as faced by a photon moving in the black hole spacetime. The potential can have maxima or minima which corresponds to the existence of unstable or stable orbits. The condition for maxima or minima are given as $\frac{\partial^2 V_{eff}}{\partial r^2} < 0$ and $\frac{\partial^2 V_{eff}}{\partial r^2} > 0$ respectively. The effective potential can be obtained from the modified radial equation which gives

$$\dot{r}^2 + V_{eff} = E^2 \tag{4.96}$$

with the effective potential taking the form

$$V_{eff} = -\frac{(a^2E^2 - L_\phi^2)}{r^2} - \frac{2M}{r^3}(aE - L_\phi)^2 + \frac{Q^2}{r^4}(aE - L_\phi)^2 + \frac{\chi}{r^3}(aE - L_\phi)^2 \tag{4.97}$$

$$-(n^2 - 1)\left[E^2 + \frac{a^2E^2}{r^2} + a^2E^2\left(\frac{2M}{r^3} - \frac{Q^2}{r^4} - \frac{\chi}{r^3}\ln\frac{r}{|\chi|}\right)\right]. \tag{4.98}$$

The plots for the effective potential are shown below. Here we basically focus on the dependence of the effective potential on the plasma parameter k.

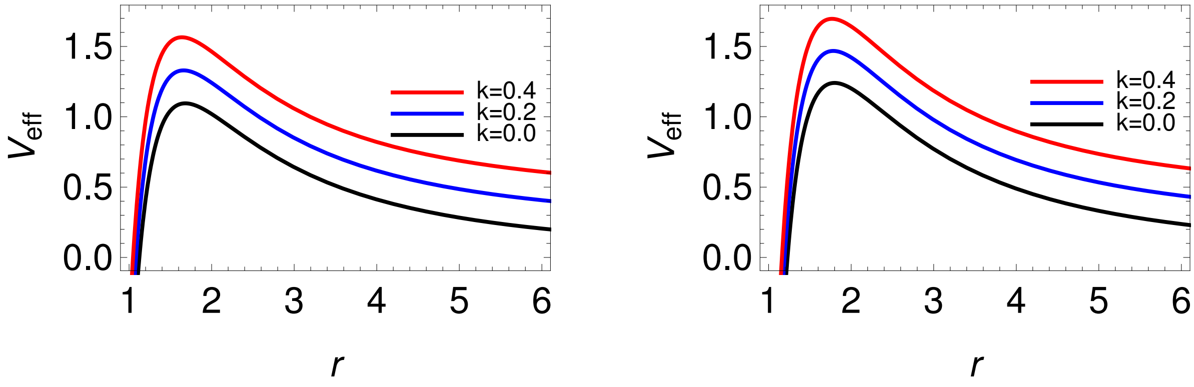

(a) a=0.5, $Q = 0.3$, $\chi = 0.2$, L_ϕ=3.0 (b) a=0.5, $Q = 0.3$, $\chi = 1.0$, L_ϕ=3.0

Figure 4.10: Variation of the effective potential (V_{eff}) for co-rotating photons with homogeneous plasma (n =constant= $\sqrt{1-k}$).

Fig.4.10 shows the effective potential (V_{eff}) encountered by the photons moving in co-rotating orbits. The plots are shown for varying values of homogeneous plasma parameter k. The left plot is shown for $\chi = 0.2$ and the right one for $\chi = 1.0$. The plots are shown by fixing various parameters as $M = 1$, $E = 1$, $a = 0.5$, $Q = 0.3$, L_ϕ=3.0. We find that with increase in plasma parameter k

the effective potential V_{eff} increases uniformly in both cases. The potential shows a maxima which corresponds to unstable photon orbits. The maxima in case of $\chi = 1.0$ are a little higher than that for $\chi = 0.2$. Also we find that the position of the maxima, which gives the unstable photon radius (r_p) slightly shifts towards left with increase in plasma parameter k.

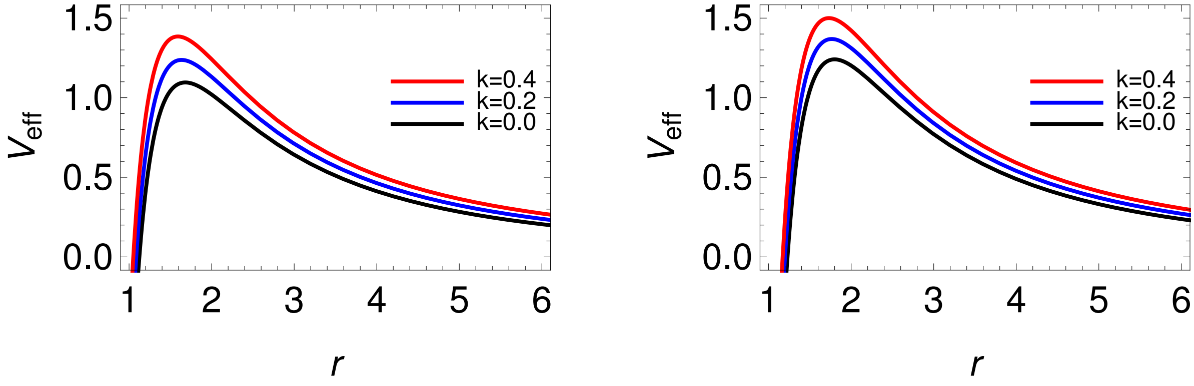

(a) a=0.5, $Q = 0.3$, $\chi = 0.2$, L_ϕ=3.0 (b) a=0.5, $Q = 0.3$, $\chi = 1.0$, L_ϕ=3.0

Figure 4.11: Variation of the effective potential (V_{eff}) for co-rotating photons with inhomogeneous plasma ($n = n(r) = \sqrt{1 - \frac{k}{r}}$).

Fig.4.11 shows the effective potential (V_{eff}) faced by the co-rotating photons with variation in plasma parameter k. The left plot is for $\chi = 0.2$ and the right one is for $\chi = 1.0$. We consider the plasma distribution to be inhomogeneous. The plots are shown by setting $M = 1$, $E = 1$, $a = 0.5$, $Q = 0.3$, L_ϕ=3.0. We find that with increase in plasma parameter (k), the effective potential V_{eff} increases uniformly in both the cases. The potential shows a maxima which corresponds to unstable photon orbits. The maxima in case of $\chi = 1.0$ are a little higher than the same for $\chi = 0.2$. Also we find that the position of the maxima shifts towards left with increase in plasma parameter k. This implies that the radius (r_p) of the unstable photon orbits decreases with increase in plasma parameter k, i.e., the orbits move close to the black hole.

The increment of effective potential in both the above cases for homogeneous and inhomogeneous plasma can be assigned to the fact that due to interaction of photons with plasma, the total energy and thereby the potential of the system increases. This can be seen by looking at the Hamiltonian ($\mathcal{H}$) which has an extra term due to plasma (eq.(4.5))

$$\begin{aligned} \mathcal{H}_{\mathcal{I}} &= -\frac{1}{2}(n^2 - 1)\left(p_0\sqrt{-g^{00}}\right)^2 \\ &= \frac{1}{2}\frac{k}{r^h}\left(p_0\sqrt{-g^{00}}\right)^2 \quad ; \quad n = \sqrt{1 - \frac{k}{r^h}}\ . \end{aligned} \tag{4.99}$$

Thus, with increase in plasma parameter k, the interaction energy increases. So by radial equation (4.96) for fixed r, we find that increase in energy increases the potential. Thus the potential of the system increases with increase in plasma parameter k.

The plots of V_{eff} shown in Fig.(4.12) displays both the co-rotating and counter rotating orbits. The co-rotating (prograde) orbits are characterised by $E > 0$ and $L_\phi > 0$ with respect to black hole spin $a > 0$ whereas the counter rotating (retrograde) orbits are characterised by $E > 0$ and $L_\phi < 0$. We observe that the unstable photon orbit radius of counter rotating orbits (r_{p2}) are greater than that of co-rotating orbits (r_{p1}) as can be seen from the maxima of the potential. This implies that the corotating orbits are near the black hole than the counter rotating ones.

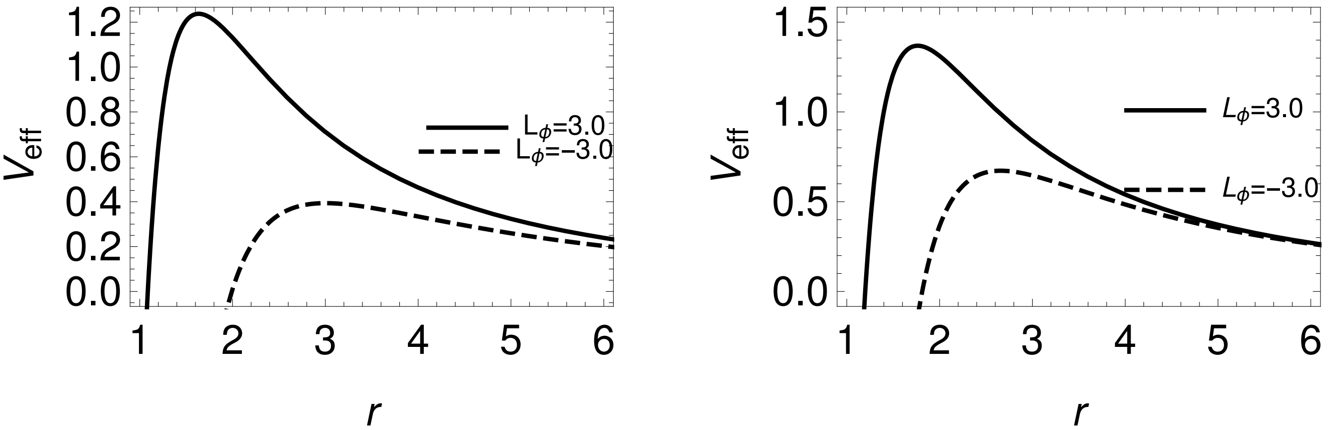

(a) a=0.5, $Q = 0.3$, $\chi = 0.2$, k=0.2

(b) a=0.5, $Q = 0.3$, $\chi = 1.0$, k=0.2

Figure 4.12: Variation of the effective potential (V_{eff}) in inhomogeneous plasma $\left(n = n(r) = \sqrt{1 - \frac{k}{r}}\right)$ for $L_\phi > 0$ and $L_\phi < 0$. The solid line corresponds to corotating and the dashed line corresponds to the counter rotating orbit.

4.7 Shadow radius R_s and constraints from the M87* observational data

In this section, we compute the black hole shadow radius R_s following the approach prescribed in [199]. The aproach considers a reference circle as shown in Fig.4.13 to calculate the shadow radius R_s. Geometrically the radius R_s of the black hole shadow can be written in terms of the celestial coordinates as [199]

$$R_s = \frac{(\alpha_t - \alpha_r)^2 + \beta_t^2}{2|\alpha_r - \alpha_t|} \tag{4.100}$$

where the silhouette of the shadow coincides with the reference circle at three different coordinates, the top point (α_t, β_t), the bottom point (α_b, β_b) and the right point $(\alpha_r, 0)$. It is to be noted that the shadow radius R_s is related to the angular diameter θ_d of the shadow as [153]

$$\theta_d = 2\frac{R_s}{d} \tag{4.101}$$

where d is the distance of $M87^*$ black hole from earth ($d = 16.8$ Mpc). The observations conducted by the EHT collaboration have obtained the value of θ_d to be 42 ± 3 μas which in radian becomes $(0.20325 \pm 0.0146) \times 10^{-9}$ rad [9]. Our main aim here is to constrain the PFDM parameter ($\frac{\chi}{M}$) and the plasma parameter (k) by comparing the theoretically calculated values of θ_d with the observational data. In the subsequent analysis, we set the charge $\frac{Q}{M}$ of the black hole to zero (that is $\frac{Q}{M} = 0$) for the sake of simplicity.

At first, we consider the Kerr limit ($\frac{\chi}{M} \to 0, k \to 0, \frac{Q}{M} \to 0$) of the black hole solution. We observe that by varying of the black hole spin $\frac{a}{M} \in [0, 1]$, the angular diameter θ_d of the shadow is obtained to be $\theta_d \in [0.1925 \times 10^{-9}, 0.1929 \times 10^{-9}]$ (in radian). This implies that all possible values of the black hole spin $\frac{a}{M}$ produces an angular diameter (θ_d) which are compatible with observational results.

Then we incorporate a homogeneous plasma background ($h = 0$) by setting $\frac{Q}{M} = 0$, $\frac{\chi}{M} = 0$. Here we

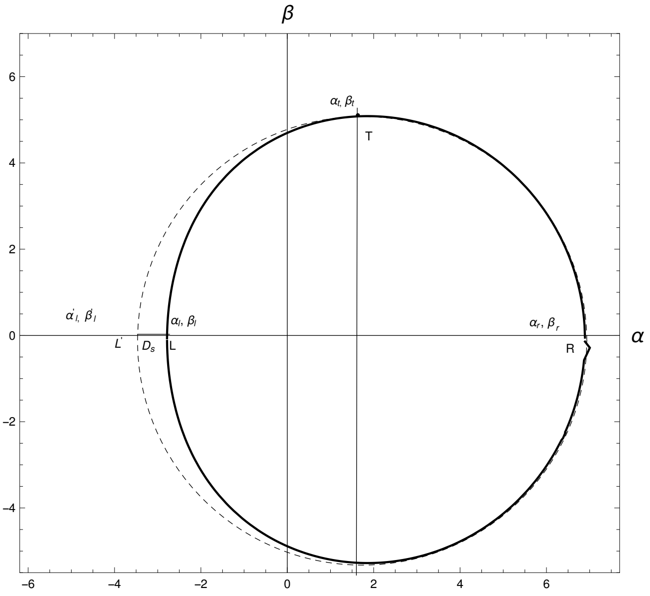

Figure 4.13: Geometrical representation of the shadow of a black hole.

try to constrain the value of the plasma parameter k for different values of spin $\frac{a}{M}$. We obtain the range of k compatible with the observational value of shadow size $\theta_d \in (0.20325 \pm 0.0146) \times 10^{-9}$ radian. The results are tabulated below in Table 4.3. Table 4.3 shows that with increase in the value of the black hole spin $\frac{a}{M}$, the allowed range for plasma parameter k decreases. Further, our analysis revealed that when we consider the inhomogeneous plasma background ($h = 1$), the resulting value of θ_d lies outside the estimated range of θ_d. This is true for each and every value of the spin parameter $\frac{a}{M}$.

$\frac{a}{M}$	k_{lower}	k_{upper}
0.1	0.0	0.976
0.2	0.0	0.909
0.3	0.0	0.805
0.4	0.0	0.677
0.5	0.0	0.536
0.6	0.0	0.396
0.7	0.0	0.266
0.8	0.0	0.154
0.9	0.0	0.067
1.0	0.0	0.020

Table 4.3: The results show the upper bound on the value of the plasma parameter k ($0 \leq k \leq k_{upper}$) at fixed value of the spin parameter compatible with observation.

Next we consider the PFDM black hole solution (with $\frac{Q}{M} \to 0$) in a homogeneous plasma background. Table(4.4) shows the allowed range of values of the PFDM parameter which is $\frac{\chi}{M} \in [0, 0.025]$. We also observe the allowed range of values for k corresponding to fixed values of $\frac{\chi}{M}$.

Then we consider the general case of plasma frequency $\omega_p(r, \theta)$. The frequency takes the form $\omega_p^2(r, \theta) = \frac{f_r(r)+f_\theta(\theta)}{r^2+a^2\cos^2\theta}$. We want to obtain the range of values of the PFDM parameter ($\frac{\chi}{M}$) compatible to that of the plasma parameter $\left(\frac{\omega_c}{\omega_0}\right)^2$ using the observed value of angular shadow (θ_d). We consider

$\frac{\chi}{M}$	k_{lower}	k_{upper}
0.010	0.000	0.904
0.015	0.000	0.903
0.020	0.770	0.901
0.025	0.875	0.899

Table 4.4: The results show the lower and upper value of the plasma parameter k at fixed value of the spin parameter, in presence of the PFDM parameter.

the two cases studied in section 4.4.1. The first one is $f_r(r) = \omega_c^2\sqrt{r}$ and $f_\theta(\theta) = 0$ and the second one is $f_r(r) = 0$ and $f_\theta(\theta) = \omega_c^2(1 + 2\sin^2\theta)$. The Tables below show the corresponding ranges of $\frac{\chi}{M}$ compatible with the ranges of $\left(\frac{\omega_c}{\omega_0}\right)^2$.

$\frac{\chi}{M}$	$\left(\frac{\omega_c}{\omega_0}\right)^2_{lower}$	$\left(\frac{\omega_c}{\omega_0}\right)^2_{upper}$
0.001	0.0	0.489
0.002	0.0	0.387
0.003	0.0	0.293
0.004	0.0	0.205
0.005	0.0	0.121
0.006	0.0	0.039

Table 4.5: Table showing the accessible range of $\left(\frac{\omega_c}{\omega_0}\right)^2$ with $f_r(r) = \omega_c^2\sqrt{r}$ and $f_\theta(\theta) = 0$ for various values of $\frac{\chi}{M}$. The results are shown at fixed value of the spin parameter ($\frac{a}{M} = 0.5$).

$\frac{\chi}{M}$	$\left(\frac{\omega_c}{\omega_0}\right)^2_{lower}$	$\left(\frac{\omega_c}{\omega_0}\right)^2_{upper}$
0.001	0.0	0.282
0.002	0.0	0.223
0.003	0.0	0.168
0.004	0.0	0.117
0.005	0.0	0.069
0.006	0.0	0.022

Table 4.6: Table showing the accessible range $\left(\frac{\omega_c}{\omega_0}\right)^2$ with $f_r(r) = 0$ and $f_\theta(\theta) = \omega_c^2(1 + 2\sin^2\theta)$ for various values of $\frac{\chi}{M}$. The results are shown at fixed value of the spin parameter ($\frac{a}{M} = 0.5$).

Tables 4.5 and 4.6 reveal that the allowed range of the PFDM parameter ($\frac{\chi}{M}$) is $\frac{\chi}{M} \in [0, 0.006]$. This entails the presence of a very small amount of dark matter in the vicinity of the black hole. Also the Tables show that dark matter and plasma can coexist as depicted from the observational range of black hole shadow θ_d. Also, we find that with the increase in PFDM parameter $\frac{\chi}{M}$ from 0 to 0.006 the allowed range of plasma parameter $\left(\frac{\omega_c}{\omega_0}\right)^2$ gradually decreases and vanishes from $\frac{\chi}{M} = 0.007$.

4.8 Summary

In this work we considered a rotating charged black hole surrounded by perfect fluid dark matter (PFDM). We also immerse the system in a plasma background having no interaction with dark matter.

We observe some unique characteristics of the black hole spacetime due to presence of PFDM which we have discussed throroughly in the last chapter. Here we analysed the motion of null particles around the black hole. We mainly focussed on analysing the impact of plasma on the trajectories of null particles. The null particles can either rotate along the spin of the black hole (co-rotating) or reverse (counter rotating). We observed that those co-rotating orbits lie close to the black hole whereas, the counter rotating ones remain comparatively far from the black hole. We found that the effect of plasma is independent of the influence of dark matter. We observed that in case of homogeneous plasma distribution, the radius of co-rotating orbits decrease whereas that for the counter rotating orbits increase with increment in plasma parameter k. On the other hand, in case of inhomogeneous plasma distribution, we found that increase in k decreases the photon radius for both types of orbits.

Then we analyse and study the unstable circular null geodesics which are responsible for the formation of the black hole shadow. Using the geodesic equation(s), we obtain the celestial coordinates (α, β). These two coordinates give the black hole shadow radius (R_s) as $R_s^2 = \alpha^2 + \beta^2$. The shadow gets formed in the celestial plane ($\alpha - \beta$ plane). We graphically represent the shadow and analyse in detail the dependence of the black hole shadow on the black hole parameters (a, Q, χ, k).

The plots reveal that the shadow gets rotated and deformed with increase in black hole spin (a). The deformation of black hole shadow occurs due to the rotational drag of the unstable photons by the motion of the black hole. The plots alos depict that with increase in charge (Q), the radius (R_s) and thereby the size of the black hole shadow reduces. The reason for this is quite obvious. The black hole shadow depends on the size of the outer event horizon of the black hole. The radius of outer event horizon is given as $r_{h+} = M + \sqrt{M^2 - Q^2}$ in absence of χ and k. With increase in Q, r_{h+} decreases and thereby R_s decreases. This ultimately reduces the size of the black hole shadow.

Next we analyse the effect of the plasma medium on the black hole shadow. The shadow is formed by the light rays encircling the black hole in unstable photon orbits. When the light rays move through plasma media, they get deviated from their original path due to variation in frequency (which depends on the medium). We considered the general case where the refractive index ($n(r,\theta)$) and plasma frequency ($\omega_p(r,\theta)$) both depends on r and θ. We found that with only radial variation $f_r(r) = \omega_c^2\sqrt{M^3 r}$ and $f_\theta(\theta) = 0$, the shadow plots reduce in size with increase in plasma parameter ω_c. Similar nature is observed in case of θ variation with $f_r(r) = 0$ and $f_\theta(\theta) = \omega_c^2 M^2\Big(1 + 2\sin^2\theta\Big)$ with the shadow size decreasing with increase in plasma parameter ω_c.

Next we consider cases where the plasma frequency is only r dependent. The refractive index in those cases take the form $\left(n = \sqrt{1 - \frac{k}{r}}\right)$ (inhomogeneous) and $\left(n = \sqrt{1-k}\right)$ (homogeneous). From the plots, we find that the extreme right of α axis corresponds to the radius of counter rotating orbits (r_{p2}) whereas that on the extreme left corresponds to the co-rotating orbits (r_{p1}). The variation of the radius of these orbits with plasma gets reflected in the black hole shadow. In particular, we observe that r_{p1} decreases with increase in the plasma parameter for fixed value of the PFDM parameter both for inhomogeneous and homogeneous plasma. However, r_{p2} decreases with increment in the plasma parameter (k) for a fixed PFDM parameter (χ) for inhomogeneous plasma, and increases for homogeneous plasma.

We have also analysed the effective potential (V_{eff}) and have found that it significantly depends on the plasma parameter (k). The maxima of the potential (V_{eff}) corresponds to the radius of the unstable photon orbits. The maxima's shift towards left both for homogeneous and inhomogeneous plasma distribution. We also find that the peak of the effective potential increases with increase in the plasma parameter k. The reason for such an increment can be related to the fact that due to plasma, the interaction energy of the total system increases and hence the potential (V_{eff}) of the system increases.

Finally, we compute the shadow radius R_s and the angular shadow size θ_d. From our theoretical results, we constrained the plasma parameter k as well as $\left(\frac{\omega_c}{\omega_0}\right)^2$ with the PFDM parameter $\frac{\chi}{M}$ by comparing the obtained values of θ_d with that observed from the $M87^*$ supermassive black hole data.

Chapter 5

Black holes in an expanding universe

5.1 Introduction

It is a well-known fact that our universe is undergoing an accelerating expansion [200], [201]. Thus any two objects in the universe must be moving away from each other. The effect is either less pronounced or superseded by gravitational attraction for nearby objects yet the effect persists. Hence it is quite instructive to incorporate cosmic expansion in case of any analysis of astrophysical systems. In this thesis, we have studied black holes and various astrophysical aspects associated with it. So consideration of cosmic expansion while studying black holes is quite realistic. In this work we are interested in studying black hole shadow and the expansion of the universe must readily effect the shadow size. Again it has been found that the size of any arbitrary object increases due to cosmological expansion [202], [203].

The above discussion motivates us to consider a black hole system which includes the cosmological expansion. The criteria the system needs to satisfy is that, it must be Schwarzschild-like close to the black hole and as we move further away the solution must boil down to the FLRW metric. The first of such model was considered by Einstein and Strauss in [204]. In this model, the geodesics are calculated in different regions and are matched at a specific radius, namely the Schücking radius [205]. Another solution was proposed by McVittie in [206] where the solution efficiently interpolates between the near and far regions. Also, it satisfies the criteria of being Schwarzschild-like at closer distances and FLRW like at far distances. However the geodesics are not completely integrable analytically[1]. Thus for analytical calculations, we need metrics which have sufficient constants of motion and the equations become completely integrable.

One special solution which has these properties is the Schwarzschild de-Sitter or Kottler black hole [207]. The Kottler metric is the solution of Einstein's field equation with a positive cosmological constant $\Lambda > 0$. Here the system basically describes a Schwarzschild black hole being embedded in a de-Sitter universe. In this case, the geodesics are completely integrable analytical calculations can be readily performed. Besides a general transformation as proposed in [208] can transform the Kottler metric to the FLRW metric where the expansion is driven by the cosmological constant Λ. Some recent works related to the case of expanding universe can be found in [93], [209]-[215].

Another thing which we discussed in the earlier chapters is that the black hole in general is found to be surrounded by material medium. The material around a black hole is at a very high temperature

---

[1] We are primarily interested in analytical calculation.

due to the immense gravitational field of the black hole. The nature of this material medium suggests that one can treat it like a highly dense plasma. In this chapter, we aim to study black hole shadow in presence of plasma as viewed by both static and co-moving observer [93]. We would like to study the impact of cosmological constant Λ as well as the plasma parameter k on the photon sphere as well as black hole shadow from the point of view of a co-moving observer who is moving away from the black hole due to cosmic expansion. We try to constraint the value of the plasma parameter on the basis of the observational results of M87* [9] and Sgr A* [58] black holes. Though it is known that almost all objects in the universe are rotating, so are the black holes. Yet our analysis carried out for non-rotating black hole can give us crude results which will help us get some insight into the plasma medium around the black hole. This chapter is based on our work [163].

5.2 Black hole shadow in presence of plasma

In this section, we discuss the analysis of the angular size of the shadow of a black hole in presence of plasma. The analysis is true for any arbitrary lapse function $f(r)$ with the metric given as

$$ds^2 = -f(r)dt^2 + \frac{dr^2}{f(r)} + r^2 d\theta^2 + r^2 \sin^2\theta d\phi^2 \ . \tag{5.1}$$

The black hole shadow is formed by the photons that encircle the black hole moving along unstable orbits. To determine the shadow size, we need to calculate the null geodesics using a Lagrangian ($\mathcal{L}$) or Hamiltonian ($\mathcal{H}$) as mentioned previously. Due to spherical symmetry, all planes are identical, so we fix the plane of choice as $\theta = \frac{\pi}{2}$. Thus the geodesic equation corresponding to θ becomes $\theta = \frac{\pi}{2}$ =constant or $\dot{\theta} = 0$. Then we calculate the other geodesics for t, ϕ and r using the Hamilton's equation of motion which are given as

$$\dot{x}^\mu = \frac{\partial \mathcal{H}}{\partial p_\mu} \ ; \ \dot{p}_\mu = -\frac{\partial \mathcal{H}}{\partial x^\mu} \ . \tag{5.2}$$

We continue our discussion further by considering a plasma background. The plasma medium can be either magnetised or non-magnetised. Consideration of magnetised plasma will resist us from performing a detailed analytical study and we need to take help of numerical methods. So for analytically studying the system under consideration, we consider cold, dust-like (having pressure $P = 0$) and non-magnetised plasma medium which corresponds to a Hamiltonian ($\mathcal{H}$) of the form [103]

$$\mathcal{H} = \frac{1}{2}\left[g^{\mu\nu}p_\mu p_\nu + \omega_p^2\right] \ . \tag{5.3}$$

Here, ω_p represents the electron plasma frequency. The refractive index (n) of the plasma medium depends on the plasma frequency ω_p as well as the photon frequency ω (as measured by any arbitrary observer) and are related as [104]

$$n^2 = 1 - \left(\frac{\omega_p}{\omega}\right)^2 \ ; \ \omega = \frac{\omega_0}{\sqrt{-g_{00}}} \tag{5.4}$$

where the second relation in equation (5.4) provides the gravitational redshift with ω_0 giving the frequency of photons as measured by a stationary observer at infinity. Since the metric given in eq.(5.1) is diagonal so its inverse can be readily computed. We can write

$$\omega = \frac{\omega_0}{\sqrt{-g_{00}}} \quad \Rightarrow \quad \hbar\omega = \frac{\hbar\omega_0}{\sqrt{-g_{00}}} \quad \Rightarrow \quad \hbar\omega = \frac{E_0}{\sqrt{-g_{00}}} \quad \Rightarrow \quad \hbar\omega = \frac{p_0}{\sqrt{-g_{00}}} \quad \Rightarrow \quad \hbar\omega = p_0\sqrt{-g^{00}} \ . \tag{5.5}$$

For $\hbar = 1$, we have $\omega = p_0\sqrt{-g^{00}}$. Using this relation and eq.(5.4) in eq.(5.3), we have

$$\mathcal{H} = \frac{1}{2}\left[g^{\mu\nu}p_\mu p_\nu + (n^2-1)g^{00}p_0^2\right] . \tag{5.6}$$

The Hamiltonian can be recast as

$$\mathcal{H} = \frac{1}{2}\left[n^2 g^{00}p_0^2 + g^{ij}p_i p_j\right] \tag{5.7}$$

where i, j runs from 1 to 3 which corresponds to the spatial coordinates. The metric and hence the Hamiltonian $\mathcal{H}$ is independent of t and ϕ. Using the Hamilton's equation of motion $\dot{p}_\mu = -\frac{\partial \mathcal{H}}{\partial x^\mu}$ and using the fact that $\omega_p = \omega_p(r)$, we get the constants of motion as p_0 =constant= $-E$ and p_3 =constant= L. Here E and L correspond to the energy and angular momentum of photons as measured by an observer stationed at infinity. Using the Hamilton's equation of motion given in eq.(5.2), we get the geodesics for t, ϕ and r as

$$\frac{dt}{d\lambda} = \frac{n^2 E}{f(r)} \tag{5.8}$$

$$\frac{d\phi}{d\lambda} = \frac{L}{r^2} \tag{5.9}$$

$$\left(\frac{dr}{d\lambda}\right)^2 = n^2E^2 - \frac{L^2}{r^2}f(r) \ . \tag{5.10}$$

Here λ denotes to the affine parameter which parametrises the trajectory of photons. Taking the ratio of eq.(s)(5.10) and (5.9), we obtain

$$\left(\frac{dr}{d\phi}\right)^2 = r^4\left[\frac{n^2E^2}{L^2} - \frac{f(r)}{r^2}\right] . \tag{5.11}$$

The above equation (5.11) is independent of time coordinate t (implying the solution being time independent as we have considered in eq.(5.1)) and also of θ (since we are interested in geodesics fixed to the equatorial plane). The equation depends on the radial coordinate r and the refractive index of plasma n and some constants of motion which are fixed for specific photons. The solution of the above equation gives the trajectory of photons in the equatorial plane and the solution can be represented as $r = r(\phi)$. This equation (5.11) can be used to evaluate the unstable circular orbits of photons moving in the equatorial plane. The conditions take the form $\frac{dr}{d\phi} = \frac{d^2r}{d\phi^2} = 0$.

Using the first condition, we obtain a constraint relation among the constants of motion (E, L) in terms of the photon orbit radius r_p. On the other hand, the second condition gives an equation in terms of spacetime parameters which can be solved to obtain the photon orbit radius r_p. The conditions take the following form

$$\frac{n^2 r^2}{f(r)}\bigg|_{r=r_p} = \frac{L^2}{E^2} \tag{5.12}$$

$$\Big(2n'rf(r) + 2nf(r) - nrf'(r)\Big)\bigg|_{r=r_p} = 0\ . \tag{5.13}$$

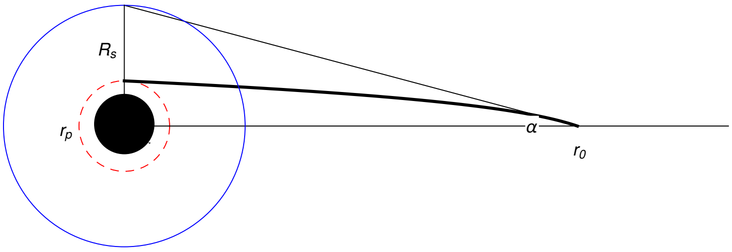

Figure 5.1: Pictorial representation of the event horizon, photon sphere and the shadow radius [163].

The second equation is used to determine r_p for fixed values of spacetime parameters and the refractive index n.

Now we wish to calculate the angular size of the black hole shadow. For this we require a detailed description of the plasma under consideration. Also we would require the conditions eq.(5.12) obtained above. A ray of light from the background source upon getting deflected due to the immense gravitational pull of the black hole, makes an angle α with respect to the observer's position r_0 as given in Fig.5.1. We observe that Fig.5.1 shows a dark disk which represents the black hole being surrounded by photon ring (shown in dotted red colour) situated at the distance $r = r_p$. Light from photon sphere (ring) travels in curved trajectory and reaches the observer making an angle α where the tangent gives the measured position of the light ray. If we consider all rays at the boundary of the cone of angle α, it forms the shadow boundary with radius R_s greater than r_p, that is $R_s > r_p > r_{h+}$. In the study, we consider a radial plasma distribution such that the refractive index n is a function of r only. Also, n' which is given as $n' = \frac{dn}{dr}$ corresponds to the derivative of n with respect to r. In order to carry out calculations explicitly, we need to assume a certain form of the refractive index (n) and thereby of the plasma frequency (ω_p). Keeping this in mind, we consider the following form for the plasma frequency[2] [104]

$$\omega_p(r)^2 = \frac{4\pi e^2}{m_e} N(r)\ \ ;\ \ N(r) = N_0 \Big(\frac{r_0}{r}\Big)^h \tag{5.14}$$

where e and m_e represents the electronic charge and mass, $N(r)$ gives the number density of electrons in the plasma medium and N_0 is a constant. Substituting the above relation in the expression of

---

[2] It is to be noted that as we are working with an axially symmetric black hole and so it is justified to assume the form of ω_p as $\omega_p^2 = \frac{f(r)}{r^h}$. However, for a rotating black hole one needs to consider the form of ω_p as $\omega_p^2 = \frac{f(r)+f(\theta)}{r^2+a^2\cos\theta}$ as shown in [157].

refractive index n in eq.(5.4), we get

$$n(r)^2 = 1 - f(r)\frac{k}{r^h} \quad ; \quad k = \frac{4\pi e^2}{m_e \omega_0^2} N_0 r_0^h \ . \tag{5.15}$$

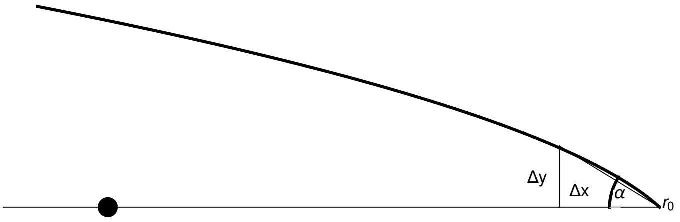

Figure 5.2: Light travelling into past from observer (r_0) making angle α [163].

With the above details in hand, we try to calculate the angular size of the black hole shadow in presence of plasma. In Fig.5.2 we find that the ray of light makes an angle α with the radial line that satisfies

$$\tan\alpha = \lim_{\Delta x \to 0} \frac{\Delta y}{\Delta x} \ . \tag{5.16}$$

From our metric we find that in the desired limit, the angular size becomes

$$\tan\alpha = \sqrt{\frac{f(r)}{r^2 \frac{n(r)^2 E^2}{L^2} - f(r)}}\Bigg|_{r=r_o} \tag{5.17}$$

where r_o is the position of the observer. The angular size of the black hole shadow in terms of $\sin\alpha$ is of the form

$$\sin^2\alpha_{sp} = \frac{f(r)}{r^2 \frac{n(r)^2 E^2}{L^2}}\Bigg|_{r=r_o} = \frac{z(r_p)^2}{z(r_0)^2} \quad ; \quad z(r)^2 = \frac{n(r)^2 r^2}{f(r)} \ . \tag{5.18}$$

5.3 Shadow of black hole with a positive cosmological constant in plasma

In this section, we consider a system having a positive cosmological constant Λ. The positive cosmological constant ($\Lambda > 0$) modifies certain characteristics of the spacetime. First of all, it introduces an additional horizon, namely, the cosmological horizon (r_C). The cosmological horizon constraints the observers existence within a certain region that is from the event horizon r_{h+} to cosmological horizon r_C ($r_{h+} < r_0 < r_C$). The interesting thing we can observe is that the photon sphere radius r_p remains unchanged implying no effect of cosmological constant Λ [93]. However the angular shadow size not only depends on the photon sphere radius r_p but also explicitly depends on the spacetime geometry (the lapse function) of the black hole and other additive features. This implies that the shadow size might can effected due to incorporation of Λ in the system.

In this work, we study a specific system namely, the Schwarzschild de-Sitter black hole or the Kottler black hole. We refrain from incorporating other matter fields into the system for simplicity. The metric of a Kottler black hole takes the form

$$ds^2 = -\Big(1 - \frac{2M}{r} - \frac{\Lambda}{3}r^2\Big)dt^2 + \frac{dr^2}{\Big(1 - \frac{2M}{r} - \frac{\Lambda}{3}r^2\Big)} + r^2 d\theta^2 + r^2 \sin^2\theta d\phi^2 \tag{5.19}$$

with the cosmological constant Λ related to the Hubble's constant H_0 as $\frac{\Lambda}{3} = \frac{H_0^2}{c^2}$. Analysing the lapse function $f(r)$ we find that the horizons lie in the range $2M < r_{h+} < 3M$, $3M < r_C < \infty$ and $\bar{r} < 0$. Here, r_{h+}, r_C and $\bar{r}$ respectively give the event horizon, cosmological horizon and the additional horizon which is unphysical. Also setting $f(r) = 0$ provides us a cubic equation of the form

$$r^3 - \frac{3}{\Lambda}r + \frac{6M}{\Lambda} = 0 \tag{5.20}$$

The requirement of real solution of eq.(5.20) constraints Λ as $0 < \Lambda < \frac{1}{9M^2}$. The geodesics evaluated at the equatorial plane ($\theta = \frac{\pi}{2}$) incorporating plasma for t, ϕ and r in case of Kottler black hole takes the form

$$\frac{dt}{d\lambda} = \frac{n^2 E}{f(r)} = \frac{n^2 E}{\Big(1 - \frac{2M}{r} - \frac{\Lambda}{3}r^2\Big)} \tag{5.21}$$

$$\frac{d\phi}{d\lambda} = \frac{L}{r^2} \tag{5.22}$$

$$\Big(\frac{dr}{d\lambda}\Big)^2 = n^2E^2 - \frac{L^2}{r^2}f(r) = n^2E^2 - \frac{L^2}{r^2}\Big(1 - \frac{2M}{r} - \frac{\Lambda}{3}r^2\Big)\ . \tag{5.23}$$

The condition for unstable circular null geodesics gives the photon sphere radius r_p and also gives a condition on the constants E, L and Λ.

$$\frac{L^2}{E^2} = \frac{n^2 r^2}{f(r)}\Bigg|_{r=r_p} \tag{5.24}$$

which simplifies to

$$\frac{E^2}{L^2} = \frac{1}{27M^2} - \frac{\Lambda}{3} \tag{5.25}$$

for $n = 1$ [93]. The angular size of the black hole shadow in presence of plasma takes the form

$$\sin^2\tilde{\alpha}_{sp} = \frac{z(r_p)^2}{z(r_0)^2} = \frac{n(r_p)^2}{n(r_0)^2}\frac{r_p^2}{r_0^2}\frac{\Big(1 - \frac{2M}{r_0} - \frac{\Lambda}{3}r_0^2\Big)}{\Big(1 - \frac{2M}{r_p} - \frac{\Lambda}{3}r_p^2\Big)}. \tag{5.26}$$

The general equation for deriving the photon sphere radius r_p for static spherically symmetric metric with cosmological constant Λ surrounded by plasma medium with refractive index n is given as

$$\Big(2n'(r)rf(r) + 2n(r)f(r) - n(r)rf'(r)\Big)\Bigg|_{r=r_p} = 0\ . \tag{5.27}$$

Let us solve try to solve the equation for different cases.

5.3.1 Analysis without plasma

In the first case we consider *Schwarzschild de Sitter metric or Kottler metric without plasma.* The lapse function is of the form

$$f(r) = 1 - \frac{2M}{r} - \frac{\Lambda}{3}r^2 \tag{5.28}$$

and the corresponding derivative with respect to radial coordinate r is

$$f'(r) = \frac{df}{dr} = \frac{2M}{r^2} - \frac{2\Lambda}{3}r \ . \tag{5.29}$$

Due to absence of plasma, the refractive index has the value $n(r) = 1$ and the derivative of n with respect to r gives $n'(r) = 0$. Replacing all the parameters in eq.(5.27), we obtain

$$2\Big(1 - \frac{2M}{r_p} - \frac{\Lambda}{3}r_p^2\Big) - r_p\Big(\frac{2M}{r_p^2} - \frac{2\Lambda}{3}r_p\Big) = 0 \ . \tag{5.30}$$

The solution of the above equation gives $r_p = 3M$ which is independent of the cosmological constant Λ. So we find that the photon sphere radius r_p is not effected by the presence of cosmological constant Λ in the metric. The corresponding angular shadow size takes the form

$$\sin^2\tilde{\alpha}_s = \frac{r_p^2}{r_0^2}\frac{\left(1 - \frac{2M}{r_0} - \frac{\Lambda}{3}r_0^2\right)}{\left(1 - \frac{2M}{r_p} - \frac{\Lambda}{3}r_p^2\right)} = \frac{\left(1 - \frac{2M}{r_0} - \frac{\Lambda}{3}r_0^2\right)}{r_0^2\left(\frac{1}{27M^2} - \frac{\Lambda}{3}\right)} \ . \tag{5.31}$$

5.3.2 Homogeneous plasma

In the second case, we consider *Schwarzschild de Sitter or Kottler metric surrounded by a homogeneous plasma media.* The refractive index of homogeneous plasma is of the form [216], [217]

$$n(r) = \sqrt{1 - kf(r)} \tag{5.32}$$

and the corresponding derivative

$$n'(r) = -\frac{1}{\sqrt{1 - kf(r)}}k\left(\frac{M}{r^2} - \frac{\Lambda}{3}r^2\right) \ . \tag{5.33}$$

Using n and n' respectively from eq.(5.32) and (5.33) in eq.(5.27), we get

$$\frac{k\Lambda^2}{9}r_p^6 - \frac{2}{3}\Lambda k r_p^4 + \frac{4k\Lambda M}{3}r_p^3 - (1-k)r_p^2 - (4k-3)Mr_p + 4kM^2 = 0. \tag{5.34}$$

The above equation is of sixth order. The first three terms in the above equation (5.34) have both k and Λ. So, in presence of plasma, the cosmological constant Λ must effect the photon sphere radius r_p. Thus the solution r_p must be a function of k and Λ. In the limit of $k \to 0$, the effect of the cosmological constnat Λ vanishes. Thus we get back the photon sphere radius r_p as 3M. The angular shadow size becomes

$$\sin^2\tilde{\alpha}_{sp} = \frac{n(r_p)^2}{n(r_0)^2}\frac{r_p^2}{r_0^2}\frac{\left(1-\frac{2M}{r_0}-\frac{\Lambda}{3}r_0^2\right)}{\left(1-\frac{2M}{r_p}-\frac{\Lambda}{3}r_p^2\right)} = \frac{\left(1-k\left(1-\frac{2M}{r_p}-\frac{\Lambda}{3}r_p^2\right)\right)}{\left(1-k\left(1-\frac{2M}{r_0}-\frac{\Lambda}{3}r_0^2\right)\right)}\frac{r_p^2}{r_0^2}\frac{\left(1-\frac{2M}{r_0}-\frac{\Lambda}{3}r_0^2\right)}{\left(1-\frac{2M}{r_p}-\frac{\Lambda}{3}r_p^2\right)}. \tag{5.35}$$

5.3.3 Inhomogeneous plasma

In the last case, we consider *Schwarzschild de Sitter or Kottler metric embedded in an inhomogeneous plasma background.* The refractive index of the inhomogeneous plasma takes the form [216], [217]

$$n(r) = \sqrt{1-\frac{k}{r}f(r)} \tag{5.36}$$

and the corresponding derivative of n with respect to r is

$$n'(r) = \frac{1}{2\sqrt{1-\frac{k}{r}f(r)}}\left(\frac{k}{r^2}-\frac{2kM}{r^3}-\frac{\Lambda k}{3}-\frac{2kM}{r^3}+\frac{2}{3}k\Lambda\right). \tag{5.37}$$

Using the values of n and n' respectively from eq.(s) (5.36) and (5.37) in eq.(5.27), we get after some simplification

$$\frac{k\Lambda^2}{9}r_p^6-\frac{2}{3}\Lambda k r_p^4+\left(\frac{4k\Lambda M}{3}-2\right)r_p^3+(6M+k)r_p^2-4kr_pM+4kM^2=0. \tag{5.38}$$

The above equation is of sixth order. Just like the case of homogeneous plasma, here also the first three terms in eq.(5.38) depend on both plasma parameter k and cosmological constnat Λ. Thus, the solution of the above equation gives r_p which is a function of k and Λ. In the limit of $k\to 0$, we get back the photon sphere radius r_p as 3M. The angular size of the black hole shadow takes the form

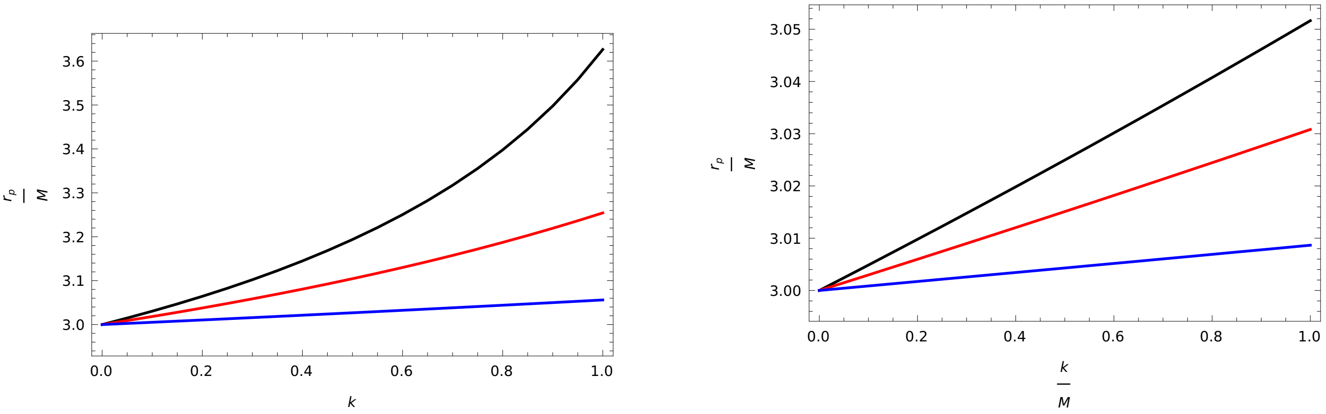

(a) Variation of photon radius $\frac{r_p}{M}$ with homogeneous plasma k.

(b) Variation of photon radius $\frac{r_p}{M}$ with inhomogeneous plasma $\frac{k}{M}$.

Figure 5.3: Graphical representation of photon sphere radius $\frac{r_p}{M}$ with plasma parameter. The plots are shown for cosmological constant (ΛM^2) values - 0.0075 (black), 0.0300 (red) and 0.0675 (blue).

$$\sin^2\tilde{\alpha}_{sp} = \frac{n(r_p)^2}{n(r_0)^2}\frac{r_p^2}{r_0^2}\frac{\left(1-\frac{2M}{r_0}-\frac{\Lambda}{3}r_0^2\right)}{\left(1-\frac{2M}{r_p}-\frac{\Lambda}{3}r_p^2\right)} = \frac{\left(1-\frac{k}{r_p}\left(1-\frac{2M}{r_p}-\frac{\Lambda}{3}r_p^2\right)\right)}{\left(1-\frac{k}{r_0}\left(1-\frac{2M}{r_0}-\frac{\Lambda}{3}r_0^2\right)\right)}\frac{r_p^2}{r_0^2}\frac{\left(1-\frac{2M}{r_0}-\frac{\Lambda}{3}r_0^2\right)}{\left(1-\frac{2M}{r_p}-\frac{\Lambda}{3}r_p^2\right)}. \tag{5.39}$$

In Fig.5.3, we have graphical shown the variation of the photon sphere radius r_p with increase in the plasma parameter. The left plot Fig.5.3 is for homogeneous plasma distribution and the right one is for the inhomogeneous plasma distribution. Both the plots reveal that with increment in the plasma parameter the photon sphere radius r_p increases. The effect is more pronounced in case of homogeneous plasma compared to the inhomogeneous case. Also, we have shown three plots in each case considering three different values of the cosmological constant Λ. We find that increment in the cosmological constant decreases the photon radius for fixed values of the plasma parameter. Again, we also observe that all the plots start from the same common point at $k = 0$ which corresponds to the case of absence of plasma in the background. In that case, the effect of cosmological constant also vanishes reducing the value of r_p to 3M. This observation can also be verified from eq.(s) (5.34) and (5.38).

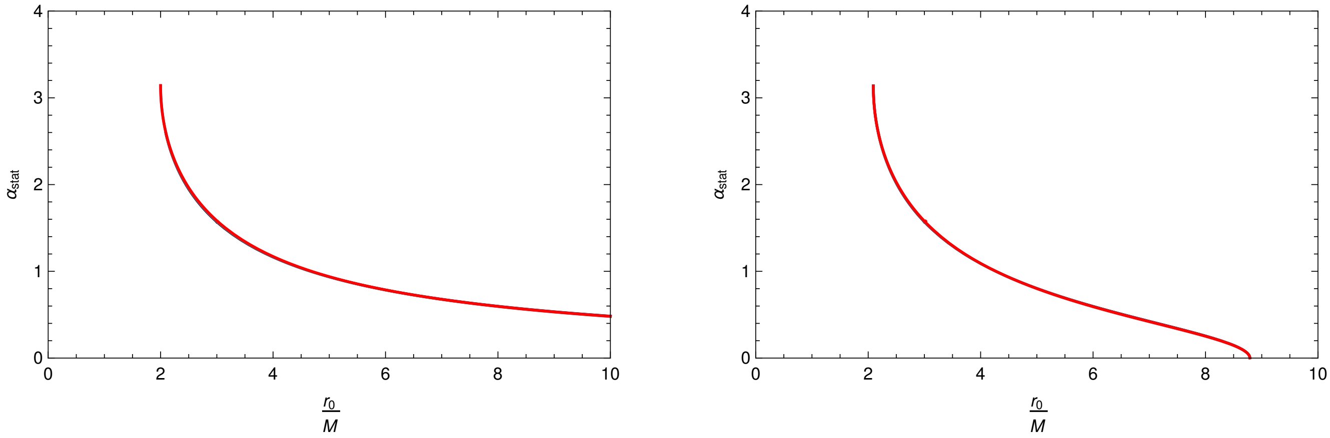

(a) Angular shadow size (α_{stat}) of the Schwarzschild black hole with respect to a static observer (r_0).

(b) Angular shadow (α_{stat}) of Schwarzschild de-Sitter black hole with respect to a static observer (r_0). The cosmological constant ΛM^2 is set to 0.03.

Figure 5.4: Variation in angular shadow size with respect to observer's position r_0. The plots are shown for plasma parameter $\frac{k}{M}$ values - 0.0 (black), 0.2 (violet) and 0.4 (red).

In Fig.5.4, we plot the angular size (α) of the black hole shadow varying the position (r_0) of the observer. The plots are shown for different values of inhomogeneous plasma parameter $\frac{k}{M}$. Analysing the plots, we find that as the observer moves from infinity (asymptotically flat black hole) or from the cosmological horizon r_C (asymptotically de-Sitter black hole) towards the black hole, the angular shadow size increases from being zero at the asymptotic location to $\frac{\pi}{2}$ at the photon sphere. As the observer moves further, the shadow size then falls back to zero at the event horizon r_{h+}. Our aim is to plot the shadow in the range $\alpha \in [0, \pi]$. To fulfill our plans we must consider $\alpha = \sin^{-1} Q$ in the range $r_p < r_0 < r_C$ and $\alpha = \pi - \sin^{-1} Q$ in the range $r_{h+} < r_0 < r_p$ [93]. Here Q gives the value of $\sin\alpha$ in terms of radial distance r_0 and other spacetime parameters.

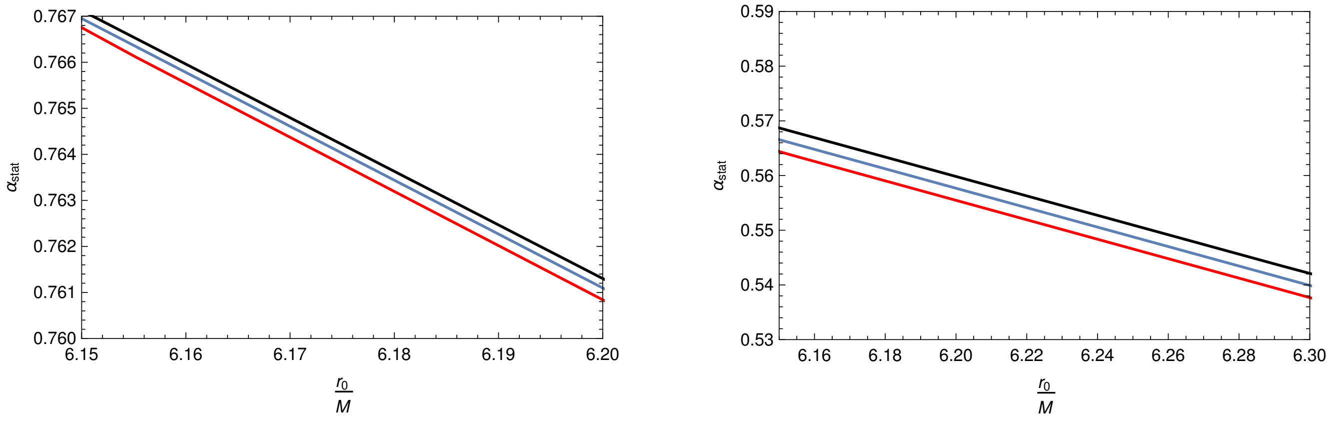

(a) Angular shadow (α_{stat}) of Schwarzschild black hole with respect to a static observer (r_0) (enlarged version).

(b) Angular shadow (α_{stat}) of Schwarzschild de-Sitter black hole with respect to a static observer (r_0) by setting ΛM^2 to 0.03 (enlarged version).

Figure 5.5: Variation in angular shadow size with respect to observer's position r_0. The plots are shown for plasma parameter $\frac{k}{M}$ values - 0.0 (black), 0.2 (violet) and 0.4 (red). The enlarged version of the above plots.

The left plot in Fig.5.4 is for Schwarzschild black hole which reveals that the observer's position can extend upto infinity. Whereas, the right plot in Fig.5.4 depicts the variation of the angular shadow size with radial distance r_0 in case of a Schwarzschild black hole embedded in a de-Sitter universe. This embedding restricts the observer upto a certain limiting radius, namely the cosmological horizon radius r_C. In case of Schwarzschikd de-Sitter black hole, the shadow size is zero at the cosmological horizon r_C and increases to $\frac{\pi}{2}$ at the photon sphere r_p. Beyond the photon sphere, as the observer moves closer to the black hole, the shadow size grows and becomes π at the event horizon.

The plots in Fig.5.5 are the enlarged version of the plots in Fig.5.4. They clearly reveal the change in the angular shadow size with variation in inhomogeneous plasma parameter $\frac{k}{M}$. The plots show that increment in plasma parameter $\frac{k}{M}$ decreases the black hole shadow size. Also we mention that the plots are shown for plasma frequency ω_p^2 having only radial dependence as $\omega_p^2 \sim \frac{1}{r}$.

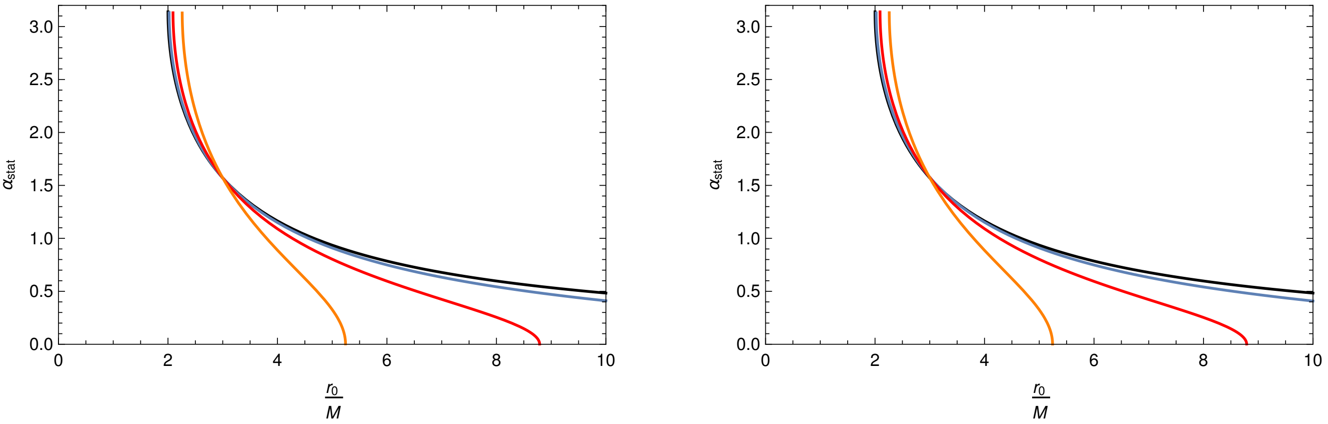

(a) Angular shadow (α_{stat}) of a Schwarzschild de-Sitter black hole with respect to a static observer ($\frac{r_0}{M}$) setting plasma parameter $\frac{k}{M} = 0.0$.

(b) Angular shadow (α_{stat}) of a Schwarzschild de-Sitter black hole with respect to a static observer ($\frac{r_0}{M}$) setting inhomogeneous plasma parameter $\frac{k}{M} = 0.2$.

Figure 5.6: Graphical representation of angular shadow size (α_{stat}) with variation in the position of a static observer ($\frac{r_0}{M}$). The plots are shown for the cosmological constant ΛM^2 values - 0.0000 (black), 0.0075 (violet), 0.0300 (red) and 0.0675 (orange).

The plots shown in Fig.5.6 depict the variation of the black hole shadow for different values of the cosmological constant Λ or in other words the Hubble's constant H_0. The plots are shown for Schwarzschild de-Sitter/Kottler black hole with the values of the cosmological constant (ΛM^2) set to 0.0000 (black), 0.0075 (violet), 0.0300 (red) and 0.0675 (orange). The plots reveal that increment in the value of Λ decreases the shadow size decreases rapidly. This implies that higher the value of Λ, closer is the cosmological horizon (r_C) to the black hole event horizon (r_{h+}). Also, the plots reveal the size of the black hole, thereby it's event horizon increases with increase in the value of the cosmological constant Λ. Hence the event horizon moves closer to the cosmological horizon with increase in Λ. As the inner horizon increases and the outer one decreases, so they must merge at some value of Λ that is $r_{h+} = r_C$) for some value pf λ. The value at which the two horizons meet is $\Lambda M^2 = 0.1111$. The left plot in Fig.5.6 is shown by setting the plasma parameter $\frac{k}{M} = 0$ and the right plot is drawn by setting the inhomogeneous plasma parameter $\frac{k}{M} = 0.2$. The two plots are almost identical since the variation due to plasma gets reflected in the photon sphere radius r_p but no effect of plasma is seen in case of r_{h+} and r_C.

5.4 Shadow from the point of view of co-moving observer

In this section, we study the effect of the cosmic expansion on the black hole shadow. The shadow, in general, is viewed by an observer stationed at a certain position in the domain of outer communication. The cosmological expansion drives the observer away from the black hole and the motion of the observer is dictated by the cosmological constant Λ. The angular size of the shadow measured by this co-moving observer is related to that measured by a static observer in terms of the aberration relation [98], [99]

$$\cos\alpha_c = \frac{\cos\alpha_s - v}{1 - v\cos\alpha_s}\ . \tag{5.40}$$

We have derived this expression previously in chapter 1. The above expression can be rewritten in terms of sine function as

$$\sin^2\alpha_c = \Big(1 - v^2\Big)\frac{\sin^2\alpha_s}{\Big(1 - v\cos\alpha_s\Big)^2} \tag{5.41}$$

where v is the relative velocity between the two observers.

In general, the co-moving observer moves away from the black hole with velocity v. This velocity is dictated by the cosmological constant Λ and thereby the Hubble constant H_0 as well as other spacetime parameters. Again, it must be pointed out that as the static observer goes from r_{h+} to r_p, the angular size of the black hole shadow changes from π to $\frac{\pi}{2}$ and then goes from $\frac{\pi}{2}$ to zero as the observer goes to r_C as discussed above. This observation is clear from the plot in the right panel of Fig.5.4. Also, in our analysis, we considered only positive values for sine and cosine functions. Thus, we put negative values by hand for a continuation of our results. Keeping these points in mind and by expressing $\cos\alpha_s$ in terms of $\sin\alpha_s$ in eq.(5.41) we get

$$\sin\alpha_c = \sqrt{\Big(1 - v^2\Big)}\frac{\sin\alpha_s}{\Big(1 \pm v\sqrt{1 - \sin^2\alpha_s}\Big)} \tag{5.42}$$

which can be rewritten as

$$\sin\alpha_c = \sqrt{\Big(1-v^2\Big)}\,\sin\alpha_s \frac{\Big(1 \mp v\sqrt{1-\sin^2\alpha_s}\Big)}{\Big(1-v^2(1-\sin^2\alpha_s)\Big)}\ . \tag{5.43}$$

The associated graphical representations show very interesting results. If we consider the shadow from the point of view of the comoving observer, we find that the shadow observed has certain features quite different from that seen by the static observer. In case of a static observer, as the observer moves away from the event horizon r_{h+} the complete dark sky as seen by him starts to reduce in size and just at the photon sphere r_p, he observes half dark and half bright sky. Further, as he moves further outward, he eventually sees a completely bright sky. Also at the location of the photon sphere (r_p), the light rays are perpendicular to the observer. On the other hand, in case of the co-moving observer the situation is not the same. For the comoving observer the effective photon sphere $\tilde{r}_p$ is somewhere outward, that is $\tilde{r}_p > r_p$. The other observations and their respective nature are identical as viewed by a static observer. Also another important fact is that the position of the comoving observer is not bound by the cosmological horizon r_C and the observer can reach upto infinity.

Now we incorporate a plasma background to observe the effect of shadow as viewed by a comoving observer. The aberration relation gets modified to a great extent due to incorporation of the plasmic medium. The expression takes the form [218]

$$\cos\alpha_{cp} = \frac{\cos\alpha_{sp} + nv}{\sqrt{\Big(n + v\cos\alpha_{sp}\Big)^2 - \Big(n^2-1\Big)\Big(1-v^2\Big)}} \tag{5.44}$$

which can be rewritten in terms of sine function as

$$\sin\alpha_{cp} = \sqrt{\Big(1-v^2\Big)}\frac{\sin\alpha_{sp}}{\sqrt{\Big(n \mp v\sqrt{1-\sin^2\alpha_{sp}}\Big)^2 - \Big(n^2-1\Big)\Big(1-v^2\Big)}}\ . \tag{5.45}$$

Setting $n=1$, we get back eq.(5.42). The above eq.(5.45) can be again rewritten as

$$\sin\alpha_{cp} = \sqrt{\Big(1-v^2\Big)}\,\sin\alpha_{sp}\frac{\sqrt{\Big(1+n^2v^2-v^2\sin^2\alpha_{sp}\Big) \mp 2nv\sqrt{\Big(1-\sin^2\alpha_{sp}\Big)}}}{\sqrt{\Big(1+n^2v^2-v^2\sin^2\alpha_{sp}\Big)^2 - 4n^2v^2\Big(1-\sin^2\alpha_{sp}\Big)}}\ . \tag{5.46}$$

Using the above expression we can determine the angular size of the black hole shadow surrounded by plasma as seen by a comoving observer moving away from the black hole.

Now, in order to calculate and graphically represent the angular size of the black hole shadow, we need to determine the velocity of the comoving observer with respect to a static observer. The derivation has been performed by Perlick et al in [93]. Also it has been done for the general case applicable in for any static and spherically symmetric spacetime by Roy et al in [208]. The velocity of the comoving observer with respect to the static observer takes the form

$$|\vec{v}| = \sqrt{1 - \frac{f(r)}{f_0(r)}}. \tag{5.47}$$

with $f(r)$ being the lapse function and $f_0(r) = f(r)\Big|_{\Lambda=0}$. In case of Kottler metric, the lapse function takes the form $f(r) = 1 - \frac{2M}{r} - \frac{\Lambda}{3}r^2$, which gives the velocity of comoving observer as

$$|\vec{v}| = \sqrt{\frac{\Lambda/3}{1 - \frac{2M}{r} - \frac{\Lambda}{3}r^2}}\,r = \frac{H_0 r}{\sqrt{1 - \frac{2M}{r} - H_0^2 r^2}}. \tag{5.48}$$

We have briefly discussed the formula for the velocity of the comoving observer with respect to the static observer in the Appendix C.

Utilising the expression of the comoving velocity of the observer, we can calculate and plot the angular shadow size as seen by a comoving observer. We have shown the plots of the angular shadow size with respect to the observer's position in Fig.5.7. The left plot represents the shadow in absence of plasma, whereas the right one shows the shadow in an inhomogeneous plasma background having the value of plasma parameter $\frac{k}{M} = 0.2$. Further, we have also shown the variation of the angular size of the black hole shadow for different values of the Hubbble constant H_0. From both the plots, for a fixed value of the observer position one can conclude that the shadow size increases with an increase in the value of Hubble constant H_0. Also, we find that the shadow size reduces and saturates to a finite value but never reaches zero size with increasing distance from the black hole.

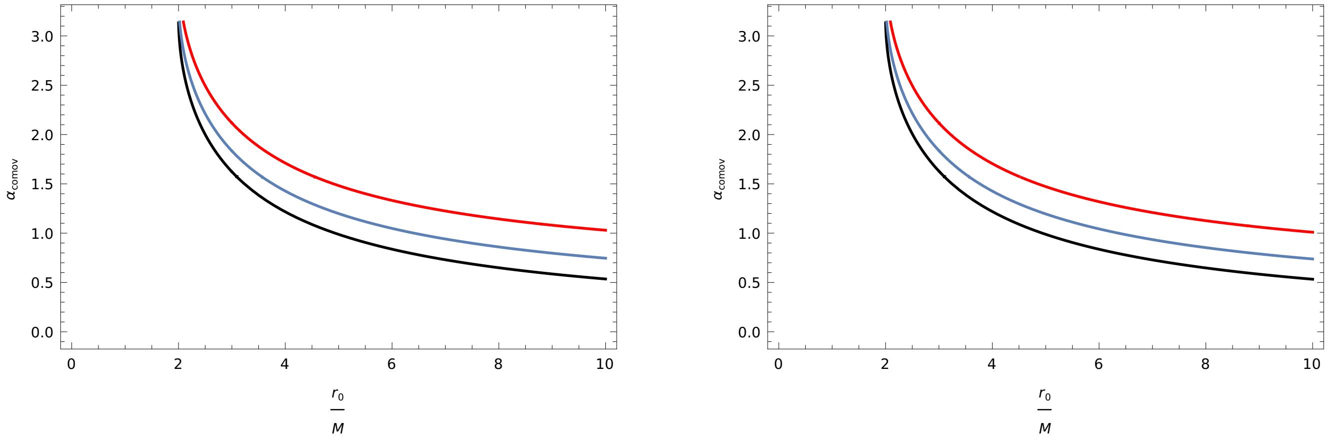

(a) Angular shadow (α_{comov}) of a Schwarzschild de-Sitter black hole with respect to a comoving observer ($\frac{r_0}{M}$) setting plasma parameter $\frac{k}{M} = 0.0$.

(b) Angular shadow (α_{comov}) of a Schwarzschild de-Sitter black hole with respect to a comoving observer ($\frac{r_0}{M}$) setting inhomogeneous plasma parameter $\frac{k}{M} = 0.2$.

Figure 5.7: Variation in the angular size of the shadow with respect to the position of the co-moving observer $\frac{r_0}{M}$. The plots are shown for different values of Hubble constant H_0M as 0.01 (black), 0.05 (violet) and 0.10 (red).

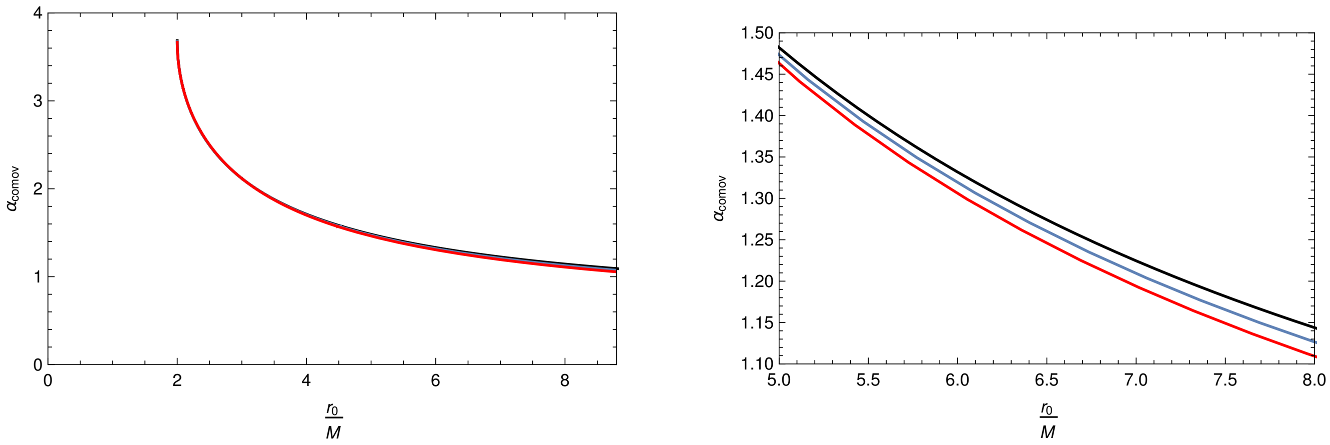

(a) Angular shadow (α_{comov}) of a Schwarzschild de-Sitter black hole with respect to a comoving observer ($\frac{r_0}{M}$).

(b) The enlarged version of the left image.

Figure 5.8: Graphical representation of angular shadow size (α_{comov}) of a Schwarzschild de-Sitter black hole with variation in the position of a comoving observer ($\frac{r_0}{M}$). The plots are shown for the inhomogeneous plasma parameter $\frac{k}{M}$ values - 0.0 (black), 0.2 (violet) and 0.4 (red) with Hubble constant $H_0M = 0.10$.

Fig.5.8 entails the effect of the plasma parameter on the angular shadow radius as seen by a comoving observer. The plots have been shown for a fixed value of the Hubble constant $H_0M = 0.1$ and for inhomogeneous plasma parameter values $\frac{k}{M} = 0.0, 0.2$ and 0.4. The plot in right is the enlarged version of the left one. We find that an increase in the value of the inhomogeneous plasma parameter $\frac{k}{M}$, decreases the angular size of the black hole shadow similar to that observed in case of a static observer.

5.5 Comparison with EHT observations

In this section we calculate the numerical value of the angular size of the black hole shadow and compare it with the observational results. We want to compare the theoretical results with the observational ones of supermassive black holes residing at the centre of M87 galaxy and our galaxy (Milky Way). We discuss them casewise.

5.5.1 Case I: M87* supermassive black hole

The observational results from the EHT Collaboration reveal that the shadow size of M87* supermassive black hole is (42±3) μas [9]. So, the angular size of the black hole shadow is restricted to be in the range (39-45) μas. For the numerical computation of shadow size, we require the distance of the black hole from earth. The distance has been measured to be (16.8 ± 0.8) MPc [9]. The mass of the black hole as measured by the *EHT* collaboration is found to be (6.5 ± 0.7) $\times 10^9$ $M_\odot$ [9]. All the above mentioned quantities are necessary to calculate the mass parameter m which is of the form $m = \frac{GM}{c^2}$. Here, G corresponds to Newton's gravitational constant and c is the velocity of light in vacuum having the standard values 6.674×10^{-11} m^{3}Kg^{-1}s^{-2} and 3×10^8 ms^{-1} respectively.
Here, the main aim is to calculate the black hole shadow as observed by a comoving observer. The comoving observer moves along with the accelerating expansion of the universe. In this work, we have considered the cosmic expansion to be driven by the cosmological constant Λ. The cosmological

constant is related to the Hubble constant H_0 by the relation $\frac{\Lambda}{3} = \frac{H_0^2}{c^2}$ [93]. The angular size of the black hole shadow given in eq.(s) (5.45) and (5.46) depend on the recession velocity of the comoving observer. The velocity of the comoving observer is given in eq.(5.48) which depends on the Hubble constant H_0. Thus, in order to determine the value of the angular size of the black hole shadow as measured by the comoving observer, we need the value of the Hubble's constant H_0 which in turn will give us the recession velocity. The value of H_0 as measured by the Planck Collaboration is (67.4 ± 0.5) km s^{-1}MPc^{-1} [219].

Apart from that, we incorporated the effect of plasma. We want to constrain the values of plasma parameter using the observed values of the angular shadow size. Hence we calculate the shadow of a black hole immersed in a plasma medium. The plasma is assumed to be spherically symmetric and the plasma frequency ω_p and thereby the refractive index n has only radial dependence. The refractive index takes the form $n = \sqrt{1 - \frac{k}{r^h} f(r)}$. For homogeneous plasma, we have $h = 0$ and for inhomogeneous plasma we consider $h = 1$. For these two cases, we calculate the angular shadow size using (5.46). The value of α gives the angular radius of the black hole shadow. We then double it to obtain the angular diameter 2α. This value is then compared to the observational result and thereby the plasma parameter k is constrained.

For calculational purposes, we convert the distance of black hole from earth r_0 as well as the photon sphere radius r_p into metres. The value of r_0 upon conversion becomes 5.184 $\times 10^{23}$ m. The photon sphere radius for the Schwarzchild and Schwarzchild de-Sitter black remains the same at $3m$ which in metres has the value 2.892 $\times 10^{13}$ m. The value of the mass parameter m is 9.64 $\times 10^{12}$ m. Also, the cosmological horizon r_C of the black hole spacetime is positioned at 1.3736 $\times 10^{26}$ metres, where we have used the mass of the M87* supermassive black hole having value (6.5 ± 0.7) $\times 10^9$ $M_\odot$ [9] and the value of the Hubble constant as (67.4 ± 0.5) km s^{-1}MPc^{-1} [219]. Using the above values, we computed both r_0 (distance of the black hole from earth) and r_C (cosmological horizon) and found that $r_0 < r_C$ implying that the observer is located well inside the horizon.

k	$\alpha_{stat}(\mu$as)
0.00	39.8643
0.05	40.7999
0.10	41.3061
0.15	42.1243
0.20	43.0210
0.25	44.0093
0.295	44.9907
0.296	45.0136

k	$\alpha_{comov}(\mu$as)
0.00	40.0150
0.05	40.9502
0.10	41.4542
0.15	42.2710
0.20	43.1633
0.25	44.1533
0.289	44.9971
0.29	45.0197

Table 5.1: Table showing the angular shadow size with change in plasma parameter k for homogeneous plasma frequency $\omega_p^2 = k = constant$.

Also we would like to point out that in the overall analysis, we have used a general expression for the velocity of the co-moving observer eq.(5.48). In order to perform numerical analysis in cosmological scales, it is needful to consider the effective velocity (v_{eff}) which is of the form [220]

$$v_{eff} = cz = H_0 D + v_p \implies v_p = cz - H_0 D \tag{5.49}$$

where v_{eff} designates the effective velocity. The effective velocity (v_{eff}) is expressed in terms of the redshift factor z, the Hubble's constant H_0, the observer's distance from the black hole designated as D and the peculiar velocity v_p. Now the redshift factor z of the M87* black hole with respect to earth is 0.00428 [221], the Hubble's constant H_0 is 67.4 km $s^{-1}MPc^{-1}$ [219] and D is 16.8 Mpc [9]. Using these values, we obtain the peculiar velocity v_p to be 178.64 km s^{-1}. However, the velocity due to cosmic expansion is 1105.36 km s^{-1} which can be obtained using eq.(5.48). In general we must have used v_{eff} for our calculations, but from the results reveal that the co-moving velocity is large compared to the peculiar velocity and hence can neglected as we have done here. Thus, our consideration of the earth as a co-moving frame neglecting the peculiar velocity is quite valid.
Table 5.1 tabulates the values of the angular size of the black hole shadow corresponding to different values of the plasma parameter k. The plasma medium considered here is homogeneous in nature with frequency $\omega_p^2 = k =$constant. The values of the angular shadow size ranges between 39 and 45 μas. Comparing the numerical values of shadow size compatible with this range gives bound on the plasma parameter k. We find that the homogeneous plasma parameter is bounded as $0 \leq k < 0.296$ for the shadow observed by the static observer and $0 \leq k < 0.29$ in case of the comoving observer. The left table in 5.1 shows a list of values for k compatible with the angular shadow size as observed by a static observer. On the other hand the right table shows the compatible range of values of k with respect to a comoving observer. We find that the range of the values of the homogeneous plasma parameter k are almost identical for both the observers.

$\frac{k}{m}$	$\alpha_{stat}(\mu$as)
0.00	39.8643
0.05	39.7534
0.10	39.6422
0.15	39.5307
0.20	39.4189
0.25	39.3067
0.30	39.1943
0.35	39.0815
0.386	39.0001

$\frac{k}{m}$	$\alpha_{comov}(\mu$as)
0.00	40.0150
0.05	39.7921
0.10	39.6801
0.15	39.6801
0.20	39.5679
0.25	39.4553
0.30	39.3424
0.35	39.2292
0.40	39.1157
0.4508	39.0000

Table 5.2: Table showing the angular shadow size with change in plasma parameter $\frac{k}{m}$ for inhomogeneous plasma frequency $\omega_p^2 = \omega_p^2(r) = \frac{k}{r}$.

Table 5.2 tabulates the values of the inhomogeneous plasma parameter $\frac{k}{m}$ compatible with the values of the angular shadow size which varies in the range 39-45 μas. The Table is constructed by considering an inhomogeneous plasma distribution having frequency $\omega_p^2(r) = \frac{k}{r}$. The left table in 5.2 is for the shadow observed by a static observer and that in the right is for a comoving observer. We found that the plasma parameter $\frac{k}{m}$ is bound in the range $0 \leq \frac{k}{m} \leq 0.386$ for the static case and in the range $0 \leq \frac{k}{m} \leq 0.4508$ for the comoving case. The ranges of the plasma parameter $\frac{k}{m}$ are quite different in case of the two observers. The range is more extended in case of comoving observer than that for the static observer.

5.5.2 Case II: Sgr A* supermassive black hole

In this case, we want to constrain the plasma parameter using the observational results of Sgr A* supermassive black hole. The constraining of various other spacetime parameters using Sgr A* have been done in [222]-[225]. We want to carry out our analysis by simply comparing the theoretical and observed values of angular shadow size of the black hole. The observed value of the angular size of the black hole shadow is (48.7 ± 7) μas [58]. For numerical analysis, we require the black hole's mass, which is $4^{+1.1}_{-0.6} \times 10^6\ M_\odot$ [58]. The black hole is located at a distance $(8277 \pm 9 \pm 33) pc$ [226] from earth. We use the value of the black hole mass as $4 \times 10^6\ M_\odot$ and distance from the black hole to earth as 8277 pc for our calculations. The angular size of the black hole shadow varies in the range (41.7 - 55.7) μas.

k	$\alpha_{stat}(\mu$as$)$
0.000	49.6868
0.050	50.5446
0.100	51.4799
0.150	52.4996
0.200	53.6172
0.250	54.8490
0.281	55.6789
0.282	55.7066

k	$\alpha_{comov}(\mu$as$)$
0.000	49.6869
0.050	50.5447
0.100	51.4800
0.150	52.4997
0.200	53.6173
0.250	54.8491
0.281	55.6790
0.282	55.7067

Table 5.3: Table showing the angular shadow size with change in plasma parameter k for homogeneous plasma frequency $\omega_p^2 = k = constant$.

We are interested in carrying out the analysis both for homogeneous and inhomogeneous plasma distribution similar to the earlier case. The refractive index in case of homogeneous plasma takes the form $n = \sqrt{1 - kf(r)}$ with k being the plasma parameter and $f(r)$ being the lapse function. Table 5.3 tabulates the angular size of the black hole shadow observed by both static and co-moving observers. We present the values of the angular shadow which lie in the desired range $(41.7 - 55.7)\mu as$ along with the compatible values of the homogeneous plasma parameter k. We find that the homogeneous plasma parameter is bounded in the range $0 \leq k < 0.282$ both for static and co-moving observers. Also, we notice that the angular shadow size is the same for both static and co-moving observer. This is due to the fact that the supermassive black hole Sgr A* and the observer on earth lie on the same galactic frame.

$\frac{k}{m}$	$\alpha_{stat}(\mu$as$)$
0.00	49.6868
0.50	48.2802
1.00	46.8166
1.50	45.2895
2.00	43.6907
2.50	42.0102
2.58	41.7330

$\frac{k}{m}$	$\alpha_{comov}(\mu$as$)$
0.00	49.6869
0.50	48.2802
1.00	46.8167
1.50	45.2896
2.00	43.6907
2.50	42.0103
2.58	41.7331

Table 5.4: Table showing the angular shadow size with change in plasma parameter $\frac{k}{m}$ for inhomogeneous plasma frequency $\omega_p^2 = \frac{k}{r}$.

Then we try to constraint the inhomogeneous plasma parameter $\frac{k}{m}$ using the angular size of black hole shadow. The refractive index in case of inhomogeneous plasma is of the form $n = \sqrt{1 - \frac{k}{r} f(r)}$. Table 5.4 tabulates the values of the angular shadow size of the black hole and the compatible values of the plasma parameter $\frac{k}{m}$. We find that the plasma parameter $\frac{k}{m}$ is bounded in the range $0 \leq \frac{k}{m} \leq 2.58$ for both static and co-moving observers. Similar to the case of homogeneous plasma, here too we find that the shadow size has the same value for both observers.

5.6 Summary

We now summarize our results. In this work, we have calculated the angular size of the shadow of a spherically symmetric black hole immersed in a plasma background as seen by both static and comoving observer. We start by considering a spherically symmetric metric black hole metric in (3+1) dimensions with arbitrary lapse function $f(r)$. Then we considered the lapse function of Schwarzchild de-Sitter/Kottler black hole having a positive cosmological constant $\Lambda > 0$ and carried out the analysis. The cosmological constant Λ is considered to be responsible for the expansion of the universe in our work. The significant part of our work is the study and analysis of the effect of a background plasma medium on the black hole shadow. We have graphically represented the angular shadow size for Schwarzschild and Schwarzschild de-Sitter black hole with variation in plasma parameter k. The plots revealed that with increase in the inhomogeneous plasma parameter k, the shadow size reduces. We have also shown the effect of plasma on the photon sphere radius r_p. Then in our later discussion we have shown the effect of Λ on the angular size of the black hole shadow. We observe that at the position of the observer which is well outside the photon sphere, the angular shadow size reduces with increase in Λ. The effect remains the same even in presence of plasma.

The graphical analysis reveal many interesting features. We observe that the angular shadow size varies in the range π to 0. The shadow size is π at the black hole horizon and goes down to zero at infinity for asymptotically flat spacetime. In case of asymptotically de-Sitter background, the black hole shadow size goes to zero at the cosmological horizon r_C. The angular shadow observed by a co-moving observer is related to that observed by a static observer via the aberration relation. The interesting feature is that in case of co-moving observer, there is no cosmological horizon and the observer can reach upto infinity. Further, in this case the shadow size does not go to zero and always remains finite. Since the observer is moving with the expansion, hence he never feels any horizon as such.

Then we graphically represent the angular shadow size incorporating the plasma effects. We observed that plasma impacts the shadow size greatly. Practically an observer can exist outside the photon sphere r_p. From his perspective the shadow size changes with variation in plasma parameter. In case of homogeneous plasma, we find that the shadow size increases with increase in plasma both for static and co-moving observer. On the other hand, we observe that the shadow size decreases with the increase in the value of the plasma parameter k for inhomogeneous plasma. We have shown the plots only for inhomogeneous plasma.

Finally, we compared the angular shadow size with the observational results of M87* and Sgr A* supermassive black hole data. Comparing our calculated results with the observed angular shadow size, we obtained bounds on the plasma parameter. We find that for homogeneous plasma, k has an upper bound of $k < 0.296$ for static observer and $k < 0.29$ for co-moving observer. In case of inhomogeneous plasma, we find that $\frac{k}{m}$ has an upper bound of $\frac{k}{m} \leq 0.386$ for static and $\frac{k}{m} \leq 0.4508$ for co-moving observer. The above bounds are for M87* supermassive black hole. In case of Sgr A*, we find that the angular shadow size is the same both for static and co-moving observers. This is due to the fact that the supermassive black hole Sgr A* and the observer residing on earth belong to the same galactic frame. The bounds on the homogeneous and inhomogeneous plasma are given as $0 \leq k < 0.282$ and $0 \leq \frac{k}{m} \leq 2.58$ respectively. The constraints are true both for static and co-moving observers.

Chapter 6

Conclusion

In this thesis our main focus was the study of black hole structure utilising the geodesic motion of massive and massless particles. The study of massive particle is important to gain insight about the fact that how matter behaves in the vicinity of the black holes. The importance of studying null geodesics is that it helps developing the black hole shadow structure and its various features.

In our first work, we considered a charged black hole in higher curvature corrected gravity theory designated as Gauss bonnet gravity in literature. The black holes are considered to be located in asymptotically AdS and Minkowski background. The increment in the Gauss Bonnet parameter γ results in the increase of shadow radius in AdS background whereas it decreases the shadow size in Minkowski background. We carried out the study in $d = 5$ spacetime dimensions since the spacetime dynamics remains uneffected by γ in $d = 4$ (realistic) spacetime dimensions. The importance of studying the black hole shadow in AdS background is that it can be related to the associated parameters of the CFT in $d = 4$ dimensions via the AdS/CFT duality. Again the importance of studying the shadow structure in Minkowski spacetime in higher dimensions is to gain insight of the possible effects of γ on the lower $d = 4$ dimensional black hole. Recently, it has been observed that the impact of γ upon the shadow structure as found in case of 4-D Gauss Bonnet gravity is similar to our analysis. Besides, we also find that plasma impacts the shadow structure considerably and has similar effect in both AdS and Minkowski background. We found that the shadow size decreases with increase in plasma parameter.

In our next two works we considered the second most dominant mass-energy component of the universe, namely the dark matter surrounding a static charged black hole. The choice of the candidate dark matter is that of perfect fluid type namely, perfect fluid dark matter or PFDM. We incorporate the Newman-Janis algorithm to turn the static charged black hole to a charged rotating one. We studied the event horizon of the black hole and found that it decreases intially and then after a certain critical value of the PFDM parameter it starts to increase. Such an observation can be explained by the fact that dark matter has a effective mass residing at the same point as that of the black hole. Below the critical value of PFDM parameter, the dark matter mass opposes the effect of the black hole mass and hence the event horizon decreases. On the other hand, after the critical value the total mass of the system is given by the dark matter mass and hence with increase in PFDM parameter, the system's mass and thereby the event horizon gradually increases. We then studied the energy and angular momentum of massive (both charged and uncharged) particles in the background and graphicaly observe how the PFDM effects them. The particles can either move along the black hole

spin (prograde or corotating motion) or opposite to the spin (retrograde or counter rotating motion). We observe that the energy (E) of the particle in prograde orbits decreases whereas that of retrograde orbits increases with increase in the radial distance (r) from the black hole and gets close to unity as the particle approaches infinity. The increment in the values of PFDM parameter and spin (a) increases the energy of the particle considerably for the prograde orbits. On the other hand in case of retrograde orbits, the energy (E) increases with the increase in PFDM parameter but falls with the increasing value of the black hole spin (a). This is because when the particle spins along the black hole, the black hole helps its motion whereas in the reverse case it opposes. We find that angular momentum of the black hole decreases with an increase in the value of the PFDM parameter below the critical value and increases above the critical value for both types of orbits. On the other hand for counter-rotating particles, the angular momentum (L) rises (-ve increase) for PFDM parameter being less than the critical value while it decreases for PFDM greater than the critical value.
We analysed both the energy (E) and angular momentum (L) of the charged particle with the variation in their charge (q). We found that increment in the value of charge (q) reduces the energy falls in prograde orbits and increases the same in case of retrograde orbits. Besides we observe that the angular momentum (L) increases with increasing q for PFDM below critical value and falls with PFDM in case of PFDM above the critical value. Also, we observed that the effective potential of the black hole encountered by photons and massive particles increases with the increasing spin (a) and charge (Q) of the black hole as also with angular momentum (L) of the particle. The change is quite sharp with the change in the angular momentum (L).
We also studied the Penrose process in PFDM background. The existence of negative energy particles are important in order to extract energy from the black hole. We found that negative energy increases with increase in negative angular momentum (counter-rotating particle) and also with increase in the charge (Q) of the black hole. The effect of dark matter on the negative energy is less pronounced even though negative energy slightly increases. More the negative energy of the particle absorbed by the black hole, more is the gain, and we found that the energy gain via Penrose process increases due to the presence of dark matter in the system. Also we found that more the black hole charge (Q), less is the energy gain (extraction of energy) and hence less efficient is the Penrose process.
We also studied the null geodesics in the PFDM background by considering the system being immersed in plasma. We calculated the corotating (r_{p1}) and counter rotating (r_{p2}) photon orbit radius and found that the counter rotating lie away from the black hole whereas the corarting ones lie closer to the black hole. We find that in absence of plasma the radius of photon orbits both for prograde and retrograde orbits decreases with increase in PFDM parameter in the lower regime and increases for PFDM parameter in the higher regime. Besides we also found that increase in the value of the spin parameter (a) increases the radius of the photon orbits. We find that in case of homogeneous plasma distribution the radius of co-rotating orbits decrease whereas that for the counter rotating orbits increase with increase in plasma parameter. Also, we find that with increase in plasma parameter in case of inhomogeneous plasma distribution the increase in plasma parameter results in decrease of photon radius for both co-rotating and counter rotating orbits.
We then use the null geodesics to calculate the black hole shadow. The plots show that the shadow gets rotated and deformed with increase in black hole spin (a). The deformation of black hole shadow occurs due to the rotational drag of the unstable photons by the black hole. We also observe that

increment in charge (Q) reduces the radius (R_s) and thereby the size of the black hole shadow. The reason for this is quite obvious. The black hole shadow is the image of the outer event horizon of the black hole and the effect of Q on the event horizon gets reflected in the shadow radius R_s. The nature of variation of the PFDM impacts the black hole shadow in the same way it effects the black hole event horizon. The reason being the shadow is the indirect image of the event horizon of the black hole.

Then we studied the effect of the plasma medium on the black hole shadow. We considered the general case where the refractive index ($n(r,\theta)$) and plasma frequency ($\omega_p(r,\theta)$) both depends on r and θ. We observed that with only radial variation $f_r(r) = \omega_c^2\sqrt{M^3 r}$ and $f_\theta(\theta) = 0$, the shadow plots reduce in size with increase in plasma parameter ω_c. Similar nature is observed in case of θ variation with $f_r(r) = 0$ and $f_\theta(\theta) = \omega_c^2 M^2\Big(1 + 2\sin^2\theta\Big)$ with the shadow size decreasing with increase of plasma parameter ω_c. After that, we considered cases where refractive index of the form $\Big(n = \sqrt{1-\frac{k}{r}}\Big)$ (inhomogeneous) and $\Big(n = \sqrt{1-k}\Big)$ (homogeneous). Analysing the plots, we find that the extreme right of α axis corresponds to the radius of counter rotating orbits (r_{p2}) whereas that on the extreme left corresponds to the co-rotating orbits (r_{p1}). The variation of the radius of these orbits with plasma gets reflected in the black hole shadow. In particular, we observe that r_{p1} decreases with increase in the plasma parameter for fixed value of the PFDM parameter both for inhomogeneous and homogeneous plasma. However, r_{p2} increases with decrease in the plasma parameter for a fixed PFDM parameter for inhomogeneous plasma, and increases for homogeneous plasma. We also put constraint on the plasma parameter k as well as $\left(\frac{\omega_c}{\omega_0}\right)^2$ with the PFDM parameter by comparing the obtained values of θ_d with that observed from the $M87^*$ supermassive black hole data.

In the last part of the thesis we considered the effect of cosmic expansion on the black hole shadow. Among the various candidates we considered that the expansion is driven by a positive cosmological constant Λ. For simplicity we calculated the shadow of a Schwarzschild de-Sitter black hole rather than a Kerr de Sitter black hole. We obtained the angular shadow size as seen by a static observer. Since the universe is expanding, any observer moves away from the other. So the realistic observer must be comoving with the expansion driven by Λ. The angular size from the point of comoving observer is calculated in terms of that observed by a static observer and the recession velocity. We also incorporated plsma in the background to make the scenario more realistic. Then we calculated and compared the angular shadow size with the observational results of M87* and Sgr A* data. Comparing our results with the observed angular shadow size, we found bounds on the plasma parameter. We found that for homogeneous plasma, k has an upper bound of $k < 0.296$ for static observer and $k < 0.29$ for co-moving observer. In case of inhomogeneous plasma, we find that $\frac{k}{m}$ has an upper bound of $\frac{k}{m} \leq 0.386$ for static and $\frac{k}{m} \leq 0.4508$ for co-moving observer. These bounds are for M87* black hole. In case of Sgr A*, we found that the angular shadow size is the same both for static and co-moving observers. This is due to the fact that the supermassive black hole Sgr A* and the observer in this case (earth) belongs to the same galactic frame. The bounds on the homogeneous and inhomogeneous plasma are given as $0 \leq k < 0.282$ and $0 \leq \frac{k}{m} \leq 2.58$ respectively.

Appendix A: Limiting cases of obtained black hole solution

The black hole solution we have obtained is associated with the following lapse function

$$f(r) = 1 - \frac{2GM}{r} + \frac{Q^2}{r^2} + \frac{\alpha}{r} ln\Big(\frac{r}{|\alpha|}\Big). \tag{1}$$

In the limit $\alpha \to 0$, we apply the L'Hopital rule to the term $-\frac{\ln(|\alpha|)}{\frac{r}{\alpha}}$ in the above equation. This leads to the Reissner-Nordström solution

$$f(r) = 1 - \frac{2GM}{r} + \frac{Q^2}{r^2}. \tag{2}$$

On the other hand, in the limit $\alpha \to 0$ and $Q \to 0$, we have

$$f(r) = 1 - \frac{2GM}{r} \tag{3}$$

which corresponds to the Schwarzchild solution.

Appendix B

In this appendix, we show the derivation of eq.(3.51). We begin our calculation with the following expressions

$$F(r) = x^2\Big(a^2 - \Delta\Big) + r^4E^2 - 2aEr^2x - \Delta r^2 = 0 \ ; \ E = \frac{1}{r^2ax}\Big[\Big(a^2 - \Delta + \frac{r\Delta^{'}}{4}\Big)x^2 + \Big(\frac{\Delta^{'}}{4}r^3 - \frac{\Delta}{2}r^2\Big)\Big] \ . \tag{4}$$

Hence we have E^2 as

$$E^2 = \frac{1}{r^4a^2x^2}\left[\Big(a^2 - \Delta + \frac{r\Delta^{'}}{4}\Big)^2x^4 + \Big(\frac{\Delta^{'}}{4}r^3 - \frac{\Delta}{2}r^2\Big)^2 + 2\Big(a^2 - \Delta + \frac{r\Delta^{'}}{4}\Big)\Big(\frac{\Delta^{'}}{4}r^3 - \frac{\Delta}{2}r^2\Big)x^2\right]. \tag{5}$$

Rearranging the expressions of E and E^2, we obtain

$$r^2axE = \Big[\Big(a^2 - \Delta + \frac{r\Delta^{'}}{4}\Big)x^2 + \Big(\frac{\Delta^{'}}{4}r^3 - \frac{\Delta}{2}r^2\Big)\Big] \tag{6}$$

$$r^4a^2x^2E^2 = \left[\Big(a^2 - \Delta + \frac{r\Delta^{'}}{4}\Big)^2x^4 + \Big(\frac{\Delta^{'}}{4}r^3 - \frac{\Delta}{2}r^2\Big)^2 + 2\Big(a^2 - \Delta + \frac{r\Delta^{'}}{4}\Big)\Big(\frac{\Delta^{'}}{4}r^3 - \frac{\Delta}{2}r^2\Big)x^2\right]. \tag{7}$$

Also multiplying $F(r) = 0$ by a^2x^2 we obtain

$$a^2x^4\Big(a^2 - \Delta\Big) + a^2x^2r^4E^2 - 2aEr^2xa^2x^2 - \Delta a^2x^2r^2 = 0. \tag{8}$$

By substituting eq.(6) and eq.(7) in eq.(8), we obtain the following expression

$$\begin{aligned} a^2x^4\Big(a^2-\Delta\Big)+\Big(a^2-\Delta+\frac{r\Delta^{'}}{4}\Big)^2x^4+\Big(\frac{\Delta^{'}}{4}r^3-\frac{\Delta}{2}r^2\Big)^2+2\Big(a^2-\Delta+\frac{r\Delta^{'}}{4}\Big)\Big(\frac{\Delta^{'}}{4}r^3-\frac{\Delta}{2}r^2\Big)x^2 \\ -2a^2x^2\left[\Big(a^2-\Delta+\frac{r\Delta^{'}}{4}\Big)x^2+\Big(\frac{\Delta^{'}}{4}r^3-\frac{\Delta}{2}r^2\Big)\right]-\Delta a^2x^2r^2=0\ . \end{aligned} \tag{9}$$

The above expression has terms with x^4, x^2 and x^0. So rearranging terms in those powers leads to

$$\begin{aligned} \Big[4\Big(\Delta-a^2-\frac{r\Delta^{'}}{4}\Big)^2-4a^2\Big(a^2-\Delta+\frac{r\Delta^{'}}{2}\Big)\Big]x^4+\Big[\Big(4a^2-4\Delta+r\Delta^{'}\Big) \\ \times\Big(\frac{r^3\Delta^{'}}{2}-r^2\Delta\Big)-2r^3a^2\Delta^{'}\Big]x^2+\Big(r^2\Delta-\frac{r^3\Delta^{'}}{2}\Big)^2=0\ . \end{aligned} \tag{10}$$

Appendix C: Determination of the velocity of the comoving observer with respect to the static observer

In **Step I**, consider the asymptotically flat version of the original metric eq.(5.1) by dropping the cosmological constant, that is, by setting $\Lambda = 0$. This gives

$$ds^2_{\Lambda=0} = -f_0(r)dt^2 + \frac{1}{f_0(r)}dr^2 + r^2\Big(d\theta^2 + \sin^2\theta d\phi^2\Big) \tag{11}$$

where $f_0(r) = f(r)\Big|_{\Lambda=0}$.
In **Step II**, the metric in isotropic coordinate can be written as

$$ds^2_{\Lambda=0} = -k(\tilde{r})dt^2 + g^2(\tilde{r})\left(d\tilde{r}^2 + \tilde{r}^2\Big(d\theta^2 + \sin^2\theta d\phi^2\Big)\right)\ . \tag{12}$$

This eq.(12) can be compared with eq.(11) to get a relation between r and $\tilde{r}$ given as

$$dr = \frac{r}{\tilde{r}}\sqrt{f_0(r)}d\tilde{r}\ . \tag{13}$$

The above relation is then used to replace r in terms of $\tilde{r}$ in eq.(5.1).

In **Step III**, transform from *twiddled* to the co-moving coordinate (r_c, t_c) as $\tilde{r} = r_c\ a(t_c)$ [206] where, r_c is the radial coordinate in the co-moving frame and a is the scale factor of the universe which is the function of time (t_c) in the co-moving frame. This leads to a differential form of $d\tilde{r}$ in terms of dr_c and dt_c. Assuming dt of the form

$$dt = B(t_c, r_c)dt_c + C(t_c, r_c)dr_c\ . \tag{14}$$

the coefficients B and C will be determined by the next steps of the algorithm. Also due to the spherical symmetry (even though we go from original → twiddled → co-moving frame), θ and ϕ parts remain intact.

In **Step IV**, rewriting the metric in terms of r_c, t_c, θ, ϕ coordinates we have

$$\begin{aligned} ds^2 &= -\left[\frac{B^2}{f(r)} - \frac{f_0(r)r^2}{f(r)}\Big(\frac{\dot{a}}{a}\Big)^2\right]dt_c^2 + \left[\frac{f_0(r)r^2}{f(r)r_c^2} - \frac{C^2}{f(r)}\right]dr_c^2 + 2\left[\frac{f_0(r)r^2}{f(r)r_c^2}\frac{\dot{a}}{a} - \frac{BC}{f(r)}\right]dt_c dr_c \\ &\quad + g^2(\tilde{r})\tilde{r}^2\Big(d\theta^2 + \sin^2\theta d\phi^2\Big) \ . \end{aligned} \tag{15}$$

Imposing the condition that the final form of the metric is *isotropic* and *diagonal*, we get

$$B = r\frac{\dot{a}}{a}\frac{f_0(r)}{f(r)}\sqrt{f(r)}\Big[\frac{f_0(r)}{f(r)} - 1\Big]^{-1/2} \quad ; \quad C = \frac{r}{r_c}\sqrt{f(r)}\Big[\frac{f_0(r)}{f(r)} - 1\Big]^{1/2} . \tag{16}$$

Thus, we determine dt and dr in terms of dt_c and dr_c. Using this relation, we can determine dt_c and dr_c in terms of dt and dr which in turn gives ∂_{t_c} and ∂_{r_c}. Finally using the normalisation condition $g_{\mu\nu}U^\mu U^\nu = -1$ and also the relation between the four velocity of the co-moving observer with respect to the static observer as

$$g_{\mu\nu}U_s^\mu U_c^\nu = -\frac{1}{\sqrt{1-v^2}} \tag{17}$$

we can determine the velocity of the co-moving frame with respect to the static frame.
Using the above algorithm the velocity (v) of the comoving observer takes the form [208]

$$|\vec{v}| = \sqrt{1 - \frac{f(r)}{f_0(r)}}. \tag{18}$$

$f(r)$ is the lapse function with cosmological constant (Λ), whereas $f_0(r)$ is devoid of that term. Besides Λ appears in the lapse function as $\frac{\Lambda}{3}r^2 = \frac{H_0^2}{c^2}r^2$. For $c = 1$, we get $\frac{\Lambda}{3}r^2 = H_0^2 r^2$. Thus, the velocity of the co-moving observer becomes

$$|\vec{v}| = \frac{H_0 r}{\sqrt{f_0(r)}}. \tag{19}$$

Bibliography

[1] S. Chandrasekhar, *The Mathematical Theory of Black Holes*, Oxford University Press, New York, (1992).

[2] V. P. Frolov, and I. D. Novikov, *Black Hole Physics: Basic Concepts and New Developments*, Kluwer Academic Publishers, NetherLands, (1998).

[3] V. P. Frolov, and A. Zelnikov, *Introduction to Black Hole Physics*, Oxford University Press, Oxford, UK (2015).

[4] F. LeBlanc, *An Introduction to Stellar Astrophysics*, Wiley Publications, (2010).

[5] S. Chandrasekhar, *An Introduction to the Study of Stellar Structure*, Dover Publications, (2010).

[6] R. Kippenhahn, A. Weigart, and, A. Weiss, *Stellar Structure and Evolution*, Springer, (2012).

[7] G.S. Bisnovatyi-Kogan, and S. K. Chakrabarti, *Observational Evidence for Black Holes in the Universe: Proceedings of a Conference held in Calcutta, India*, Springer, NetherLands, (1999).

[8] The LIGO Collaboration, *Observation of Gravitational Waves from a Binary Black Hole Merger*, *Phys. Rev. Lett.* **116** (2016) 061102.

[9] Event Horizon Telescope Collaboration, *First M87 Event Horizon Telescope Results. I. The Shadow of the Supermassive Black Hole*, *Astrophys. J. Lett.* **875** (2019) L1.

[10] C. Bambi, *Black Holes: A Laboratory for Testing Strong Gravity*, Springer (2017).

[11] A. Einstein, *Ann. Phys.* **49** (1916) 769 (*Ann. Phys.* **14** (2005) 517).

[12] K. Schwarzschild, *Sitzber. Dent. Akad. Wiss.*, Berlin *K1. Math.-Phys. Tech.* 189 (1916).

[13] D. Finkelstein, *Past-Future Asymmetry of the Gravitational Field of a Point Particle*, *Phys. Rev.*, **110** (1958) 965–967.

[14] R. P. Kerr, *Gravitational Field of a Spinning Mass as an Example of Algebraically Special Metrics*, *Phys. Rev. Lett.* **11** (1963) 237.

[15] E. T. Newman et al, *Metric of a Rotating, Charged Mass*, *J. Math. Phys.* **6** (1965) 918-919.

[16] W. Israel, *Event Horizons in Static Vacuum Space-Times Phys. Rev.* **164** (1967) 1776.

[17] B. Carter, *Axisymmetric Black Hole Has Only Two Degrees of Freedom Phys. Rev. Lett.* **26** (1971) 331.

[18] D.C. Robinson, *Uniqueness of the Kerr Black Hole Phys. Rev. Lett.* **34** (1975) 905.

[19] C. W. Misner, K. S. Thorne, and J. A. Wheeler, *Gravitation*, Princeton University Press, USA (1973).

[20] I. Kuntz, *Gravitational Theories Beyond General Relativity* (Doctoral Thesis), Springer (2019).

[21] R. Penrose, *Gravitational Collapse and Space-Time Singularities*, *Phys. Rev. Lett.* **14** (1965) 57.

[22] S.W. Hawking, and R. Penrose, *The Singularities of Gravitational Collapse and Cosmology*, *Proc. Roy. Soc. Lond. A* **314** (1970) 529.

[23] R. Penrose, *Gravitational collapse: The role of general relativity*, *Riv. Nuovo Cim.* **1** (1969) 252 (*Gen. Rel. Grav.* **34** (2002) 1141).

[24] Y. B. Zel'dovich, *The Fate of a Star and the Evolution of Gravitational Energy upon Accretion*, *Sov. Phys. Doklady* **9** (1964) 195–197.

[25] E. Salphater, *Accretion of interstellar matter by massive objects*, *Astrophys. J.*, **140** (1964) 796-800.

[26] C. T. Bolton, *Identification of Cygnus X-1 with HDE 226868*, *Nature*, **235**, (1972) 271–273.

[27] B. L. Webster, and P. Murdin, *Cygnus X-1 – a Spectroscopic Binary with a Heavy Companion?*, *Nature*, **235**, (1972) 37–38.

[28] D. Lüst, and W. Vleeshouwers, *Black Hole Information and Thermodynamics*, Springer (2019).

[29] S. W. Hawking, *Particle Creation by Black Holes*, *Commun. Math. Phys.*, **43** (1975) 199–220.

[30] J.M. Bardeen, B. Carter, and S. W. Hawking, *The four laws of black hole mechanics*, *Commun.Math. Phys.* **31** (1973) 161–170.

[31] R. M. Wald, *The Thermodynamics of Black Holes*, *Living Rev. in Rel.* **4**, (2001) 6.

[32] S. Carlip, *Quantum gravity: a progress report*, *Rep. Prog. Phys.*, **64** (2001) 885.

[33] C. Kiefer, *Quantum gravity: general introduction and recent developments*, *Ann.Phys. (Leipzig)* **15** (2006) 1-2, 129-148.

[34] C. Rovelli, *Loop Quantum Gravity*, *Living Rev. Relativ.* **11** (2008) 5.

[35] A. Ashtekar, and E. Bianchi, *A short review of loop quantum gravity*, *Rep. Prog. Phys.* (2021) 042001.

[36] C. Bambi, *Astrophysical Black Holes: A Compact Pedagogical Review*, *Ann. Phys. (Berlin)*, (2018) 1700430.

[37] R.A. Remillard, and J.E. McClintock, *X-ray Properties of Black-Hole Binaries*, *Ann. Rev. Astron. Astrophys.* **44**, (2006) 49.

[38] A. Gould, *Measuring the Remnant Mass Function of the Galactic Bulge*, *Astrophys. J.* **535** (2000) 928.

[39] L. Wyrzykowski et al, *Black hole, neutron star and white dwarf candidates from microlensing with OGLE-III*, *Mon. Not. Roy. Astron. Soc.*, **458** (2016) 3012.

[40] J. Kormendy, and D. Richstone, *nward Bound—The Search For Supermassive Black Holes In Galactic Nuclei*, *Ann. Rev. Astron. Astrophys.* **33** (1995) 581.

[41] M. C. Miller, and E. J. M. Colbert, *Intermediate-Mass Black Holes*, *Int. J. Mod. Phys. D* **13** (2004) 1.

[42] The LIGO Collaboration, *GW190521: A Binary Black Hole Merger with a Total Mass of 150* $M_\odot$, *Phys. Rev. Lett.* **125** (2020) 101102.

[43] K. C. Jacobs, and P. O. Seitzer, *Mini-Black-Holes Are Forming Now*, *Gen. Relativ. Gravit.* **8** (1977) 1, 7-13.

[44] B. J. Carr, and S. B. Giddings, *Quantum black holes*, *Scientific American* **292** (2005) 48-55.

[45] S. W. Hawking, *Gravitationally collapsed objects of very low mass*, *Mon. Not. Roy. Astron. Soc.*, **152** (1971) 75.

[46] S.N. Zhang, W. Cui, and W. Chen, *Black Hole Spin in X-Ray Binaries: Observational Consequences*, *Astrophys. J.* **482** (1997) 2, L155-L158.

[47] L. W. Brenneman, and C. S. Reynolds, *Constraining Black Hole Spin via X-Ray Spectroscopy*, *Astrophys. J.* **652** (2006) 1028.

[48] A. R. Ingram, and S. E. Motta, *A review of quasi-periodic oscillations from black hole X-ray binaries: Observation and theory*, *New Astron. Rev.*, **85** (2019) 101524.

[49] H. Falcke, F. Melia, and E. Agol, *Viewing the shadow of the black hole at the Galactic center*, *Astrophys. J. Lett.* **528** (2000) L13.

[50] Event Horizon Telescope Collaboration, *First M87 Event Horizon Telescope Results. II. Array and Instrumentation*, *Astrophys. J. Lett.* **875** (2019) L2.

[51] Event Horizon Telescope Collaboration, *First M87 Event Horizon Telescope Results. III. Data Processing and Calibration*, *Astrophys. J. Lett.* **875** (2019) L3.

[52] Event Horizon Telescope Collaboration, *First M87 Event Horizon Telescope Results. IV. Imaging the Central Supermassive Black Hole*, *Astrophys. J. Lett.* **875** (2019) L4.

[53] Event Horizon Telescope Collaboration, *First M87 Event Horizon Telescope Results. V. Physical Origin of the Asymmetric Ring*, *Astrophys. J. Lett.* **875** (2019) L5.

[54] Event Horizon Telescope Collaboration, *First M87 Event Horizon Telescope Results. VI. The Shadow and Mass of the Central Black Hole*, *Astrophys. J. Lett.* **875** (2019) L6.

[55] Event Horizon Telescope Collaboration, *First M87 Event Horizon Telescope Results. VII. Polarization of the Ring*, *Astrophys. J. Lett.* **910** (2021) L12.

[56] Event Horizon Telescope Collaboration, *First M87 Event Horizon Telescope Results. VIII. Magnetic Field Structure near The Event Horizon*, *Astrophys. J. Lett.* **910** (2021) L13.

[57] Event Horizon Telescope Collaboration, *Polarimetric properties of Event Horizon Telescope targets from ALMA, Goddi, Martí-Vidal, Messias, and the EHT Collaboration*, *Astrophys. J. Lett.* **910** (2021) XX.

[58] Event Horizon Telescope Collaboration, *First Sagittarius A* Event Horizon Telescope Results. I. The Shadow of the Supermassive Black Hole in the Center of the Milky Way*, *Astrophys. J. Lett.* **930** (2022) L12.

[59] Event Horizon Telescope Collaboration, *First Sagittarius A* Event Horizon Telescope Results. II. EHT and Multiwavelength Observations, Data Processing, and Calibration*, *Astrophys. J. Lett.* **930** (2022) L13.

[60] Event Horizon Telescope Collaboration, *First Sagittarius A* Event Horizon Telescope Results. III. Imaging of the Galactic Center Supermassive Black Hole*, *Astrophys. J. Lett.* **930** (2022) L14.

[61] Event Horizon Telescope Collaboration, *First Sagittarius A* Event Horizon Telescope Results. IV. Variability, Morphology, and Black Hole Mass*, *Astrophys. J. Lett.* **930** (2022) L15.

[62] Event Horizon Telescope Collaboration, *First Sagittarius A* Event Horizon Telescope Results. V. Testing Astrophysical Models of the Galactic Center Black Hole*, *Astrophys. J. Lett.* **930** (2022) L16.

[63] Event Horizon Telescope Collaboration, *First Sagittarius A* Event Horizon Telescope Results. VI. Testing the Black Hole Metric*, *Astrophys. J. Lett.* **930** (2022) L17.

[64] S. Caroll, *Spacetime and Geometry: An Introduction to General Relativity*, Addison Wesley (2003).

[65] L. Ryder, *Introduction to General Relativity*, Cambridge University Press (2009).

[66] S. Weinberg, *Gravitation and Cosmology:Principles and applications of the General Relativity*, Wiley Publications (1971).

[67] A. Das, *Lectures on Gravitation*, World Scientific Publishing (2011).

[68] E. Teo, *Spherical Photon Orbits around a Kerr Black Hole*, *Gen. Relativ. Gravit.* **35** (2003) 11.

[69] E. Teo, *Spherical orbits around a Kerr Black Hole*, *Gen. Relativ. Gravit.* **53** (2021) 10.

[70] E. Berti, V. Cardoso, and A. O. Starinets, *Quasinormal modes of black holes and black branes*, *Class. Quantum Grav.* **26** (2009) 163001.

[71] R. A. Konoplya, and A. Zhidenko, *Quasinormal modes of black holes: From astrophysics to string theory*, *Rev. Mod. Phys* **83** (2011) 793.

[72] V. Cardoso et al., *Geodesic stability, Lyapunov exponents, and quasinormal modes*, *Phys. Rev. D* **79** (2009) 064016.

[73] K. Jusufi, *Quasinormal modes of black holes surrounded by dark matter and their connection with the shadow radius*, *Phys. Rev. D* **101** (2020) 084055.

[74] K. Jusufi, *Connection between the shadow radius and quasinormal modes in rotating spacetimes*, *Phys. Rev. D* **101** (2020) 124063.

[75] R. Penrose, R.M. Flyod, *Extraction of rotational energy from a black hole*, *Nature Physical Science*, **229** (1971) 177-179.

[76] M. Bhat, S. Dhurandhar and N. Dadhich, *Energetics of the Kerr-Newman black hole by the penrose process*, *J. Astrophys. Astr.*, **6** (1985) 85−100.

[77] R. D. Blandford, and R. L. Znajek, *Electromagnetic extraction of energy from Kerr black holes*, *Mon. Not. R. Astron. Soc.*, **179** (1977) 3, 433-456.

[78] C. Bambi, *Astrophysics of Black Holes*, Springer (2016).

[79] V. Perlick, and O. Yu. Tsupko, *Calculating black hole shadows: Review of analytical studies*, *Phys. Reps.* **947** (2022) 1-39.

[80] J. L. Synge, *The escape of photons from gravitationally intense stars*, *Mon. Not. R. Astron. Soc.* **131** (1966) 463-466.

[81] J. M. Bardeen, *Timelike and null geodesics in the Kerr metric*, *Black holes (Les astres occlus)* (1973) 215-239.

[82] P. J. Young, *Capture of particles from plunge orbits by a black hole*, *Phys. Rev. D* **14** (1976) 3281.

[83] J. P. Luminet, I*mage of a spherical black hole with thin accretion disk*, *Astron. Astrophys.* **75** (1979) 228.

[84] J. P. Luminet, *Seeing black holes: From the computer to the telescope*, *Universe* **4** (2018) 86.

[85] I. G. Dymnikova, *Motion of particles and photons in the gravitational field of a rotating body*, *Sov. Phys. Usp.* **29** (1986) 215.

[86] J. Fukue, *Silhouette of a dressed black hole*, *Publ. Astron. Soc. Japan* **55** (2003) 155.

[87] A.E. Broderick, A. Loeb, *Imaging the black hole silhouette of M87: Implications for jet formation and black hole spin*, *Astrophy. J.* **697** (2009) 1164.

[88] T. Johannsen, D. Psaltis, *Testing the no-hair theorem with observations in the electromagnetic spectrum. II. Black hole images*, *Astrophys. J.* **718** (2010) 446.

[89] M.D. Johnson, A. Lupsasca, A. Strominger, et al, *Universal interferometric signatures of a black hole's photon ring*, *Science Advances* **6** (2020) 12.

[90] S.E. Gralla, D. E. Holz, R.M. Wald, *Black hole shadows, photon rings, and lensing rings*, *Phys. Rev. D* **100** (2019) 024018.

[91] P. V. P. Cunha, and C. Herdeiro, *Shadows and strong gravitational lensing: a brief review*, *Gen.Rel.Grav.* **50** (2018) 4, 42.

[92] A. Chowdhuri, S. Ghosh, and A. Bhattacharya, *A review on analytical studies in Gravitational Lensing*, *Front. Phys.* **11** (2023) 1113909.

[93] V. Perlick, O. Yu. Tsupko, G. S. Bisnovatyi-Kogan, *Black hole shadow in an expanding universe with a cosmological constant*, *Phys. Rev. D* **97** (2018) 104062.

[94] A. E. Vazquez, and E. P. Esteban, *Nuovo Cim. B* **119** (2004) 489.

[95] A. Grenzebach, V. Perlick, C. Lämmerzahl, *Photon Regions and Shadows of Kerr-Newman-NUT Black Holes with a Cosmological Constant*, *Phys. Rev. D* **89** (2014) 124004.

[96] A. Saha, S. Madhav Modumudi and S. Gangopadhyay, *Shadow of a noncommutative geometry inspired Ayón Beato García black hole*, *Gen. Rel. Grav.* **50** (2018) 103.

[97] A. Grenzebach, *The Shadow of Black Holes: An Analytic Description*, Springer (2016).

[98] D. Lebedev and K. Lake, *On the influence of the cosmological constant on trajectories of light and associated measurements in Schwarzschild de Sitter space*, arXiv:1308.4931.

[99] D. Lebedev and K. Lake, *Relativistic aberration and the cosmological constant in gravitational lensing I: Introduction*, arXiv:1609.05183.

[100] F. F. Chen, *Introduction to Plasma Physics*, Plenum Press, New York (1974).

[101] C. Chiuderi, and M. Velli, *Basics of Plasma Astrophysics*, Springer (2015).

[102] S. Chandrasekhar, *Plasma Physics*, The University of Chicago Press, USA (1960).

[103] J. L. Synge, *Relativity. The General Theory*, North-Holland, Amsterdam, (1960).

[104] A. Rogers, *Frequency-dependent effects of gravitational lensing within plasma*, *Mon. Not. Royal Astron. Soc.* **451** (2015) 1, 17-25.

[105] V. Perlick, O. Yu. Tsupko, *Light propagation in a plasma on Kerr spacetime: Separation of the Hamilton-Jacobi equation and calculation of the shadow*, *Phys. Rev. D* **95** (2017) 104003.

[106] A. Das, A. Saha and S. Gangopadhyay, *Shadow of charged black holes in Gauss—Bonnet gravity*, *Eur. Phys. J. C*, **80** (2020) 180.

[107] R. A. Breuer, J. Ehlers, *Propagation of electromagnetic waves through magnetized plasmas in arbitrary gravitational fields*, *Astron. Astrophys.* **96** (1981) 1-2, 293-295.

[108] K. Hioki and K.I. Maeda, *Measurement of the Kerr spin parameter by observation of a compact object's shadow*, *Phys. Rev. D* **80** (2009) 024042.

[109] A de Vries, *The apparent shape of a rotating charged black hole, closed photon orbits and the bifurcation set A_4*, *Class. Quantum Grav.* **17** (2000) 123

[110] A. Övgün, İ. Sakallı and J. Saavedraa, *Shadow cast and deflection angle of Kerr-Newman-Kasuya spacetime*, *JCAP* **10** (2018) 041.

[111] S. W. Wei, Y. C. Zou, Y. X. Liu, R. B. Mann, *Curvature radius and Kerr black hole shadow*, *JCAP* **08** (2019) 030.

[112] A. Abdujabbarov, M. Amir, B. Ahmedov and S. G. Ghosh, *Shadow of rotating regular black holes*, *Phys. Rev. D* **93** (2016) 104004.

[113] M. Wang, S. Chen, J. Jing, *Shadow casted by a Konoplya-Zhidenko rotating non-Kerr black hole*, *JCAP* **10** (2017) 051.

[114] A. K. Mishra, S. Chakraborty, S. Sarkar, *Understanding photon sphere and black hole shadow in dynamically evolving spacetimes*, *Phys. Rev. D* **99** (2019) 104080.

[115] R. Kumar, B. P. Singh, S. G. Ghosh, *Shadow and deflection angle of rotating black hole in asymptotically safe gravity*, *Annals Phys.* **120** (2020) 168252.

[116] R. A. Hennigar, M. B. J. Poshteh, and R. B. Mann, *Shadows, signals, and stability in Einsteinian cubic gravity*, *Phys. Rev. D* **97** (2018) 064041.

[117] H. Khodabakhshi, A. Giaimo, R. B. Mann, *Einstein Quartic Gravity: Shadows, Signals, and Stability*, *Phys. Rev. D* **102** (2020) 044038.

[118] M. Amir, S. G. Ghosh, *Shapes of rotating nonsingular black hole shadows*, *Phys. Rev. D* **94** (2016) 024054.

[119] R. Shaikh, *Black hole shadow in a general rotating spacetime obtained through Newman-Janis algorithm*, *Phys. Rev. D* **100** (2019) 024028.

[120] E. Contreras, Á. Rincón, G. Panotopoulos, P. Bargueño, and B. Koch, *Black hole shadow of a rotating scale-dependent black hole*, *Phys. Rev. D* **101** (2020) 064053.

[121] H. Lü and H. D. Lyu, *Schwarzschild black holes have the largest size*, *Phys. Rev. D* **101** (2020) 044059.

[122] X. H. Feng, H. Lü, *On the size of rotating black holes*, *Eur. Phys. J. C* **80** (2020) 551.

[123] R. Kumar, S. G. Ghosh, and A. Wang, *Gravitational deflection of light and shadow cast by rotating Kalb-Ramond black holes*, *Phys. Rev. D* **101** (2020) 104001.

[124] L. Ma, H. Lü, *Bounds on photon spheres and shadows of charged black holes in Einstein-Gauss-Bonnet-Maxwell gravity*, *Phys. Letters B* **807** (2020) 135535.

[125] R. A. Konoplya and A. Zhidenko, *Analytical representation for metrics of scalarized Einstein-Maxwell black holes and their shadows*, *Phys. Rev. D* **100** (2019) 044015.

[126] R. Kumar, S. G. Ghosh, and A. Wang, *Shadow cast and deflection of light by charged rotating regular black holes*, *Phys. Rev. D* **100** (2019) 124024.

[127] S. Dastan, R. Saffari, S. Soroushfar, *Shadow of a Kerr-Sen dilaton-axion Black Hole*, arXiv:1610.09477 [gr-qc].

[128] L. Amarilla, E. F. Eiroa, *Shadow of a rotating braneworld black hole*, *Phys. Rev. D* **85** (2012) 064019.

[129] L. Amarilla, E. F. Eiroa, *Shadow of a Kaluza-Klein rotating dilaton black hole*, *Phys. Rev. D* **87** (2013) 044057.

[130] L. Amarilla, E. F. Eiroa, G. Giribet, *Null geodesics and shadow of a rotating black hole in extended Chern-Simons modified gravity*, *Phys. Rev. D* **81** (2010) 124045.

[131] S. Dastan, R. Saffari, S. Soroushfar, *Shadow of a Charged Rotating Black Hole in f(R) Gravity*, arXiv:1606.06994 [gr-qc].

[132] R. Kumar, B. P. Singh, Md. S. Ali, S. G. Ghosh, *Rotating black hole shadow in Rastall theory*, arXiv:1712.09793 [gr-qc].

[133] T. Vetsov, G. Gyulchev, S. Yazadjiev, *Shadows of Black Holes in Vector-Tensor Galileons Modified Gravity*, arXiv:1801.04592 [gr-qc].

[134] H. M. Wang, Y. M. Xu, S. W. Wei, *Shadows of Kerr-like black holes in a modified gravity theory*, *JCAP* **03** (2019) 046.

[135] V. Perlick, O. Yu. Tsupko, and G. S. Bisnovatyi-Kogan, *Influence of a plasma on the shadow of a spherically symmetric black hole*, *Phys. Rev. D* **92** (2015) 104031.

[136] F. Atamurotov, B. Ahmedov, and A. Abdujabbarov, *Optical properties of black holes in the presence of a plasma: The shadow*, *Phys. Rev. D* **92** (2015) 084005.

[137] M. Sharif, S. Iftikhar , *Shadow of a charged rotating non-commutative black hole*, *Eur. Phys. J. C* **76** (2016) 630.

[138] G. S. Bisnovatyi-Kogan, O. Yu. Tsupko, *Gravitational Lensing in Presence of Plasma: Strong Lens Systems, Black Hole Lensing and Shadow*, *Universe* **3** (2017) 3, 57.

[139] A. Abdujabbarov, B. Toshmatov, Z. Stuchlík and B. Ahmedov, *Shadow of the rotating black hole with quintessential energy in the presence of plasma*, *IJMPD* **26** (2017) 6, 1750051.

[140] Y. Huang, Y. P. Dong and D. J. Liu, *Revisiting the shadow of a black hole in the presence of a plasma*, *IJMPD* **27** (2018) 12, 1850114.

[141] B. Ahmedov, B. Turimov, Z. Stuchlík and A. Tursunov, *Optical properties of magnetized black hole in plasma*, *IJMPD: Conference Series* **49** (2019) 1960018.

[142] G. Z. Babar, A. Z. Babar, F. Atamurotov, *Optical properties of Kerr–Newman spacetime in the presence of plasma*, *Eur. Phys. J. C* **80** (2020) 761.

[143] A. Chowdhuri, A. Bhattacharyya, *Shadow analysis for rotating black holes in the presence of plasma for an expanding universe*, *Phys. Rev. D* **104** (2021) 064039.

[144] R. G. Cai, *Gauss-Bonnet black holes in AdS spaces*, *Phys. Rev. D* **65** (2002) 084014.

[145] R. G. Cai, and Q. Guo, *Gauss-Bonnet black holes in dS spaces*, *Phys. Rev. D* **69** (2004) 104025.

[146] H. C. Kim, and R. G. Cai, *Slowly rotating charged Gauss-Bonnet black holes in AdS spaces*, *Phys. Rev. D* **77** (2008) 024045.

[147] J. Polchinski, *String theory Vol.I*, Cambridge University Press, (2005).

[148] B. Zweibach, *A First Course in String Theory*, Cambridge University Press, (2009).

[149] C. Garraffo, and G. Giribet, *The Lovelock Black Holes*, *Mod. Phys. Lett. A* **23** (2008) 1801-1818.

[150] D. Lovelock, *Divergence-free tensorial concomitants*, *Aeq. Math.* **4** (1970) 27-38.

[151] D. Lovelock, *The Einstein tensor and its generalizations*, *J.Math.Phys.* **12** (1971) 498-501.

[152] A. Abdujabbarov et al., *Energetics and optical properties of 6-dimensional rotating black hole in pure Gauss-Bonnet gravity*, *Eur. Phys. J. C.* **75** (2015) 399.

[153] R. Kumar, and S. G. Ghosh, *Rotating black holes in 4D Einstein-Gauss-Bonnet gravity and its shadow*, *JCAP* **07** (2020) 053.

[154] J. Maldacena, *The Large-N Limit of Superconformal Field Theories and Supergravity*, *International Journal of Theoretical Physics* **38** (1999) 1113–1133.

[155] G. T. Horowitz, and V. E. Hubeny, *Quasinormal modes of AdS black holes and the approach to thermal equilibrium*, *Phys. Rev. D* **62** (2000) 024027.

[156] A. Das, A. Saha, and S. Gangopadhyay, *Investigation of circular geodesics in a rotating charged black hole in the presence of perfect fluid dark matter*, *Class. Quantum Grav.* **38** (2021) 065015.

[157] A. Das, A. Saha, and S. Gangopadhyay, *Study of circular geodesics and shadow of rotating charged black hole surrounded by perfect fluid dark matter immersed in plasma*, *Class. Quantum Grav.* **39** (2022) 075005.

[158] Z. Xu, X. Hou, J. Wang, *Kerr-anti-de Sitter/de Sitter black hole in perfect fluid dark matter background*, *Class. Quantum Grav.* **35** (2018) 115003.

[159] S. Haroon, M. Jamil, K. Jusufi, K. Lin and R. B. Mann, *Shadow and deflection angle of rotating black holes in perfect fluid dark matter with a cosmological constant*, *Phys. Rev. D* **99** (2019) 044015.

[160] V. V. Kiselev, *Quintessence and black holes*, *Class. Quantum Grav.* **20** (2003) 6, 1187.

[161] V. V. Kiselev, *Quintessential solution of dark matter rotation curves and its simulation by extra dimensions*, arXiv: 0303031 [gr-qc].

[162] M. H. Li, K. C. Yang, *Galactic dark matter in the phantom field*, *Class. Quantum Grav.* **86** (2012) 123015.

[163] A. Das, A. Saha, and S. Gangopadhyay, *Shadow of Kottler black hole in the presence of plasma for a co-moving observer*, *Class. Quantum Grav.* **40** (2023) 015008.

[164] C. Rovelli, *Covariant Loop quantum Gravity*, Cambridge University Press (2014).

[165] D. G. Boulware, and S. Deser, *String-Generated Gravity Models*, *Phys. Rev. Lett.* **55** (1985) 2656.

[166] P. V.P. Cunha et.al, *Shadows of Einstein–dilaton–Gauss–Bonnet black holes Phys. Lett. B* **768** (2017) 373-379.

[167] D. Raine, and E. Thomas, *Black Holes An Introduction*, Imperial College Press, London (2005).

[168] U. Papnoi et al., *Shadow of five-dimensional rotating Myers-Perry black hole*, *Phys. Rev. D* **90** (2014) 024073.

[169] S. W. Wei, and Y. X. Liu, *Observing the shadow of Einstein-Maxwell-Dilaton-Axion black hole*, *JCAP* **11** (2013) 063.

[170] Y. Décanini, A. Folacci, and B. Raffaelli, *Fine structure of high-energy absorption cross sections for black holes*, *Class. Quantum Grav.* **28** (2011) 175021.

[171] B. P. Singh, and S. G. Ghosh, *Shadow of Schwarzschild–Tangherlini black holes*, *Ann. of Phys.* **395** (2018) 127-137.

[172] K. Hashimoto, S. Kinoshita, and K. Murata, *Einstein Rings in Holography*, *Phys. Rev. Lett.* **123** (2019) 031602.

[173] Y. Liu et al., *Holographic Einstein ring of a charged AdS black hole*, *J. High Energ. Phys.* **2022** (2022) 189.

[174] X. X. Zeng et al., *Holographic Einstein rings of a Gauss-Bonnet AdS black hole*, arXiv:2302.03692v2 [gr-qc].

[175] K. Garett, and G. Duda, *Dark Matter: A Primer*, *2011* (2010) 968283.

[176] G. Bertone, and D. Hooper, *History of dark matter*, *Rev. Mod. Phys.* **90** (2018) 045002.

[177] V. C. Rubin, Jr. W. K. Ford, and N. Thonnard, *Rotational properties of 21 SC galaxies with a large range of luminosities and radii, from NGC 4605 (R=4kpc) to UGC 2885 (R=122kpc)*, *Astro. Phys. J.* **238** (1980) 471.

[178] J.F. Navarro, C.S. Frenk and S.D.M. White, *The Structure of Cold Dark Matter Halos*, *Astrophysical Journal*, **462** (1996) 563.

[179] S. Tulin and H. Yu, *Dark matter self-interactions and small scale structure*, *Phys. Rep.* **730** (2018) 1-57.

[180] V.V. Kiselev, *Vector field and rotational curves in dark galactic halos*, *Class. Quant. Grav.*, **22** (2005) 541-558.

[181] F. Zwicky, *The redshift of extragalactic nebulae*, *Helv. Phys.Acta.* **6** (1933) 110.

[182] X. Hou, Z. Xu and J. Wang *Rotating black hole shadow in perfect fluid dark matter*, *JCAP*, **12** (2018) 040.

[183] Z. Xu, X. Hou, J. Wang and Y. Liao, *Perfect Fluid Dark Matter Influence on Thermodynamics and Phase Transition for a Reissner-Nordstrom-Anti-de Sitter Black Hole*, *Adv. in High Energy Phys.*, (2019) 2434390.

[184] B. Toshmatov, A. Abdujabbarov, B. Ahmedov and Z. Stuchlik, *Particle motion and Penrose processes around rotating regular black hole*, *Astrophys. Space Sci.*, **357** (2015) 1, 41.

[185] S. Haroon et al, *The effects of running gravitational coupling on rotating black holes*, *Eur. Phys. J. C*, **78** (2018) 519.

[186] M. Nozawa and K. Maeda, *Energy extraction from higher dimensional black holes and black rings*, *Phys. Rev. D* **71** (2005) 084028.

[187] M. Azreg-Aïnou, *Generating rotating regular black hole solutions without complexification*, *Phys. Rev. D*, **90** (2014) 6, 064041.

[188] E.J.G. de Urreta and M. Socolovsky, *Extended Newman-Janis algorithm for rotating and Kerr-Newman de Sitter and anti de Sitter metrics*, arXiv:1504.01728 [gr-qc].

[189] R. Shaikh, *Black hole shadow in a general rotating spacetime obtained through Newman-Janis algorithm*, *Phys. Rev. D*, **100** (2019) 2, 024028.

[190] Y. Heyderzade and F. Darabi, *Black hole solutions surrounded by perfect fluid in Rastall theory*, *Physics Letters B*, **771** (2017) 365-373.

[191] R.M. Wald, *General Relativity*, University of Chicago Press, UK (1984).

[192] E.T. Newman and A.I. Janis, *Note on the Kerr Spinning-Particle Metric*, *Journal of Mathematical Physics*, **6** (1965) 915-917.

[193] S. Iftikar and M. Shahzadi, *Circular motion around a rotating black hole in quintessential dark energy*, *Eur. Phys. J. C*, **79** (2019) 6, 473.

[194] E. Hackmann and H. Xu, *Charged particle motion in Kerr-Newmann space-times*, *Phys. Rev. D*, **87** (2013) 12, 124030.

[195] A.N. Aliev and N. Ozdemir, *Motion of charged particles around a rotating black hole in a magnetic field*, *Mon. Not. R. Astron. Soc.*, **336** (2002) 241-248.

[196] R.I. Ivanov and E.M. Prodanov, *Pseudo−Newtonian potential for charged particle in Kerr−Newman geometry*, *Phys. Lett. B*, **611** (2005) 34-38.

[197] C. Q. Liu, C. K. Ding, J. L. Jing, *Effects of Homogeneous Plasma on Strong Gravitational Lensing of Kerr Black Holes*, *Chin. Phys. Lett.* **34** (2017) 9, 090401.

[198] R. Shaikh, K. Pal, K. Pal and T. Sarkar, *Constraining alternatives to the Kerr black hole*, *Mon. Not. Royal Astron. Soc.* **506** (2021), 1229–1236.

[199] K. Hioki and K. Maeda, *Measurement of the Kerr spin parameter by observation of a compact objects shadow*, *Phys. Rev. D* **80** (2009) 024042.

[200] S. Perlmutter et al., *Measurements of Omega and Lambda from 42 High-Redshift Supernovae*, *Astrophys. J.* **517** (1999) 565.

[201] A. G. Riess et al., *Observational Evidence from Supernovae for an Accelerating Universe and a Cosmological Constant Astron. J.* **116** (1998) 1009.

[202] M.P. Hobson, G.P. Efstathiou, A.N. Lasenby, *General Relativity: An Introduction for Physicists*, Cambridge University Press, Cambridge, (2006).

[203] V. Mukhanov, *Physical Foundations of Cosmology*, Cambridge University Press, Cambridge, (2005).

[204] A. Einstein, E.G. Straus, *The influence of the expansion of space on the gravitation fields surrounding the individual stars*, *Rev. Modern Phys.* **17** (1945) 120.

[205] E. Schücking, *Das Schwarzschildsche Linienelement und die Expansion des Weltalls*, *Z. Phys.* **137** (1954) 595.

[206] G.C. McVittie, *The mass-particle in an expanding universe*, *Mon. Not. R. Astron. Soc.* **93** (1933) 325.

[207] F. Kottler, *Über die physikalischen Grundlagen der Einsteinschen Gravitationstheorie*, *Ann. Phys.* (Berlin) **361**, 401 (1918).

[208] R. Roy and S. Chakrabarti, *Study on black hole shadows in asymptotically de Sitter spacetimes*, *Phys. Rev. D* **102** (2020) 024059.

[209] G. S. Bisnovatyi-Kogan and O. Yu. Tsupko, *Shadow of a black hole at cosmological distances*, *Phys. Rev. D* **98** (2018) 084020.

[210] J. T. Firouzjaee and A. Allahyari, *Black hole shadow with a cosmological constant for cosmological observers*, *Eur. Phys. J. C.* **79** (2019) 930.

[211] O. Yu. Tsupko and G. S. Bisnovatyi-Kogan, *First analytical calculation of black hole shadow in McVittie metric*, *IJMPD* **29**, 9 (2020) 2050062.

[212] P. C. Li, M. Guo and B. Chen, *Shadow of a spinning black hole in an expanding universe*, *Phys. Rev. D* **101** (2020) 084041.

[213] A. Chowdhuri and A. Bhattacharyya, *Shadow analysis for rotating black holes in the presence of plasma for an expanding universe*, *Phys. Rev. D* **104** (2021) 064039.

[214] I. I. Cotăescu, *Light from Schwarzschild black holes in de Sitter expanding universe*, *Eur. Phys. J. C.* **81** (2021) 32.

[215] M. Afrin and S. G. Ghosh, *Estimating the Cosmological Constant from Shadows of Kerr de-Sitter Black Holes*, *Universe* **8** (2022) 52.

[216] G. S. Bisnovatyi-Kogan and O. Yu. Tsupko, *Gravitational lensing in a non-uniform plasma* , *Mon. Not. R. Astron. Soc.* **404** (2010) 4.

[217] G. S. Bisnovatyi-Kogan, O. Yu. Tsupko, *Gravitational Lensing in Presence of Plasma: Strong Lens Systems, Black Hole Lensing and Shadow*, *Universe* **3** (2017) 3, 57.

[218] V. Perlick, *Ray Optics, Fermat's Principle, and Applications to General Relativity*, (Springer, Berlin, 2000).

[219] Planck Collaboration, *Planck 2018 results VI. Cosmological parameters*, *Astro. and Astron.* **641** (2020) A6.

[220] T. M. Davis and M. I. Scrimgeour, *Deriving accurate peculiar velocities (even at high redshift)*, *Mon. Not. Royal Astron. Soc.* **442** (2014) 1117-1122.

[221] M. Cappellari et al, *The ATLAS^{3D} project- I. A volume-limited sample of 260 nearby early-type galaxies: science goals and selection criteria*, *Mon. Not. Royal Astron. Soc.* **413** (2011) 2, 813-836.

[222] S. Vagnozzi et al, *Horizon-scale tests of gravity theories and fundamental physics from the Event Horizon Telescope image of Sagittarius A**, arXiv: 2205.07787.

[223] S. G. Ghosh and M. Afrin, *Constraining Kerr-like black holes with Event Horizon Telescope results of Sgr A**, arXiv: 2206.02488.

[224] R. K. Walia, S. G. Ghosh and S. D. Maharaj, *Testing Rotating Regular Metrics with EHT Results of Sgr A**, arXiv: 2207.00078.

[225] I. Sengo, P. V.P. Cunha, C. A. R. Herdeiro and E. Radu, *Kerr black holes with synchronised Proca hair: lensing, shadows and EHT constraints*, arXiv: 2209.06237.

[226] GRAVITY Collaboration, *Deep images of the Galactic center with GRAVITY*, *Astro. and Astron.* **657** (2022) A82.